Politecnico di Milano
School of Civil, Environmental and Land Management Engineering
Master of Science in Civil Engineering

DESCRIPTION AND SIMULATION OF THUNDERSTORM DOWNBURSTS AND THEIR EFFECT ON CIVIL STRUCTURES

MASTER THESIS OF

DARIO RAFAEL FERNANDEZ CASTELLON

SUPERVISOR

PROFESSOR LUCA MARTINELLI

CO-SUPERVISOR

DR FRANCESCO FOTI

SEPTEMBER 12 2018

AKNOWLEGMENTS

First, I want to thank God for allowing me to achieve this important goal in my life. For protecting me when I felt and for taking me by his hand in this difficult period. Also, to my family for their support during this period, my mother and wife but especially to Dario J., with this I want to tell you son that all the things you wish to reach are possible when you have the conviction in your mind and God in your heart.

I would also thank my advisor Dr. Francesco Foti for his incredible and outstanding guidance during this hard period, for his quick answers and accurate assistances. To professor Martinelli for his sage advices and for giving the opportunity of achieving one of the most important goals in my career. And to professor Perotti for his availability and the instructions during the thesis and academic activities highlighting the advices for the construction of the computer codes for convolution integral, mass matrix and modal analysis.

Finally, I dedicate this goal to my colleagues, I would like to inspire you guys in the same way you did for me. You all will always have my admiration and I can only thank God and life to put me in your way. So much I learned in this period from you and hope I could also give you something in return. Especially to Juan, Ricardo, Roxana, Camila, Rafael, Eduardo, Arantxa, Benito and Daniel, the Dream-Team. Without you guys this goal could not be possible.

TABLE OF CONTENTS

CHAPTER 1. INTRODUCTION 16
1.1 A definition of "downburst" 16
1.2 The "discovery" of the downburst: some historical & meteorological remarks........ 17
1.3 Scope of the Current study 21
1.4 Thesis organization........ 22
CHAPTER 2. STATE OF THE ART........ 24
2.1 Wind Engineering Concepts 27
2.1.1 Wind velocity standard decomposition 27
2.1.2 An introduction to the modelling of turbulence........ 29
2.1.3 Evolutionary Power spectrum........ 36
2.2 Sampling information........ 46
2.3 Models based on CFD analysis 47
2.3.1 Impinging jet........ 48
2.3.2 Vortex ring model........ 50
2.3.3 Cooling source model........ 50
2.4 Models based on Wind Tunnel testing 53
2.5 Empirical models........ 55
2.5.1 Vertical profile........ 56
2.5.2 Model: Holmes & Oliver 2000........ 58
2.5.3 Model: Chen & Letchford2004........ 64
2.5.4 MODEL: SOLARI 2017 71
2.5.5 MODEL: CARACOGLIA 2017........ 79
2.5.6 MODEL: CANOR CARACOGLIA DENÖEL 2016........ 84
CHAPTER 3. DOWNBURST OUTFLOW MODEL 88
3.1 Wind velocity decomposition........ 88
3.2 Vertical profile........ 89
3.2.1 Comparison 89
3.2.2 Selection........ 91
3.2.3 Observations 92
3.3 Tracking path........ 92

3.3.1 Hypothesis 92
3.3.2 Initial conditions and geometric quantities 93
3.4 Mean velocity 95
3.4.1 Intensification function from impinging jet model (Radial diffusion) 95
3.4.2 Intensification function from records 98
3.4.3 Selection 99
3.5 PSD function & Integral length scales 99
3.6 Amplitude modulating function 102
3.6.1 μ(t) function (Solari, et al. 2017) 102
3.6.2 Family of functions (Caracoglia and Le 2017) 103
3.6.3 Functions depending on the mean velocity (Chen and Letchford 2004) (Canor, et al. 2016) 104
3.6.4 Selection 105
3.7 Spatial Coherence function 106
3.8 Cross Power Spectrum function 106
3.9 Generation for Single-Point 108
3.9.1 Deterministic mean 108
3.9.2 Random turbulence 110
3.10 Generation for Multi-Point 115
3.10.1 Deterministic mean 115
3.10.2 Random Turbulence 120
CHAPTER 4. SDOF SYSTEM ANALYSIS 123
4.1 Structure 123
4.2 Aerodynamic Forces 124
4.3 Time domain analysis 127
4.3.1 Generation of time histories 127
4.3.2 Direct Integration of the equations of motion 127
4.4 Aeroelastic Damping Study 129
4.4.1 Graphical Result Comparison 132
4.4.2 Numerical Result Comparison 137
4.4.3 Normalized Root Mean Squared Error 137

4.4.4 Study on Natural Frequency 141
4.5 Direct frequency domain analysis 143
4.5.1 Formulation of the Evolutionary Power Spectral Density (EVPSD) 143
4.5.2 Structural frequency response function 144
4.5.3 EPSD of the structural response 145
4.6 Data consistency checks 148
4.6.1 Frequency response function 148
4.7 Parametric Study: Rigid (High frequency) structures 153
4.7.1 Study of the variance 153
4.7.2 Error Measurement 154
4.7.3 Canonical form of the equation of motion 155
4.7.4 Reference period of the downburst 156
4.7.5 Parameters and set 157
4.7.6 Structure input parameters 159
4.7.7 Downburst input parameters 161
4.7.8 Results 162
4.7.9 Conclusions 169
4.8 Parametric Study: Flexible (Low frequency) structures 170
4.8.1 Parameter set 170
4.8.2 Results 172
4.8.3 Numerical approach 185
4.8.4 Response evaluation on time domain 186
4.8.5 Conclusions 190
CHAPTER 5. ASSESSMENT OF FAILURE PROBABILITY 191
5.1 Scope of the analysis 191
5.2 Case of study 191
5.3 Limit state 192
5.4 Deterministic component (mean) 193
5.5 Failure Probability and Reliability Index 193
5.6 Atmospheric Boundary Layer Model 194
5.7 Equivalent Downburst model 195

5.8 Test Setting 201
5.9 Results 202
CHAPTER 6. MDOF SYSTEM ANALYSIS 205
6.1 Wind Field Simulation 205
6.2 Structural Description 205
6.2.1 Mass matrix 205
6.2.2 Stiffness matrix 209
6.2.3 Transformation of coordinates 215
6.2.4 Eigenvalue problem: free vibration 217
6.2.5 Damping matrix 219
6.2.6 Modal coordinates and superposition 221
6.3 Aeroelastic effects on slender structures 222
6.4 Time domain analysis 230
6.1 Direct frequency domain analysis 231
6.2 Numerical Application 232
6.2.1 Structure parameters 233
6.2.2 Aerodynamical Properties 234
6.2.3 Downburst Properties 235
6.2.4 Response 236
6.1 Conclusions 236
CONCLUSIONS 238
References 240
APPENDIX A: Code benchmarking 244
APPENDIX B: SAP 2000 Dynamic testing 259
APPENDIX C: VARIANCE ANALYSIS GRAPHICS 275

LIST OF FIGURES

Figure 1-1: Pattern of uprooted threes. Adapted from: (Wilson and Wakimoto 2001) 18
Figure 1-2:Airflow at the instant of the Flight 66 incident. Adapted from: (Wilson and Wakimoto 2001). 18
Figure 1-3: Doppler Radar of the first downburst record. Adapted from: (Wilson and Wakimoto 2001). 19
Figure 1-4: Downburst vertical structure. Adapted from: (Wilson and Wakimoto 2001) 20
Figure 2-1: Schematic downburst formation. Adapted from (Fujita 1985) 25
Figure 2-2: Captured downburst formation 25
Figure 2-3: 3D scheme of downburst. Adapted from (Robert, 2014) 25
Figure 2-4: wind forces over immersed body 27
Figure 2-5: Taylor hypothesis 29
Figure 2-6: Representation of Autocorrelation function 30
Figure 2-7 Random signals and their autocorrelation function 31
Figure 2-8: Wind components: reference system. 33
Figure 2-9: PSD & Unilateral PSD 34
Figure 2-10: Representation of power spectrum for stationary process. 37
Figure 2-11: Representation of evolutionary spectra for non-stationary process. a) Evolutionary Spectrum b) time sections 38
Figure 2-12: FRF function. 43
Figure 2-13: Fourier analysis representation 46
Figure 2-14: Nyquist frequency- mirror 47
Figure 2-15: CFD models for downburst. Adapted from (Elawady 2016). 48
Figure 2-16: Vertical profile using CFD. Adapted from (Shehata, et al. 2005) 49
Figure 2-17: Peak horizontal velocity (Vref) at 10m height. Adapted from (Shehata, et al. 2005) .. 49
Figure 2-18: Axial force in leg element of tower. Adapted from (Shehata, et al. 2005) 50
Figure 2-19: Downburst formation with cooling source model. Adapted from (Mason, et al., Numerical simulation of downburst winds 2009) 51
Figure 2-20: Downburst formation with cooling source model. Adapted from (Vermire, et al. 2011) 51
Figure 2-21 Vertical Profile. Adapted from (Vermire, et al. 2011) 52
Figure 2-22: Intensification function. Adapted from (Mason, et al. 2009) 52
Figure 2-23: Typical downburst generated in WindEEE Chamber. Adapted from: (Elawady 2016). 53
Figure 2-24: Generic simulation of downburst wind field. Adapted from: (Elawady 2016) 53
Figure 2-25: Generic wind decomposition. Adapted from: (Elawady 2016) 54
Figure 2-26: Downburst geometrical definitions. Adapted from (Elawady 2016) 55
Figure 2-27: Vertical profiles of downburst 58
Figure 2-28: Horizontal profile Holmes 2000 59
Figure 2-29: Table of summary for identification of tracking velocity. Adapted from (Oliver 1992) 60
Figure 2-30: Wind components from Holmes 2000 61

Figure 2-31: Simulated wind speed Holmes 2000 62
Figure 2-32: Data check of impinging jet model 63
Figure 2-33: Andrews AFB downburst- AIRFORCE ONE event 1983 63
Figure 2-34: Downburst foot print-Adapted from (Holmes and Oliver 2000) 64
Figure 2-35: Comparison between downburst vertical profiles. Adapted from Chen 65
Figure 2-36: Kaimal's Power Spectrum vs a) frequency b) circular frequency 67
Figure 2-37: Typical time History of Chen model 70
Figure 2-38: Velocity vertical profile for Solari's model (a) scale of 600m (b) scale of 100m. Adapted from (Solari, et al. 2017) 73
Figure 2-39: γ(t) from the 93 records. Adapted from (G. Solari, M. Burlando, et al. 2015) 74
Figure 2-40: Solari-model normalized PSD 75
Figure 2-41: μ(t) functions from records of downbursts. Adapted from (G. Solari, M. Burlando, et al. 2015) 76
Figure 2-42: Solari model's turbulent component. Adapted from (Solari, et al. 2017). 77
Figure 2-43: Solari-model Time history of Wind velocity. Adapted from (Solari, et al. 2017). 77
Figure 2-44: Time history of downburst registered from WP & WPS. Adapted from (Solari, et al. 2017). 78
Figure 2-45: Caracoglia- plot of amplitude modulating functions. Adapted from (Caracoglia and Le 2017). 82
Figure 2-46: Typical Generation with Model-Caraclogia. Adapted from (Caracoglia and Le 2017). 82
Figure 2-47: Comparison between amplitude modulating functions and AFB record. Adapted from (Caracoglia and Le 2017). 83
Figure 2-48:Von Karman's PSD 86
Figure 2-49: Amplitude modulating function 86
Figure 3-1:Vertical nosed profile of downburst empirical models 90
Figure 3-2: equivalent velocity profile for boundary layer model 90
Figure 3-3:Vertical profile comparison 91
Figure 3-4: Table of summary for identification of tracking velocity. Adapted from (Oliver 1992). 92
Figure 3-5 Graphical representation of downburst & structure model (Observation points) 93
Figure 3-6: Downburst track plan view 94
Figure 3-7: Impinging Jet model from for downburst. Adapted from (Caracoglia and Le 2017) 96
Figure 3-8: Radial velocity profile 97
Figure 3-9: Υ(t) function. Adapted from (G. Solari, M. Burlando, et al. 2015) 98
Figure 3-10: Solari's model time history generation. Adapted from (Solari, et al. 2017). 99
Figure 3-11: Fit of PSD function for Lv=30m. adapted from Solari 2015. 100
Figure 3-12: Table of Integral length scales. Adapted from Solari 2015. 101
Figure 3-13:Von Karman's PSD 102
Figure 3-14: Solari's μ(t) function. Adapted from (G. Solari, M. Burlando, et al. 2015). 102
Figure 3-15: Family of amplitude modulating functions. Adapted from (Caracoglia and Le 2017) 104
Figure 3-16: Amplitude modulating function 106

Figure 3-17: Vertical profile 109
Figure 3-18: Mean velocity component 109
Figure 3-19: Time function a(t) 110
Figure 3-20:Shape of Unilateral PSD 111
Figure 3-21: Turbulence random generation 112
Figure 3-22: Random generation of Wind velocity field 113
Figure 3-23: Synchronization process of wind components 114
Figure 3-24: Desynchronization process of wind components 114
Figure 3-25: 2D frame with 3D downburst. Front view 116
Figure 3-26: Downburst track. Plan view 116
Figure 3-27: Mean velocity and approximation angle for track angle of 2° 117
Figure 3-28: Mean velocity and approximation angle for track angle of 10° 118
Figure 3-29: Mean velocity and approximation angle for track angle of 15° 119
Figure 3-30: Mean velocity and approximation angle for track angle of 30° 119
Figure 3-31: Mean velocity and approximation angle for track angle of 45° 120
Figure 3-32: Turbulent component of generic point 122
Figure 3-33: Full velocity outflow of generic point 122
Figure 4-1: a) Simple Structure b) equivalent SDOF system 123
Figure 4-2: Normalized-Aeroelastic damping coefficient 131
Figure 4-3: Generic simulation time history comparison 133
Figure 4-4: Comparison of Time varying maximum 134
Figure 4-5: Comparison of Time varying mean 135
Figure 4-6: Comparison of Time varying variance 136
Figure 4-7: Dynamic effect on the aeroelastic damping behavior. 142
Figure 4-8:EVPSD of turbulent component 144
Figure 4-9: a) Impulse Response Function f_n=3.35hz ζ=2% b) amplitude modulating function 147
Figure 4-10: EVPSD of the displacement 148
Figure 4-11. Graphic comparison of Transfer functions, t=152 [sec] dt=0.05[sec] 149
Figure 4-12: Graphical comparison, increased resolution, t=152 [sec]. dt=0.01[sec] 150
Figure 4-13: Comparison of FRF of the three approaches, t=152 [sec]. dt=0.2[sec] 151
Figure 4-14: FRF comparison Increasing resolution, t=152 [sec] dt=0.1[sec] 151
Figure 4-15: EFRF Analytical Figure 4-16: EFRF Function Numerical 152
Figure 4-17: Mean velocity component 156
Figure 4-18: Cross section 159
Figure 4-19: Displacement time history 161
Figure 4-20: Peak Index of the variance comparison β(1.04x10-4 to 1.99x10-3) ζ(0.8 to 4 [%]). ... 162
Figure 4-21: NRMSE of the variance comparison β(1.04x10-4 to 1.99x10-3) ζ(0.8 to 4 [%]). 163
Figure 4-22: Graphical comparison of the variance β=1.04e-4 ζ=0.8% 164
Figure 4-23: Graphical comparison of the variance β=1.36e-3 ζ=4% 164
Figure 4-24: Graphical comparison of the variance β=1.04e-4 ζ=1.2% 165

Figure 4-25: Graphical comparison of the variance β=1.99e-3 ζ=4% 165
Figure 4-26: Convergence check for maximum value of variance in time domain 166
Figure 4-27: Convergence check for mean value of variance in time domain 167
Figure 4-28: Convergence check for Index parameter of the comparison 167
Figure 4-29: Convergence check for NRMSE of the comparison. 168
Figure 4-30: Peak Index of the variance comparison Tn(0.5 to 10) ζ(0.1 to 1.5 [%]). 172
Figure 4-31: NRMSE of the variance comparison Tn(0.5 to 10) ζ(0.1 to 1.5 [%]) 173
Figure 4-32:Var. Comp. Tn=0.5 sec ζ=0.1% 174
Figure 4-33:Var. Comp. Tn=0.5 sec ζ=0.5% 174
Figure 4-34:Var. Comp. Tn=0.5 sec ζ=1% 175
Figure 4-35:Var. Comp. Tn=0.5 sec ζ=1.5% 175
Figure 4-36:Var. Comp. Tn=1 sec ζ=0.1% 176
Figure 4-37:Var. Comp. Tn=1 sec ζ=0.5% 176
Figure 4-38:Var. Comp. Tn=1 sec ζ=1% 177
Figure 4-39:Var. Comp. Tn=1 sec ζ=1.5% 177
Figure 4-40:Von Karman spectrum 178
Figure 4-41:Var. Comp. Tn=5 sec ζ=0.1% 178
Figure 4-42:Var. Comp. Tn=10 sec ζ=0.1% 179
Figure 4-43:Var. Comp. Tn=5 sec ζ=1% 179
Figure 4-44:Var. Comp. Tn=5 sec ζ=1.5% 180
Figure 4-45:Var. Comp. Tn=10 sec ζ=1% 180
Figure 4-46:Var. Comp. Tn=10 sec ζ=1.5% 181
Figure 4-47:Amplitude modulating function 182
Figure 4-48:Impulse response function for Tn=0.5 sec ζ=0.1% 182
Figure 4-49:Impulse response function for Tn=0.5 sec ζ=1% 183
Figure 4-50:Impulse response function for Tn=10 sec ζ=0.1% 184
Figure 4-51:Impulse response function for Tn=10 sec ζ=1% 184
Figure 4-52: Variance computed for the time domain Tn=10[sec], ζ=0.1% 185
Figure 4-53: Comparison of the Variance computed for the time domain and frequency domain Tn=10[sec], ζ=0.1% 186
Figure 4-54: Input/output comparison. Tn=0.32 sec and ζ=2%. 187
Figure 4-55: Input/output comparison. Tn=0.5 sec and ζ=2%. 187
Figure 4-56: Input/output comparison. Tn=0.5 sec and ζ=0.5%. 188
Figure 4-57: Input/output comparison. Tn=0.5 sec and ζ=0.1%. 188
Figure 4-58: Input/output comparison. Tn=10 sec and ζ=2%. 189
Figure 4-59: Input/output comparison. Tn=10 sec and ζ=0.1%. 189
Figure 5-1 Structure reduced model a) Real structure b) equivalent 1mode structure c) equivalent 1dof system 191
Figure 5-2: Structural behavior of cantilever beam 192
Figure 5-3: Vertical profile ABL model 194

Figure 5-4: Vertical profile vmax=25 m/s 196
Figure 5-5: Mean velocity vmax=25 m/s 196
Figure 5-6: Vertical profile vmax=27.5 m/s 197
Figure 5-7: Mean velocity vmax=27.5 m/s 197
Figure 5-8: Vertical profile vmax=28.5 m/s 198
Figure 5-9: Mean velocity vmax=28.5 m/s 198
Figure 5-10: Vertical profile vmax=30 m/s 199
Figure 5-11: Mean velocity vmax=30 m/s 199
Figure 5-12: Vertical profile vmax=32.5 m/s 200
Figure 5-13: Mean velocity vmax=32.5 m/s 200
Figure 5-14: Downburst failure probability vs v_{max} 203
Figure 5-15: Peaks of downburst wind fields from WP and WPS.Aadapted from (Solari, et al. 2015) 203
Figure 6-1 Inertia forces 206
Figure 6-2: Lumped mass 208
Figure 6-3: elastic restoring forces 209
Figure 6-4: Reference frame for beam 2D DOF 210
Figure 6-5: Reference frame for beam 3D DOF 212
Figure 6-6: Generic element 3point definition 215
Figure 6-7: Displacements and forces on the degrees of freedom 216
Figure 6-8: Damping forces 220
Figure 6-9 Slender body with wind actions 223
Figure 6-10:Aerodynamic forces acting in a bluff body in body reference system 224
Figure 6-11: 2D frame with 3D downburst. a) Front view. b) Plan view 232
Figure 6-12: Cross section 233
Figure 6-13: Strouhal Number. Adapted from (Carassale, et al. 2012) 234
Figure 6-14: Drag coefficient for square section. Adapted from (Carassale, et al. 2012). 235
Figure 6-15: Lift coefficient. Adapted from (Carassale, et al. 2012). 235
Figure 6-16: Turbulent component of the displacement 236
Figure 6-17: Full displacement in y-direction with beta computed. 237
Figure 6-18: Full displacement in y-direction with beta equal zero 237
Figure 0-1: Sap2000 model 259
Figure 0-2: Acceleration time history Sap2000 model 260
Figure 0-3: Response displacement time history Sap2000 model 260
Figure 0-4: Response displacement time history TDA_SDOF model 261

LIST OF TABLES

Table 2-1: Integral length scales 32
Table 2-2: Sampling data 76
Table 3-1: Parameters to define vertical profile 89
Table 3-2: Sampling parameters 108
Table 3-3: Parameters to define horizontal component 108
Table 3-4: Integral length scales 110
Table 3-5: Downburst simulation parameters 115
Table 4-1: Structure simulation parameters 130
Table 4-2: Maximum response 137
Table 4-3: Mean response 137
Table 4-4: Normalized Mean Squared Errors 140
Table 4-5: Values of the parameter Cb 158
Table 4-6: Values of the parameter Cm 158
Table 4-7: Structure simulation parameters 160
Table 4-8: Downburst simulation parameters 161
Table 4-9: Values of the parameter Cb 170
Table 4-10: Values of the parameter Cm 170
Table 4-11: Structure simulation parameters 171
Table 4-12: Downburst simulation parameters 171
Table 5-1: ABL model parameters 194
Table 5-2: Parameters to define downburst outflow 195
Table 5-3: Material simulation parameters 201
Table 5-4: Cross section simulation parameters 201
Table 5-5: Limit displacement 202
Table 5-6: Safety Coefficient 202
Table 5-7: Failure probability 202
Table 6-1: Material simulation parameters 233
Table 6-2: Cross section simulation parameters 233

“…The only truly stochastic process is the human choice due to our free will, all the rest was deterministically engineered by God. Is just that we are not able to understand…”

CHAPTER 1. INTRODUCTION

1.1 A definition of “downburst”

The downburst is a meteorological phenomenon, first studied and defined by Fujita (Fujita 1985) as a “strong downdraft which induces an outburst of damaging winds on or near the ground”. According to (Fujita 1985), downbursts can be classified depending on the extension of their diameter as *microburst* and *macroburst*. While microbursts are characterized by diameters of 4km or less, macrobursts present much larger diameters. A further definition, proposed by Wilson and coworkers (Wilson, Roberts, et al. 1984), states that for microburst the maximum distance between winds blowing in opposite directions is less than or equal to 4km and the difference in velocity is greater than 10 m/s.

The earliest available records of a downburst were obtained in the framework of the Doppler radar projects of NIMORD (Northern Illinois Meteorological Research on Downburst), JAWS (Joint Airport Wind Shear) and MIST (Microburst and Sever Thunderstorms) (Wilson and Wakimoto 2001). Those projects were accomplished by Fujita and his team and allowed to build the first mathematical models for the downburst wind fields. A more recent research in the topic of registration of real field downburst is due to Prof. Solari and his team, and has been developed in the framework of the European ports monitoring network WP (Wind and Ports) and WPS (Wind Ports and Sea), see e.g.: (Solari, et al. 2017). Solari and coworkers recorded and processed a large number of time histories of downburst wind fields, providing a strong experimental foundation for the modelling of this meteorological phenomenon,

Several attempts have also been made to reproduce downbursts within the controlled area of the wind tunnels. Within this framework, it’s worth mentioning the contribution of the team of the University of Western Ontario (UWO) in Canada, leaded by Prof. El Damatty, see e.g. (University of Western Ontario UWO s.f.). Basically, they developed a unique three-dimensional wind test chamber which allows for the reproduction of the Impinging jet wind field. The wind tunnel simulations served as the basis to develop simulation models and design procedures for structures subjected to downburst wind fields, such as Power Line systems (Elawady 2016).

The effect of downburst over medium-rise long structures such as overhead electrical transmission lines (OHL), indeed, has been a major concern in the recent times. Hawes and Dempsey (Hawes and Dempsey 1993) stated that 93% of the failures power lines in Australia were due to downburst. Kanak (Kanak 2007) reported the collapse of several towers of European power line systems due to a macroburst wind field. Failures of OHL towers due to strong downburst winds also occurred in north America. McCarthy and Melness (McCarthy and Melness 1996), for example, reported the collapse of 19 towers during the Manitoba Hydro incident of September 5 1996 and the more recent failure of two guyed towers in Ontario occurred in 2006 (HYDRO ONE NETWORKS INC 2006).

Several models are currently available in the literature to simulate the downburst wind velocity fields and their effects on structures. There are, among the others: numerical models based on the numerical integration of the Navier Stokes equations using Computational Fluid Dynamic (CFD) tools; scaled measurements made inside specialized wind tunnel applications; and empirical models based on the data gathered in the radar projects. Even though all of them will be mentioned herein, the development of this study is mainly referred to the empirical models. The latter, indeed, can be conveniently adopted to define the action of the downburst on civil structures, without requiring the application of cumbersome numerical solutions or expensive testing.

1.2 The "discovery" of the downburst: some historical & meteorological remarks

The term "downburst" made his appearance in the scientific literature in the 70's, and since that time a constantly increasing number of studies has been devoted to its investigation. The relatively recent history of the "discovery" of the downbursts has been extensively discussed, among the others, by Wilson and Wakimoto (2001) and is briefly reviewed in this section.

As it was already mentioned the downburst phenomenon was first identified and recorded by Fujita during the 1970's and the 1980's. The early studies on this type of wind structures were driven by several aircraft's crashes occurred in those decades. The research results of Fujita were published with the seal of the University of Chicago and sponsored by the National Center of Atmospheric Research (NCAR) (Wilson and Wakimoto 2001).

The Eastern Airlines flight 66 of June 1975 is the first aircraft crash associated to a downburst. In the incident there were registered 112 casualties and 12 people were injured, while the airplane attempted to land in the New York's international airport-JFK. Due to unusual wind velocity records at the moment of the landing Fujita was involved in the investigation ending up with the hypothesis of a diverging outflow produced by a convective downdraft of dry air of the parent thunderstorm. The hypothesis was based on the strange starburst patterns of the uprooted trees in the zone of the landing Figure 1-1.

The hypotheses on the causes of the aircraft crash and on the existence of the downburst made by Fujita were reinforced by the wind field records of the near flights operative in the instant of the incident. Among the others, there were the flight TWA 843 coming from Milan and the Eastern Airlines Flight 902. The latter aborted its attempt to land due to the strong winds registered in the airport. Based on the records of these different flights Fujita was able to generate the space-time analysis of the airflow schematically depicted in Figure 1-2.

The developments made by Fujita in these early stages of the research received a huge impulse from the NCAR. The Agency allowed the Scientist to record real field measurement of the thunderstorms with Doppler radars. Three Radar projects were then executed by the team leading to proof the existence of downburst, measure the wind fields first in the macroscale of the phenomenon and then in the microscale for studying the velocity structure.

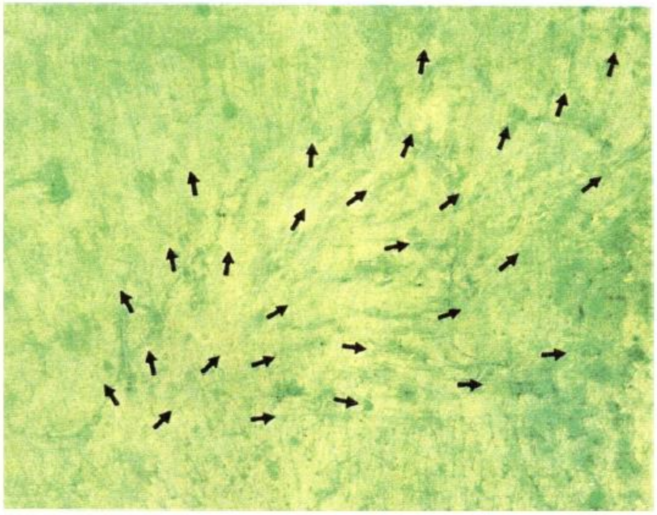

Figure 1-1: Pattern of uprooted threes. Adapted from: (Wilson and Wakimoto 2001)

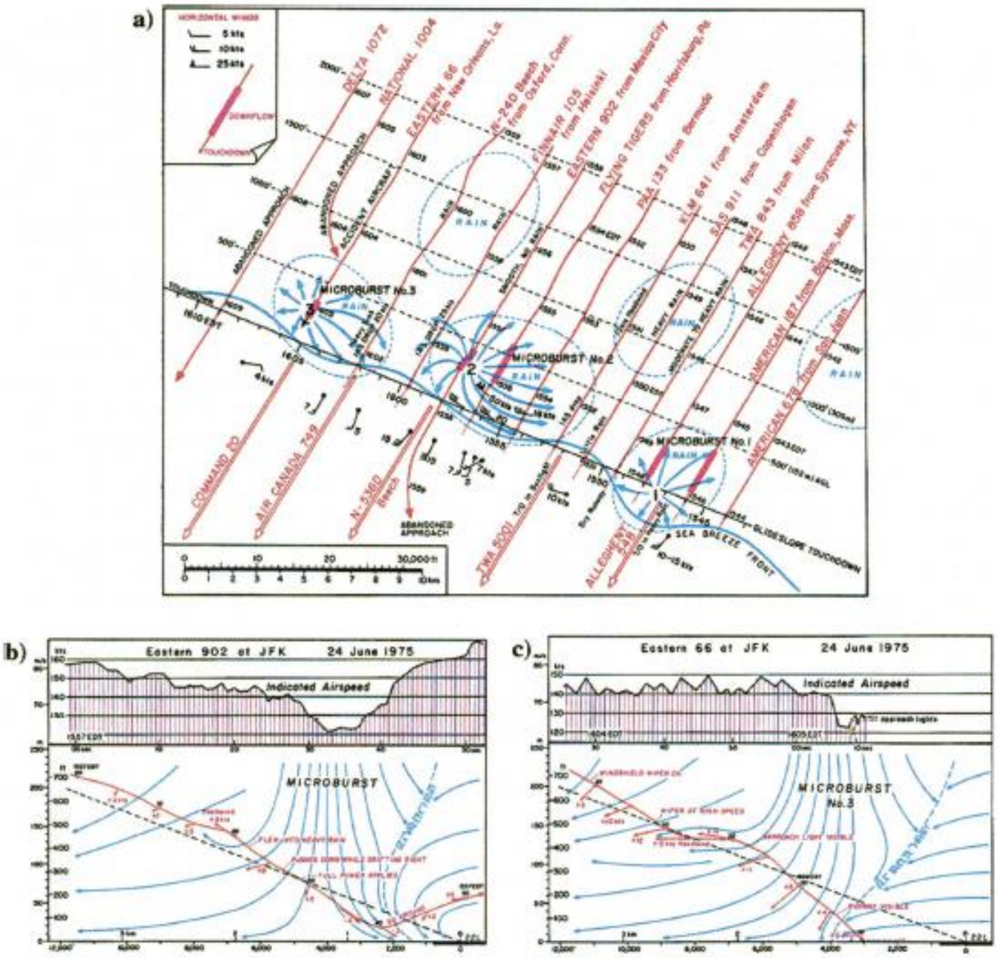

Figure 1-2:Airflow at the instant of the Flight 66 incident. Adapted from: (Wilson and Wakimoto 2001).

The first of these projects was the North Illinois Meteorological Research on Downburst, NIMROD, carried out in the north of Illinois during the spring and summer of 1978. In the project, the radars were located at 60km between each other. Even though the relatively large distance between the radars did not allow to measure the three-dimensional structure of the airflow, the measures were able to capture a downburst event. It’s worth noting here how at that time, the occurrence of downburst was not ascertained and therefore there was a strong need of evidences proving their existence. In particular, the first downburst registered by the aforementioned project was on May 1978. The corresponding doppler radar record is shown Figure 1-3 (Bull-eye). In total 50 downbursts were recorded by the NIMROD project.

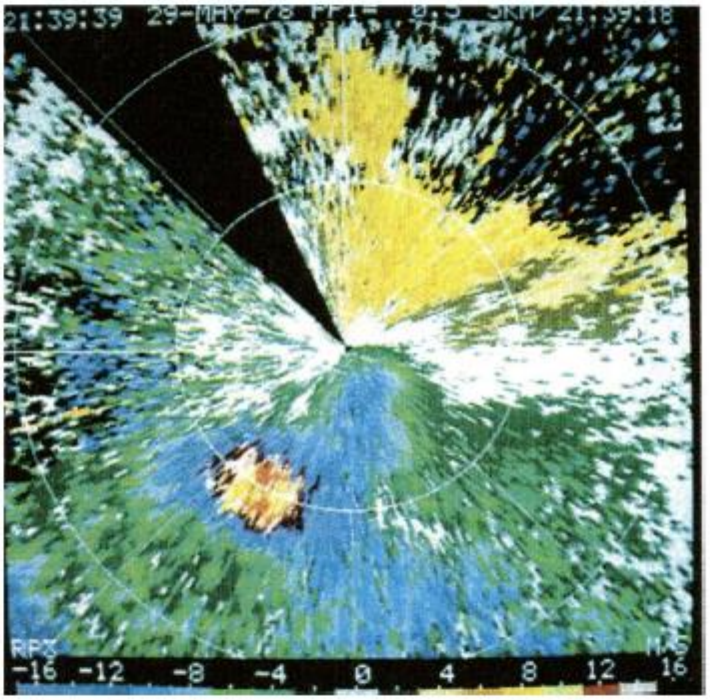

Figure 1-3: Doppler Radar of the first downburst record. Adapted from: (Wilson and Wakimoto 2001).

The successful results of the NIMROD project permitted the further development of the radar project Joint Airport Wind Shear (JAWS). The main feature of this project was the radar spacing of 12-28km. The project was made during the spring and summer of 1982 in Denver Colorado area where the microbursts are very frequent. Due to the relatively close spacing of the radar units, the observation of the three-dimensional structure of the airflows was possible together with the description of the wind profile by means of the range-height indicators (RHI). Figure 1-4 shows the structure of a downburst that caused the landing abort of two commercial flights. In total 186 downbursts were recorded by the JAWS project.

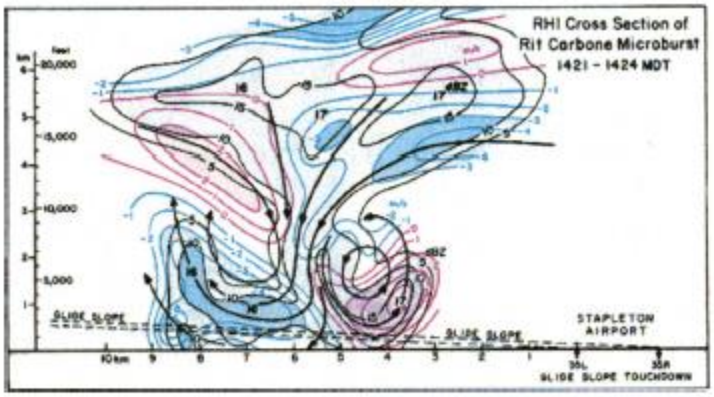

Figure 1-4: Downburst vertical structure. Adapted from: (Wilson and Wakimoto 2001)

The third project was the Microburst and Severe Thunderstorms (MIST), carried out in Alabama during the summer of 1986 with three doppler radars spaced at 13 to 25 km. Unfortunately, 1986 was a draught year in the southeast of the United States. Nevertheless, a couple of downbursts were captured and well registered during the project. Among those, it is possible to highlight the so-called Monrovia microburst in which, due to a favorable chain of situations, it was possible to capture the entire behavior of downburst together with a proof of the mechanism for early warning procedure of the downburst. This latter is based on the observation of the downburst echo or radar signature that occurs few minutes before the event materialization.

The studies conducted by Fujita and the teams of NCAR and the University of Chicago were significant for the discovery of the downburst. In addition, the radar projects NIMROD, JAWS and MIST allowed to a description of the airflows related with downburst velocity fields and the three-dimensional structure together with the procedure of early warning to prevent accidents like those of the Flight 66. In fact, the results of the research of the team lead to a training program in the aeronautical community to mitigate the casualties of downburst in this sector, reducing the accidents to zero between 1985 to 1994.

The studies on the downburst velocity fields are not related only to aeronautical applications, since civil structures are also affected by the high intensity outflows of this phenomenon. Further developments departing from the discoveries of Fujita, which were essential to arrive at the definitions of the downburst's effects on structural elements available nowadays, will be briefly reviewed in this document (**§** 2.5).

1.3 Scope of the Current study

The action of downburst outflows over civil structures is not well covered by the building codes as it is for synoptic winds. Now the design code including a basic model for the application of downburst is the Australian New Zeeland standard for Overhead line design (AS/NZS 7000 2010). The state-of-the-art research on this topic is divided in three major branches: the simulations in the CFD based on the numerical solution of the Navier-Stokes equations, the analytical or semi-analytical models based on stochastic dynamics and the reproduction of downburst inside wind tunnels. There is also a further sub-class of the analytical models, which can be identified in the models stemming from the work of (Kwon and Kareem 2009). These models provide a code-like-approach based on the developments available for synoptic winds with some differences to account for the non-stationarity of downburst outflows.

Since the effect of the downburst outflow wind fields can have a major impact on large structures and infrastructures, such as power line systems and bridges, the scope of this study is to provide information on the dynamic response of civil structures submitted to simulated downburst wind velocity fields.

The developments needed to achieve the goals of this research, involve the definition of a downburst wind field model. This must account for all the parameters and effects able to reproduce a real measurement of this phenomenon. Moreover, the model must respect the available literature on the downburst definition. Therefore, the scope of this thesis is to make a first step towards a unified methodology able to describe a downburst wind field for structural calculation purposes.

In addition, the structural response of the system will be assessed in time and frequency domain. Basically, the idea is to guarantee data consistency and profit from the characteristics of both approaches for further steps of the research. It is necessary to develop a Finite Element model able to perform both types of analysis and account for the aerodynamic effects. It should be highlighted that the results of both methodologies will be compared, for some archetypal case studies, to evidence the accuracy on the structural response evaluation and to check the dependence of the same on the damping ratio and the dynamic sensitivity of the system.

Finally, the comparison between the effect on the structural response of downburst wind velocity fields will be compared with those coming of the standard Atmospheric Boundary Layer model available in design codes. This with aim of assess the increment in the failure probability, defined as the reach of limit state (not necessarily collapse), of a structure due the effect of the downburst outflow velocity field.

1.4 Thesis organization

This thesis is divided in chapters with specific purposes. Each one provides the theoretical aspects and, in cases where applicable, the numerical examples involved in the developments of the objectives explained in the scope of the thesis. Therefore, special sections will be developed to the definition of the wind velocity field, to the structure simulation and response and others to the results comparison.

Chapter 1 provides a global and historical overview of the downburst phenomenon and the general framework of the thesis. This chapter, therefore corresponds to an introductory definition of the developments that will be made later inside the body of the thesis.

Chapter 2 provides the state of the art, i.e. the available models for defining the downburst wind velocity field and the comparison between the different options defined in the literature. The main goal of this chapter is to define the downburst phenomena not only from a meteorological point of view, but also, from an engineering one. Therefore, in its development there will be found the similitudes and differences between the variety of models highlighting which models provides a better definition of each specific downburst parameter. From a practical point of view, In this chapter there will be showed the techniques implemented for the wind simulation in the literature dealing with this subject, the parameters defined and some relevant results in terms of the simulated wind fields.

On Chapter 3 the results of the different models will be checked and compared to obtain a specific view of each parameter involved in the definition of the downburst model. A very important aspect that will be exposed in this chapter is the unified notation and the development of a model for wind velocity simulation of the downburst.

The most important aspect that will be considered in the comparison is the capability of the models to reproduce available records of downburst signals, such as, the classical Andrews Airforce Base (Fujita 1985) and the records of WP (Wind and Ports) and WPS (Wind Ports and Sea) projects (Solari, et al. 2017). To this aim several parameters must also be considered, as an overview: the vertical profile of velocity, radial diffusion or intensification functions (time and space), the amplitude modulating function, the turbulence definition (including integral length scales and power spectral densities) and the coherence functions.

In Chapter 4 the aerodynamic effects of downburst on a reduced structural model with a single degree of freedom (SDOF) will be assessed. The study of this type of structure enables to concentrate on the wind field definition since the simple structural response could be modelled very easily. Moreover, the application of modal approach in case of classically damped structures (please notice that this might not be the case for systems sensitive to aeroelastic effects), leads to a decomposition of the many dynamic degrees of freedom into many decoupled systems of SDOF that could be analyzed independently and the superimposed i.e. the SDOF response proposed in chapter 4 can be extended to MDOF if special requirements are fulfilled.

In Chapter 4, the analysis of the system will be made in both frequency and time domain. A parametric study varying the mechanical parameters: damping ratio and natural frequency, will be developed for different downburst simulated wind fields. This with the aim of studying the dynamic the effect of the downburst on the structures by changing the original parameters controlling the problem, damping and period ratio. Special provisions for the error measurements and accuracy of the testing will be also provided.

Chapter 5 presents a comparison between the downburst wind velocity model and the traditional atmospheric boundary layer model. The aim of this chapter is to assess the probability of exceedance of a certain limit state. In this chapter it will be proposed a methodology to verify how much the performance of a system designed with the usual design rules is capable of resist a downburst outflow inside the framework of the probable scenarios.

The analysis of MDOF systems will be provided in Chapter 6. The aim of this chapter is to study the case of structures for which the decoupling of the equations of motion into singe DOF systems with the modal approach is not feasible due to the aeroelastic effects. Therefore, definitions for the wind induced vibrations will be provided, as well as, the aeroelastic decomposition in mean velocity effects, turbulent effects and the aeroelastic matrixes coupling the wind effects with the structural response i.e. aeroelastic damping and stiffness matrix.

All the provisions of aeroelasticity will be considered since important civil structures such as cables and bridges due to their high flexibility have shown large sensibility to these effects, due to their natural frequencies closer to those of the turbulent wind excitation.

Also, on chapter 6 there will be given the definitions for the Finite Element tool developed for solving MDOF systems, accounting for modal analysis, generation of the aerodynamic forces and solution of the dynamic problem by Direct integration of the equations of motion (Newmark Method).

CHAPTER 2. STATE OF THE ART

Downbursts belong to a class of meteorological phenomena known as High Intensity Wind event (HIW) and are typically associated with thunderstorms. (Byers and Braham 1949) define thunderstorms as an atmospheric phenomenon composed by cells of air, their mechanism can be divided in three major stages occurring in period from 30 to 60 minutes. First step is the convective updraft of warm air accumulating mass forming a large size cumulus at high elevations, this updraft transports also warm moist. When the amount of mass reaches a critical point, the moisture starts to densify and cool until the updraft is halted and becomes instable (the cumulus becomes a cumulonimbus) and a downdraft of cold air occurs. Finally, the thunderstorm dissipates energy though a downdraft of cool air, the downburst is the divergent outflow generated after the impinging of the downdraft with the surface of the earth (Chay and Letchford 2002). Moreover, according to (Fujita 1985) downbursts are those downdrafts of cold air that impinges on the ground producing a radial outflow and a *vortex ring*.

A graphical representation of the downburst formation could be seen in Figure 2-1 and Figure 2-2. In both images it could be seen the evolution of the two last stages of the thunderstorm from left to right. The first on the left refers to the arrival of the critical point and starting of the downdraft of the cumulus, the central and right-hand pictures show the impinging and the later divergence of the flow in radial directions. Conversely, on Figure 2-3 there is a global representation of the downdraft divergence in the radial direction.

It is important to state that the downburst has properties from the mother thunderstorm that will define its behavior. Therefore together with the diverging radial outflow there is the mother storm tracking velocity that moves the downburst at a certain speed and direction (Oliver 1992) adding a constant component to the movement that must be vectorially added to the radial one (Holmes and Oliver 2000).

Moreover, the outflow wind field close to impact point behaves differently than the typical atmospheric boundary layer i.e. the downbursts are characterized to be outflows having short duration, and particularly transient, non-synoptic, non-stationary and high intensity wind fields (Caracoglia and Le 2017). For the simulation of the aerodynamic effect the non-stationarity of wind field creates a total change in the way the turbulence and mean wind speed are considered in the formulation, mainly because the available studies on synoptic wind fields show that Atmospheric boundary layer winds are characterized by a constant mean velocity (in the observation period of 10min to 1 hour)) (Van der Hooven 1957) and stationary turbulence i.e. its statistical properties do not change on time.

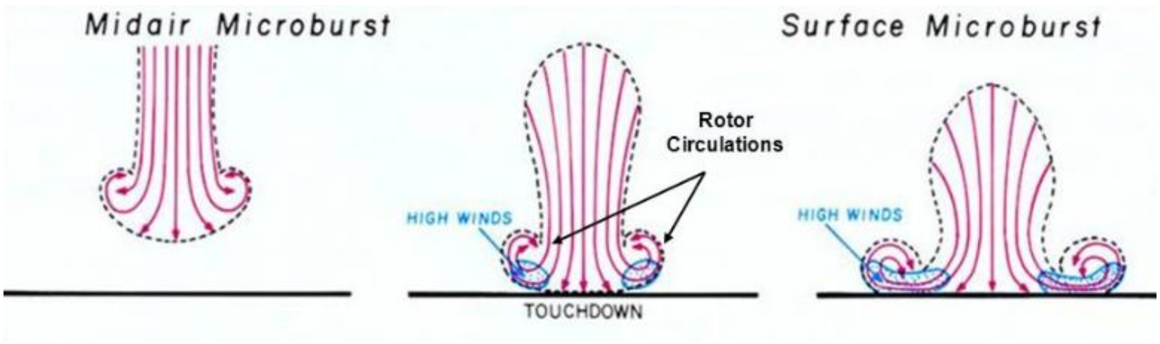

Figure 2-1: Schematic downburst formation. Adapted from (Fujita 1985)

Figure 2-2: Captured downburst formation

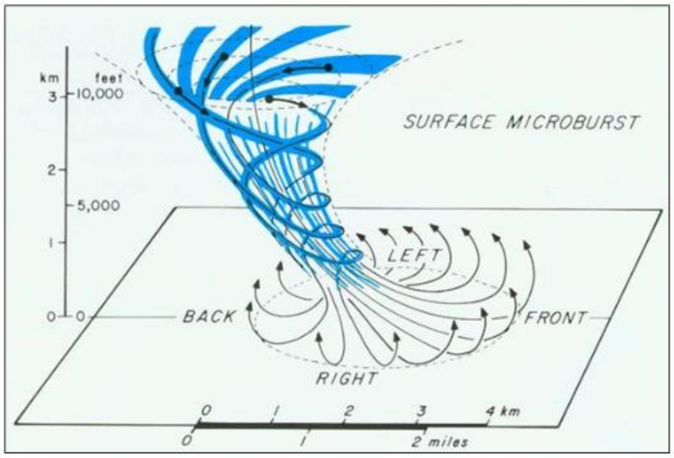

Figure 2-3: 3D scheme of downburst. Adapted from (Robert, 2014)

Several models to describe the properties of the downburst and effectively simulate their outflow wind field are available in the literature. Even though, each author gives an original orientation to the specific research and therefore every model developed is different from the other, three major groups can be distinguished.

The first group corresponds to the simulations made with CFD computer codes. From a practical point of view, this group encloses three possible models for the description of the downburst. The so-called Ring Vortex model, consisting on the outflow ring that is formed during the descendent downdraft of cool air (Ivan 1986) (Vicroy 1992). The impinging jet model proposed originally by (Fujita 1985), and used later in several other models, is based on the idealization of the downdraft as the impulsive jet impinging into a wall or flat surface creating a divergent outflow, just as the downburst phenomenon. The last model type is the Cooling Source model, composed by a dry, non-hydrostatic, sub-cloud and axisymmetric model (Mason, et al. 2009).

The second group corresponds to the contributions of the team of the University of West Ontario (UWO), who developed a unique tool for the simulation of downburst wind fields, a wind chamber or wind tunnel called de the WindEEE which allows for the controlled reproduction of the downdraft and divergent outflow of the downburst. Even though, the scope of this study is not capable to reproduce their reach, the results of their test will be considered in the simulated downburst wind fields used in the following chapters. In general, the parameters such as critical angle of approximation and loading conditions of the UWO studies (Elawady 2016) could be implemented for the case of study of powerlines systems in a further step of the research.

The third group corresponding to empirical models based on the observation of real downburst records. Those are going to be the models studied herein. In general, the feasibility of the reproducing this type of models makes their implementation simple and allows the development of a further routine or methodology for engineering applications that can be then implemented in design codes. The models available in the literature for this aim are based on the laws of probability defining the downburst non-stationarity by means of the suitable numerical models, the implementation of the evolutionary spectra proposed by (Priestley 1965) is a common factor in the majority of those models and is one of the crucial parameters defining the problem since is the one describing the major difference between the downburst outflow velocity field and the traditional atmospheric boundary layer model i.e. it accounts for the non-stationarity.

2.1 Wind Engineering Concepts

Before starting the study of the available models a few concepts related to the behavior of the Downburst and general ideas of wind engineering will be given.

2.1.1 Wind velocity standard decomposition

The dynamic forces acting in an immersed body, such as those acting on a structure exposed to the action of the wind, can be defined as shown in Figure 2-4. The forces depend in general on the aerodynamic coefficients (see also CHAPTER 6), the air density for standard civil engineering conditions (ρ=1.25 kg/m3) the exposure area and the relative wind velocity between the flow and the structure movement. From the set of parameters governing the aerodynamic behavior of the system, as shown in Equation 2-1, those depending on the incoming wind flow are the relative velocity *V(t)* and the relative angle of attack *α* i.e. the air density and exposure area *B* (defined by structure shape) are almost constant for civil engineering applications. Therefore, special provisions must be given for the wind velocity and the aerodynamic drag, lift and moment coefficients (*Cd Cl Cm,* respectively) for defining the structural response.

A foreword: even though for the description of downburst the wind velocity due to the non-stationarity is not strictly the same as for synoptic winds inside the framework of the Atmospheric Boundary Layer model, the same approach for the decomposition of the wind velocity used for standard application has been widely adapted in the literature (Solari, et al. 2017) (Canor, et al. 2016) (Chen and Letchford 2004) (Caracoglia and Le 2017) therefore, will also be followed herein.

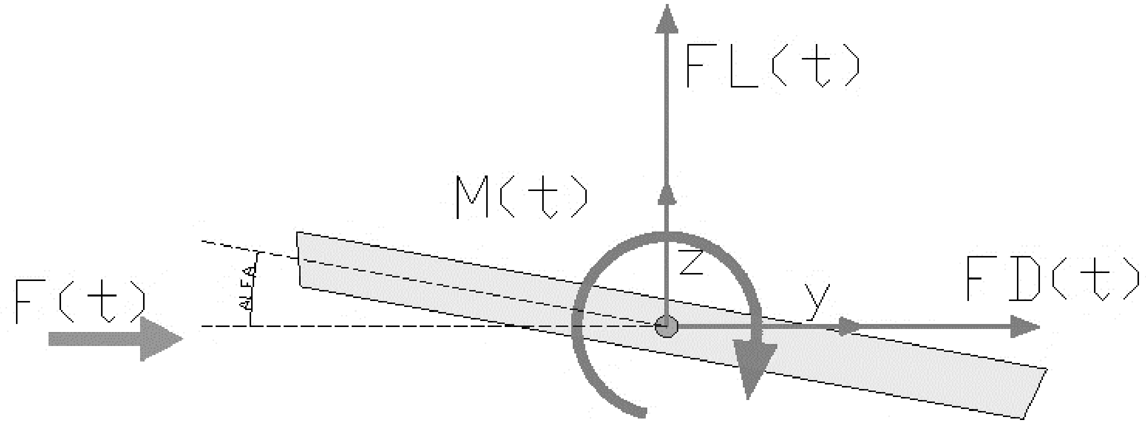

Figure 2-4: wind forces over immersed body

Equation 2-1

$$F_D = \frac{1}{2}\rho V(t)^2 B C_D(\alpha)$$

$$F_L = \frac{1}{2}\rho V(t)^2 B C_L(\alpha)$$

$$M = \frac{1}{2}\rho V(t)^2 B^2 C_M(\alpha)$$

As already described before, the downburst can be idealized as a downdraft that impinges the ground creating an intense radial outflow (Fujita 1990) (Fujita 1985). According to the available studies of the literature (Solari, et al. 2017), the radial velocity can be expressed as a decomposition of a mean $\mathrm{V}_{mean}(\mathrm{z},\mathrm{t})$ and a turbulent $\mathrm{V}'(\mathrm{z},\mathrm{t})$ components Equation 2-2. The particularity of the downburst wind field is due to the time variant mean value, since generally the mean value is considered as a static parameter for synoptic winds.

Equation 2-2

$$\mathrm{V}(\mathrm{z},\mathrm{t}) = \mathrm{V}_{mean}(\mathrm{z},\mathrm{t}) + \mathrm{V}'(\mathrm{z},\mathrm{t})$$

It can be highlighted a dependence of both the wind velocity field components (mean and turbulent) on the height over the ground *z* and time *t*. The studies have shown that the mean velocity can be conceived as a slowly varying mean since it is associated to a low frequency content, while the turbulent component is characterized by a high frequency content (Chen and Letchford 2004) (Solari, et al. 2017) (Caracoglia and Le 2017).

The slowly varying mean component, then, can be decomposed in time and space as a vertical profile multiplying a time varying function as in Equation 2-3.

Equation 2-3

$$\mathrm{V}_{mean}(\mathrm{z},\mathrm{t}) = \mathrm{V}_z(\mathrm{z}) * \gamma(\mathrm{t})$$

In the further developments the provisions for the definition of the vertical profile $\mathrm{V}_z(\mathrm{z})$ and the time modulation function γ(t), will be detailed.

Regarding the turbulent velocity component, the classical definition for synoptic winds using a Power Spectral Density function is also valid as will be explained in the **§** 3.5. A modification shall be applied however, to consider the non-stationarity of the problem which makes a time dependence of the statistical spectral moments. Therefore, a time modulating function a(t) is introduced in the model of the wind velocity field affecting a stationary gaussian random process $v'(z,t)$. A possible scheme of the wind could be as given in Equation 2-4.

Equation 2-4

$$V(z,t) = V_z(z) * \gamma(t) + a(t) * v'(z,t)$$

Whenever the amplitude modulation function is taken constant and equal to the unit, the turbulent component corresponds to a classical zero mean stochastic process, that can be described through the standard procedures available for the synoptic winds.

2.1.2 An introduction to the modelling of turbulence

Wind phenomena inside the atmospheric boundary layer are characterized by an inherent turbulence, produced by the collision of air particles with obstacles present in the terrain and topography. For the case of downburst, the turbulence is also produced by the impinging jet itself i.e. the impact of the downstream flow with the ground generate a full turbulent flow.

This chaotic and irregular motion, can only be described by the laws of the probability, therefore might be better studied using a stochastic approach rather than a deterministic one.

2.1.2.1 Taylor hypothesis

The turbulent flow present in the wind field can be represented as the superposition of whirls of different sizes. Those irregular swirls of motion are known as eddies. From a practical point of view, to obtain the data at different points within the same eddy and at same time is not an easy task. Therefore, the hypothesis proposed by Taylor in 1938 is usually stated: the eddy turbulent properties are assumed to be frozen. Therefore, the measurement of one point at two different times can be used to approximately model the behavior of the turbulent wind component. A graphical representation of this idea is sketched in Figure 2-5.

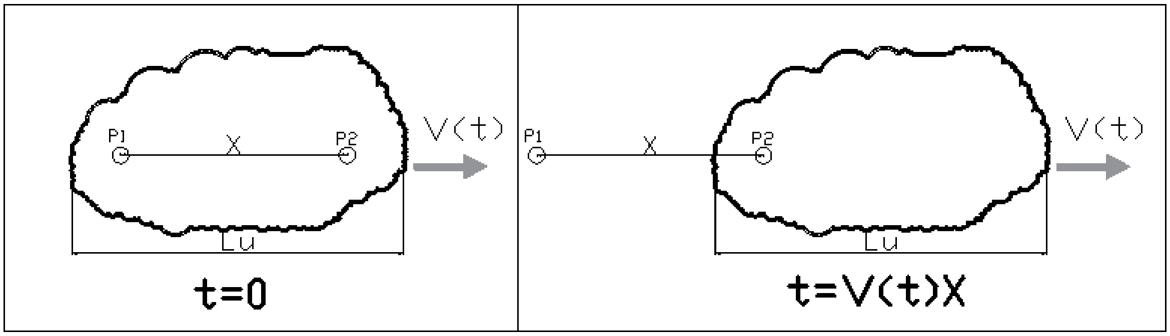

Figure 2-5: Taylor hypothesis

2.1.2.2 Autocorrelation and Cross correlation function

The autocorrelation function provides the measure of how much a signal is close to itself but offset a certain time window, τ. Graphically, the meaning of this function is represented in Figure 2-6, while in Figure 2-7 the autocorrelation function for typical random signals is given.

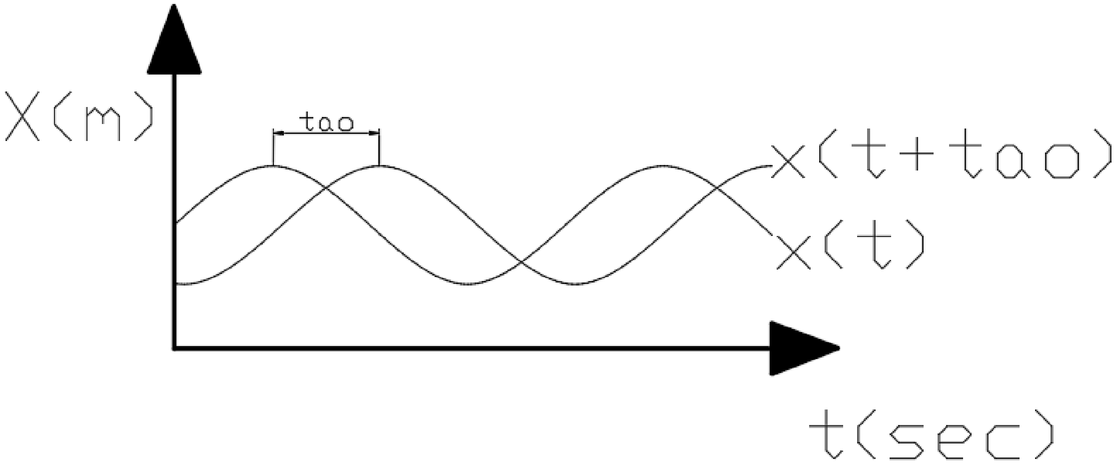

Figure 2-6: Representation of Autocorrelation function

The autocorrelation function can be computed as follows:

Equation 2-5

$$R_{xx}(\tau) = \lim_{T\to\infty} \frac{1}{T}\int_0^T x(t) * x(t+\tau)dt$$

Properties of the autocorrelation function

- For zero-time window, τ=0, the autocorrelation function is the mean square value, ${\psi_x}^2$, of the process.
- The autocorrelation function is an even function.
- The autocorrelation function is always decreasing.

Equation 2-6

$$\begin{cases} R_{xx}(\tau = 0) = \lim_{T\to\infty} \frac{1}{T}\int_0^T x(t) * x(t+0)dt = {\psi_x}^2 & (a) \\ R_{xx}(\tau) = R_{xx}(-\tau) & (b) \\ R_{xx}(0) \geq R_{xx}(\tau) & (c) \end{cases}$$

It is usual to represent the autocorrelation function in its non-dimensional form:

Equation 2-7

$$\overline{R_{xx}}(\tau) = \frac{R_{xx}(\tau)}{R_{xx}(0)} = \frac{R_{xx}(\tau)}{{\psi_x}^2} \rightarrow -1 \leq \overline{R_{xx}}(\tau) \leq 1$$

Equation 2-8

$$\begin{cases} \overline{R_{xx}}(\tau) = 1; maximum\ correlation \\ \overline{R_{xx}}(\tau) = 0; no\ correlation \end{cases}$$

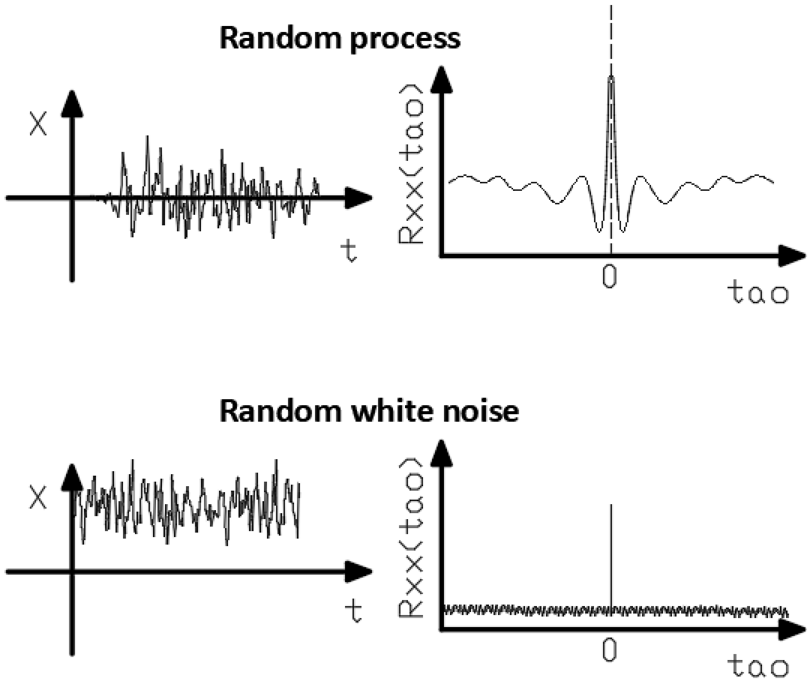

Figure 2-7 Random signals and their autocorrelation function

Considering two different time histories (e.g. the records of the same physical process at two different points in space, or the input and output processed of a mechanical system) it is possible to define the cross-correlation as the function giving a measure of how the two signals are related to each other. Analogously with what was already defined for the autocorrelation function, the cross-correlation can be defined as:

Equation 2-9

$$R_{xy}(\tau) = \lim_{T\to\infty} \frac{1}{T} \int_0^T x(t) * y(t+\tau) dt$$

2.1.2.3 Integral length scale

An important parameter linked to the Taylor hypothesis is the so-called integral length scale, L_v. This parameter gives a measure of the length of an eddy for which the hypothesis of frozen turbulence properties can be assumed to be valid. The Integral length scale can be defined by means of the cross-correlation and autocorrelation functions.

The integral length scale is a measure of the size of the vortex in the wind, it depends on the turbulent component measured (longitudinal, transversal or vertical) and the direction (x,y,z). The expression defining this parameter is given in Equation 2-10.

Equation 2-10

$$L_v^x = \int_0^\infty R_{vv}(r_x)dr_x$$

R_{vv} (r_x) represent the space cross-correlation function of two point separated by a distance r_x. In general, there could be found 9 different length scales as Table 2-1: Integral length scales.

Table 2-1: Integral length scales

Longitudinal component v	L_v^x	L_v^y	L_v^z
Transversal component u	L_u^x	L_u^y	L_u^z
Vertical component w	L_w^x	L_w^y	L_w^z

For the single point in space the wind coordinates v, u and w named respectively longitudinal, transversal and vertical components are as shown in Figure 2-8.

With the Taylor hypothesis for the assessment of the eddy properties, it is possible to use the available measurements in only one point. In this way, with the well-known time correlation function $R_v(\tau)$ for the computation of the *integral time scale* $T_v^x(z)$, Equation 2-11. The *integral length scale* will be related to the *integral time scale* by means of the mean wind velocity as shown in Equation 2-12. The variation of the mean velocity with height of the ground couples the *integral length and time scales* with the height.

Equation 2-11

$$T_v^x(z) = \int_0^\infty R_v(z,\tau)d\tau$$

Equation 2-12

$$L_v^x(z) = T_v^x(z) * V(z)$$

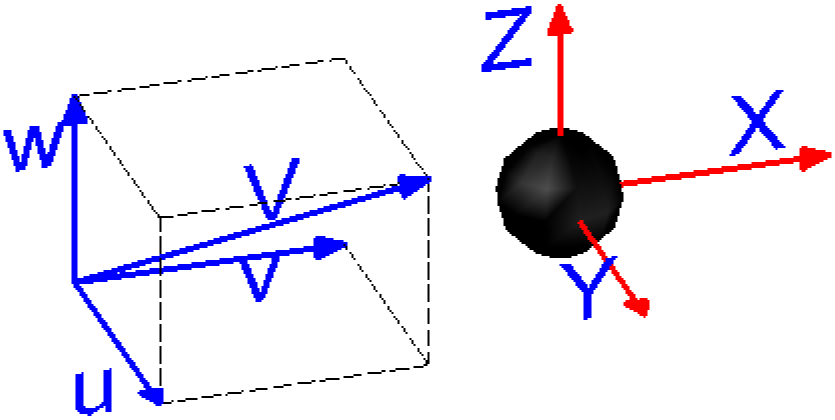

Figure 2-8: Wind components: reference system.

For the synoptic winds there are empirical expressions to obtain the integral length scale, as those provide by Eurocode 1 very similar to the one given for example in ASCE 7, Equation 2-13.

Equation 2-13

$$L_v^x(z) = 300 * (\frac{z}{200})^{\alpha}$$

Since the physical mechanisms at the origin of the downburst are strongly different compared with the ones of the atmospheric boundary layer winds and gusts, the use of the available empirical formulas to compute the integral length scales are not useful. Experimental tests must be performed to obtain this parameter (G. Solari, M. Burlando, et al. 2015). In the present work the integral length scale are given in **§** 3.5.

2.1.2.4 Power spectral density

Analogously to the autocorrelation function which gives the description of signal on the time domain, the Power Spectral Density, gives the description of the signal in the frequency domain. The PSD function gives a measure of how the energy content of a signal is distributed among the different vibration frequencies. Furthermore, the PSD (S_{xx}) is the Fourier transform of the autocorrelation function Equation 2-14. For engineering purposes, the use of the *unilateral* PSD (G_{xx}) is widely adapted (Figure 2-9). The latter can be defined as Equation 2-15.

Equation 2-14

$$S_{xx}(f) = \int_{-\infty}^{+\infty} R_{xx}(\tau) e^{-i2\pi f\tau} d\tau$$

Equation 2-15

$$\begin{cases} G_{xx}(f) = 0\ for\ f < 0 \\ G_{xx}(f) = 2S_{xx}(f)\ for\ f \geq 0 \\ G_{xx}(f) = 2\int_{-\infty}^{+\infty} R_{xx}(\tau)e^{-i2\pi f\tau}d\tau \end{cases}$$

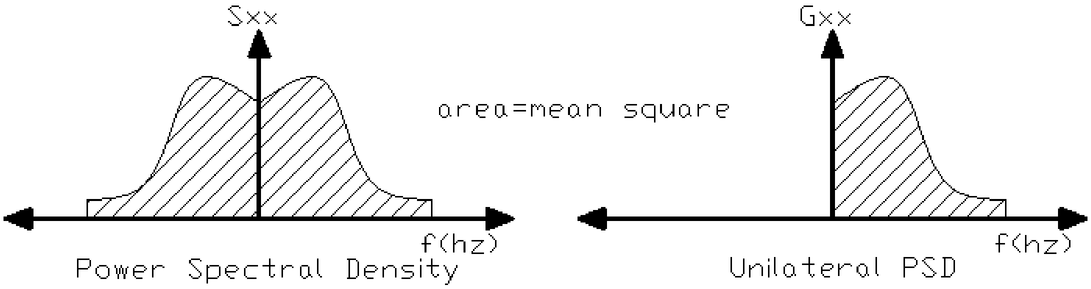

Figure 2-9: PSD & Unilateral PSD

From the properties of the autocorrelation function it is possible to recover those of the PSD.

Equation 2-16

$$R_{xx}(0) = {\psi_x}^2 = \int_{-\infty}^{+\infty} S_{xx}(f)df \rightarrow \int_{0}^{+\infty} G_{xx}(f)df = {\psi_x}^2$$

The area below the curve of the PSD is the mean square value. For the case of a zero-mean process, this area is the variance of the process. In addition, for very small interval of frequency the Equation 2-17 gives the mean square value for the interval comprised between f and f+Δf.

Equation 2-17

$$G_{xx}(f) * \Delta f = {\psi_x}^2(f)$$

$G_{xx}(f)$ is a real quantity.

Equation 2-18

$$G_{xx}(f) = 2\int_{-\infty}^{+\infty} R_{xx}(\tau)e^{-i2\pi f\tau}d\tau \rightarrow 2\int_{-\infty}^{+\infty} R_{xx}(\tau)[\cos(2\pi f\tau) - isin(2\pi f\tau)]d\tau$$

Analyzing the right side:

Equation 2-19

$$\int_{-\infty}^{+\infty} R_{xx}(\tau)sin(2\pi f\tau)d\tau = \int_{-\infty}^{0} R_{xx}(\tau)sin(2\pi f\tau)d\tau + \int_{0}^{+\infty} R_{xx}(\tau)sin(2\pi f\tau)d\tau$$

Since the autocorrelation function is an even function Equation 2-6 b) and the sine function is an odd function with sin (2πft) =-sin (-2 πft), the sine function cancels itself in the developments of the integral, cancelling the imaginary component of the PSD function as well. On other hand, the cosine is an even function therefore it doubles itself in the integration process. Therefore, the Unilateral PSD is greater than zero and can be obtained as Equation 2-20.

Equation 2-20

$$G_{xx}(f) = 2\int_{-\infty}^{+\infty} R_{xx}(\tau)\cos(2\pi f\tau)\,d\tau \rightarrow 4\int_{0}^{+\infty} R_{xx}(\tau)\cos(2\pi f\tau)\,d\tau$$

The turbulent component of the wind velocity is supposed to be a stationary Gaussian random process with zero mean. To this aim, several spectra are available in the literature. One of the spectrums widely used in the wind field application is the so-called Von Karman Spectrum given in Equation 2-21. The expression of the PSD is in the normalized form.

Equation 2-21

$$\frac{f * S_{xx}(f)}{{\sigma_x}^2} = {4 * (\frac{fL_v^x}{\bar{V}(z)})} \Big/ {[1 + 70.8(\frac{fL_v^x}{\bar{V}(z)})^2]^{5/6}}$$

It is worth noting that the same definition of PSD functions is valid for non-stationary random process by considering the amplitude modulating function as defined by (Priestley 1965).

Eurocode 1 provides an analogous expression for the definition of the non-dimensional PSD function.

Equation 2-22

$$\frac{f * S_{xx}(f)}{{\sigma_x}^2} = {6.8 * (\frac{fL_v^x}{\bar{V}(z)})} \Big/ {[1 + 10\,\frac{fL_v^x}{\bar{V}(z)}]^{5/3}}$$

2.1.2.5 Cross Power Spectral Density and Coherence function

Again, considering two random process x(t) and y (t) it is possible to define the cross-power spectral density CPSD, as the Fourier transform of the cross-correlation function.

Equation 2-23

$$G_{xy}(f) = 2\int_{-\infty}^{+\infty} R_{xy}(\tau)e^{-i2\pi f\tau}d\tau$$

Introducing the Coherence as the function describing the statistical dependence between the two signals described in the former paragraph, it might be possible to recall in an alternative way the CPSD. Is important now to remark that, the statistical dependency is due to the spatial dimension of the swirls in the wind field and the Taylor hypothesis. The coherence function could be obtained as shown in Equation 2-24.

Equation 2-24

$$coh_{xy}(f) = \sqrt{\frac{\left|G_{xy}(f)\right|^2}{G_{xx}(f) * G_{yy}(f)}}$$

Or conversely,

Equation 2-25

$$G_{xy}(f) = coh_{xy}(f)\sqrt{G_{xx}(x,f) * G_{yy}(y,f)}$$

While the CPSD is a complex quantity, the coherence function is real. The former might be expressed in terms of the modulus and phase or as the sum of an imaginary (out of phase) and real (in phase) part. In chapter 6.1 Wind Field it will be exposed the Coherence function used in the models available to define the Downburst wind field.

The classical expression, also the simplest one, to recall the coherence function is an empirical formulation proposed by Davenport (Davenport 1968).

Equation 2-26

$$coh_{xy}(\Delta y, f) = \exp[-\mathrm{cy} * \frac{\Delta y * f}{\bar{V}}]$$

With Cy being the non-dimensional decay constant, the typical value for this parameter is 10, whether for synoptic or not-synoptic winds. And Δy stands for the separation between the points in study.

2.1.3 Evolutionary Power spectrum

The evolutionary spectrum characterizes a random process with statistical properties that change with time i.e. a non-stationary process. In a very brief description, it is possible to state that the evolutionary spectrum generalizes the concept of the power spectrum i.e. a process with the same probability distribution over the time line to a process in which the probability distribution varies with time. This could be seen graphically in Figure 2-10 and Figure 2-11.

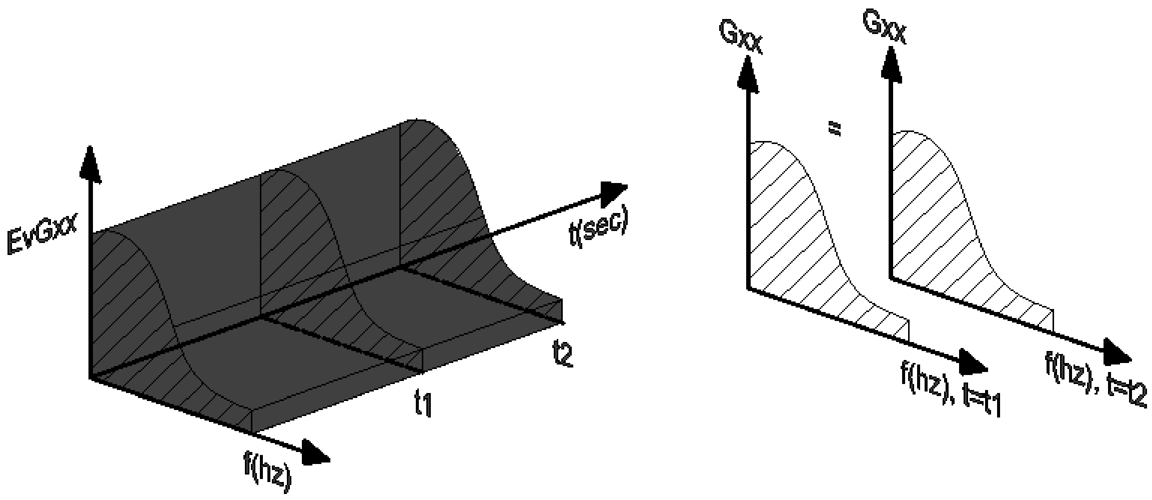

Figure 2-10: Representation of power spectrum for stationary process.

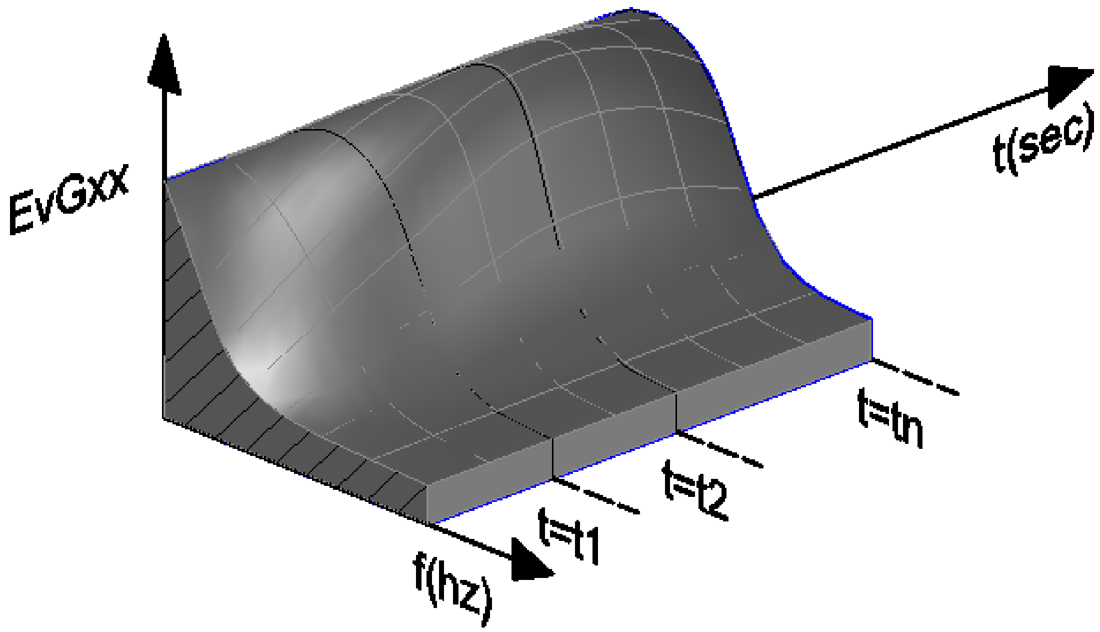

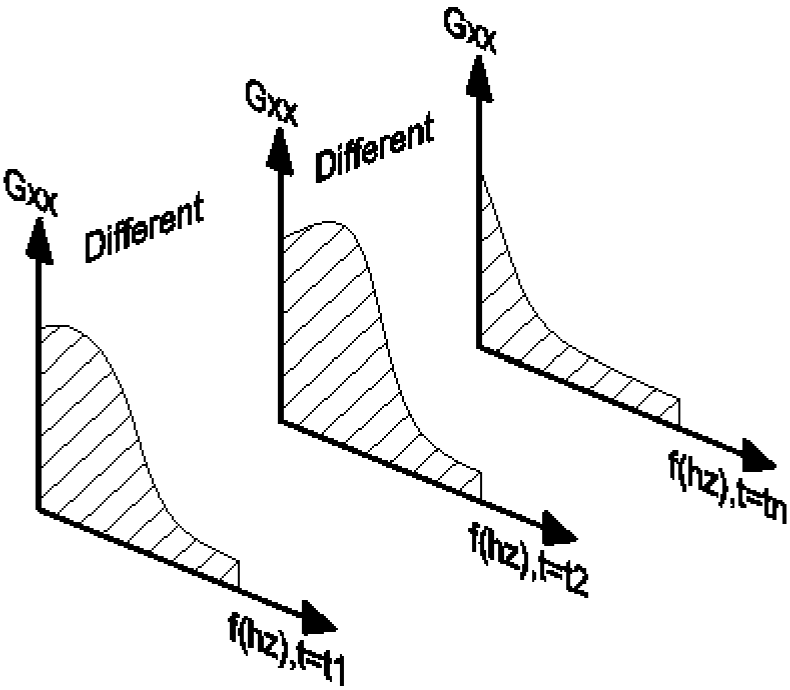

Figure 2-11: Representation of evolutionary spectra for non-stationary process. a) Evolutionary Spectrum b) time sections

It often happens that the assumption of stationarity of random process is not verified in practice. In fact, downbursts are an example of a non-stationary process. It is necessary to extend the concept of the PSD, as a function describing the energy distribution over the frequency content of a signal, to the case of non-stationary process. This can be achieved with the definitions that will be provided in the following.

Considering a discrete non-stationary process, $X(t)$, characterized by an evolutionary spectrum as that shown in Figure 2-11, the following relation can be written:

Equation 2-27

$$X(t) = \begin{cases} X^1(t), & t < t_1 \\ X^2(t), & t \geq t_1 \end{cases}$$

Where $X^1(t)$ and $X^2(t)$ are assumed to be two stationary process with different autocovariance functions. t is the time variable and t_1 is a given instant of time. For a known t_1 it is possible to estimate two PSD functions: one valid for the interval $t < t_1, X^1(t)$, and other valid for the interval $t \geq t_1, X^2(t)$.

If the process of Equation 2-27 is characterized by further time instants $t_2, \dots, t_n$, it can be described by more stationary PSD functions $X^3(t), \dots, X^n(t)$ belonging to the non-stationary process $X(t)$ as in Equation 2-28. Therefore, it is possible to discretize the latter into *n* stationary process with PSD functions $X^1(t), X^2(t), \dots, X^n(t)$.

Equation 2-28

$$X(t) = \begin{cases} X^1(t), & t_1 > t \\ X^2(t), & t_2 > t \geq t_1 \\ X^3(t), & t_3 > t \geq t_2 \\ & \vdots \\ X^n(t), & t_{n-1} > t \geq t_n \end{cases}$$

Therefore, it is possible to generalize the concept to a time-dependent spectrum.

2.1.3.1 Preliminary definitions of stationary process

The random process in discrete form can be obtained by the following relation:

Equation 2-29

$$x^{(j)}(t) = \sum_{n=-\infty}^{+\infty} {X_n}^{(j)}\, e^{i2\pi n\Delta f t}$$

Where $X_n^{(j)}$ is the n-th harmonic component of the random process (Equation 2-30):

Equation 2-30

$$X_n^{(j)} = \frac{1}{T}\int_{-T/2}^{+T/2} x^{(j)}(t) e^{-i2\pi n\Delta f t} dt;\ \Delta f = \frac{1}{T}$$

Where the frequency interval is Δf and T is the associated time window. Replacing Equation 2-30 in Equation 2-29, it is obtained:

Equation 2-31

$$x^{(j)}(t) = \sum_{n=-\infty}^{+\infty} e^{i2\pi n\Delta f t} \Delta f \int_{-T/2}^{+T/2} x^{(j)}(t) e^{-i2\pi n\Delta f t} dt$$

For the case in which the $T \to \infty$, the frequency interval becomes smaller $\Delta f \to df$ and $n\Delta f \to f$. Therefore, the following integrals can be obtained:

Equation 2-32

$$X^{(j)}(f) = \int_{-\infty}^{+\infty} x^{(j)}(t) e^{-i2\pi f t} dt\, ; (Fourier\ Transform)$$

Equation 2-33

$$x^{(j)}(t) = \int_{-\infty}^{+\infty} X^{(j)}(f) e^{i2\pi f t} df\, ; (Inverse\ Fourier\ Transform)$$

Besides, based on the previous equations, it is possible to define the following expression, presented in Equation 2-34 (Perotti 2017):

Equation 2-34

$$d\varphi_x(f) = \lim_{T\to\infty}\frac{1}{T}\int_{-T/_2}^{+T/_2} x^{(j)}(t)e^{-i2\pi ft}dt$$

Hence, the Equation 2-33 becomes:

Equation 2-35

$$x^{(j)}(t) = \int_{-\infty}^{+\infty} e^{i2\pi ft}d\varphi_x(f)$$

Denoting the statistic expected value of x as E[x], the autocorrelation function, for a time window τ going from time instant t_1 to time instant t_2, is defined as:

Equation 2-36

$$R_x(\tau = t_2 - t_1) = E[x^*(t)x(t+\tau)]$$

With x* denoting complex conjugate.

The time instants t_1 and t_2 are associated to the frequencies f_1 and f_2. Replacing Equation 2-35, evaluated at the time instants t_1 and t_2, in Equation 2-36, it is obtained:

Equation 2-37

$$\begin{aligned} R_x(\tau) &= E\left[\int_{-\infty}^{+\infty} e^{-i2\pi f_1 t}d\varphi^*{}_x(f_1)\int_{-\infty}^{+\infty} e^{i2\pi f_2(t+\tau)}d\varphi_x(f_2)\right] \\ &= \int_{-\infty}^{+\infty} e^{i2\pi f_2\tau}\int_{-\infty}^{+\infty} e^{i2\pi t(f_2-f_1)}\,E\left[d\varphi_x(f_2)d\varphi^*{}_x(f_1)\right] \end{aligned}$$

Introducing the following definition (Perotti 2017):

Equation 2-38

$$\bar{S}_x(f_2)df_2 = \int_{-\infty}^{+\infty} e^{i2\pi t(f_2-f_1)}\,E\left[d\varphi_x(f_2)d\varphi^*{}_x(f_1)\right]$$

With $\bar{S}_x(f)$ the stationary power spectrum of the x(t) process. Replacing Equation 2-38 in Equation 2-37, it is obtained:

Equation 2-39

$$R_x(\tau) = \int_{-\infty}^{+\infty} e^{i2\pi f_2\tau}\,\bar{S}_x(f_2)df_2$$

The process $d\varphi_x(f)$ is orthogonal and the following relation can be written:

Equation 2-40

$$E\left[d\varphi_x(f_2)d{\varphi^*}_x(f_1)\right] = \delta(f_1 - f_2)\bar{S}_x(f_2)df_1df_2$$

Where the $\delta(f)$, is the Dirac-delta function equal to 1 when $f_1=f_2$, and 0 elsewhere. For the case $f_1=f_2.$ It is possible to write:

Equation 2-41

$$E[|d\varphi_x|^2] = \bar{S}_x(f)df$$

Dividing by df:

Equation 2-42

$$\bar{S}_x(f) = \frac{E[|d\varphi_x|^2]}{df}$$

From Equation 2-42 it is possible to recall that the units of $d\varphi_x$ are the square root of the frequency [$\sqrt{df}$].

Based on the previous equations, it can be observed the definition of $d\varphi_x(f)$ (Equation 2-34), its units (Equation 2-42), and the orthogonality property (Equation 2-40).

2.1.3.2 Non-stationary process

Supposing a zero mean stochastic process $x^{(j)}(t)$, which is continuous, complex valued, and exists for the real time interval $-\infty<t< +\infty$. The process can adopt the following representation:

Equation 2-43

$$x^{(j)}(t) = \int_{-\infty}^{+\infty} \Psi(t,f)X^{(j)}(f)e^{i2\pi ft}df$$

In which, $X^{(j)}(f)$ is a stationary spectral representation of $x^{(j)}(t)$. $\Psi(t,f)$ belongs to a family or set of functions (Priestley 1965), which works as a modulating function that accounts for the variation of the spectral properties with time and frequency. For the case of stationary process, $\Psi(t,f)$ assumes a value equal to the unity. Therefore, it is important to remark the stationary nature of the $euler\ or\ exponential$ (e^x) function makes it suitable to describe the stationary process but not capable to reproduce the non-stationarity.

In fact, the decomposition of the complex exponential as a sum of sine and cosine waves gives the interpretation of energy distribution over a frequency content. However, the stationary behavior of the sine and cosine waves only allows the description of stationary process. To consider the case of non-stationary process, it is necessary to use functions with also non-stationarity, but without the loss of the oscillatory behavior (to avoid the loss of the physical interpretation).

2.1.3.3 Evolutionary power spectra

The variance of the process X(t) can be computed as shown in Equation 2-44. Since this parameter contents the square of the amplitude of the signal, it gives a measure of the energy content at time t. Then, Equation 2-44 represents the decomposition of the total energy of the signal as the contribution of each frequency f.

Equation 2-44

$$\sigma_X{}^2 \equiv R_{t,t} = \int_{-\infty}^{+\infty} \Psi^2(f,t)\,\overline{S_x}(f)df$$

Where the Evolutionary Power Spectrum (EVPS) can be defined as Equation 2-45 (Perotti 2017):

Equation 2-45

$$EVS_x(f,t) = \Psi^2(f,t)\bar{S}_x(f)$$

In addition, to standardize the definition of the EVPS, the amplitude modulating function, Ψ, is normalized to have unit value at zero time (Equation 2-46); and, therefore, its Fourier transform will have unit integrals. More information of these developments can be found in (Priestley 1965).

Equation 2-46

$$\Psi(f,t=0) = 1$$

2.1.3.4 Uniformly modulated process

Considering a non-stationary process $x(t)$, with the following representation:

Equation 2-47

$$x(t) = C(t)x^{(o)}(t)$$

With $x^{(o)}(t)$ being a stationary process with zero mean and spectrum $\bar{S}_x(f)$. The function C(t) (with C(0)=1) has a Fourier transform whose modulus has an absolute maximum at the origin. Since $x^{(o)}(t)$ is stationary, it is possible to write:

$$x^{(o)}(t) = \int_{-\infty}^{+\infty} e^{i2\pi ft} d\varphi_x(f)$$

Like in Equation 2-41, $d\varphi_x(f)$ is an orthogonal process and Equation 2-40 is still valid (Perotti 2017):

Equation 2-48

$$E|d\varphi_x(f)|^2 = \bar{S}_x(f)df$$

Hence, the uniformly modulated non-stationary process is defined in Equation 2-49 (analogous to the previous Equation 2-43):

Equation 2-49

$$x(t) = \int_{-\infty}^{+\infty} C(t)\, e^{i2\pi f t} d\varphi_x(f)$$

If the evolutionary power spectrum given in Equation 2-45 were associated to the family of functions $\Psi(\mathrm{f},\mathrm{t})$={C(t)}, it could be rewritten as:

Equation 2-50

$$EVS_x(f,t) = |C(t)|^2 \bar{S}_x(f)$$

Therefore, it is possible to define the uniformly modulated process as a special case of the non-stationary process, in which all the spectral components are only modulated over the time, i.e. the dependency of the amplitude modulating function on frequency is negligible.

The studies made on the downburst records express the possibility of defining their turbulence as a *uniformly modulated* non-stationary random field process.

2.1.3.5 *Evolutionary frequency response function*

To obtain the response, $y(t)$, of a mechanical system subjected to an input excitation, $x(t)$, it is important to define the system associated *Frequency Response Function* FRF, H, also known as *Transfer Function* TF. This is the function that measures how the structural system modifies the amplitude and offset the phase of the input signal Figure 2-12. Analogous to the linear transformation of signals made by the filters.

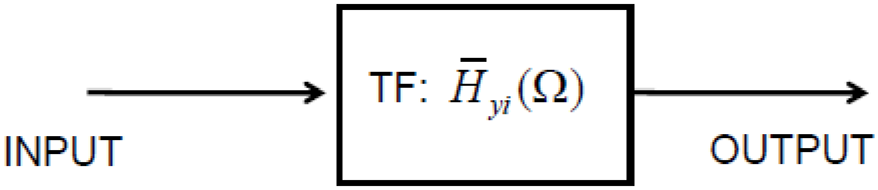

Figure 2-12: FRF function.

For the case in which the input signal is associated to a non-stationary stochastic random process the concept of the FRF function shall be extended to the evolutionary spectrum.

Supposing the dynamic equilibrium equation of an oscillator, subjected excitation $x(t)$ associated to a non-stationary random process as defined in Equation 2-51. Its response $y(t)$ can be obtained by Equation 2-52.

Equation 2-51

$$x(t) = \int_{-\infty}^{\infty} \Psi(f,t) e^{i2\pi f t} d\varphi_x(f)$$

Equation 2-52

$$y(t) = \int_0^t x(\tau)h(t-\tau)d\tau$$

Where the $h(t-\tau)$ is the impulse response function evaluated in the time window $t-\tau$.

By squaring the quantities of Equation 2-52, taking the average through all the realizations (Perotti 2017) is possible to handle the problem in the frequency domain.

Equation 2-53

$$\sigma_Y{}^2 = E[y^2(t)] = E\left[\left|\int_0^t x(\tau)h(t-\tau)d\tau\right|^2\right]$$

Replacing Equation 2-51 in Equation 2-53:

Equation 2-54

$$\begin{aligned} E[y^2(t)] &= E\left[\left|\int_0^t \int_{-\infty}^{\infty} \Psi(f,t)e^{i2\pi ft}d\varphi_x(f)\, h(t-\tau)d\tau\right|^2\right] \\ &= \left|\int_0^t \Psi(f,t)h(t-\tau)e^{i2\pi ft}d\tau \quad \right|^2 E[|d\varphi_x|^2] \end{aligned}$$

Hence, the evolutionary power spectrum of the response can be written as follows:

Equation 2-55

$$EVS_Y(f,t) = |H(f,t)|^2\bar{S}_x(f)$$

Where the *generalized transfer function,* $H(f,t)$, respect to the family of functions $\Psi(f,t)$ is defined as:

Equation 2-56

$$H(f,t) = \int_0^t \Psi(f,t-\tau)h(\tau)e^{-2\pi f\tau}d\tau$$

Because of the causality property the response is equal to zero for all the times t < 0, corresponding to values t < τ within the integral Equation 2-56: then, it is possible to assume that the upper bound of the integral Equation 2-56 tends to infinity.

The lower bound of the integral Equation 2-56 can be assumed equal to minus infinity if whether t is required to evaluate the vibrations of the system far from the time t, such that the initial conditions can be neglected or the excitation before the initial time is zero.

Therefore, Equation 2-56 becomes:

Equation 2-57

$$H(f,t) = \int_{-\infty}^{+\infty} \Psi(f, t-\tau) h(\tau) e^{-2\pi f \tau} d\tau$$

For the case of uniformly modulated process Equation 2-57 becomes Equation 2-58 and equation Equation 2-55 becomes Equation 2-59:

Equation 2-58

$$H(f,t) = \int_{-\infty}^{+\infty} C(t-\tau) h(\tau) e^{-2\pi f \tau} d\tau$$

Equation 2-59

$$EVS_Y(f,t) \cong |H(f)|^2 EVS_X(f,t) = \overbrace{|H(f)|^2 |C(t)|^2}\, \bar{S}_x(f)$$

Grouping the terms by side of the stationary spectrum $\bar{S}_x(f)$ is possible to obtain the evolutionary power spectral density of the response as:

Equation 2-60

$$EVS_Y(f,t) \cong |H(f,t)|^2 \bar{S}_x(f)$$

And to approximate the EFRF to:

Equation 2-61

$$H(f,t) \cong H(f)C(t)$$

2.2 Sampling information

The Fourier analysis is the tool allowing the transformation from time to frequency domain. For non-periodic signals, it works by lapping copies of the signal in the time axis every time window T (corresponding to record duration). Graphically it is shown in Figure 2-13. Briefly explaining, the generated signal goes from zero to T inside the time window, but the Fourier analysis artificially repeats M times the signal to make the approximation with series of sines and cosines.

All the harmonics contained in the signal are multiple of the first harmonic. Therefore, the first harmonic will give the spacing in frequency domain known as the *frequency resolution* and by definition it is the inverse of the time window Equation 2-62. Thus, the higher the time window the better the resolution in frequency.

Equation 2-62

$$\Delta f = \frac{1}{T}$$

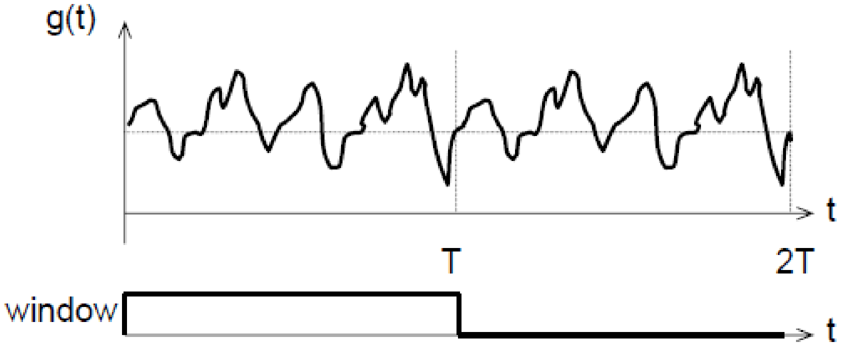

Figure 2-13: Fourier analysis representation

The sampling frequency corresponds to the frequency on which the data is gathered or as in this case simulated. An important parameter linked to this one, is the so-called Nyquist frequency computed as Equation 2-63. This one describes the range of frequencies until which it will be possible to see a representative data on the frequency domain i.e. harmonics or signals with frequency content greater than Nyquist frequency could not be seen due to symmetry of the spectral representation-mirroring (Figure 2-14: Nyquist frequency- mirror).

Equation 2-63

$$f_{Ny} = \frac{f_{samp}}{2}$$

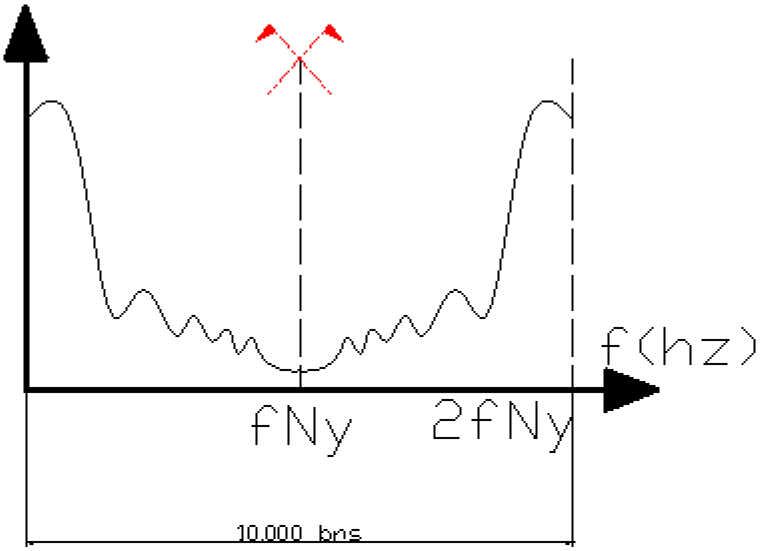

Figure 2-14: Nyquist frequency- mirror

The sampling in time is the inverse of the sampling frequency Equation 2-64. It is very important for the integration of the equations of motion since it ensures the accuracy and, in some cases, also the stability of the numerical solution. Therefore, for the developments of the present study its definition and so the sampling frequency will be governed by the Newmark method requirements rather than the sampling or frequency representation of the signal.

Equation 2-64

$$\Delta t = \frac{1}{f_{samp}}$$

To check if the sampling definitions are well done the number of points between frequency and time must coincide.

Equation 2-65

$$\begin{cases} N = \dfrac{T}{\Delta t} \\ N = \dfrac{f_{samp}}{\Delta f} \end{cases}$$

2.3 Models based on CFD analysis

There are many studies available in the literature to reproduce numerically the downburst behavior using the Computational Fluid Dynamic tools (CFD). Mainly three different techniques have been used to this aim, either the Ring vortex model, the Impinging jet model or the Cooling source model. A graphical description of each type is given in Figure 2-15.

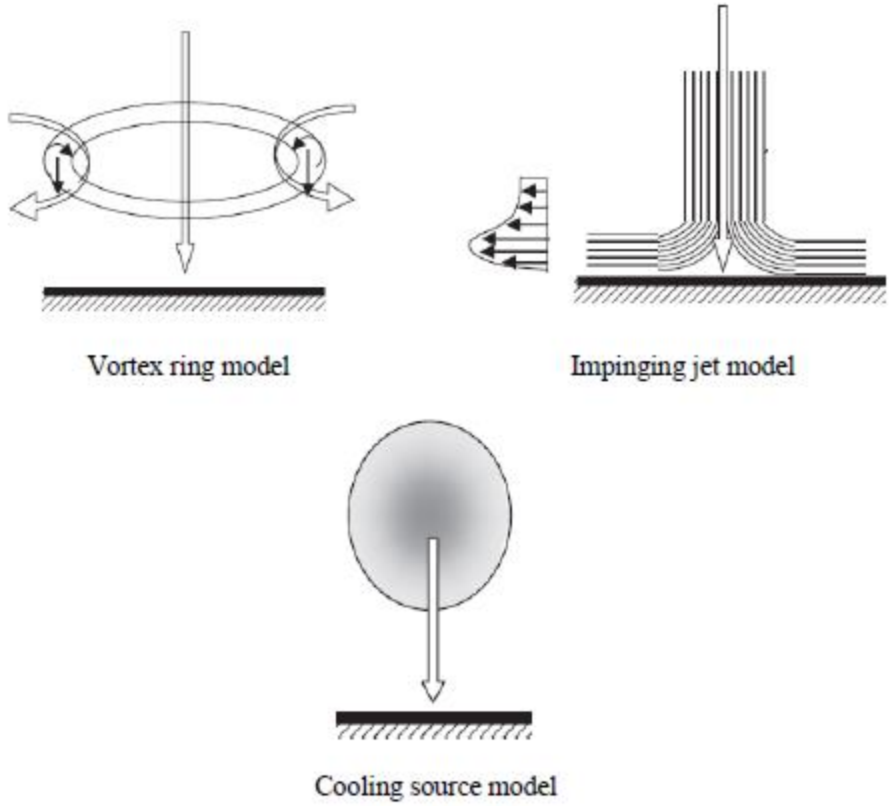

Figure 2-15: CFD models for downburst. Adapted from (Elawady 2016).

2.3.1 Impinging jet

This corresponds to original model suggested by (Fujita 1985) to describe the downburst behavior. It is based on the analogy between the downdraft impacting with the ground and an impulsive jet impinging with a wall or flat surface (Shehata, et al. 2005) (Hangan, et al. 2003).

The impinging jet simulations inside the framework of the CFD are capable to reproduce the mean velocity field of the downburst. However, either the truculence neither the translation velocity can be accurately captured with this type of simulations.

From the studies presented in (Shehata, et al. 2005) it is possible to highlight two components: the vertical profile of the wind velocity as that shown in Figure 2-16 and an intensification function normalized with the reference velocity Figure 2-17.

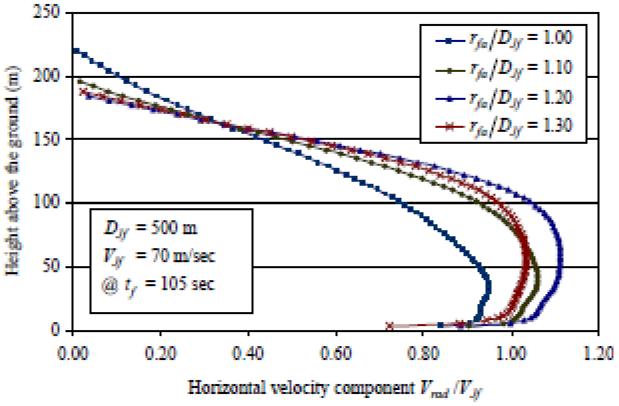

Figure 2-16: Vertical profile using CFD. Adapted from (Shehata, et al. 2005)

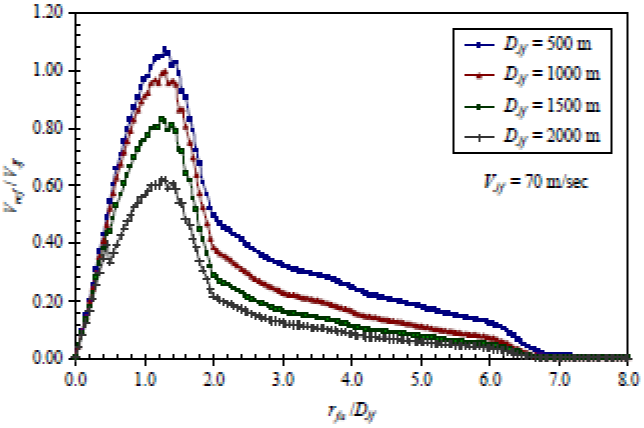

Figure 2-17: Peak horizontal velocity (Vref) at 10m height. Adapted from (Shehata, et al. 2005)

Finally, a representation of a structural response (axial force in the leg of a latticed tower - research case of study) produced by the wind field over the structure is presented in the study of (Shehata, et al. 2005) as shown in Figure 2-18. The importance of this structural parameter is that it gives a measure of the mean wind velocity acting on the tower, in addition the author provides also a comparison with the value obtained by standard atmospheric boundary layer model.

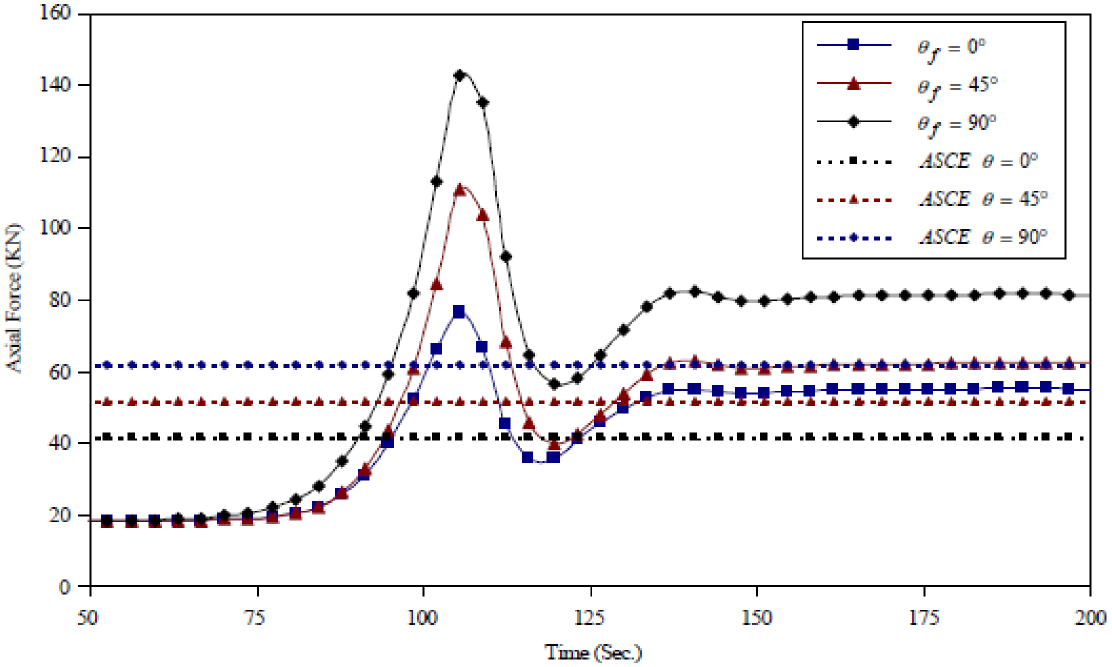

Figure 2-18: Axial force in leg element of tower. Adapted from (Shehata, et al. 2005)

2.3.2 Vortex ring model

This type of model reproduces the vortex formed during the downdraft of cool air. It is worth to stress that the ring vortex model application to reproduce downburst (according to Savory 2001) showed to be not capable of correctly describing the wind field near to the ground after the downdraft impact (Elawady 2016).

2.3.3 Cooling source model

This type of models is based on the simulation of the downdraft by means of a temperature change which affects the buoyancy term of the energy conservation equation (Mason, et al. 2009) (Vermire, et al. 2011).

The simulation of downburst wind fields with the cooling source model allows to reproduce accurately the wind velocity field features in the region near to the surface (Mason, et al. 2009) (Vermire, et al. 2011) . it is worth noting that the simulations made by (Vermire, et al. 2011) the translation component was considered, (Mason, et al. 2009) on the other hand neglect their effects by stating that the environmental effects are almost invariable for engineering applications.

The typical representation of a downburst simulated in with the cooling source model could be seen in Figure 2-19 and Figure 2-20.

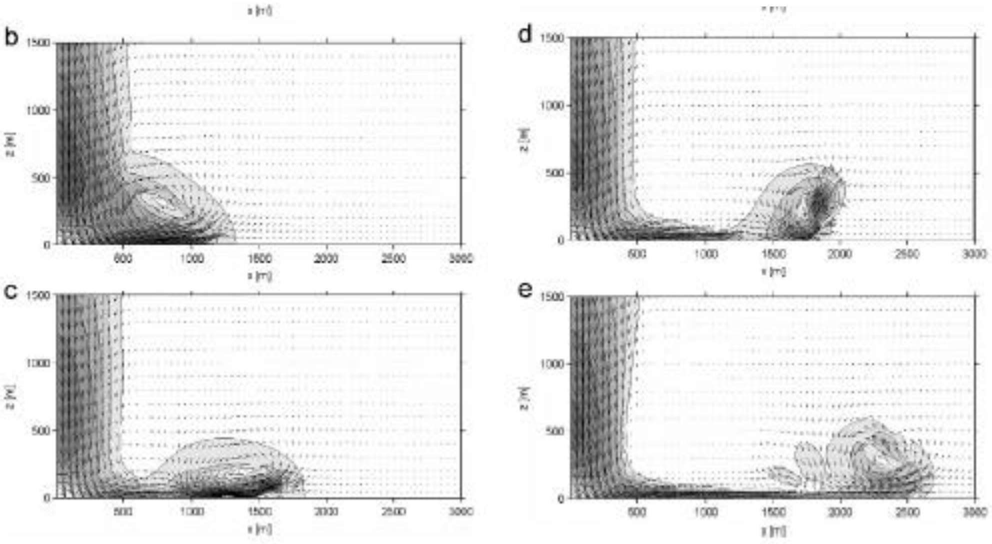

Figure 2-19: Downburst formation with cooling source model. Adapted from (Mason, et al., Numerical simulation of downburst winds 2009)

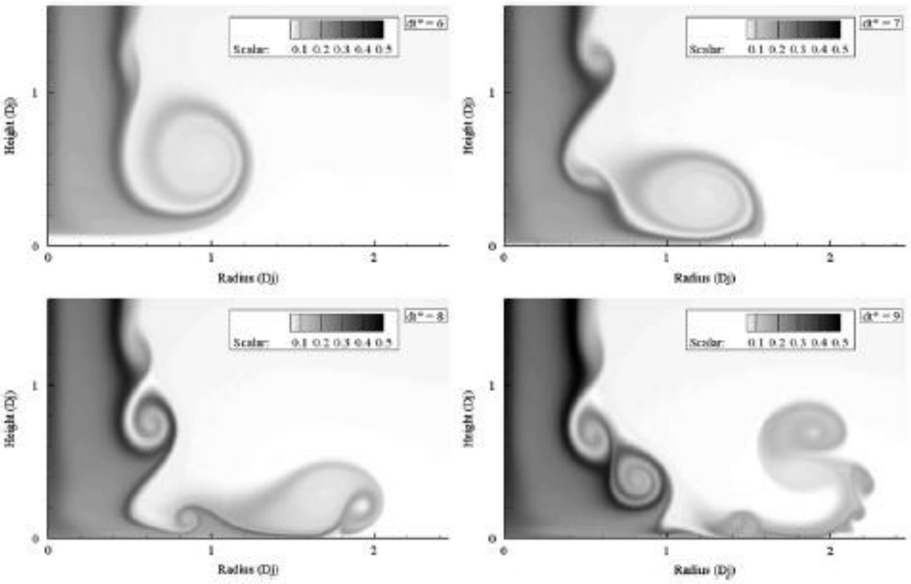

Figure 2-20: Downburst formation with cooling source model. Adapted from (Vermire, et al. 2011)

The mean velocity field is correctly reproduced with this method. A typical simulation of the vertical profile could be seen Figure 2-21. Regarding the radial diffusion function, it is possible to make reference to the term umax/ustrom from (Mason, et al. 2009) showed in Figure 2-22.

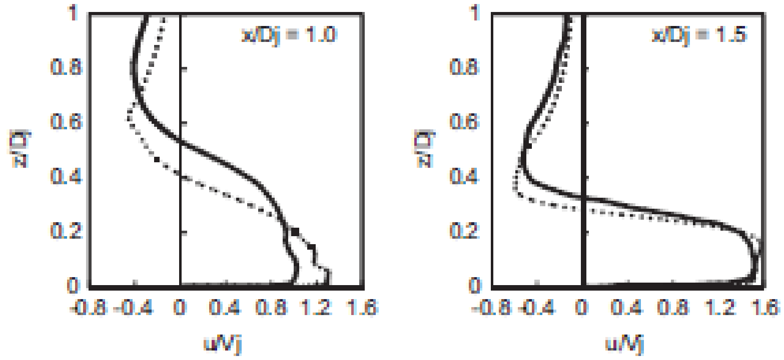

Fig. 10. Vertical profiles of the horizontal component of velocity for the current study (dashed) and Kim and Hangan (2007) (solid) at the time of local maximum outflow velocity at $x/Dj = 1.0$ and 1.5.

Figure 2-21 Vertical Profile. Adapted from (Vermire, et al. 2011)

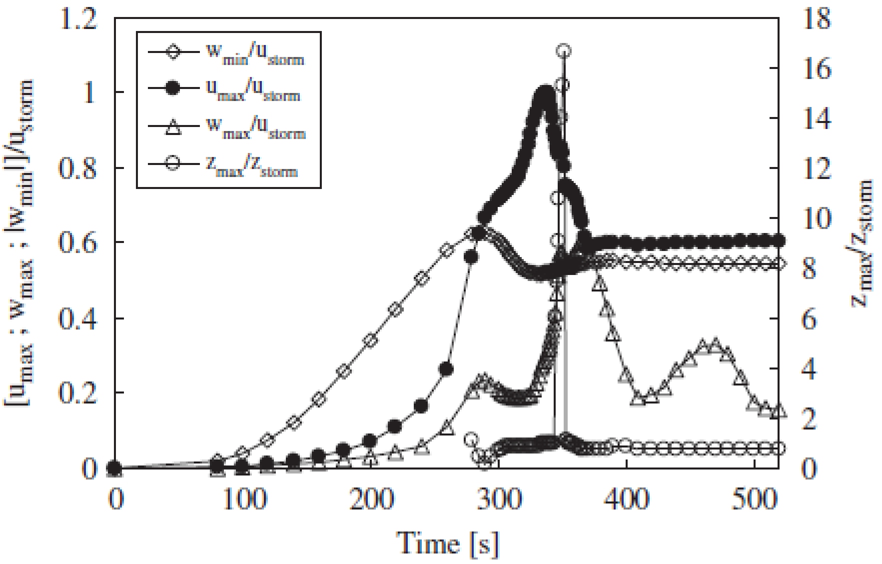

Figure 2-22: Intensification function. Adapted from (Mason, et al. 2009)

2.4 Models based on Wind Tunnel testing

The wind dome or wind chamber WindEEE is the facility used by the University of Western Ontario (UWO) to generate thunderstorms and tornados. It is a hexagonal chamber with maximum width of 25 [m] and height of 3.8 [m]. To generate downbursts, the chamber pressurizes air in an upper plenum and then it releases the air which impinges with the ground of the chamber. A typical downburst formation adapted from (Elawady 2016) can be seen in Figure 2-23.

Figure 2-23: Typical downburst generated in WindEEE Chamber. Adapted from: (Elawady 2016)

To measure the downburst simulated wind fields, the UWO team use two sets of Cobra probes with sampling frequency of 156 Hz. Therefore, the velocity field rather than been generated by means of analytical expressions is fully measured by the reproduction of the phenomena. A typical recording of downburst wind velocity outflows generated inside WindEEE chamber are given in Figure 2-24.

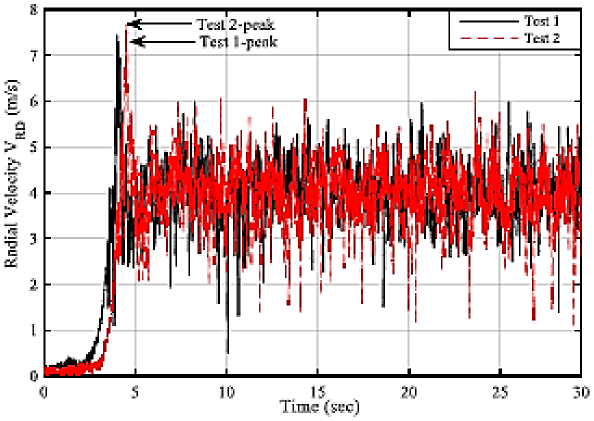

Figure 2-24: Generic simulation of downburst wind field. Adapted from: (Elawady 2016)

It is important to highlight that in Figure 2-24 two downburst records, named as Test 1 and Test 2, were over imposed to check data consistency. Basically, both signals show high relationship between each other and according to (Elawady 2016) the error is lower than 3%. The delay between the two signals is associated to human control of the WindEEE mechanisms.

By means of a moving average technique the wind velocity record is decomposed into slowly varying mean and a turbulent component, similar to what is implemented in (G. Solari, M. Burlando, et al. 2015). The particular definition of this approach is the cutting frequency, taken as 1.5 the vortex shedding frequency. According to (Elawady 2016) the moving average frequency was 1.15 [Hz], for a Strouhal number of 0.35 [-] a downburst diameter of 3.2 [m] and radial velocity of 7 [m/s]. a typical decomposition of a record can be seen in Figure 2-25.

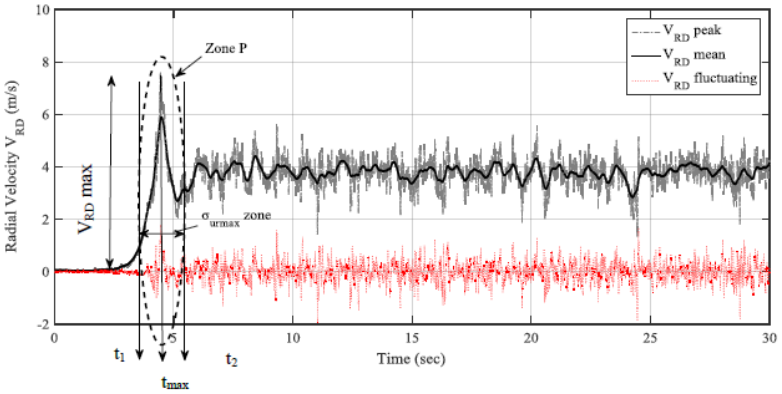

Figure 2-25: Generic wind decomposition. Adapted from: (Elawady 2016)

During the research it was performed a parametric study with the aim of reporting the critical configurations of downburst location which make the higher structure internal forces for power line systems. In addition, it was also assessed the Dynamic Amplification Factor of the structural response.

It was basically found that for guyed towers, the critical angle of attack ϴ (as defined in Figure 2-26) is that aligned with the power line track and producing no conductor forces. For self-supported towers the worst condition is an angle of attack orthogonal to the line track, producing the higher transversal forces in the cables. Finally, for the critical situation in the cross arms of the towers the downburst must attack in an angle of 52[°] respect to the orthogonal segment to the tower in consideration.

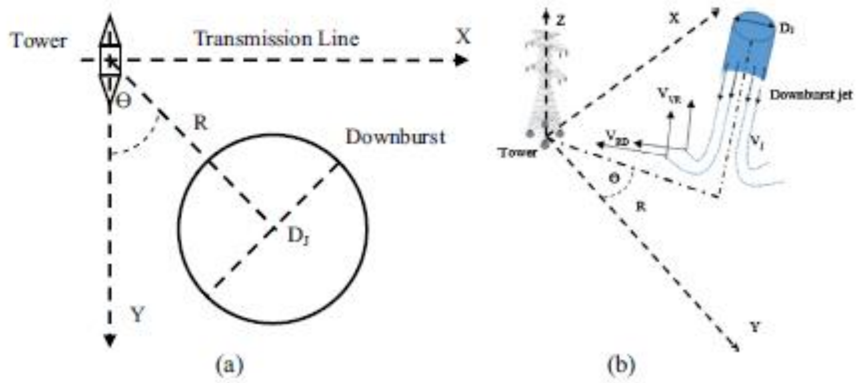

Figure 2-26: Downburst geometrical definitions. Adapted from (Elawady 2016)

The Dynamic Amplification Factor (DAF) in the study was computed by splitting the structural response into the background and resonant parts of process. To extract the background response, the above-mentioned moving average technique was applied. Then the PSD function of the response was computed to finally obtain the resonant respond. The results show that the maximum DAF expected is 1.23 (23% of resonant response) for the base moment.

Since the nature of this model is based on experimental testing and it reproduces the phenomena, the expressions for an analytical simulation of the generic downburst wind fields cannot be directly obtained. However, it will be useful for defining the critical configuration of downburst actions in the cases of study and a measure of the DAF but not a significant contribution to the simulation of the wind outflow.

2.5 Empirical models

Aiming at providing a common framework for the comparison of the different models of downburst available in the literature, the similar components of each model will be placed inside categories. In a very general way, all the models coincide in a decomposition of the wind velocity in a slowly varying mean value and a turbulent component. Then the mean value is divided in a vertical profile and a radial diffusion function (whether of time, space or both). The turbulent component is handled as the zero mean random process with an evolutionary PSD. The concept of the amplitude modulating function allows to make the relation between stationary and non-stationary spectra (Priestley 1965).

Once the description of the wind field components is done, is time for the generation of the simulated wind fields, again a common point in the empirical models. However, many techniques among those available in the literature are used and every author has preference for a particular one. Finally, the verification of the simulated wind filed is performed by comparing them with real measurements of downburst from radar recordings. The latter aspect is crucial since provides the actual validation of the model, i.e. if a model is feasible to implement with less computational effort than others but is not able to reproduce the real recorded behavior of the downburst, it cannot be considered as useful.

Besides the wind field definition, another important parameter is the structural response assessment. Again, every author has his own way to solve the dynamic problems. Whether in the time domain or frequency domain.

Therefore, the methodology of comparison by categories will rely on the following:

- Model description.
- Overview of the techniques implemented.
- Radial diffusion function. (time or space).
- Power Spectral density for turbulence definition.
- Amplitude modulating function.
- Coherence function.
- Generation of the wind field
- Structural response.
- Model validation with real data.

2.5.1 Vertical profile

One the most important aspects defining the downburst velocities is its nosed vertical profile, differing from the logarithmic one, which is characteristic of the Atmospheric Boundary layer winds. Since the models giving a description of the vertical profile of the downburst velocity field are presented and compared in the literature available for the other models as starting point, an initial comparison of those will be presented first.

The first aspect to verify in the construction of the downburst model is the vertical distribution of the radial velocity component. The principal models describing the vertical profile were proposed by Osegura and Bowles (Osegura and Bowles 1988), Vicroy (Vicroy 1992) and Wood and Kwok (Wood and Kwok 1998).

The model of Osegura and Bowles approximates the real behavior that satisfies the requirements of fluid mass continuity i.e. the mass of the fluid remains constant therefore the rate of mass entering into the system is the same going out

Equation 2-66. One important aspect of this model is the fact that it does not directly include within the set of the model parameters the maximum (registered or probable) velocity of the storm. The latter, however, can be easily related to the model parameters, as it will be shown in the following.

Equation 2-66

$$\frac{\partial \rho}{\partial t} + \nabla \cdot (\rho u) = 0$$

The vertical distribution of the wind velocity field according to this model can be computed according to Equation 2-67.

Equation 2-67

$$V(z) = \left(\frac{\lambda D^2}{2r}\right)[1 - e^{-\left(\frac{r}{D}\right)^2}](e^{-z/z^*} - e^{-z/\epsilon})$$

The profile gives the velocity at any height Z depending on the distance to the downburst center r. D, represents the characteristic radius of the downburst which is multiplied by a scale factor λ with unit inverse of second [1/s], z* stands for the characteristic height and ε is a characteristic height in the boundary layer in. All distances in meters. Regarding the maximum velocity of the given the profile it can be seen in Equation 2-68, where the $\bar{F}(zmax)$ depends on the characteristic heights of the boundary layer z* & ε, the given numeric value is valid for 200[m] and 30[m] of both parameters respectively.

Equation 2-68

$$V_{max} = \left(\frac{\lambda D^2}{2r}\right)[1 - e^{-\left(\frac{r}{D}\right)^2}]\bar{F}(Z_{max}) \rightarrow \left(\frac{\lambda D^2}{3.3r}\right)[1 - e^{-\left(\frac{r}{D}\right)^2}]$$

The models introduced by Wood and Vicroy are similar in the sense that both consider directly the maximum velocity (Vmax) that is expected or registered in the thunderstorm downburst and that neglect any possible contribution coming from relative position of the downburst respect to the observation point. Therefore, while the Osegura vertical distribution of horizontal velocity component depends on the position to the thunderstorm downburst center, the other models are depending on the characteristics of the wind itself, making them more suitable for implementation purposes.

The expression to obtain the Vicroy and Wood model are given in Equation 2-69 and Equation 2-70 respectively.

Equation 2-69

$$V(z) = 1.22 * V_{max} * [e^{-0.15z/z_{max}} - e^{3.2175/z_{max}}]$$

Equation 2-70

$$V(z) = 1.55 * V_{max} * \left(\frac{z}{\delta}\right)^{1/6} [1 - \mathrm{erf}(0.7\frac{z}{\delta})]$$

The height for which occurs the maximum velocity is z_{max}, V_{max} stands for the reference mean velocity of the process and δ is the height where V(z) is half of Vmax.

Graphically the three profiles could be seen in Figure 2-27. A better description of the same will be given in **§** 3.2.1

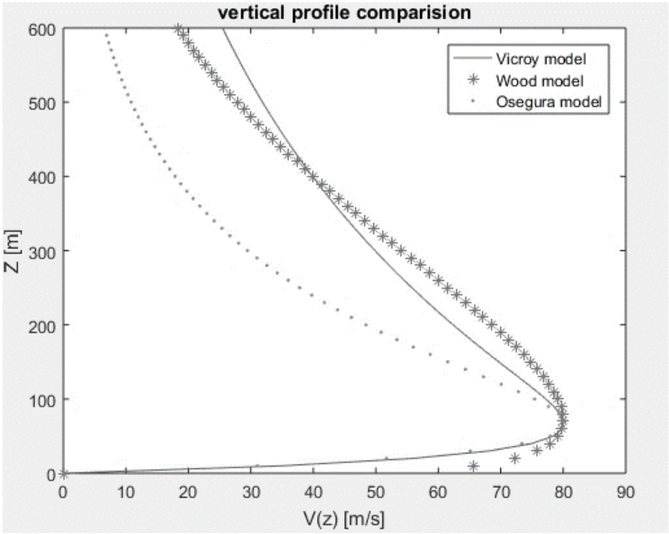

Figure 2-27: Vertical profiles of downburst

2.5.2 Model: Holmes & Oliver 2000

2.5.2.1 Description of the model

The model developed by (Holmes and Oliver 2000) presents a description of the outflow winds of downbursts by means of the horizontal component of the wind velocity arriving from the center of the storm to an arbitrary observation point. This could be considered as one of the first attempts to build a model for engineering simulation of this phenomenon. The main objective of the model is to reconstruct the anemometer records of the Andrews Air Force Base (AFB) and to develop a methodology to assess the effect of downburst on power line systems.

A foreword on this model: this is based on the hypothesis that downbursts can be represented as an impinging jet flow that crashes against a wall or flat surface causing a divergent flow from the center of the downburst or impact point, giving rise to a radial component of the outflow (Hjelmfelt 1998).

The model gives an expression for the horizontal component (parallel to the ground) of the wind speed and orientation in a traveling downburst. This is achieved by making the vector summation of the radial component from the impinging jet model with the translation speed of the mother storm that carries the downburst. This definition clearly matches the records of the downburst available and therefore has been widely used in the models developed after its introduction.

Even though this model does not provide all the same components than the others, is important to bring it in for evaluation since it is one of the earliest definitions of the downburst wind field and serves as foundation for the later models.

2.5.2.2 Techniques implemented

Deterministic computation of the outflow and tracking components to a further description of the downburst wind velocity’s horizontal component. No turbulence included therefore non-special techniques for wind generation or integrations of the equations of motion.

2.5.2.3 Vertical profile

The model provides only a description of the wind component parallel to the ground. Vertical profiles were not specified in its construction.

2.5.2.4 Radial diffusion function

The mean value is computed as the vector summation of the radial component and the translational one.

Radial velocity

The horizontal profile is divided in two zones, the first is the so-called “stagnation region”, where the velocity increases linearly until a point of maximum. In the second zone, the velocity profile exhibits an exponential decreasing. The model can be seen in Figure 2-28,adapted from (Holmes and Oliver 2000).

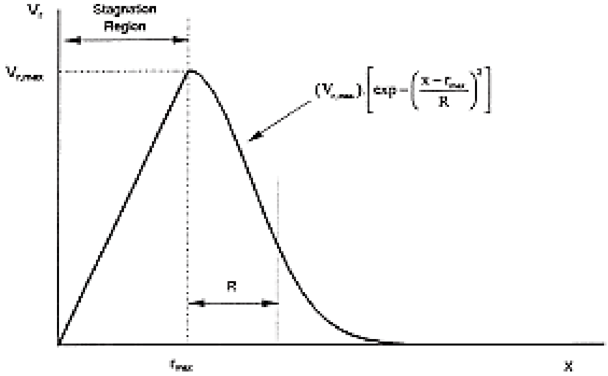

Figure 2-28: Horizontal profile Holmes 2000

The radial velocity as function of time and the distance between the observation point and the downburst center can be computed as follows:

Equation 2-71

$$V_r = \begin{cases} V_{r,max} * \exp[-t/T] * (x/r_{max})\,, & x < r_{max} \\ V_{r,max} * \exp[-t/T] * \exp[-\frac{x - r_{max}}{R}]^2, & x \geq r_{max} \end{cases}$$

Where: $V_{r,max}$ is the maximum velocity registered, r_{max} is the value of the radial coordinate where the maximum value of velocity occurs. R is 50% of r_{max}. Small t is the time of the downburst and capital T is a time constant.

Translation velocity

The mother thunderstorm to which the downburst belongs has a mean wind speed tracking component that moves the downdraft and consequently the outflow. Evidence of this velocity component were found by (Oliver 1992) who described it as the environmental velocity. The study developed by Oliver, consisted in the recording of the wind fields at two close observation stations in Sidney (the stations of Bankstown and Mascot, located at a relative distance of 18 km). If a unique downburst event produced the “strongest” records in both stations, it was possible to obtain the time that the storm took for covering the distance between the two stations. From (Holmes and Oliver 2000) it is possible to obtain a summarized table with the important information:

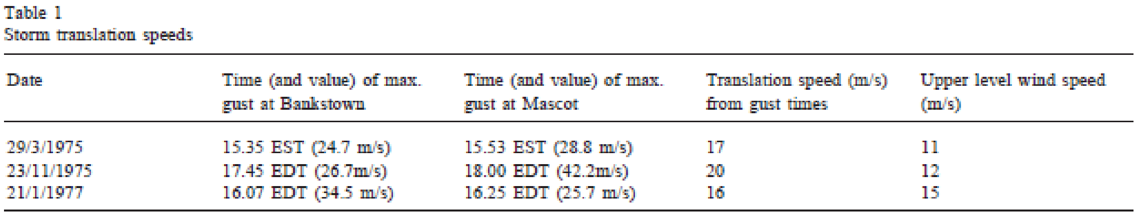

Table 1
Storm translation speeds

Date	Time (and value) of max. gust at Bankstown	Time (and value) of max. gust at Mascot	Translation speed (m/s) from gust times	Upper level wind speed (m/s)
29/3/1975	15.35 EST (24.7 m/s)	15.53 EST (28.8 m/s)	17	11
23/11/1975	17.45 EDT (26.7m/s)	18.00 EDT (42.2m/s)	20	12
21/1/1977	16.07 EDT (34.5 m/s)	16.25 EDT (25.7 m/s)	16	15

Figure 2-29: Table of summary for identification of tracking velocity. Adapted from (Oliver 1992)

Vector summation

With a clear definition of the horizontal wind components is possible then to represent them in graphical form to then introduce their vector summation.

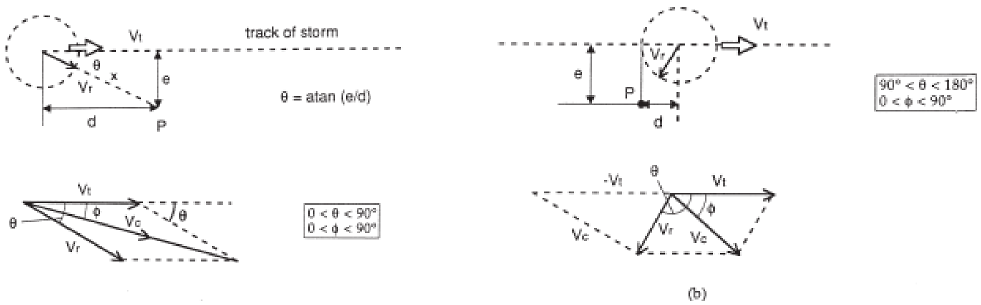

Figure 2-30: Wind components from Holmes 2000

Denoting with V_c the combined velocity from the vector summation computed with the Cosine rule and ϴ the angle measured between the downburst track and the radial component of the velocity, we can introduce the following equation:

Equation 2-72

$$V_c^{\,2} = V_r^{\,2} + Vt^2 + 2V_r * Vt * cos\theta$$

The angle of approximation ϕ of the combined velocity respect to the observation point, then, can be calculated as:

Equation 2-73

$$\text{Cos}\ \phi = \frac{V_c^{\,2} + Vt^2 - V_r^{\,2}}{2V_c Vt}$$

2.5.2.5 Turbulence: Power spectral density

No turbulence introduced

2.5.2.6 Coherence function

No turbulence introduced

2.5.2.7 Generation of the time histories

The model allows for the definition of a mean velocity function that varies on time (or space coordinate x) for a fixed reference value of velocity $V_{r,max}$. Therefore, it is possible to construct one the components involved in the wind velocity decomposition, the time history (shown in Figure 2-31) can be compared with a representative record of downburst, such as the AFB reference time history.

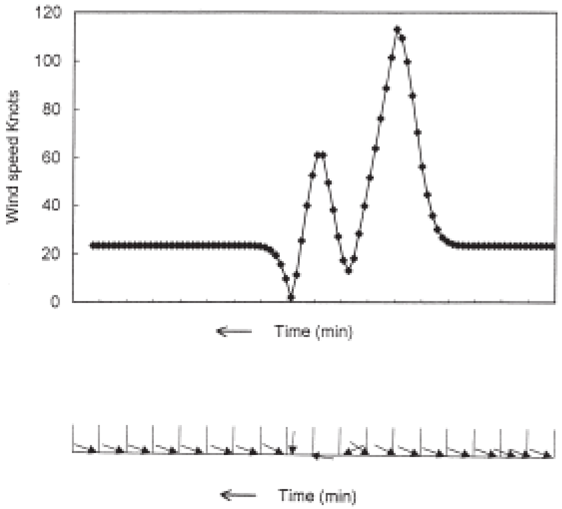

Figure 2-31: Simulated wind speed Holmes 2000

2.5.2.8 Structural response

Not applicable

2.5.2.9 Data consistency

The model provided in Figure 2-28 for the impinging jet model was compared with data gathered from the radar observations of downburst (Hjelmfelt 1998) observing a good match in the radial component description with the measured data giving in this way a validation of the consistency of the empirical definition of this function. The comparison adapted from (Holmes and Oliver 2000) is given in Figure 2-32.

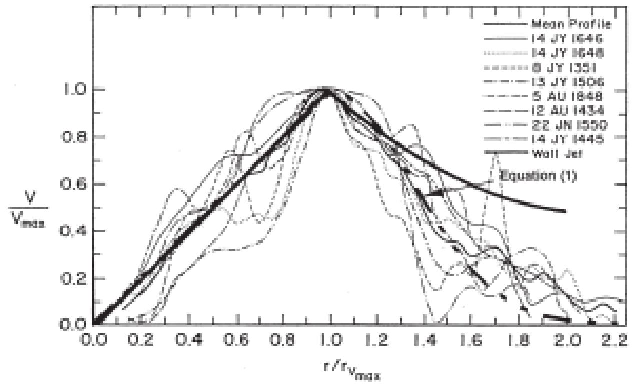

Figure 2-32: Data check of impinging jet model

Regarding the confrontation of the mean velocity profile with the tendency of the AFB record, it is possible to see a satisfactory matching between the empirical model and the results of the measurements in general terms. However, going to the details, a discrepancy in the angle of approximation could be found, this fact could be disregarded since the mean wind speed was projected in a correct way.

From Figure 2-31 and Figure 2-33 it is possible to see that the model captures the first peak of the downburst and the crossing of the storm eye. It is worth noting that the time axis is going from right to left, contrary to the standard convention for representing the time axis in civil engineering applications.

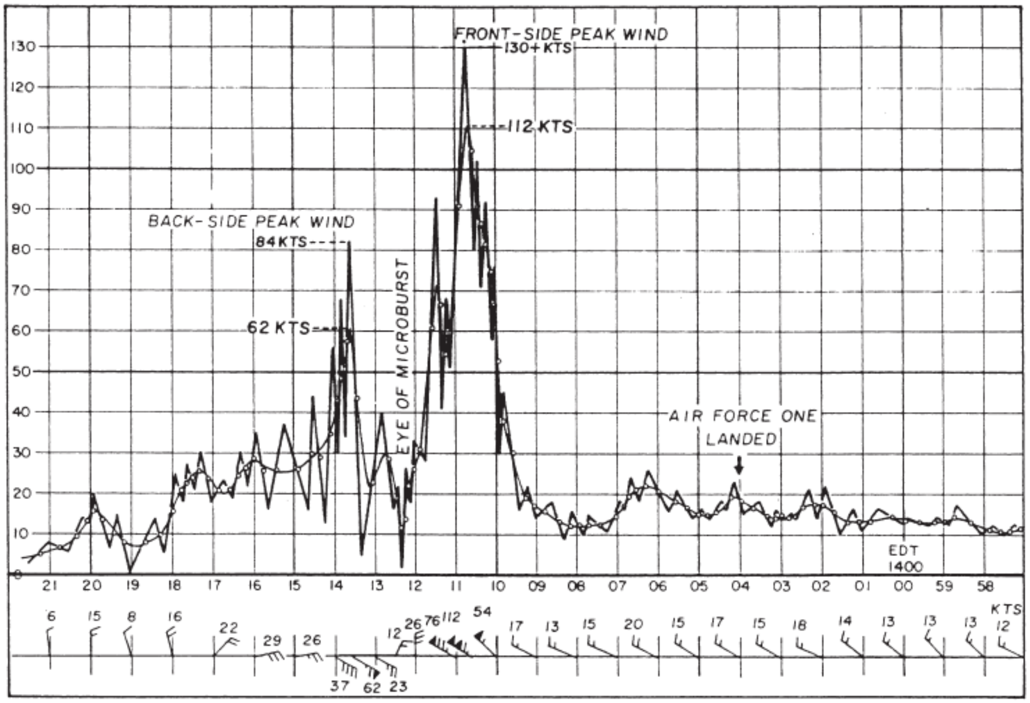

Figure 2-33: Andrews AFB downburst- AIRFORCE ONE event 1983

2.5.2.10 Observations and conclusions

This model is important for the development of the further ones, since its distribution of horizontal wind speed acts as a time function for the description of the mean wind velocities given a reference value for this parameter.

A typical foot print of the downburst wind velocity computed by this model can be seen in

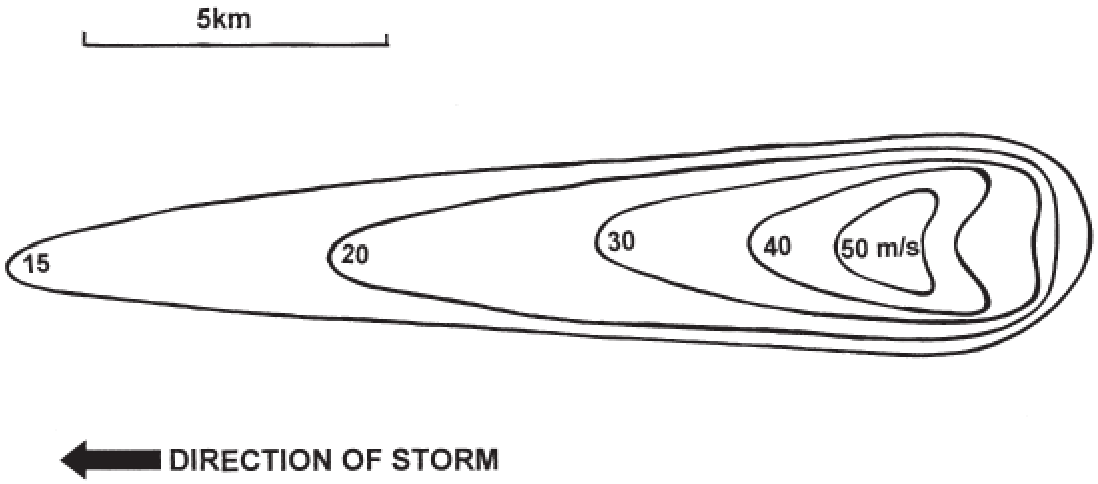

Figure 2-34: Downburst foot print-Adapted from (Holmes and Oliver 2000)

2.5.3 Model: Chen & Letchford2004

2.5.3.1 Description of the model

The model is a deterministic-stochastic hybrid model, consisting in the decomposition of the downburst velocity field as the summation of a slowly varying mean with a non-stationary stochastic turbulent component. It is based on the definition of downburst given by Fujita 1985, and the study is aimed to reproduce the wind simulation with radar registration of the events made during the programs JAWS and NIMROD.

This model corresponds to one of the first full models for downburst analytical description introducing the turbulent component in the formulation and proposing a generation of the wind velocity time histories using the cross power spectral density. This model is therefore used as basis for later developments on the field.

2.5.3.2 Overview of the Techniques implemented

Spectral Representation Method SRM for generation of time histories using CPSD. Based on the Sinozhuka-Deodatis method (Shinozuka and Deodatis 1991) (Deodatis 1989).

2.5.3.3 Vertical profile

In Figure 2-35 it is shown a comparison made of the three available models for vertical profiles made by Chen.

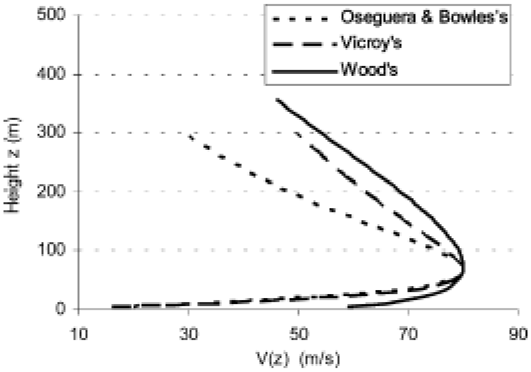

Figure 2-35: Comparison between downburst vertical profiles. Adapted from Chen

2.5.3.4 Radial diffusion function

This model uses as departing point for the horizontal stagnation function the description of Holmes (Holmes and Oliver 2000). However, it uses the radial component based in space coordinates rather than time. The radial component is:

Equation 2-74

$$
\mathrm{V}_r = \begin{cases} \mathrm{V}_{r,max}\,(\mathrm{x}/\mathrm{r}_{max})\,, & \mathrm{x} < \mathrm{r}_{max} \\ \mathrm{V}_{r,max} * \exp[-\dfrac{x-\mathrm{r}_{max}}{R}]^2, & \mathrm{x} \geq \mathrm{r}_{max} \end{cases}
$$

Keeping the same notation already given for (Holmes and Oliver 2000) definition given in **§** 2.5.2 . Additionally, the translation velocity is a given value in this process Vt(t).

Introducing *do* as the distance between the downburst center and the observation point and *e* the eccentricity between this and the straight line defining the track of the downburst, the radial coordinate at any time will be the distance given by current time and the tracking velocity with respect to the initial conditions (*do, e*). The radial velocity vector will be then:

Equation 2-75

$$V_r(t) = \frac{x}{|x|} * V_r(|x|)$$

With *x* being only function of time. For fixed initial conditions and hypothesis of constant tracking velocity.

The combined velocity at any time will be given by the vector summation of the tracking and the radial components.

Equation 2-76

$$\mathrm{V}_c(\mathrm{t}) = \mathrm{V}_r(\mathrm{t}) + \mathrm{Vt}$$

Introducing the horizontal profile function as a function of time, so-called time function as:

Equation 2-77

$$\mathrm{f(t)} = \frac{|V_c(t)|}{Max|V_c(t)|}$$

This time function shapes the mean velocity profile over time for a given maximum value depending on the vertical profile due to the normalization. The maximum value of the envelope function will be given for the alignment of the radial component and the tracking one.

Finally, the mean value will be given by the reference velocity at the height z from the vertical profile $\mathrm{V(z)}$ and the time intensification function $\mathrm{f(t)}$:

Equation 2-78

$$\mathrm{V}_{mean}(\mathrm{z,t}) = \mathrm{V(z)} * \mathrm{f(t)}$$

2.5.3.5 *Power Spectral density for turbulence definition.*

The turbulence in this model was defined by means of the double-sized normalized power spectral density proposed by (Kaimal 1972) the expression is given in Equation 2-79.

Equation 2-79

$$S_{v\prime}\ \ (z,f) = \frac{200{v_s}^2}{2}\frac{z}{V(z)}\frac{1}{[1+50\dfrac{f\,z}{V(z)}]^{5/3}}\frac{1}{6{v_s}^2}$$

Where the term v_s accounts for shear velocity of the flow, the value recommended by the author is 1.76[m/s]. *z,* accounts for the height of the observation point and *f* accounts the frequency.

It is worth noting that the spectrum used for the simulation inside this thesis work depends on the frequency (In Hz) and not on the circular frequency (In Rad/sec) as presented originally by the author. Therefore, both representation of the spectrum depending on frequency and circular frequency are presented in Figure 2-36.

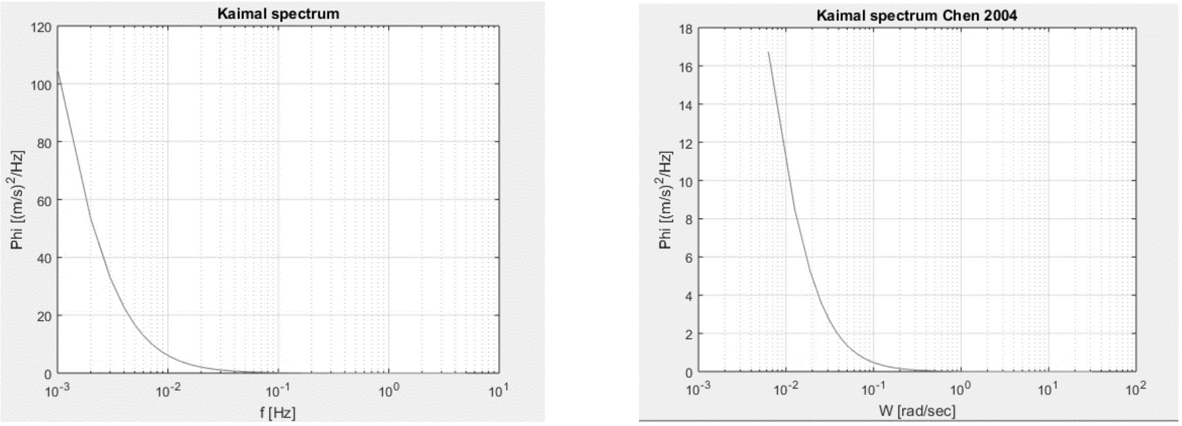

(a) (b)

Figure 2-36: Kaimal's Power Spectrum vs a) frequency b) circular frequency

2.5.3.6 Amplitude modulating function.

The studies from *Wind Science and Engineering Research Center* on the Evolutionary Power Spectral Density have shown that the deviation of the turbulent component of the downburst wind velocity field is close to the 25% of the mean velocity at the same time instant. This allows to assume that the frequency structure of the turbulence does not changes on time i.e. the turbulence can be represented as an amplitude-modulated stationary process based in PSD.

The amplitude modulating function*, a*, proposed by (Chen and Letchford 2004) is a fraction of the mean velocity function as shown in Equation 2-80.

Equation 2-80

$$a(z,t) = 0.25\ V_{mean}(z,t)$$

With the amplitude modulating function, Chen-model allows to directly write the Evolutionary PSD as:

Equation 2-81

$$EVS_{v'}(t,z,f) = |a(z,t)|^2 S_{v'}(z,f)$$

Replacing Equation 2-80 in Equation 2-81

Equation 2-82

$$\mathrm{EvS_{v'}(t,z,f)} = |0.25\ \mathrm{V}_{mean}(\mathrm{z,t})|^2\mathrm{S_{v\prime}(z,f)}$$

2.5.3.7 Coherence function.

Inside the model the Cross Power Spectral density is introduced in the same way explained in **§** 2.1.2, brought for convenience in Equation 2-83. Moreover, the coherence function implemented is the classical one proposed by (Davenport 1968) Equation 2-84.

Equation 2-83

$$S_{vv\prime}(z1, z2f) = coh(\mathit{\Delta} z, f)\sqrt{S_{v\prime}1(z1, f) * S_{v\prime}2(z2, f)}$$

Equation 2-84

$$coh(\mathit{\Delta} z, f) = \exp[-\mathrm{cz} * \frac{\Delta z * f}{\bar{V}(z1, z2)}]$$

With Cz being the non-dimensional decay constant, the typical value for this parameter is 10, whether for synoptic or not-synoptic winds. And $\mathit{\Delta} z$ stands for the separation between the points in study at heights z1 and z2 in meters. And $\bar{V}(z1, z2)$ is the average velocity between both points.

The evolutionary cross power spectral density is given by:

$$EVS_{vv\prime}(t, z1, z2, f) = a(z1, t) * \overline{a(z2, t)}coh(\mathit{\Delta} z, f)\sqrt{S_{v\prime}1(z1, f) * S_{v\prime}2(z2, f)}$$

2.5.3.8 Generation of the wind field

The generation of the random velocities of the wind outflow are made by using the Spectral Representation Method SRM proposed by (Shinozuka and Deodatis 1991). The generation is made for the case of stationary wind velocity field and then converted into a non-stationary field by means of the amplitude modulating function as explained in **§** 2.1.3 Evolutionary Power spectrum.

The cross-spectral density matrix *Svv'(f)* is Hermitian, then, it can be represented through the product of two triangular matrices with the Cholesky factorization Equation 2-85. From now on the notation of frequency will change from natural frequency *f* to circular frequency ω.

Equation 2-85

$$\mathrm{S_{vv'}}(\omega) = \mathrm{H}(\omega)\overline{\mathrm{H}}^{T}(\omega)$$

With H(ω) being a lower triangular matrix. Among the properties of the cross-spectral density is its complex value, therefore H(ω) can be represented in complex notation as an amplitude and a phase as:

Equation 2-86

$$\mathrm{H_{jk}}(\omega) = \left|\mathrm{H_{jk}}(\omega)\right| e^{i\theta jk(\omega)}$$

With j and k indicating the point, j going from 1 to the number of points and k going from 1 to j. always j≥k. The phase is then:

Equation 2-87

$$\theta_{\mathrm{jk}}(\omega) = \tan^{-1}\{\frac{Im[H_{jk}(\omega)]}{Re[H_{jk}(\omega)]}\}$$

Then the wind velocity stochastic process can be simulated by superposition of harmonic series of frequencies, with the number of frequency points (steps), N tending to infinity.

Equation 2-88

$$\mathrm{v}'(\mathrm{zj},\mathrm{t}) = 2\sum_{m=1}^{j}\sum_{l=1}^{N}\left|H_{jm}(\omega_{ml})\right|\sqrt{\Delta\omega}\ cos[\omega_{ml}t - \theta_{jm}(\omega_{ml}) + 2\pi Rnd(0,1)]$$

With m and l are pointers for the points and frequencies respectively. $\Delta\omega$ the frequency resolution given by the Nyquist (Or cut-off) frequency over the number of points. Rnd is the random phase running from 0 to 2π. And the generic frequency ω_{ml} is given by:

Equation 2-89

$$\omega_{ml} = (\mathrm{l}-1)\Delta\omega + \frac{m}{n}\Delta\omega$$

The process results extremely demanding from a computational effort point of view.

2.5.3.9 Downburst wind velocity time history

After the sum of the mean and the fluctuating part the time history that Chen-model produces is like that shown in Figure 2-37.

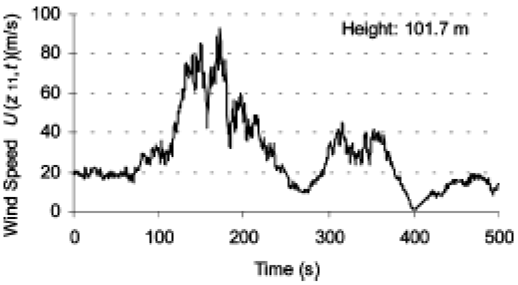

Figure 2-37: Typical time History of Chen model

2.5.3.10 Structural response

The structural response is evaluated by means of the integration of the equations of motion. Not specified method

2.5.3.11 Model validation

It can be seen that the mode proposed (Chen and Letchford 2004)can successfully reproduce a non-synoptic wind event. Indeed, comparing the behavior of the simulated wind and the event registered Andrews FB 1983 (Figure 2-33) we can see that in both cases two peaks separated by a local minimum of wind velocities can be clearly recognized. This effect is due to the time function and the vector summation operations carried out to determine it. Basically, when the storm is approaching the observation point the translational and the radial components are summing up (first peak), after the crossing of the storms eye, the effect of the radial and translational components is counteracting and thus we see a reduction of the second peak. It is worth noting that in the AFB record the time axis is growing from right to left while in the generic generation of wind speed of Chen-model is going from left to right as usual Figure 2-37.

2.5.4 MODEL: SOLARI 2017

2.5.4.1 Model description

The model proposed by Solari and the team of University of Genoa (Solari, et al. 2017) is based on real recordings of downburst outflows velocity fields gathered by Wind Ports and Wind Ports and Sea projects (WP & WPS). This model provides a decomposition based on the turbulence index *Iu* measured from the field recordings and considers the non-stationarity by adding two functions of time, one (γ(t)) for the horizontal profile of the mean velocity and the other (μ(t)) to modulate the gaussian stationary random field of the turbulence. The values that those functions can take come from the recordings. Regarding the vertical profile that one proposed by (Wood and Kwok 1998) is adopted.

An important matter of this model is that it uses a slightly different procedure for the wind velocity decomposition compared with the one given in 2.1.1. The model takes the wind velocity, as usual, as the summation of a slowly varying mean value and a turbulent stochastic component.

Equation 2-90

$$\mathrm{V}(\mathrm{z},\mathrm{t}) = \mathrm{V}_{mean}(\mathrm{z},\mathrm{t}) + \mathrm{v}'(\mathrm{z},\mathrm{t})$$

Z is the height where the velocity is computed, t is a time from 0 to ΔT with ΔT being a time interval between 10 to 60 minutes.

The fluctuation is decomposed by considering a stationary gaussian random process with unit variance, $\bar{\mathrm{v}}'(\mathrm{t})$, with a slowly varying standard deviation $\mathrm{\sigma v}(\mathrm{z},\mathrm{t})$, as it is shown Equation 2-91.

Equation 2-91

$$\mathrm{v}'(\mathrm{z},\mathrm{t}) = \sigma_{v}(\mathrm{z},\mathrm{t})\bar{\mathrm{v}}'(\mathrm{z},\mathrm{t})$$

By performing the standard process of extraction of the mean value and from the definition of turbulence intensity (Equation 2-92) the outflow velocity can be expressed in the way Equation 2-93

Introducing the turbulence intensity, we obtain:

Equation 2-92

$$\mathrm{I}_{v}(\mathrm{z},\mathrm{t}) = \frac{\sigma_{v}(\mathrm{z},\mathrm{t})}{\mathrm{V}_{\mathrm{t}}(\mathrm{z},\mathrm{t})}$$

Equation 2-93

$$V(z,t) = V_{mean}(z,t)[1 + I_v(z,t)\bar{v}'(z,t)]$$

The mean value is decomposed in the product of a maximum velocity parameter and two non-dimensional functions: one in time and the other in vertical distribution. The same is done for the turbulence intensity.

Equation 2-94

$$V_{mean}(z,t) = V_{max}(h)\alpha(z)\gamma(t)$$

Equation 2-95

$$I_v(z,t) = \bar{I}_v(h)\beta(z)\mu(t)$$

Where:

- $\alpha(t)$ is the vertical nosed profile from (Wood and Kwok 1998).
- The vertical profile of the turbulence $\beta(z)$ can be taken as 1 since the results from the recordings seems to neglect the dependency of the turbulence intensity with height.
- $\gamma(t)$ & $\mu(t)$ are the functions for the horizontal profile of the mean velocity and to modulate the gaussian stationary random field of the turbulence, respectively.
- $\bar{I}v(h)$& $Vmax(h)$ are respectively the reference turbulence intensity and the maximum possible velocity at the observation point with coordinates h.

The final expression for the velocity field finally reads as follows:

Equation 2-96

$$V(z,t) = V_{max}(h)\alpha(z)\gamma(t)[1 + \bar{I}_v(h)\beta(z)\mu(t)\bar{v}'(z,t)]$$

2.5.4.2 Overview of the techniques implemented

The model used for the definition of the wind velocity field is a hybrid deterministic-stochastic with deterministic mean value and stochastic turbulent fluctuation. The simulation uses a Monte Carlo Algorithm based on the spectral representation method using the Fast Fourier Transform and Proper Orthogonal Decomposition.

To obtain the standard deviation from the data it was made a moving average filter with moving average period of 30 sec.

2.5.4.3 Vertical profile

The function α(z) builds the vertical profile based on (Wood and Kwok 1998). This function depends on the height Z, the height in which the velocity is half of its value Z* (6*Zm) and Zm is the height for which the velocity is maximum. The function is given as:

Equation 2-97

$$\alpha(z) = \left(\frac{z}{h}\right)^{1/6} \frac{1-\mathrm{erf}\left(0.70 \cdot \frac{z}{z*}\right)}{1-\mathrm{erf}\left(0.70 \cdot \frac{h}{z*}\right)}$$

The velocity will be given by:

Equation 2-98

$$\bar{v}_{max}(z) = \mathrm{V}_{max} * \alpha(z)$$

In the definition of the model there were contemplated different heights of the wind velocity maximum occurrence [25,50,75,100]. Moreover, with the aim of appreciating in detail the maximum effects and the dissipation of the downburst wind velocity fields respect to height two different scales for the vertical profile where studied, one for medium height (100m) Figure 2-38. (b) and other for large height (600m) Figure 2-38. (a) respectively.

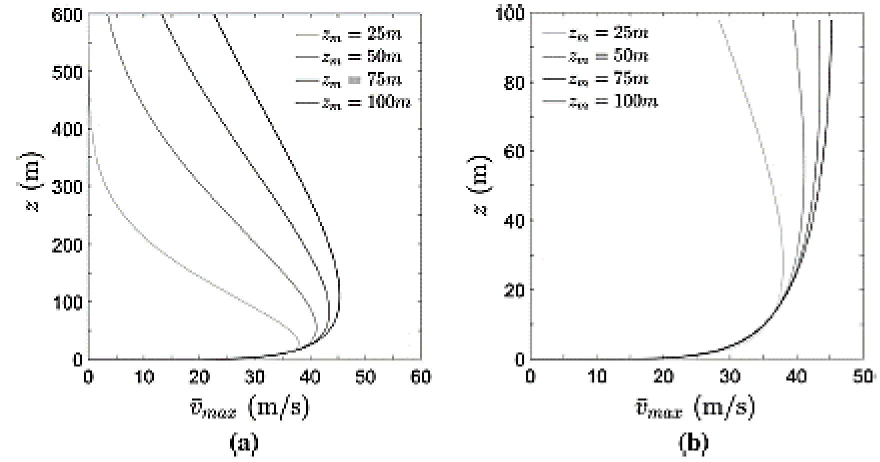

Figure 2-38: Velocity vertical profile for Solari's model (a) scale of 600m (b) scale of 100m. Adapted from (Solari, et al. 2017)

The analysis of the data shows that the function β(z) is a constant value 1, thus has a negligible contribution.

2.5.4.4 Radial diffusion function of time

The time function of the mean velocity γ(t) was extracted from 93 recorded downbursts studied during the WP and WPS projects. The measured functions are shown in Figure 2-39. It is important to highlight that the time line is placed in such a way that the zero time corresponds for the recording of the maximum wind velocity.

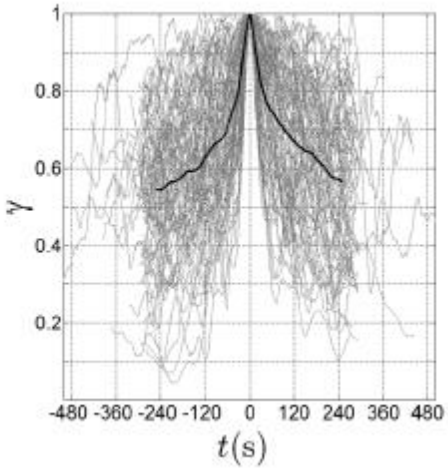

Figure 2-39: γ(t) from the 93 records. Adapted from (G. Solari, M. Burlando, et al. 2015)

2.5.4.5 Power spectral density

Within the framework of the monitoring projects WPS and WP, Solari and coworkers gathered real data of the thunderstorm downburst occurring in the network of some European ports. The analysis of this information shows that the spectrum that matches better the description of the turbulent component of the downburst wind filed among those studied on (Solari and Piccardo 2001) is the PSD shown in Equation 2-99. Where the along wind turbulent component is denoted as, v..

Equation 2-99

$$S_{v\prime}\,(z,f)=\frac{6.868\,\frac{L_v}{V_z(z)}}{[1+10.302\frac{fL_v}{V_z(z)}]^{5/3}}$$

Where the term L_v is the integral length scale in the along wind direction. From (G. Solari, M. Burlando, et al. 2015) the value adopted for this parameter is 34.6 m. It is worth noting that this quantity is very small compared with that of the synoptic winds (G. Solari, M. Burlando, et al. 2015). The V_z (z) stands for the velocity of the vertical profile at the observation point height z.

The normalized PSD is shown in Figure 2-40

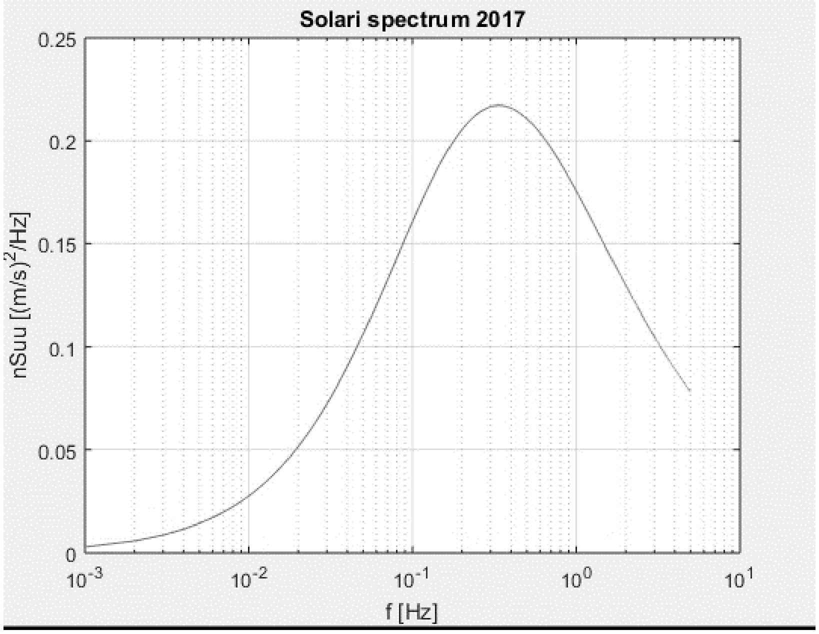

Figure 2-40: Solari-model normalized PSD

2.5.4.6 Amplitude modulating function

The amplitude modulating function μ(t) was, as anticipated, measured from the 93 records of downbursts of the projects WP and WPS. The time line in those functions is synchronized with the γ(t) so that both registers start at the same time, therefore the zero in the former functions coincides with the -250 seconds of the latter and the peak is at the mid time.

The recorded functions are shown in Figure 2-41.

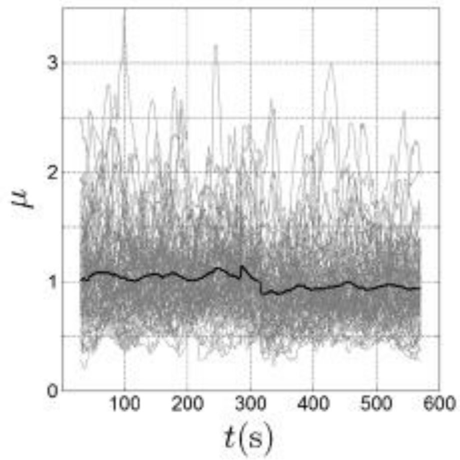

Figure 2-41: μ(t) functions from records of downbursts. Adapted from (G. Solari, M. Burlando, et al. 2015)

2.5.4.7 Coherence function

The coherence function accounted in the model is a 1-dimension coherence functions like the classical proposed by (Davenport 1968). The two points along the vertical dimension have coordinates z and z'.

Equation 2-100

$$\mathrm{Coh_{vv'}(z, z', f)} = \exp\{\frac{2\,f\ Cv|z-z'|}{V_z(z)+V_z(z')}\}$$

2.5.4.8 Generation of wind field

The fluctuation component was simulated with a Monte Carlo algorithm based on power spectral representation. The techniques implemented are the FFT for computing the components of the harmonics in the spectra and the Proper Orthogonal Decomposition to factorize the Power Spectral Density matrix of the fluctuation.

The sampling parameters used in the simulation are reported in Table 2-2.

Table 2-2: Sampling data

Parameter	Value	Units
Time interval T	600	Sec
Frequency resolution, Δf	1/600	Hz
Time step, Δt	0.1	Sec
Sampling frequency, F_{samp}	10	Hz
Nyquist frequency, F_{cut}	5	Hz
Number of simulations, N	1000	und

A typical time history of the wind velocity turbulent component could be seen in Figure 2-42.

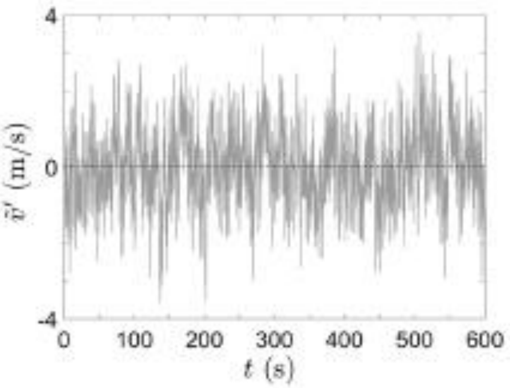

Figure 2-42: Solari model's turbulent component. Adapted from (Solari, et al. 2017).

2.5.4.9 Downburst wind velocity time history

For building the complete time histories of the wind velocity field in the model there were over imposed the 1.000 Monte Carlo Simulations with the 93 measured pairs of μ(t)& γ(t) and the 4 vertical profiles defining the mean velocity. In total 372.000 thunderstorms outflows velocity fields where analyzed inside their study. A typical generation of those mentioned is shown in Figure 2-43.

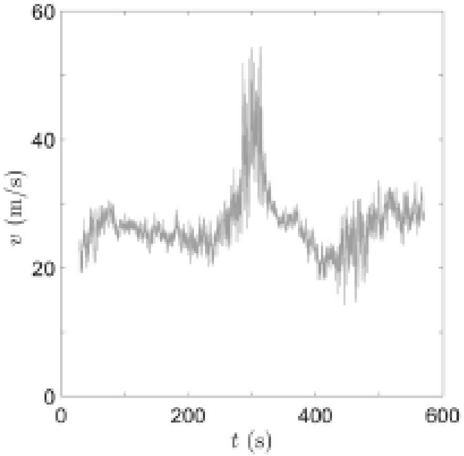

Figure 2-43: Solari-model Time history of Wind velocity. Adapted from (Solari, et al. 2017).

2.5.4.10 Structural response

The structural response was obtained by the integration of the equations of motion in time domain.

2.5.4.11 Model Validation

It is possible to appreciate that the model does not capture the crossing of the storm eye, this might be because the original target time histories do not capture it either (Figure 2-44). Moreover, the amplitude of the wind velocities is neither the same for both records. It's important to compare the phenomena observed by Solari and that observed from Fujita.

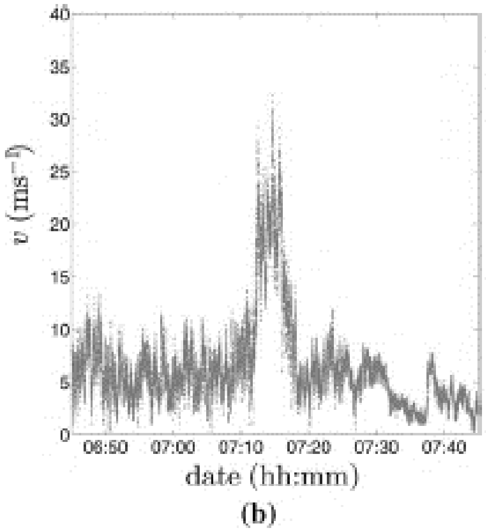

Figure 2-44: Time history of downburst registered from WP & WPS. Adapted from (Solari, et al. 2017).

2.5.5 MODEL: CARACOGLIA 2017

2.5.5.1 Description of the model

The model proposed by (Caracoglia and Le 2017) provides a procedure for simulating the wind field of the downbursts outflows based on the record of the Andrews AFB event (Fujita 1985).The model formulation is close to that proposed by (Chen and Letchford 2004) adding some assumptions:

- The downburst translates along a straight line, which corresponds to the thunderstorm track.
- Translation velocity is constant and independent from the height.
- Downburst track is parallel to the body axis.
- Average horizontal wind direction of the total wind velocity is constant during the storm evolution.

The mean velocity is given by the vector summation of the tracking component and of the radial one.

The vertical profiles implemented in the model are those proposed by (Wood and Kwok 1998) and (Vicroy 1992) already discussed in **§** 2.5.1. It is important to highlight that Wood's model represents better the downburst wind field when the maximum radial velocity is near to ground while the profile proposed by Vicroy is more appropriate for the case of maximum radial velocity at high elevations.

2.5.5.2 Techniques implemented

Spectral Representation Method based on both the Cholesky decomposition and/or the proper orthogonal decomposition of the Cross-Spectral density matrix.

2.5.5.3 Radial diffusion function

The mean velocity inside this model was as usual computed as the vector summation of the radial component and the tracking component. The main characteristic of the mean velocity of this model can be found in its radial component, in which there are introduced a time-dependent and a space dependent intensification functions. The radial velocity going from the downburst to the observation point could be found as:

Equation 2-101

$$V_r(z,t) = \Pi(t)\, V_z(z)\, I(r)$$

In which, $\Pi(t)$ is the time intesification function and $I(r)$ the space intesinfication function. They can be computed as follows:

Equation 2-102

$$\Pi(t) = \begin{cases} \dfrac{t}{t_o}, & t \leq t_o \\ exp(-\dfrac{t-t_o}{T}), & t > t_o \end{cases}$$

Equation 2-103

$$I(r) = \begin{cases} \dfrac{r}{r_{max}}, & r \leq r_{max} \\ exp[(-\dfrac{r-r_{max}}{r^*})^2], & r > r_{max} \end{cases}$$

Where T is the total time duration of the phenomenon, t is the current time of observation and to is the time at which the radial velocity reaches its maximum. The radial coordinate in which the downburst outflow reaches it maximum value is noted as r_{max} and r^* is one half of this distance.

2.5.5.4 Power Spectral Density

The PSD Svv' of the point with coordinates P (*xp,yp,zp*) used in this model:

Equation 2-104

$$\frac{\omega \, Svv'(\omega, P)}{2\pi \, {\sigma_v}^2(z)} = \frac{0.6X(\omega,P)}{(2+X^2)^{5/6}}$$

With ω standing for the circular frequency, the variance of the process is written as ${\sigma_v}^2(z)$ and X from Equation 2-105.

Equation 2-105

$$X(\omega,P) = \frac{1600\,\omega}{2\pi \, V_t(t,P)}$$

2.5.5.5 Amplitude modulating function

The evolutionary spectral representation of the downburst outflow fluctuation is made by modulating the amplitude of the standard stationary random process. To reproduce the Andrews

AFB record of the Downburst (Fujita 1985) the model implements three families of functions for achieving the modulation. The families proposed are Cosine-like, Exponential-like and Sawtooth-like, the latter is a multilinear group of functions which emulates the shape a sawtooth.

Equation 2-106

$$Cosine - Like\text{:}\ \ Acos(P,t) = [1 - \frac{cos(2\pi/t_o)}{2}]^{\eta}$$

Equation 2-107

$$Exponential - Like\text{:}\ \ Aexp(P,t) = \alpha o\ t^{\beta o} e^{-\lambda t}$$

Equation 2-108

$$Sawtooth - Like\text{:}$$

$$\widehat{A}_k(x,y,z,t) = \begin{cases} i_1, & 0 \leqslant t \leqslant t_1 \\ [(1-i_1)/(t_{max1}-t_1)](t-t_1)+i_1, & t_1 < t \leqslant t_{max1} \\ [(i_2-1)/(t_2-t_{max1})](t-t_{max1})+1, & t_{max1} < t \leqslant t_2 \\ [(1-i_2)/(t_{max2}-t_2)](t-t_2)+i_2, & t_2 < t \leqslant t_{max2} \\ [(i_3-1)/(t_3-t_{max2})](t-t_{max2})+i_3, & t_{max2} < t \leqslant t_3 \\ i_4, & t_3 < t \leqslant T \end{cases}.$$

For further details in the definition of the parameters governing the functions refer to (Caracoglia and Le 2017).

A typical generation of turbulence modulated with the functions given in Equation 2-106 to Equation 2-108 could be seen in Figure 2-45.

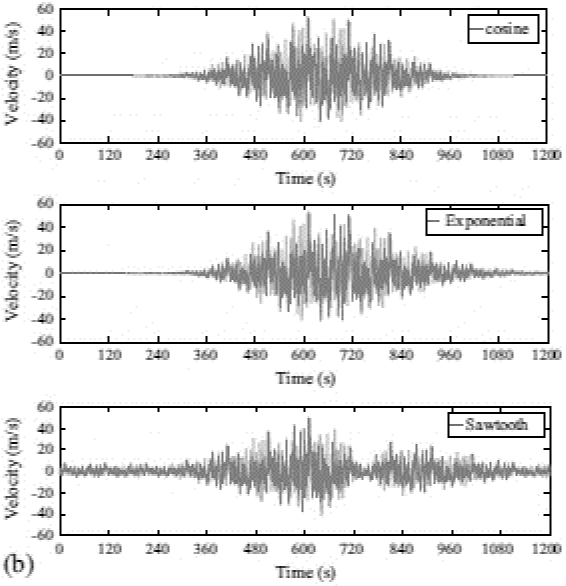

Figure 2-45: Caracoglia- plot of amplitude modulating functions. Adapted from (Caracoglia and Le 2017).

2.5.5.6 Coherence function

The coherence function is the usual proposed by (Davenport 1968).}

2.5.5.7 Generation of wind field

A typical generation of wind velocity field of downburst with this model could be seen in Figure 2-46.

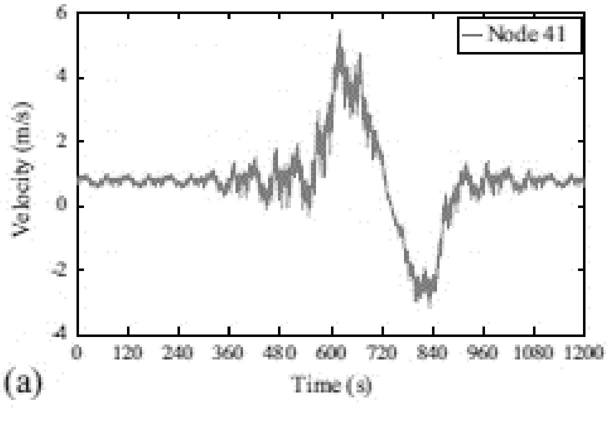

Figure 2-46: Typical Generation with Model-Caraclogia. Adapted from (Caracoglia and Le 2017).

2.5.5.8 Structural response

The structural response was computed using the Garleking Wavelet Method for solving the equations of motion.

2.5.5.9 Model validation

The Figure 2-47 represents the matching between the families of amplitude modulating functions and the original record the AFB event.

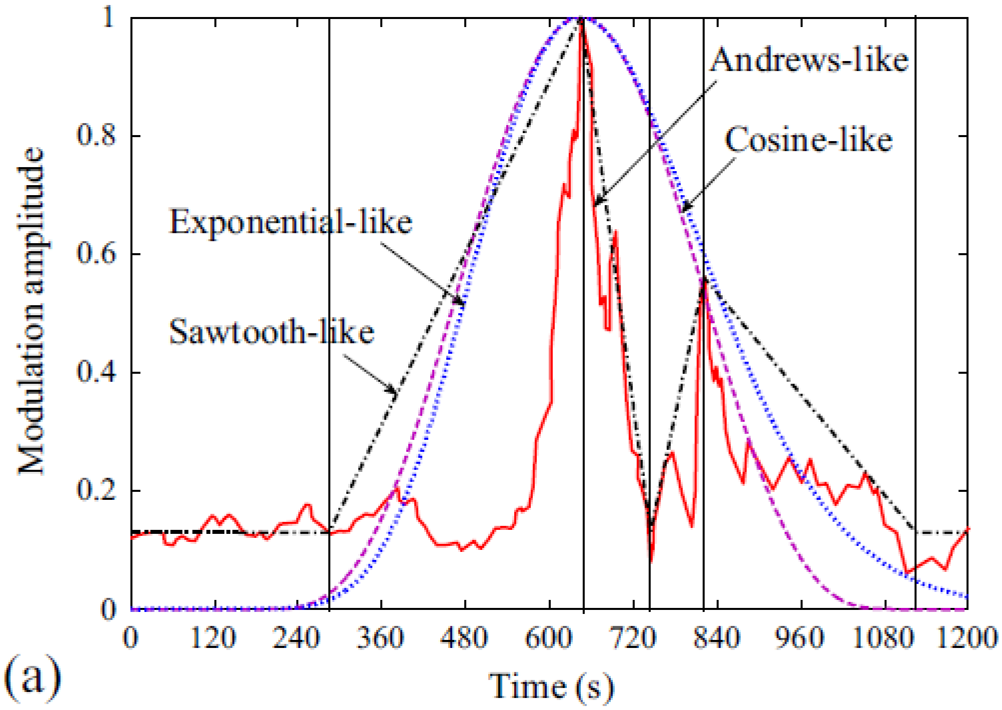

Figure 2-47: Comparison between amplitude modulating functions and AFB record. Adapted from (Caracoglia and Le 2017).

It is important to highlight that the function which better describes the recorded time history is the multilinear Sawtooth-Like family.

The time history given in Figure 2-46 of a generic simulation of the wind velocity filed of the downburst outflow is not fully coinciding with the AFB record i.e. the model does not represent the second peak of the downburst tracking that is appreciable in the original record.

2.5.5.10 Observations

The author of this model expresses the need of the evaluation of a unified model for solving the equations of motion for the non-stationary downburst outflows over slender structures in which there is the coupling between the aerodynamics and the velocities of the body i.e. consider the aeroelastic phenomenon.

2.5.6 MODEL: CANOR CARACOGLIA DENÖEL 2016

2.5.6.1 Model description.

To test a procedure of analysis in the frequency domain for slender structures subjected to non-stationary phenomena, it was developed a model (Canor, et al. 2016) of the downbursts outflows to provide an example of non-stationary wind effects. Therefore, this model was not based strictly in the reproduction of a specific record but to produce a valid, general representation of the downburst wind field. Additionally, it gives a practical selection of functions to define a downburst model.

The wind velocity is decomposed through the standard procedure. The mean velocity was as usual given by the vector summation of the radial and the tracking component. Regarding the vertical profile, there were implemented the provisions given by (Wood and Kwok 1998).

2.5.6.2 Overview of the techniques implemented.

Numerical evaluation of the convolution integral between the impulse response function and the amplitude modulating function. Decomposition of the complex matrix of the frequency response function.

2.5.6.3 Radial diffusion function. (time or space).

The function shaping the radial component and therefore the mean velocity is varying with the radial coordinate. The used function is based in the model of (Holmes and Oliver 2000) Equation 2-109, with the inclusion of a sign function on the radial coordinate Equation 2-110.

Equation 2-109

$$v_r(r) = V_{r,max} * \begin{cases} \dfrac{r}{r_{max}}, & 0 < r < r_{max} \\ exp(-\dfrac{(r - r_{max})^2}{Rr^2}), & r \geq r_{max} \end{cases}$$

Equation 2-110

$$\boldsymbol{V}_r = \frac{r}{|r|} v_r(|r|)$$

Where Vr,max is the maximum velocity of the process and its radial coordinate from the stagnation point is r_{max} and Rr is a scaling length.

The mean component is obtained as the usual vector summation of radial and tracking component

Equation 2-111

$$V(t) = |V_r + V_t|$$

The envelope function of the mean velocity component is obtained by normalizing Equation 2-111 to one in the time interval [0,T] with T the duration of the phenomenon and Vt the constant tracking component.

2.5.6.4 Power Spectral density for turbulence definition.

The power spectral density used in this model is the Von Karman spectrum. In its dimensional form the spectrum is given in Equation 2-112

Equation 2-112

$$S_v(f, z) = \frac{4L_v(z)}{Vz(z)} \frac{\sigma_v^2}{[1 + 70.78(\frac{f\, L_v(z)}{Vz(z)})^2]^{5/6}}$$

The variance can be obtained from the mean velocity and the turbulence intensity as was already showed for other models. Regarding the turbulence intensity and integral length scale the model uses the definitions of (Eurocode1 n.d.) Equation 2-113 & Equation 2-114.

Equation 2-113

$$I_v(z) = I_{v10}(\frac{10}{z})^{1/6}$$

Equation 2-114

$$L_v(z) = 300(\frac{max(z, 2)}{200})^{0.52}$$

The Von Karman PSD is plotted on Figure 2-48.

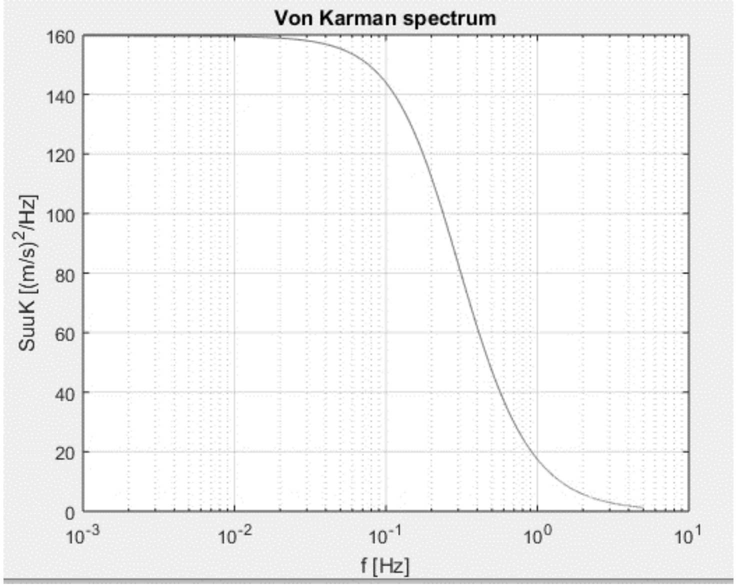

Figure 2-48:Von Karman's PSD

2.5.6.5 Amplitude modulating function.

The amplitude modulating function according to this model is the same functions as that shaping the mean velocity and can be seen in Figure 2-49.

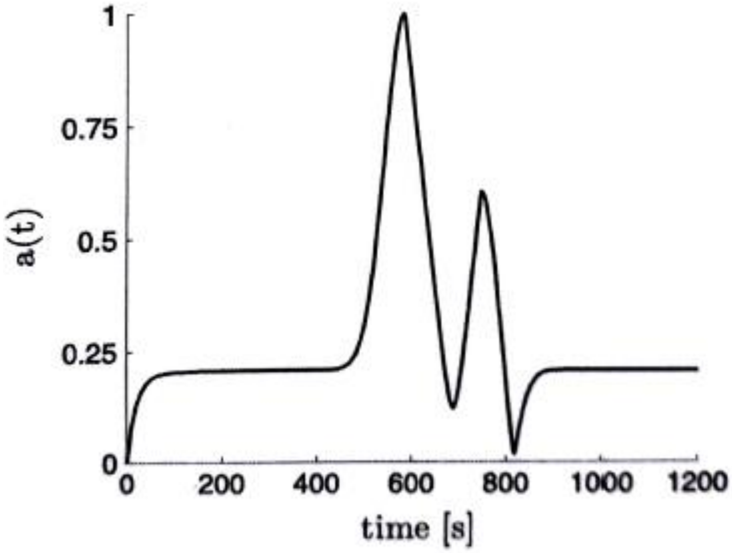

Figure 2-49: Amplitude modulating function

2.5.6.6 Coherence function.

The coherence function implemented in the model for the points at height Zi and Zj is that proposed by (Davenport 1968).

Equation 2-115

$$Coh\left(f, z_i, z_j\right) = exp\left[\frac{2\ Cr\ f\ \left|z_i - z_j\right|}{Vz(z_i) + Vz\left(z_j\right)}\right]$$

2.5.6.7 Generation of the wind field

Since the scope of the research was to evaluate the structural response in the frequency domain, in the report of the model it was not given any generic simulation of the downburst wind field. However, for the validation of the model there were made 600 generations of the outflow using a Monte Carlo simulation, not shown in the publication.

2.5.6.8 Structural response.

The evolutionary power spectral density of the response (in modal coordinates) was computed by the evaluating the evolutionary transfer function $G(t, to, \omega)$ and the standard stationary power spectral density of the buffeting force $Sp(\omega)$ as shown in Equation 2-116. The index * stands for complex conjugate.

Equation 2-116

$$S_q(t, t_o, \omega) = G(t, t_o, \omega) S_p(\omega)\ G^*(t, t_o, \omega)$$

To obtain the evolutionary transfer function several approaches were implemented in the model for further information on this topic refer to (Canor, et al. 2016).

2.5.6.9 Model validation.

No comparisons where made with real recorded downburst in the report of the model. However, the model validation was made comparing the structural response computed by the frequency domain with those of the time domain having a good consistency between the two approaches.

CHAPTER 3. DOWNBURST OUTFLOW MODEL

The empirical models exposed in **§** 2.5 will be compared in this chapter. It is important to recall that the models based on the CFD simulations, as well as, those based on the reproduction of the downburst outflow in the wind tunnel are out of the scope of this thesis.

The components of the wind velocity field associated to downbursts that will be examined in this chapter are the velocity decomposition, the vertical profile, the mean velocity, the turbulent power spectrum, the amplitude modulating function and the coherence function.

After the selection of the different components, it will be explained the artificial generation procedure for simulating the wind velocity field implemented in this study. The generated outflows differ from the single point in space based in the PSD and the multi-point generation which must account for the spatial correlation and therefore is based on the Cross-PSD of the turbulence.

3.1 Wind velocity decomposition

The standard wind velocity decomposition, already exposed in the **§** 2.1.1, is valid for the description of the downburst implemented in this study. The important passages will be repeated here for convenience.

The velocity is represented as the sum of the slowly varying-mean, $\mathrm{V}_{mean}(\mathrm{z},\mathrm{t})$, and the fluctuating, $\mathrm{V}'(\mathrm{z},\mathrm{t})$, components:

Equation 3-1

$$\mathrm{V}(\mathrm{z},\mathrm{t}) = \mathrm{V}_{mean}(\mathrm{z},\mathrm{t}) + \mathrm{V}'(\mathrm{z},\mathrm{t})$$

The term slowly-varying is referred to a mean velocity component which varies with a frequency much lower than the frequency content of the turbulence. The mean velocity for a fixed observation point with reference height *z,* can be represented as the velocity of the vertical profile at the height z (Vz) modulated by a function which carries the evolution of the mean velocity with time $\gamma(\mathrm{t})$.

Equation 3-2

$$\mathrm{V}_{mean}(\mathrm{z},\mathrm{t}) = \mathrm{V}_{z}(\mathrm{z}) * \gamma(\mathrm{t})$$

From the studies of (Solari, et al. 2017) and (Canor, et al. 2016) in which the turbulence is modulated by a function depending on time only and according to **§** 2.1.3.3 it is possible to represent the fluctuating component as a *slowly varying-uniformly modulated* non-stationary process. With the following expression valid:

Equation 3-3

$$V'(z,t) = v'(z,t) * a(t)$$

With a(t) analogous to the C(t) function defined in **§** 2.1.3.3 and $v'(z,t)$ a stationary random process. The velocity field of Equation 3-1 can be expressed as:

Equation 3-4

$$V(z,t) = V_z(z) * \gamma(t) + a(t) * v'(z,t)$$

3.2 Vertical profile

3.2.1 Comparison

The experiment conducted by (Chen and Letchford 2004) gives a comparison of the three empirical (Wood and Kwok 1998) (Vicroy 1992) (Osegura and Bowles 1988) models for the vertical profile. In the report Chen provided a set of parameters to define the profiles with the same common characteristics. These set of parameters is listed in Table 3-1.

Table 3-1: Parameters to define vertical profile

Parameter	Osegura	Vicroy	Wood
r [m]	1121		
D [m]	1000		
z*[m]	200		
ε[m]	30		
λ[1/sec]	0.414		
Vmax[m/s]	80	80	80
zmax [m]	65	67	73
δ [m]			400

Graphically it is possible to appreciate the characteristics of the vertical profiles in Figure 3-1. On the other hand, Figure 3-2 shows the standard boundary layer vertical profile with the same reference velocity. Figure 3-3 shows the superposition of the four profiles.

In first instance it is possible to appreciate the difference in the shape of both functions. While the ABL model provides a logarithmic trend tending to a limit value (gradient velocity) the downburst model has a nosed shape with maxima at mid-height elevation flowed by high rate decay.

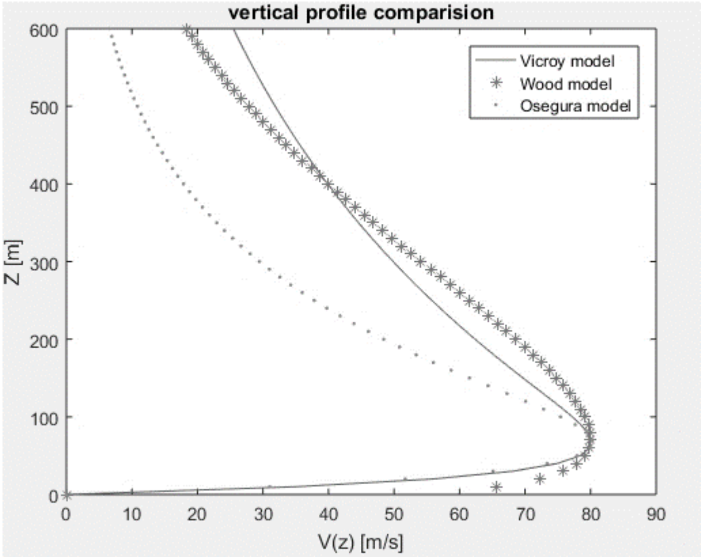

Figure 3-1:Vertical nosed profile of downburst empirical models

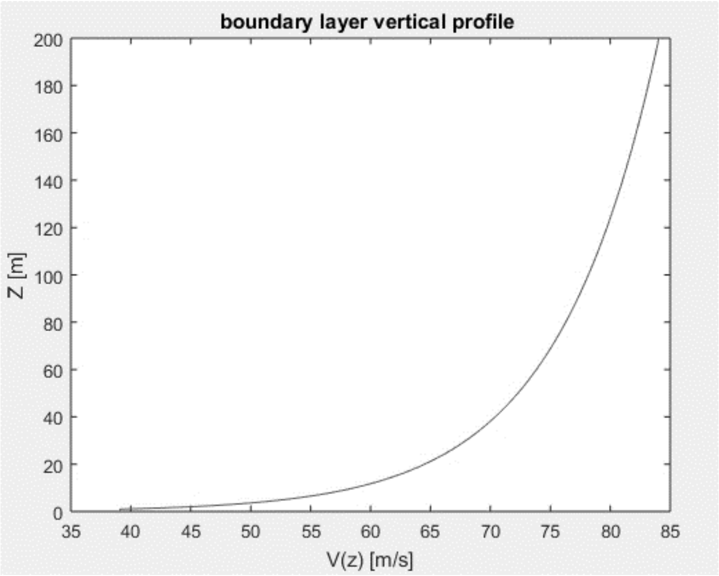

Figure 3-2: equivalent velocity profile for boundary layer model

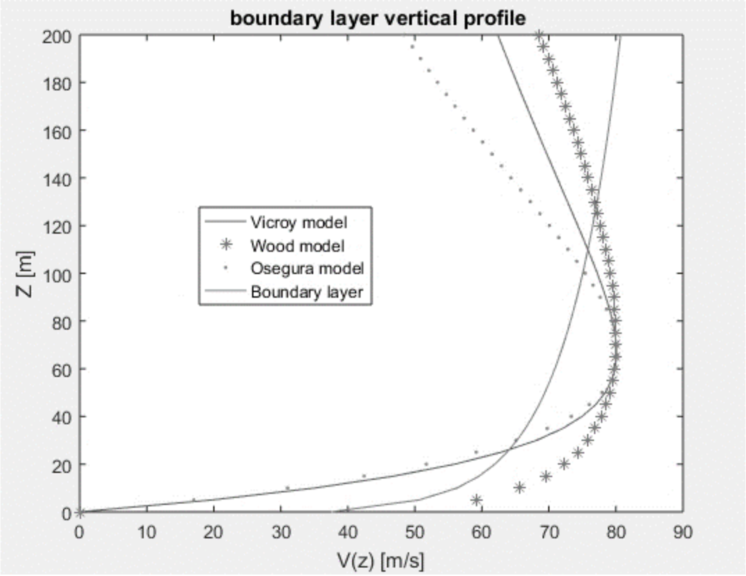

Figure 3-3:Vertical profile comparison

Since the downburst wind field is characterized by a mid-height maximum, it will affect in greater measure (compared with synoptic winds) medium rise structures between 30 and 120 m, such as, transmission lines systems, bridges and communication towers.

According to Figure 3-1 it is important to state that Osegura model is always providing lower velocity values compared with the other two models, so it could be used as *lower bound* for the vertical distribution of the wind velocity profile within the downburst. In addition, the implementation of this model results complex since it is governed by many empirical parameters.

Therefore, it become important to pay more attention to the other two models available. In Figure 3-1 It can be appreciated how Wood's model envelopes the other vertical profiles until a certain height from which Vicroy's model gives greater values. Thus, it could be possible to state that while the former is more conservative for cases in which the maximum radial velocity is located near the ground, the latter is suitable for cases in which the maximum velocity occurs at higher elevations. (Caracoglia and Le 2017).

3.2.2 Selection

For the application of the present study the model that was chosen for the defining the vertical profile was Vicroy's model (Vicroy 1992). Because it gives a mid-evaluation of the other two vertical profiles and requires less parameters for its implementation. The expression of the vertical profile is then:

Equation 3-5

$$V(z) = 1.22 * V_{max} * [e^{-0.15z/z_{max}} - e^{3.2175/z_{max}}]$$

3.2.3 Observations

For the implementation of a standard procedure for the analytical model of the thunderstorm downburst phenomenon, it is essential to define empirically or adopt by statistical distributions the values for the maximum radial velocity (V_{max}) and the associated height Z_{max} Therefore, it is important to aim a further research in the construction of a downburst aeolian map as it has been already implemented for synoptic winds.

3.3 Tracking path

The observations made by (Oliver 1992) of different downbursts that took place in Australia has shown that a significant component of the horizontal wind velocity comes from the translation speed of the mother storm or “environmental” speed, V_t. From the data recorded in the field it was possible to obtain a measure on this parameter. It is brought here for convenience on Figure 3-4. adapted from (Holmes and Oliver 2000).

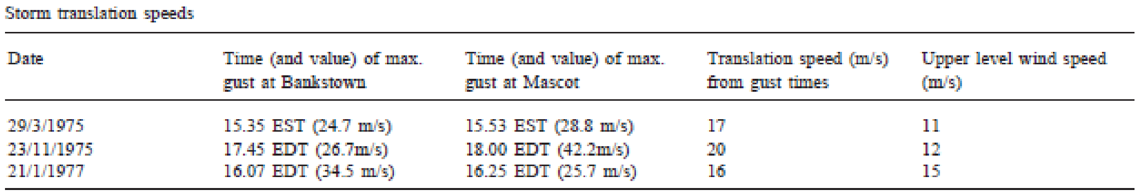

Storm translation speeds

Date	Time (and value) of max. gust at Bankstown	Time (and value) of max. gust at Mascot	Translation speed (m/s) from gust times	Upper level wind speed (m/s)
29/3/1975	15.35 EST (24.7 m/s)	15.53 EST (28.8 m/s)	17	11
23/11/1975	17.45 EDT (26.7m/s)	18.00 EDT (42.2m/s)	20	12
21/1/1977	16.07 EDT (34.5 m/s)	16.25 EDT (25.7 m/s)	16	15

Figure 3-4: Table of summary for identification of tracking velocity. Adapted from (Oliver 1992).

Before defining the effect of the translation velocity, V_t, on the downburst wind velocity field some restrictions must be applied to this parameter to avoid leaving it as an open parameter.

3.3.1 Hypothesis

First, the downburst must be idealized for the case of study. A model defining the tracking path and the set of wind properties must be accounted. Therefore, it is useful to make some hypothesis on the wind field of the storm. The simulation of the downburst even though is constrained to the study of the structural response on the severe situation, it might not lose the sense of the characteristics observed in real measurements and reported in the available literature (Solari, et al. 2017), (Holmes and Oliver 2000) i.e. the downburst mean velocity should have the shape of the available records.

The hypothesis on the wind velocity field of simulation are:

- The wind can attack the structure at any point in the 3D space.
- The mother storm track could follow any possible track.
- The downburst storm can completely pass through 2D plane during the simulation.
- The tracking speed of the mother storm is constant during the period of observation.

The graphical representation of the wind velocity model can be seen in Figure 3-5.

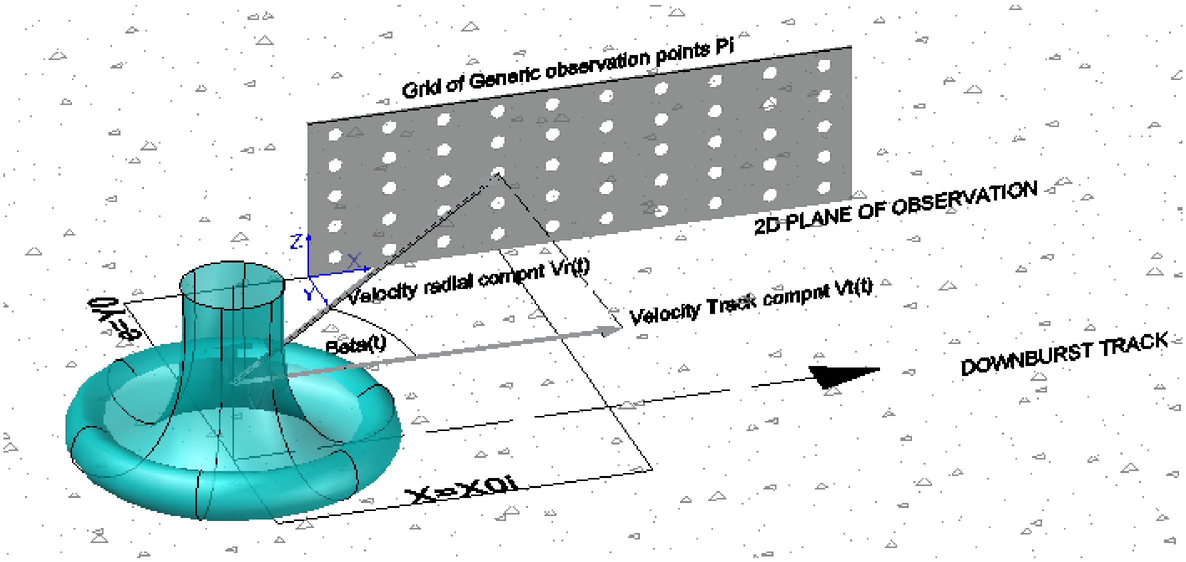

Figure 3-5 Graphical representation of downburst & structure model (Observation points)

3.3.2 Initial conditions and geometric quantities

Having defined the hypothesis of the downburst track and its effects over the structure, it is important to define now the wind characteristics. There are, as expected, specific settings that must be fixed to get a coherent definition of the wind velocity field for all the generic points inside the structure.

For the generic point *i* inside the 2D plane of observation, the initial coordinates related to the downburst center are x_o, y_o and Z which defines respectively the abscissa, eccentricity and height. It is worth noting that during the simulation of the wind velocity field, while the height of each generic point remains constant, the *x & y-coordinates* varies with the time as shown in Figure 3-6.

The set of this parameters is important in the definition of the wind velocity field for both types of analysis (time and frequency), since those parameters will define not only the time history at every point but also, the amplitude modulating function a(t) which affects the distribution of the frequencies in the EPSD over the time.

The variation of the *x-coordinate* of the downburst center with time will be influenced by the tracking velocity of the mother storm according to (Holmes and Oliver 2000).

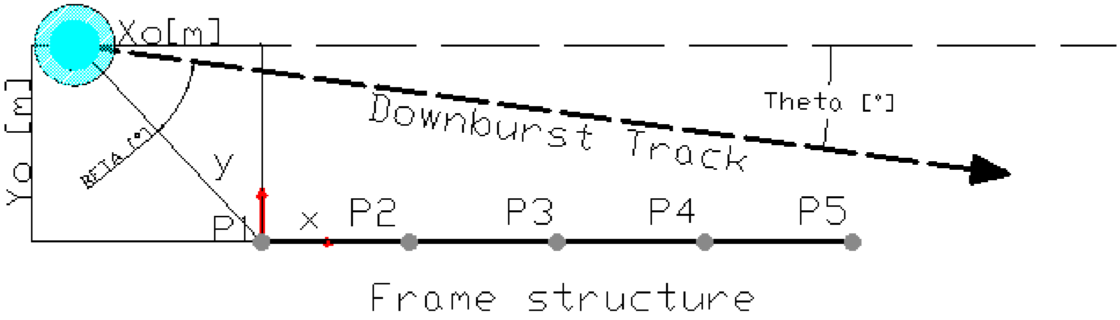

Figure 3-6: Downburst track plan view

Equation 3-6

$$x(t) = cos(\vartheta)V_t * t$$

And the *y-coordinate*:

Equation 3-7

$$y(t) = sin(\vartheta)V_t * t$$

In matrix notation:

Equation 3-8

$$\text{Dwb Center} = \begin{bmatrix} x_i(t) \\ y_i(t) \\ Z \end{bmatrix} = V_t * t \begin{bmatrix} cos(\vartheta) \\ sin(\vartheta) \\ 0 \end{bmatrix}, with\ intial\ P0 = \begin{bmatrix} x_o \\ y_o \\ Z \end{bmatrix}$$

After a generic time *t* the position of the downburst center respect to the observation point could be taken as:

Equation 3-9

$$Pt(t) = \begin{bmatrix} x(t) \\ y(t) \\ Z \end{bmatrix} = \begin{bmatrix} x_o \\ y_o \\ Z \end{bmatrix} - V_t * t \begin{bmatrix} cos(\vartheta) \\ sin(\vartheta) \\ 0 \end{bmatrix}$$

Where $P0$ are the initial coordinates of the downburst center and $Pt(t)$those at the generic time *t*.

Due to the difference in spatial location of each generic point respect to the downburst center, there is, as expected, a difference in the approximation angle. The approximation angle is important for the definition of the velocity components and the estimation of the intensification functions (time and space). For the case of the MDOF in addition, also the aeroelastic effect is affected by the wind approximation angle, since the aerodynamic components of the forces differ from the wind reference frame to the correspondent of the structure.

Special considerations taken inside the model will be explained at the decomposition stage of the aeroelastic effects for each case of study, since those differ from the structural characteristics.

The radial coordinate of the movement at initial time is:

Equation 3-10

$$\mathrm{r}_o^2 = \mathrm{y}_o^2 + x_o^2$$

3.4 Mean velocity

The definition of the mean velocity that will be implemented in this study considers the three-dimensional airflow structure of the downburst. It differs from the models available in the literature since those account only for a bidimensional structure of the wind velocity field. The mean wind velocity presented in the following depends on the referent velocity at the height of the observation point modulated by the two intensification functions in time and space, As proposed by (Caracoglia and Le 2017).

It is worth noting that the nature of the intensification functions will make the mean velocity to be a dynamic quantity. In addition, it will be slowly varying in time with respect to the frequency content of fluctuating component. Therefore, the mean velocity is not going to be a constant parameter as it is for the classical synoptic winds.

Looking at the models available in literature, it is possible to observe that the authors differ in the way the intensification function is defined. It will be useful then, to group the proposed functions according to their nature. In the models proposed by (Chen and Letchford 2004) (Caracoglia and Le 2017) and (Canor, et al. 2016) the intensification functions are computed based on the (Holmes and Oliver 2000) and the impinging jet hypothesis. In the model proposed by Solari (Solari, et al. 2017), the function is measured from 93 records of downbursts. On the other hand, the applications of CFD and wind tunnel show the shape resultant from the model hypothesis, therefore it is possible to state that it is a result rather than an input.

3.4.1 Intensification function from impinging jet model (Radial diffusion)

The intensification function $\gamma(\mathrm{t})$ shaping the mean wind profile comes from the vector summation of two components, the radial velocity component and the translational velocity component. The former is the idealization of the outflow as the distribution of an axisymmetric impinging jet Figure 3-7 (Poreh y Cermak 1959) and the latter is “environmental” velocity coming from the mother storm (Oliver 1992) already defined in **§** 3.3.

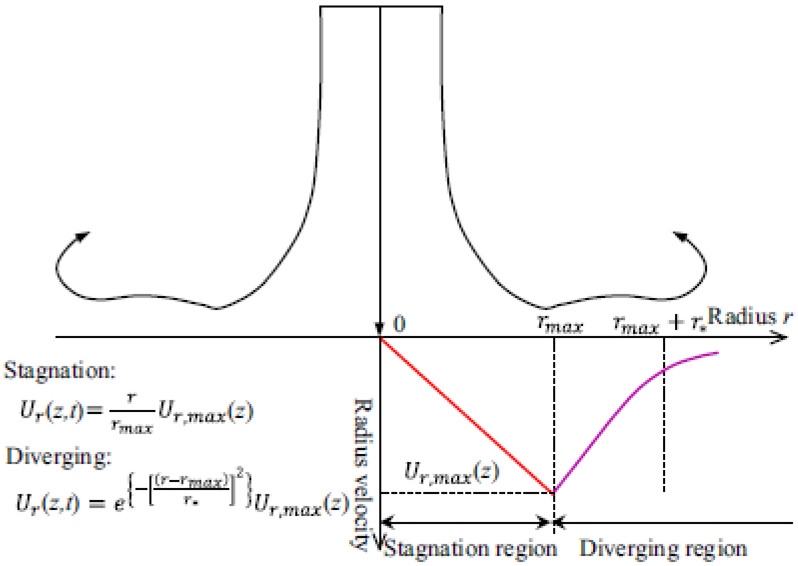

Figure 3-7: Impinging Jet model from for downburst. Adapted from (Caracoglia and Le 2017)

According to (Holmes and Oliver 2000) the wind velocity behavior of the impinging jet model can be represented as linearly increasing from the center of impact (storm eye) until the region where it reaches the maximum velocity the so-called stagnation point. After this region, the behavior is closer to an exponential decrease in a zone known as the wall jet or diverging region. The radial *r-coordinate* is the distance between the storm center and the observation point and introducing r_{max} as the stagnation point coordinate we can delimit the regions and compute the space intensification function, $F_s(r)$, as:

Equation 3-11

$$F_s(r) = \begin{cases} (r/r_{max}), & r < r_{max} \\ e^{-\alpha}, & r \geq r_{max} \end{cases}$$

With:

Equation 3-12

$$\alpha = (\frac{r - r_{max}}{R})^2$$

Denoting with *R* the radial length scale of the thunderstorm downburst, that from empirical measurements could be taken as the half of r_{max}. The final evaluation of this function could be seen in Figure 3-8 adapted from (Chen and Letchford 2004).

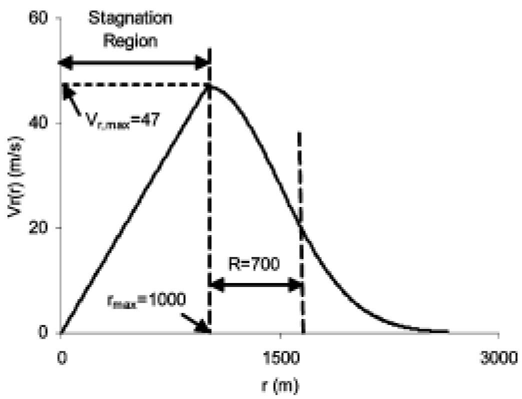

Figure 3-8: Radial velocity profile

In addition, the downburst intensity evolves with time (Caracoglia and Le 2017). Therefore, a time intensification function $F_t(t)$ shall be introduced to the radial velocity Equation 3-13 .

Equation 3-13

$$F_t(t) = \begin{cases} (t/t_o), & t \le t_o \\ e^{-\eta}, & t > t_o \end{cases}$$

With:

Equation 3-14

$$\eta = \frac{t - t_o}{T}$$

Where *T* is the total duration of the record, *t* is the time variable and *to* the time instant in which the wind velocity reaches it maximum value.

The mean radial velocity component, $V_r(r,z,t)$, is computed by Equation 3-15.

Equation 3-15

$$V_r(r,z,t) = V_z(z) * Fs(r) * Ft(t)$$

With the idealized tracking path given in **§** 3.3 it is possible to compute the radial coordinate of a point in space, with respect to the downburst center at any time as:

Equation 3-16

$$\mathrm{r}^2(\mathrm{t}) = (\mathrm{y}_o - sin(\vartheta)V_t * t)^2 + (\mathrm{x}_o - cos(\vartheta)V_t * \mathrm{t})^2$$

Where Vt is the tracking velocity of the mother storm already defined in **§** 3.3.

Finally, the angle of approximation to the generic *point-I* of coordinates (x_{oi}, y_{oi}) could be determined as follows:

Equation 3-17

$$\beta_i(t) = \mathrm{acos}(\frac{x_{oi} - cos(\vartheta)V_t * t}{r(t)}) - \vartheta$$

The vectoral notation for the radial velocity becomes:

Equation 3-18

$$\overrightarrow{V_r}(t)^1 = \frac{r}{|r|} * V_r(r, z, t)$$

The expression giving the combined velocity, $V_c(t)$, can be obtained by the cosine law (Caracoglia and Le 2017) Equation 3-19. The dependency on the height of the observation point z, is neglected since the tracking speed is the constant over the height.

Equation 3-19

$$V_c(t)^2 = V_r(t)^2 + V_t{}^2 + 2 * V_r(t) * V_t * Cos\beta(t)$$

And finally, the time function can be simply the normalization of the horizontal velocity component.

Equation 3-20

$$\gamma(t) = \frac{|V_c(t)|}{|\max(V_c(t))|}$$

3.4.2 Intensification function from records

The time function given by Solari (Solari, et al. 2017) comes from the study of records of downburst gathered by the WP and WPS projects. There were extracted 93-time histories of full-scale measurements in the field. The 93-time histories of γ(t) can be seen in Figure 3-9. The thick lines represent the mean values, the abscissa of all time histories is shifted to obtain the maximum value (1) at time zero.

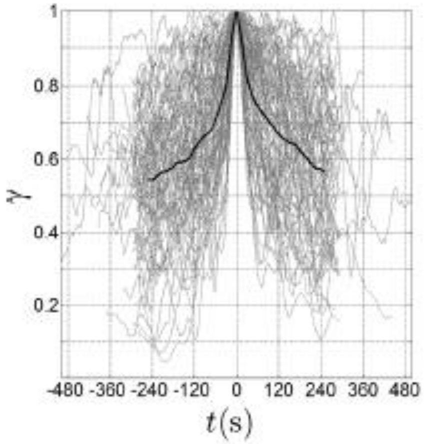

Figure 3-9: Y(t) function. Adapted from (G. Solari, M. Burlando, et al. 2015)

Since the intensification function gives the shape to the mean wind velocity, it also influences the final shape of the generated time history. It is possible to see a generic simulation of the wind

---

[1] The radial coordinate dependence on time makes the Vr also function of time

velocity field provided by the study of (Solari, et al. 2017). The result of this model can be referred as real downburst wind field since it is taken from the actual records of the phenomena, even though the turbulent component was generated with a Monte Carlo simulation.

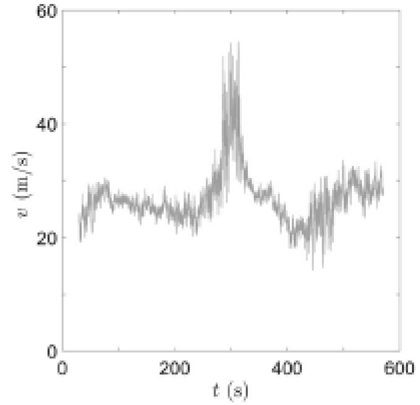

Figure 3-10: Solari's model time history generation. Adapted from (Solari, et al. 2017).

3.4.3 Selection

In conclusion, the mean wind velocity that will be taken in this study is that given by the impinging jet model and close to the model of (Caracoglia and Le 2017) i.e. a reference velocity coming from the vertical profile moderated by intensification functions in time and space, as it was anticipated. An expression similar to (Solari, et al. 2017) cannot be implemented in the present study since it requires the record of downbursts velocity fields that are not available now.

The Equation 3-21 expresses the mean velocity field.

Equation 3-21

$$V_{mean}(z,t) = V_z(z) * \gamma(t)$$

With $\gamma(t)$ from Equation 3-20.

3.5 PSD function & Integral length scales

The power spectral density function that will be selected is the Von Karman spectrum. This spectrum has been widely used for the description of stationary wind velocity fields. Therefore, its implementation and characteristics are well known from a practical point of view. The expression giving the Von Karman PSD will be brought here for convenience:

Equation 3-22

$$S_v(f,z) = \frac{4L_v(z)}{Vz(z)} \frac{\sigma_v^2}{[1 + 70.78(\frac{f\, L_v(z)}{V_z(z)})^2]^{5/6}}$$

The variance can be obtained from the mean velocity and the turbulence intensity as was already showed for other models. Regarding the turbulence intensity and integral length scale the model (Canor, et al. 2016) suggest to use the definitions of (Eurocode1 n.d.) Equation 3-23 & Equation 3-24.

Equation 3-23

$$I_v(z) = I_{v10}(\frac{10}{z})^{1/6}$$

Equation 3-24

$$L_v(z) = 300(\frac{max(z,2)}{200})^{0.52}$$

However, for the integral length scales and turbulence intensity of downburst it results more accurate to adopt the values proposed by (G. Solari, M. Burlando, et al. 2015). Those come from real data gathered on the WP project. Therefore, they give a better representation of the downburst phenomenon compared with that obtained with standard expressions for synoptic winds.

The identification of the integral length scales of the records was made using an inverse relation of the PSD function. From the practical point of view, it consisted in measuring the integral length scale fitting the measured PSD with that given theoretically. Graphically it could be seen in Figure 3-11.

It is worth noting that the measurements were made in ports and the associated terrain category is category 0 related to sea or costal area exposed to open sea inside the framework of Eurocode 1. Therefore, this study will be limited to the application of this type of terrain category since this will affect the energy content in the PSD function.

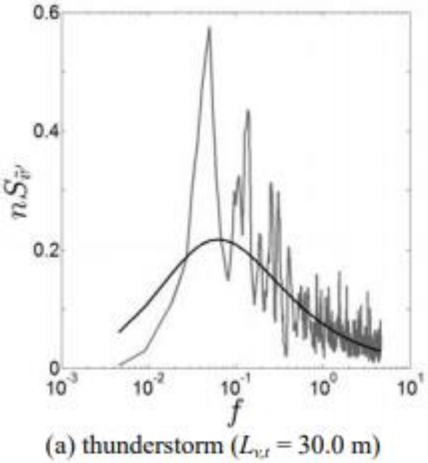

Figure 3-11: Fit of PSD function for Lv=30m. adapted from Solari 2015.

From the different stations of the WP project it was possible to recall the average values and the statistical characteristics of the entire population of the integral length scales computed as before. The data is reported in Figure 3-12.

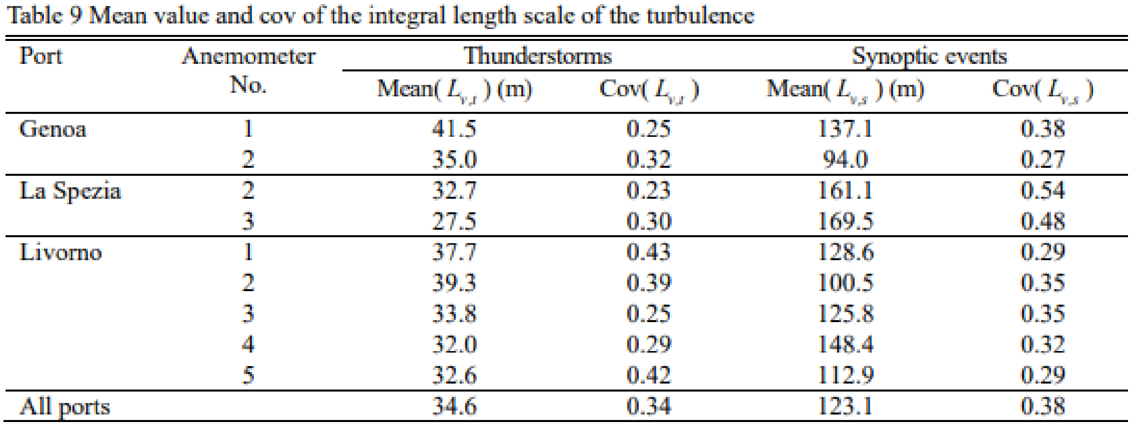

Table 9 Mean value and cov of the integral length scale of the turbulence

Port	Anemometer No.	Thunderstorms		Synoptic events	
		Mean($L_{v,t}$) (m)	Cov($L_{v,t}$)	Mean($L_{v,s}$) (m)	Cov($L_{v,s}$)
Genoa	1	41.5	0.25	137.1	0.38
	2	35.0	0.32	94.0	0.27
La Spezia	2	32.7	0.23	161.1	0.54
	3	27.5	0.30	169.5	0.48
Livorno	1	37.7	0.43	128.6	0.29
	2	39.3	0.39	100.5	0.35
	3	33.8	0.25	125.8	0.35
	4	32.0	0.29	148.4	0.32
	5	32.6	0.42	112.9	0.29
All ports		34.6	0.34	123.1	0.38

Figure 3-12: Table of Integral length scales. Adapted from Solari 2015.

The recommendation of (Solari, et al. 2015) is to use the mean value for the integral length scale and the turbulence intensity of 34.6 [m] and 0.12 [-] respectively.

It is worth noting that the values of the integral length scale proposed for thunderstorms are very small compared with the ones of synoptic winds (120-180 m). This can be attributed to the down-drafted and divergent characteristics of the downburst which tend to produce small sized eddies compared with synoptic winds.

The approximated relations for the other integral length scales could be taken as:

Equation 3-25

$$L_u^x \approx 0.25\, L_v^x \qquad L_w^x \approx 0.1\, L_v^x \quad (a)$$

$$L_v^y \approx 0.3\, L_v^x \qquad L_v^z \approx 0.2\, L_v^x \quad (b)$$

Finally, the Von Karman PSD is plotted on Figure 3-13.

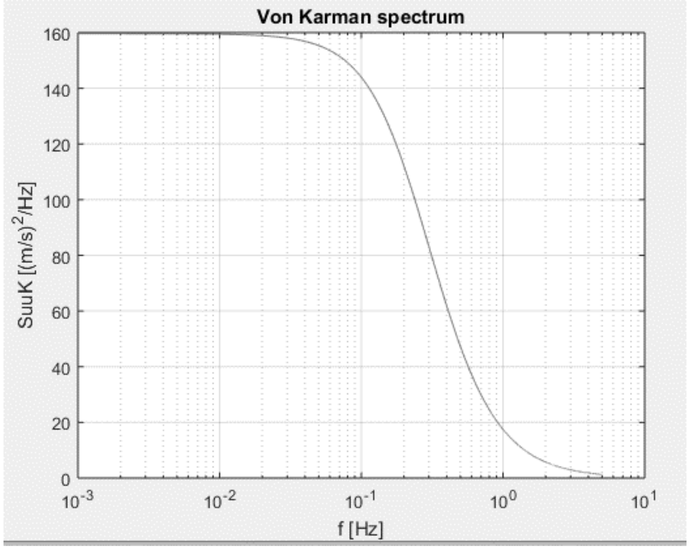

Figure 3-13:Von Karman's PSD

3.6 Amplitude modulating function

One important aspect, still debated in the scientific community, is the definition of the amplitude modulating function. Each empirical model presented in **§** 2.5 has a different function to describe it. Highlighting the most important contributions on this topic three different type of functions will be presented in the following.

3.6.1 μ(t) function (Solari, et al. 2017)

In the model proposed by Solari the function to modulate the turbulent component was μ(t). It was obtained from records of the WP and WPS projects. The 93-time histories recorded of this function are presented in Figure 3-14.

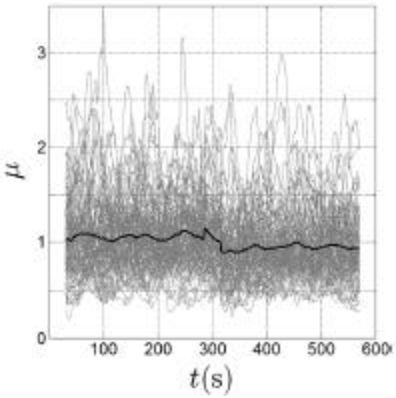

Figure 3-14: Solari's μ(t) function. Adapted from (G. Solari, M. Burlando, et al. 2015).

However, due to high fluctuation and randomness of μ(t) an attempt to reproduce it will not be practical for the matters of this thesis.

3.6.2 Family of functions (Caracoglia and Le 2017)

To describe the amplitude modulating function (Caracoglia and Le 2017) proposes three different family of functions. Those were implemented to comparatively assess which one fits better in the behavior of the Andrews AFB thunderstorm. The expression provided by their study to compute the modulating functions were given in **§** 2.5.5.5 and graphically the comparison could be appreciated in Figure 2-45: Caracoglia- plot of amplitude modulating functions.

Analyzing the data proposed by the author, it is possible to conclude that the best group of functions to describe the modulating behavior is the so-called Sawtooth-like functions. Recalling the expression of this family of functions as recalled in Equation 3-26 and shown in Figure 3-15.

Equation 3-26

$$A(t) = \begin{cases} i1 & 0 \leq t \leq t1 \\ \left[\dfrac{1 - i1}{(tmax1 - t1)}\right](t - t1) + i1 & t1 < t \leq tmax1 \\ \left[\dfrac{i2 - 1}{(t2 - tmax1)}\right](t - tmax1) + 1 & tmax1 < t \leq t2 \\ \left[\dfrac{1 - i2}{(tmax2 - t2)}\right](t - t2) + i2 & t2 < t \leq tmax2 \\ \left[\dfrac{i3 - 1}{(t3 - tmax2)}\right](t - tmax2) + i1 & tmax < t \leq t3 \\ i4 & t3 < t \leq T \end{cases}$$

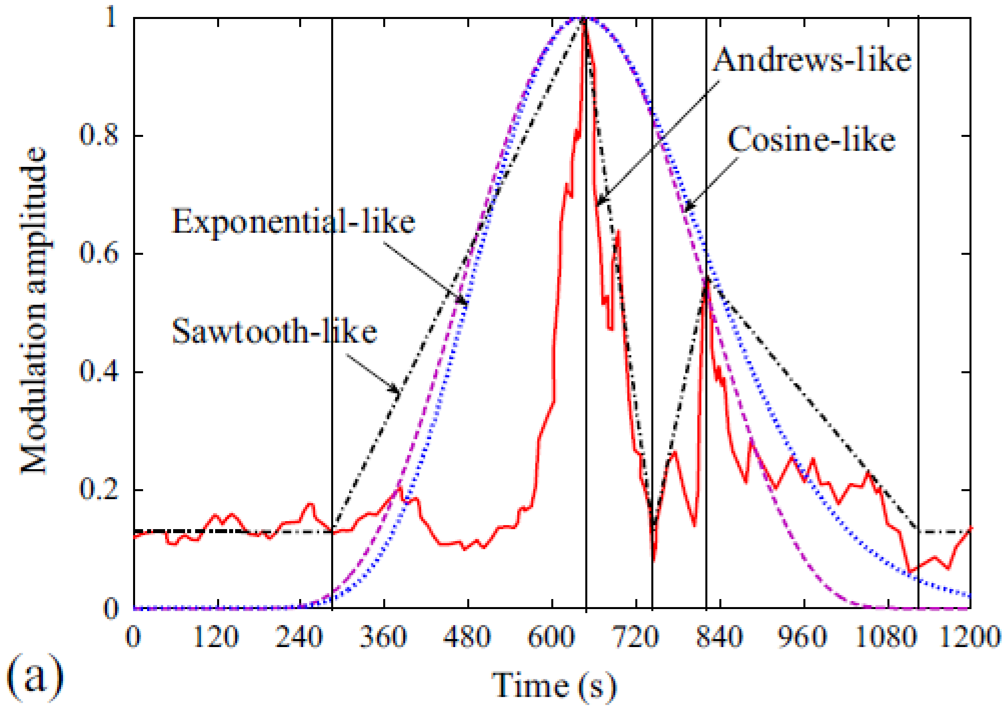

Figure 3-15: Family of amplitude modulating functions. Adapted from (Caracoglia and Le 2017)

3.6.3 Functions depending on the mean velocity (Chen and Letchford 2004) (Canor, et al. 2016)

On the model developed by Chen (Chen and Letchford 2004) is described the modulation function as one quarter of the mean velocity profile. This value gives a rise to a good representation of the turbulence component. However, since it depends on the mean value directly, for very strong downbursts the numeric results could reach high values. Analogously Yang (Yang y Hong 2016) describes this function as 0.08 to 0.11 of the mean velocity, this seems more accurate compared with (Chen and Letchford 2004) since the coefficient is lower.

On the other hand, (Canor, et al. 2016) suggest using as time envelope for the PSD the same function enveloping the mean velocity, the so-called intensification function $\gamma(t)$.

3.6.4 Selection

The Sawtooth-like family of functions from Caracoglia present a cumbersome approach to define the amplitude modulating functions, as it requires the implementation of a multilinear model.

On the other hand, the randomness of $\mu(t)$ leaves its implementation feasible only if the data from the records are available. Moreover, this requires the use of the coherent $\gamma(t)$ from the WP and WPS records i.e. those functions could not be used without the other.

From the practical point of view, it results attractive to use the same $\gamma(t)$ function to describe both mean value and amplitude modulating function as proposed by (Canor, et al. 2016). Moreover, since the intensification function is normalized its magnitude will not be affected by reference velocity of the downburst as it happens for the models of Chen (Chen and Letchford 2004) and Yang (Yang y Hong 2016).

Therefore, the amplitude modulating function can be defined as:

Equation 3-27

$$a(t) = \gamma(t)$$

from now on, due to the equivalence between both functions the intensification function and the amplitude modulating function will be often called as *a(t)* in the notation of this document.

Finally, after deciding the amplitude modulating function, a typical plot of it can be seen in Figure 3-16.

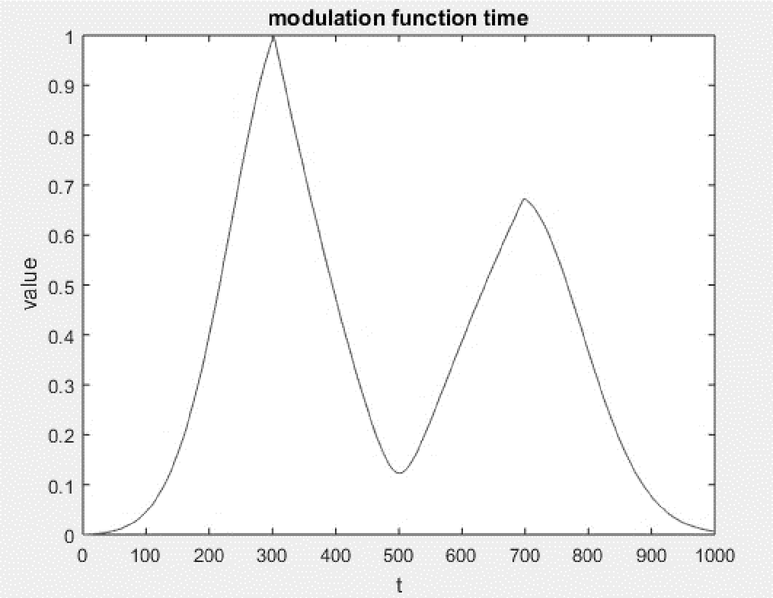

Figure 3-16: Amplitude modulating function

3.7 Spatial Coherence function

The correlation represents the statistical dependence between two signals of the same stochastic process. The correlation could be defined by means of the coherence as the function. Since no discrepancies were given in the description of this parameter the classical spatial coherence function proposed by (Davenport 1968) will be used in this study.

Equation 3-28

$$coh_{ij}(x_i, x_j, z_i, z_j, f) = \exp\left[-2 * \mathrm{C} * \frac{\|X_{ij}\| * f}{V_{\max\_i}(z_i) + V_{\max\_j}(z_j)}\right]$$

With C being the non-dimensional decay constant, the typical value for this parameter is 10, whether for synoptic or not-synoptic winds. The operator $\|X_{ij}\|$ stands for the Euclidean norm of *point-i* & *point-j* which represents the distance between the points.

3.8 Cross Power Spectrum function

Recalling the analysis of two random process $x_i(t)$ and $x_j(t)$ correlated to each other and belonging to the same process, but relative to different points in space, It is possible to define the Cross Power Spectral Density CPSD as the Fourier transform of the cross-correlation function, as defined in the paragraph **§** 2.1.2.5.

Equation 3-29

$$S_{xixj} = \int_{-\infty}^{+\infty} R_{xixj}(\tau) e^{-2i\pi f\tau} d\tau$$

Alternatively, for the case of wind engineering applications of random processes correlated in space it is possible to obtain the CPSD from the definition of the coherence function. It shall be first computed the PSD of the realizations (S_{xi}, S_{xj}…, S_{xn}) and the spatial coherence function between the points according to Equation 3-28. The expression to obtain the CPSD is therefore:

Equation 3-30

$$S_{xixj} = Coh_{ij}\sqrt{S_{xi} * S_{xj}}$$

All the terms S_{xi} and S_{xixj} are function of frequency. Special reference must be done with respect to the non-synoptic wind fields i.e. the statistical properties of the CPSD function (S_{xixj}) are no more stationary. Therefore, the dimension of time must be introduced in the evaluation of the function, the Evolutionary Cross Power Spectral Density function ECPSD ($EVCSxixj$) could be seen in a discrete way as the variation of the CPSD function in different instants of time.

Equation 3-31

$$EVCSxixj(f,t) = \{S_{xixj}(f, t = t_1)|S_{xixj}(f, t = t_2)| \cdots |S_{xixj}(f, t = t_n)\}$$

The spectral density terms of Equation 3-31 can be obtained as **§** 2.1.3.2 . However, for the cross-spectral density terms, the procedure of Equation 3-32 must be applied.

Equation 3-32

$$EVCSxixj = Coh_{ij}\sqrt{EVS_{xi} * EVS_{xj}} \quad \text{(a)}$$

$$EVCSxixj = Coh_{ij}\sqrt{|a_i(t)|^2 S_{xi} * |a_j(t)|^2 S_{xj}} \quad \text{(b)}$$

$$EVCSxixj = |a_i(t) * a_j(t)| * \{Coh_{ij}\sqrt{S_{xi} * S_{xj}}\} \quad \text{(c)}$$

It is worth noting that the amplitude modulating functions in the Equation 3-32 (b) and (c) are different for the *point-i* and the *point-j* since each one has different initial conditions and coordinates.

3.9 Generation for Single-Point

3.9.1 Deterministic mean

It will be made a generation of the wind velocity field in a single point to give an example of the implemented model. The sampling information of the analysis is reported in Table 3-2, while the downburst parameters are given in Table 3-3.

Table 3-2: Sampling parameters

parameter	**Expression**	**Value**	**Units**
Sampling freq, fs_{amp}	-	20	[Hz]
Nyquist freq, F_{ny}	$f_{samp}/2$	10	[Hz]
Sampling time, dt	$1/f_{samp}$	0.05	[sec]
Frequency resolution, df	1/T	$2x10^{-3}$	[Hz]
Time window, T	1/df	500	[sec]
Sampling points, n	T/dt	10.000	[-]
Time vector, t	[0:dt:T-dt]	-	[sec]

Table 3-3: Parameters to define horizontal component

Parameter	Value
Integral length scale L_v	34.6 [m]
Max velocity V_{max}	80 [m/s]
Track velocity V_t	12 [m/s]
Height of max velocity Z_{max}	67 [m]
Downburst diameter $D=r_{max}$	1000 [m]
Initial X coordinate x_o	-2500 [m]
Initial Y coordinate y_o	150 [m]

With the given information it was possible to build the vertical profile in Figure 3-17, the mean velocity profile shown in Figure 3-18 and its correspondent time function is shown in Figure 3-19.

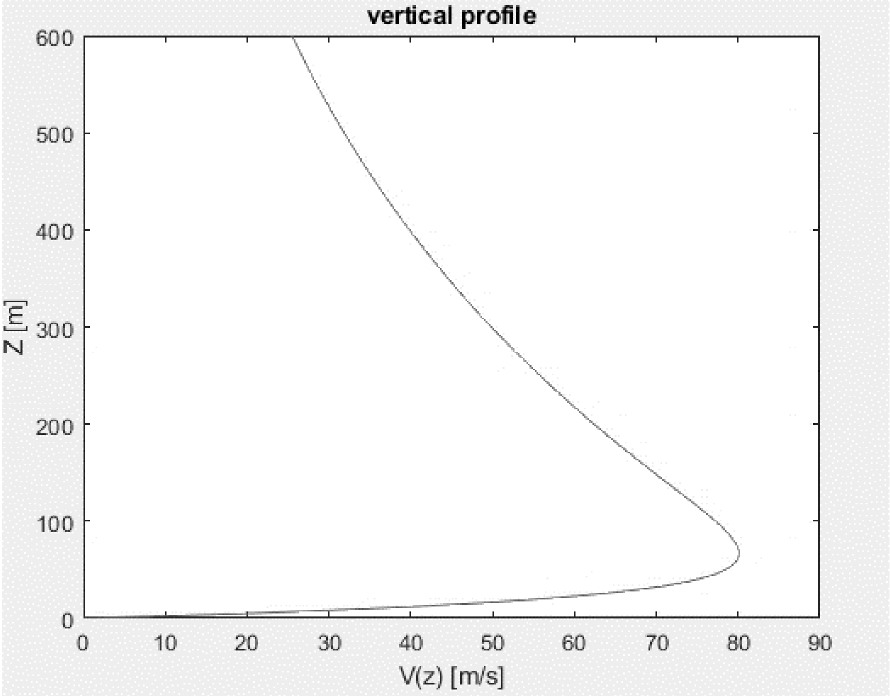

Figure 3-17: Vertical profile

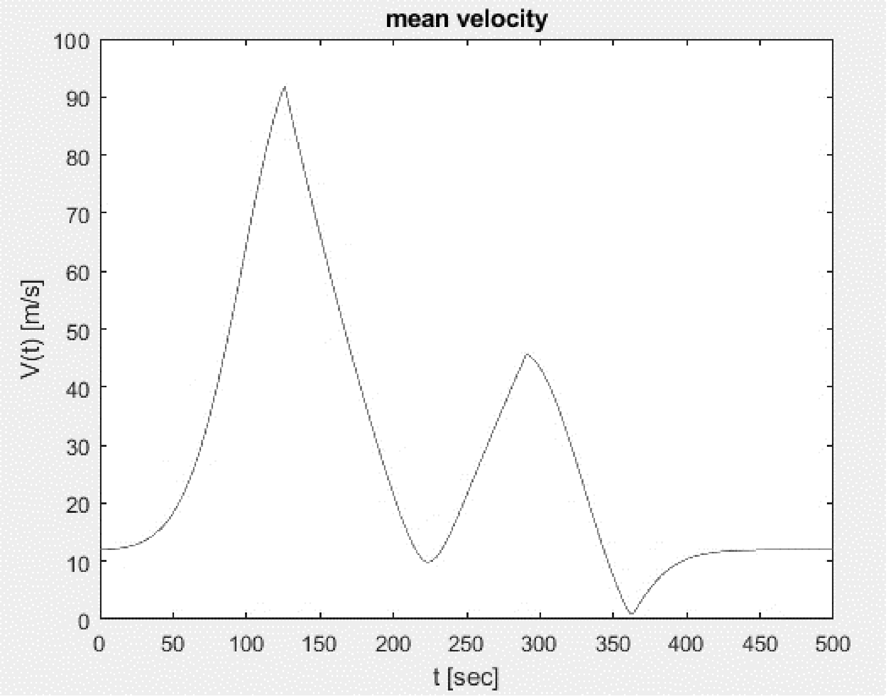

Figure 3-18: Mean velocity component

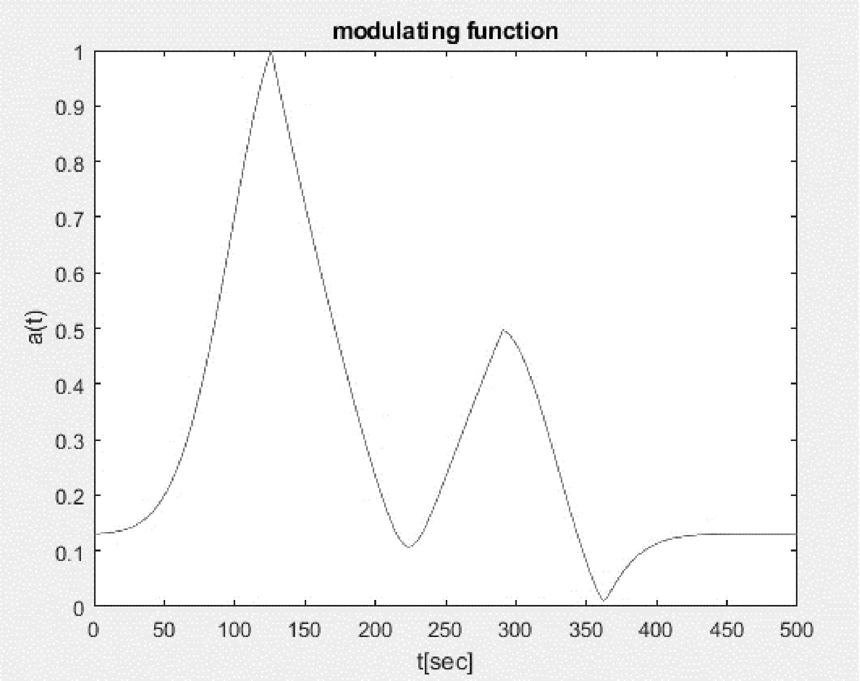

Figure 3-19: Time function a(t)

3.9.2 Random turbulence

The random fluctuating part of the wind outflow is reproduced by a Monte Carlo algorithm based in the Power Spectral Density. As it was stated before, the PSD function that will be used in this study is the Von Karman PSD. Recalling its definition for convenience in Equation 3-33. Where the velocity component v' is the turbulence in the along wind direction.

Equation 3-33

$$S_{v'}K(f,z) = \frac{4\,L_v}{V(z)} \frac{I_v V(z)^2}{\left(1 + 70.78\left(\frac{f\,L_v}{V(z)}\right)\right)^{\frac{5}{6}}}$$

Where the term V(z) is the vertical profile of the wind speed that for this case will be taken as Vmax. The frequency vector is represented as f. The turbulence intensity adopted is 0.12 and the integral length scales are reported Table 3-4.

Table 3-4: Integral length scales

Direction	x	y	z
Longitudinal component v	34.6	10.38	6.92
Transversal component u	8.65	2.59	1.73
Vertical component w	3.46	1.038	0.692

The generation of time histories for the fluctuating part of the wind outflow uses the harmonic superposition method. This approach corresponds to the inverse Fourier transform of the power spectrum as Equation 3-34. Moreover, the signal discretization is contained on the frequency vector, therefore every term in the frequency vector fi is a harmonic of the frequency step (δf).

Equation 3-34

$$v'(t) = \sum_{i=1}^{lentgh\,(f)} Ai * sen(2\pi f_i\, t + \varphi)$$

Where the angle φ is the phase. As it was explained before, the PSD is giving a measure of the energy of the system. These can be transformed into the amplitude of the signal for every harmonic Ai. However, this function is not containing any information regarding the phase φ of the harmonics. Therefore, a random generation from 0 to 2π of this parameter was carried out in this analysis.

Considering a single harmonic signal of amplitude A_i, the variance of the random variable will be $A_i^2/2$. For a given frequency interval (from f_o to $f_o + \delta_f$) the contribution to second spectral moment (variance) given by the harmonic *fi* in the middle of interval (valid for δ_f sufficient small) will be given by Equation 3-35 and represented in Figure 3-20.

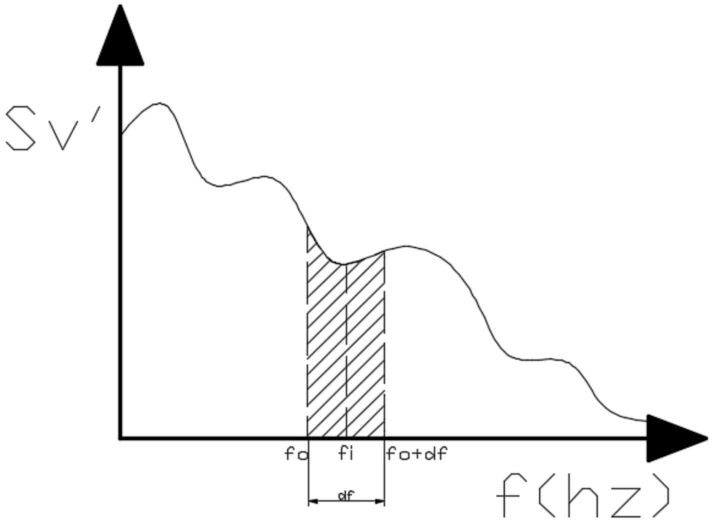

Figure 3-20:Shape of Unilateral PSD

Equation 3-35

$$\sigma^2 = \int_{fo}^{fo+\delta f} G_{v\prime}(f) * df \cong G_{v'}(fo) * \delta_f$$

To get the amplitude of the generic harmonic i of δf, it is necessary to transform the PSD available into a power spectrum. Then, with the properties of the variance (Equation 3-36) it is possible to obtain the amplitude of the harmonic at frequency fi. As it was explained before, the superposition of the harmonics gives the description of the simulated wind velocity field (Equation 3-34).

Equation 3-36

$$\begin{cases} G_{v'}(f) = 2 * S_{v'}(f) * df \quad Power\ Spectrum \\ Ai = \sqrt{G_{v'}(f = f_i) * 2} \quad Amplitude \end{cases}$$

Figure 3-21 provides an example a single random generation.

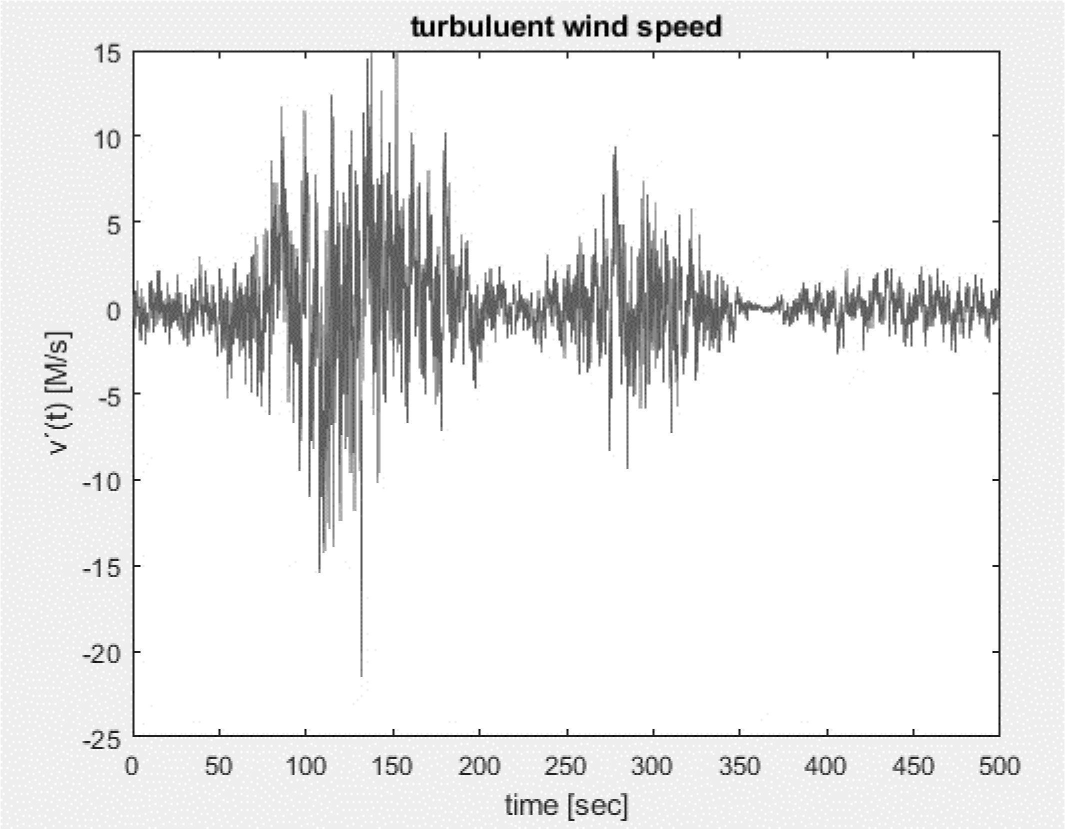

Figure 3-21: Turbulence random generation

After summing it up with the mean component it is possible to obtain a full random generation of the thunderstorm downburst wind velocity field, this can be seen on Figure 3-22.

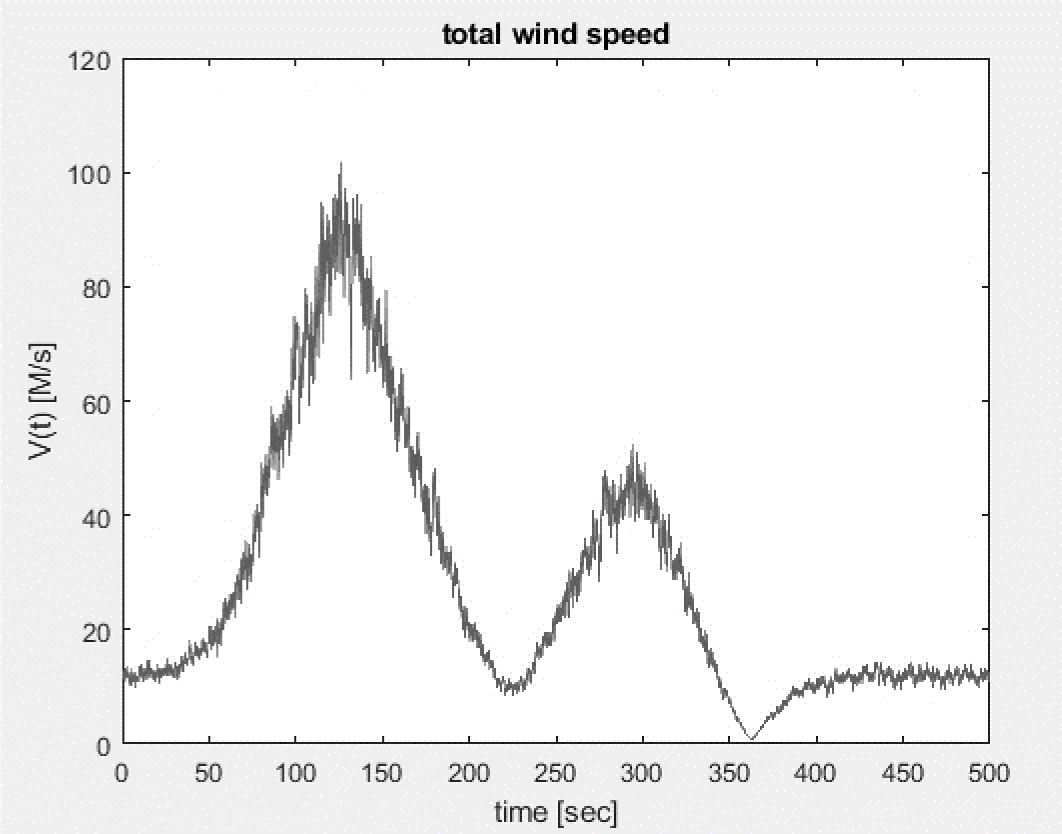

Figure 3-22: Random generation of Wind velocity field

Considering the generated time history, it is useful to describe how the model was able to capture the behavior of downburst velocity field comparing it with data registered by (Fujita 1985) for the case reported in Figure 2-33: Andrews AFB downburst- AIRFORCE ONE event 1983.

- From zero to 50 seconds it is possible to see that only the tracking velocity of the mother thunderstorm is captured i.e. the arrival of the downburst is captured by the model.
- At approximately 120 seconds is possible to see the first peak which corresponds to maximum wind velocity, this is produced by the synchronization between the tracking velocity and the radial component. Figure 3-23.
- Then, between 200 and 250 seconds it is the zero-crossing, the minimum velocity possible which corresponds to the eye of storm passing at its closet distance to the observation point. At this stage the radial component counterbalances the tracking.
- After the zero crossing, at 300 seconds is the second peak, referring again to the maximum wind velocity component of the impinging jet model but this time opposing the tracking speed since the downburst is getting away from the observation point. Figure 3-24.

- By last is the absence of radial component, once again only tracking speed could be seen in the time history.
- This behavior evidences a clear dependence on the initial coordinates X0 and Y0.
- Clearly the amplitude modulation function described in the previous chapters, shapes correctly the generated time history.

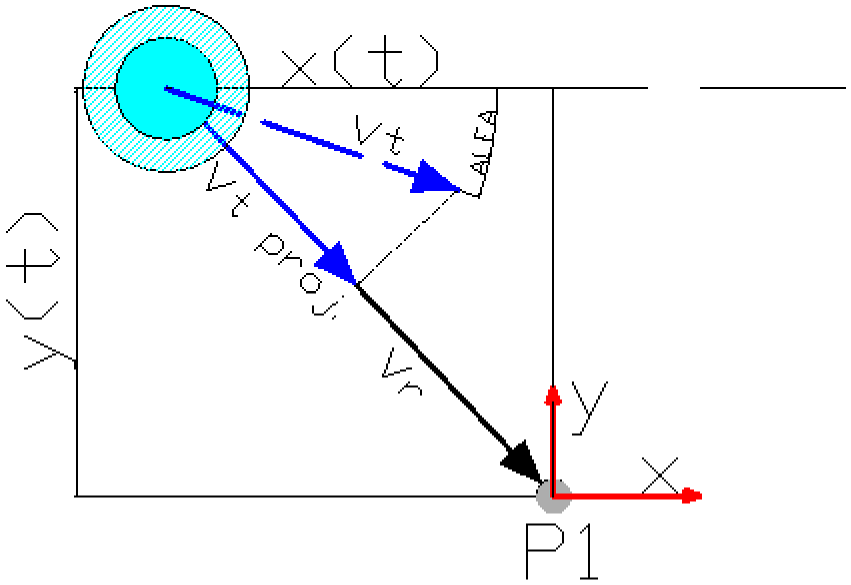

Figure 3-23: Synchronization process of wind components

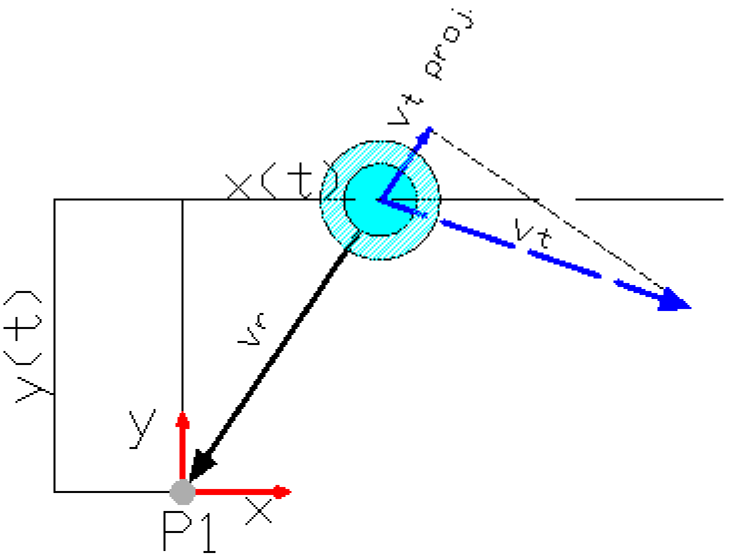

Figure 3-24: Desynchronization process of wind components

Due to the non-ergodicity of the process, one generic simulation is not representative of the wind velocity field. Therefore, the simulation procedure must be performed several times to obtain a vast amount of time histories of the turbulent component (statistic population) that becomes representative of the downburst wind velocity field.

3.10 Generation for Multi-Point

The generation of the Multi-Point follows the same procedure of the Single-Point.

To provide an example of application, a structure as that shown Figure 3-25 was analyzed over the effect of a downburst outflow. The wind field was generated in the grid points of the structure. The geometry of the grid is regular, with 5[m] story height and 6[m] span between columns.

3.10.1 Deterministic mean

While the sampling parameters are those given in Table 3-2 for SDOF, the downburst wind field parameters for MDOF are those reported in Table 3-5: Downburst simulation parameters, graphically Figure 3-26.

Table 3-5: Downburst simulation parameters

PARAMETER	**VALUE**
Integral length scale L_v	34.6 [m]
Max velocity V_{max}	80 [m/s]
Track velocity V_t	12 [m/s]
Height of max velocity Z_{max}	67 [m]
Downburst diameter D=rmax	1000 [m]
Intial X_o	-2500 [m]
Initial y_o	150 [m]
Angle of tracking theta	2° 10° 15° 30°

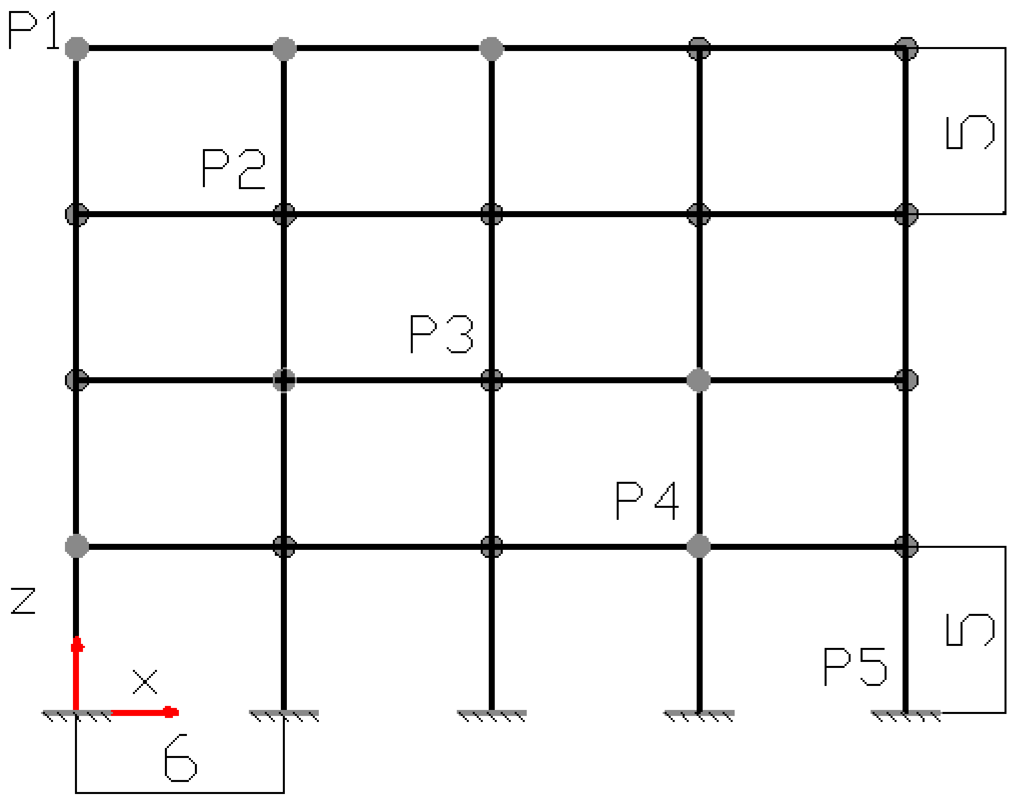

Figure 3-25: 2D frame with 3D downburst. Front view

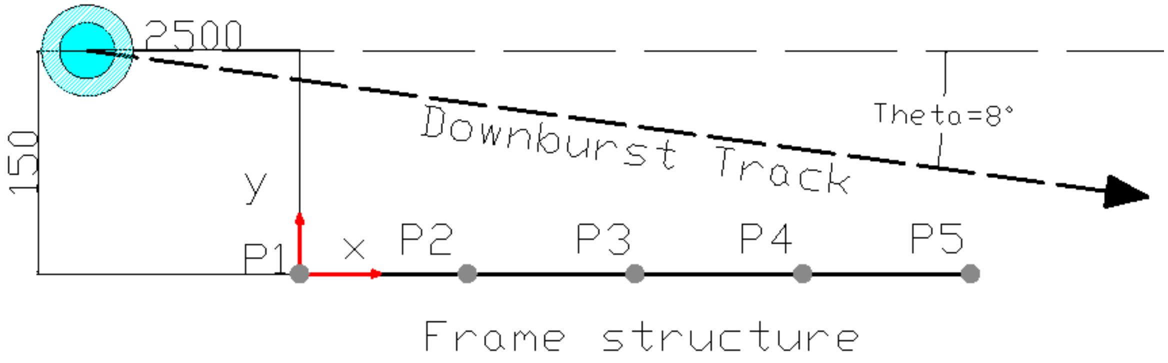

Figure 3-26: Downburst track. Plan view

A representative sample of the mean velocity profiles and the angle of approximation for the points in the diagonal of the grid identified as P1, P2, P3, P4, P5 for different angles of downburst track are given from Figure 3-27 to Figure 3-31.

For theta =2°

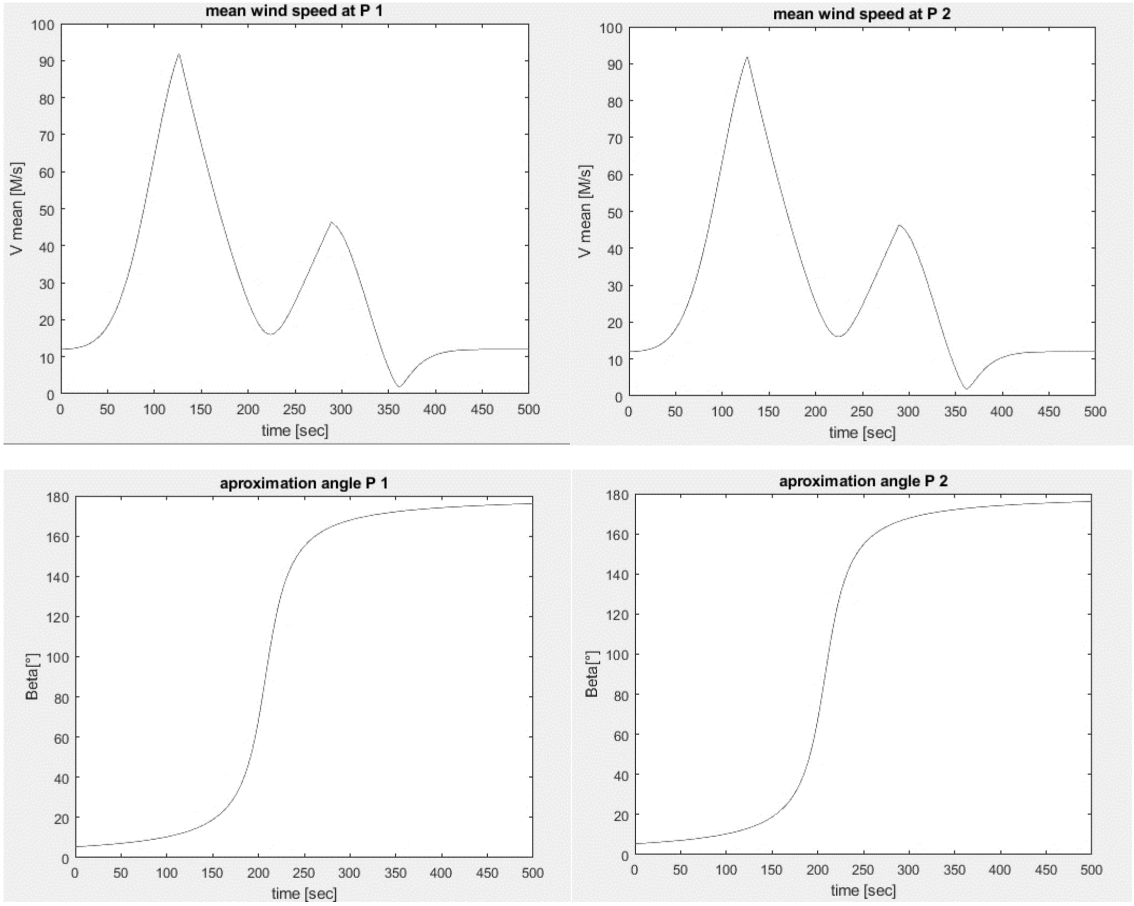
mean wind speed at P 1

mean wind speed at P 2

aproximation angle P 1

aproximation angle P 2

Figure 3-27: Mean velocity and approximation angle for track angle of 2°

For theta =10°

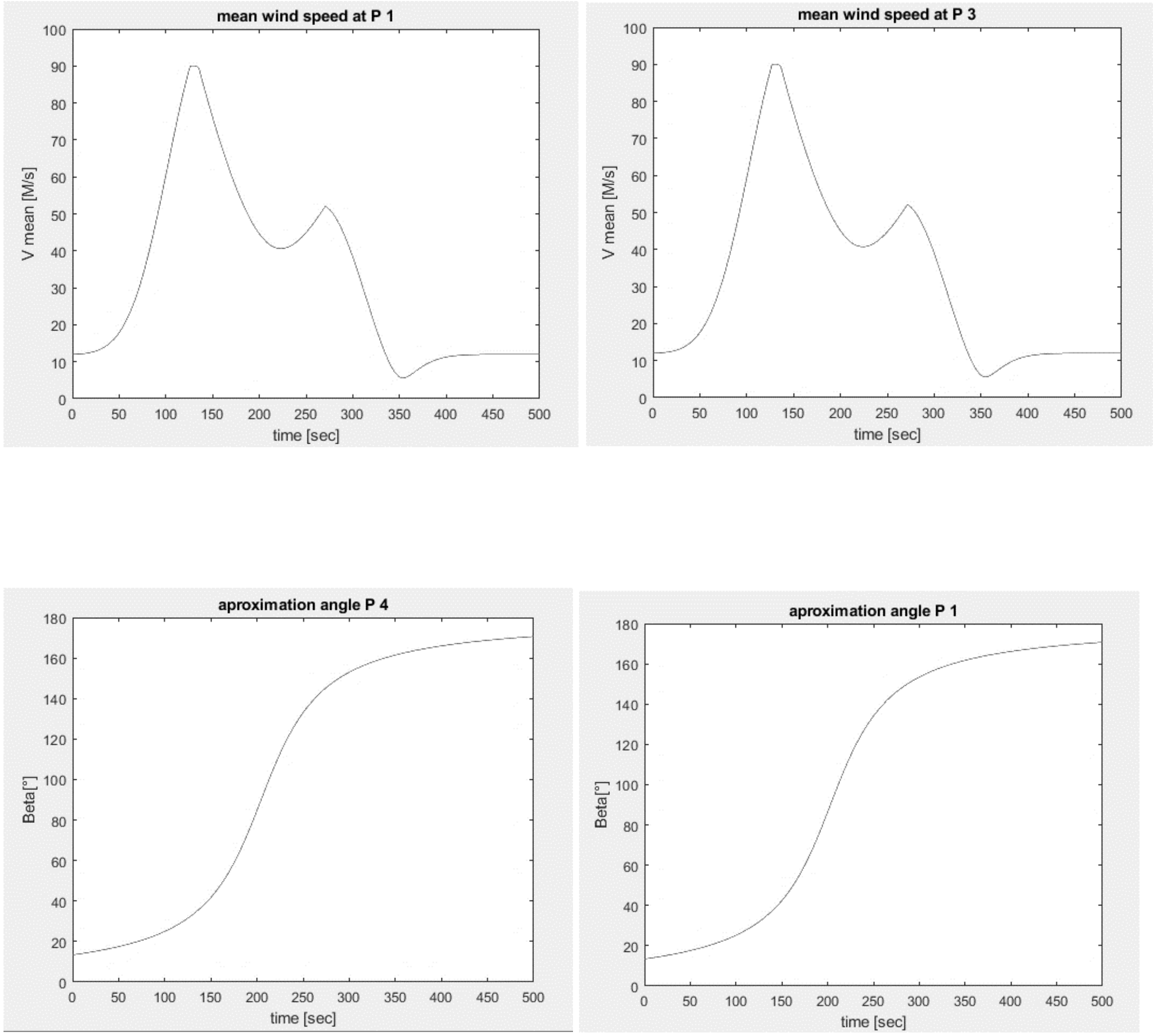

Figure 3-28: Mean velocity and approximation angle for track angle of 10°

For theta =15°

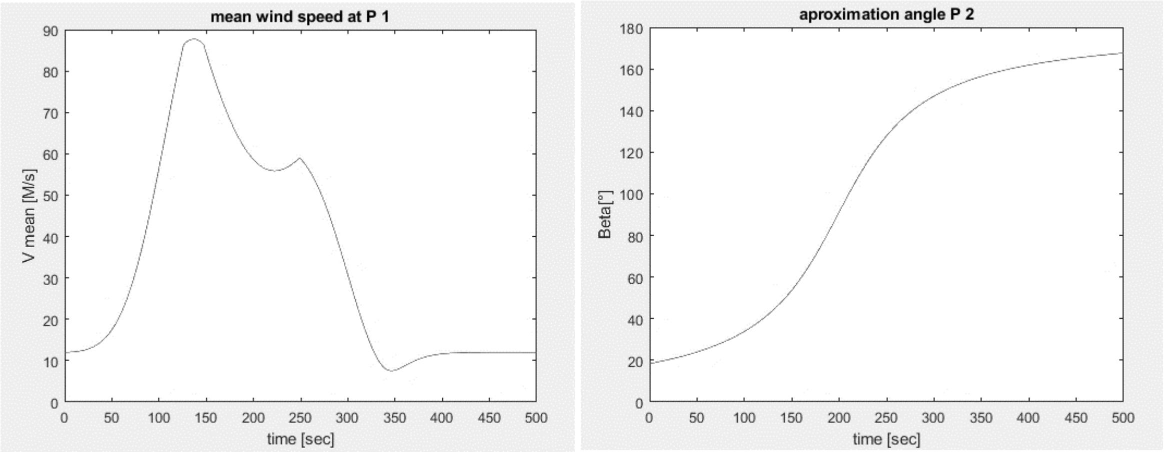

Figure 3-29: Mean velocity and approximation angle for track angle of 15°

For theta= 30°

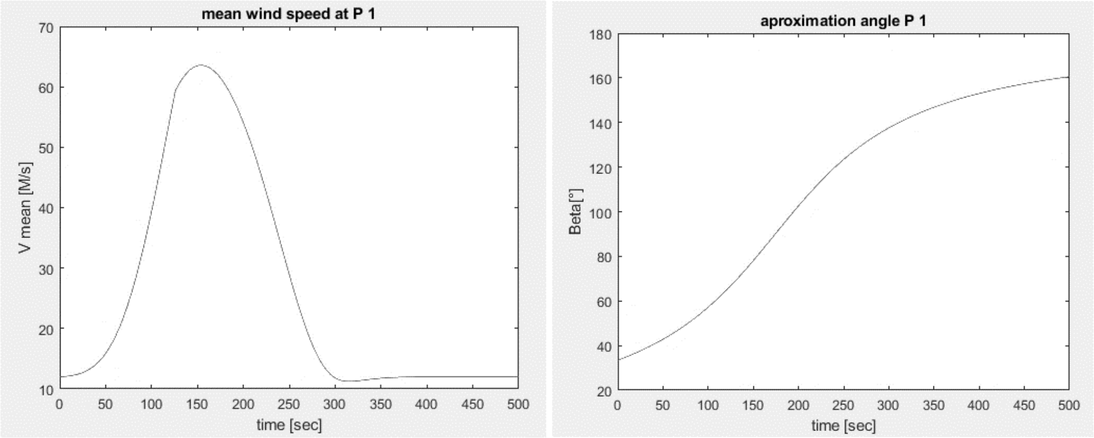

Figure 3-30: Mean velocity and approximation angle for track angle of 30°

For theta= 45°

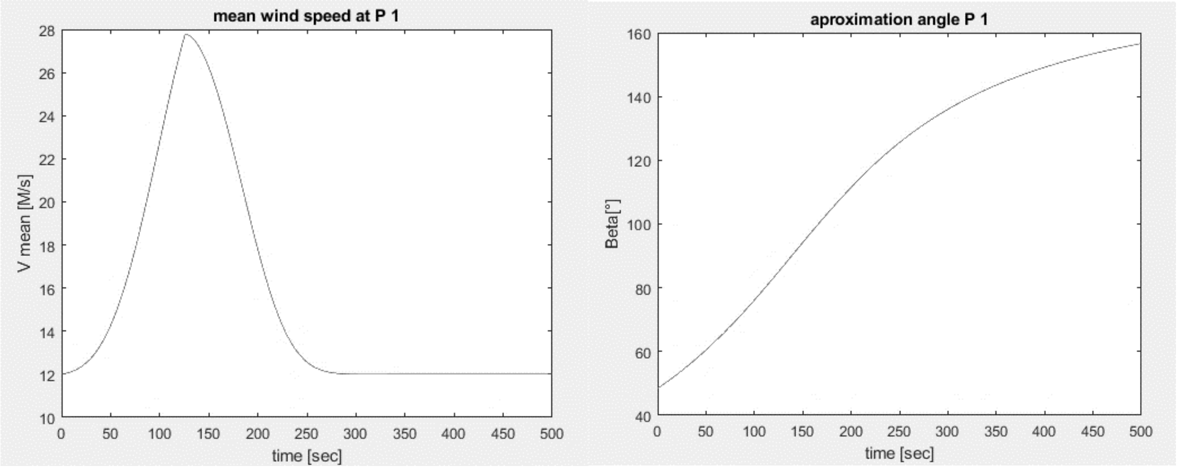

Figure 3-31: Mean velocity and approximation angle for track angle of 45°

3.10.2 Random Turbulence

The random process of the turbulence could be represented as an n-variate stochastic vector process ***V***(t) in which n is the number of points where the wind effect is discretized over the structure. The ***V***(t), can be decomposed into a summation of n n-variate fully coherent normal vectors ***Y***j(t) independent of each other as shown in Equation 3-37.

Equation 3-37

$$\boldsymbol{V}(t) = \sum_{j=1}^{n} \boldsymbol{Y}_j(t)$$

To perform what is given in Equation 3-37, (Di Paola and Gullo 2001) proposed to decompose the cross-PSD matrix into the basis of the eigenvectors of the matrix itself. Calling **Ψ** a matrix containing the eigenvectors of cross-PSD matrix the following relationship may hold:

Equation 3-38

$$\boldsymbol{\Psi}(\omega)^{\boldsymbol{T}} \boldsymbol{CS}_v{}'(\omega) \boldsymbol{\Psi}(\boldsymbol{\omega}) = \boldsymbol{\Lambda}(\omega)$$

Where $\boldsymbol{CS}_v{}'(\omega)$ is the cross-PSD matrix and $\boldsymbol{\Lambda}(\omega)$ is a diagonal matrix containing the eigenvalues *λj* (j=1, 2, …, n) of the $\boldsymbol{CS}_v{}'(\omega)$ matrix associated with the $\boldsymbol{\psi}_j(\omega)$ eigenvector.

The vectors ***Y***j(t) assume the following:

Equation 3-39

$$\boldsymbol{Y}_{\mathrm{j}}(\mathrm{t}) = \int_{-\infty}^{+\infty} \boldsymbol{\psi}_j(\omega)\sqrt{\lambda_j(\omega)}\; e^{i\omega t} dB_j$$

With dB_j accounting for a zero mean normal complex process having orthogonal increments

Equation 3-40

$$E\left[dB_j\right] = 0; \quad dB_j = dB_j^{*}$$

$$E\left[dB_j(\omega_r) dB_j(\omega_s)\right] = \delta_{\omega r\ \omega s}\, \delta_{jk} d\omega r$$

In Equation 3-40 the term δ_{pq} is the so-called Kronecker delta ($\delta_{pq} = 0\ for\ p \neq q$; $\delta_{pq} = 1\ for\ p = q$). And the symbol * denotes complex conjugate.

In discretized way the vectors ***Y***j(t) can be written in the form:

Equation 3-41

$$\boldsymbol{Y}_j(t) = \sum_{k=-N}^{N} \boldsymbol{\psi}_j(\omega k)\sqrt{\lambda_j\ (\omega k)\Delta\omega}\; e^{i\omega k t} P_k^{(j)}$$

Where NΔω is the cutoff frequency. $P_k^{(j)}$ is a zero mean normal complex random variable, which fulfill the following orthogonality condition:

Equation 3-42

$$E\left[P_k^{(j)}\ P_r^{(s)}\right] = \delta_{js}\, \delta_{kr}; \quad P_r^{(s)} = P_{-r}^{(s)*}$$

Taking the only real form of $\boldsymbol{Y}j(t)$:

Equation 3-43

$$\boldsymbol{Y}_j(t) = 2\sum_{k=1}^{N} \boldsymbol{\psi}_j(\omega k)\sqrt{\lambda_j\ (\omega k)\Delta\omega}(\cos \omega k t\, R_k^{(j)} - \sin \omega k t\, I_k^{(j)})$$

The $R_k^{(j)}$and $I_k^{(j)}$ terms stands for the real and the imaginary parts of $P_r^{(s)}$ respectively.

The simulation of the random field suggests that once the modal decomposition is made, the vector $\boldsymbol{V}(t)$ containing the generated turbulence in the *n-points* can be assembled as the sum of the *n* independent random process whose PSD functions are the *λj(ω)* denotes as $Wj(t)$.

Equation 3-44

$$\boldsymbol{V}(t) = \sum_{j=1}^{n} \boldsymbol{\psi}_j\, W_j(t)$$

From Equation 3-39 it is possible to analogously determine the $Wj(t)$ as:

Equation 3-45

$$W_j(t) = \int_{-\infty}^{+\infty} \sqrt{\lambda_j(\omega)}\ e^{i\omega t} dB_j$$

3.10.2.1 Numerical Example

Following the procedure explained before it was possible to build a Monte Carlo simulation of the wind velocity field for 20 points of the structure showed in Figure 3-25. Examples of the generic simulations could be seen on Figure 3-32 and the full velocity outflow including the slowly varying mean Figure 3-33.

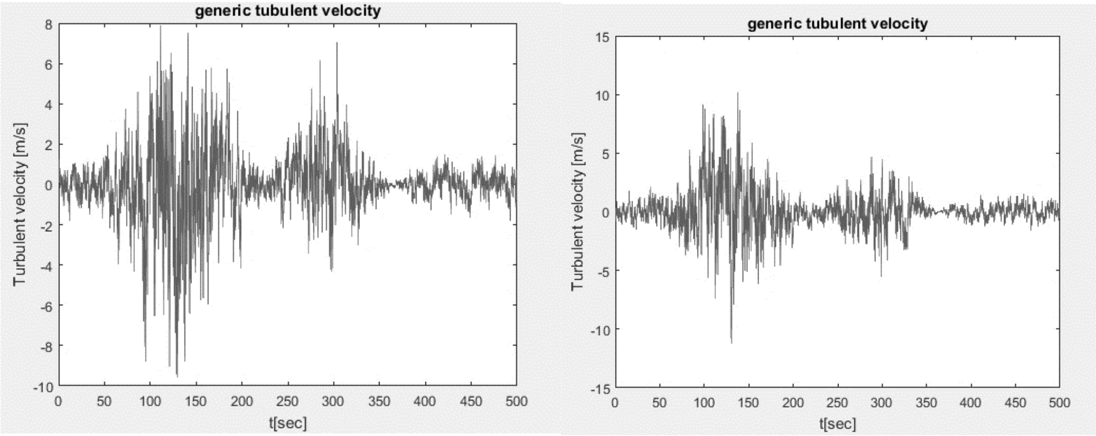

Figure 3-32: Turbulent component of generic point

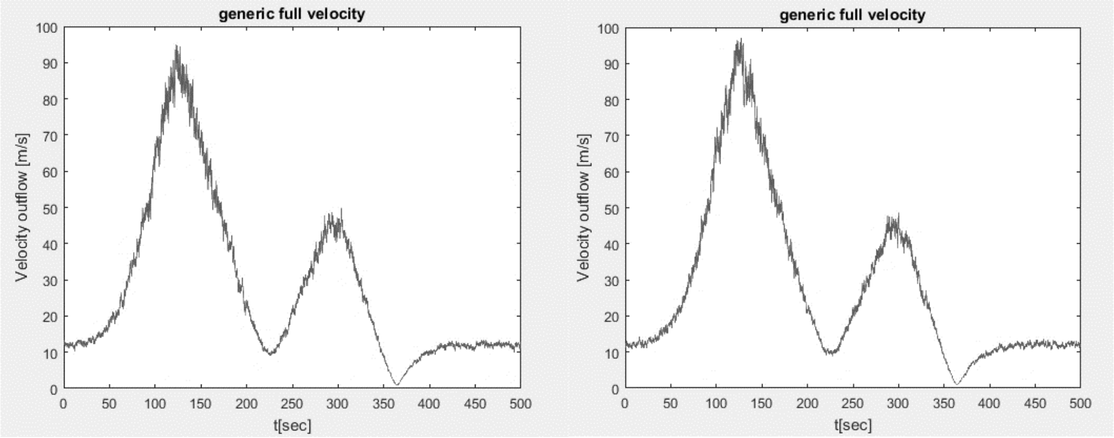

Figure 3-33: Full velocity outflow of generic point

CHAPTER 4. SDOF SYSTEM ANALYSIS

To study the dynamic response of the structures subjected to downburst outflows it can be necessary first to analyze the case of a single degree of freedom structure. The system will be analyzed in time domain and frequency domain to compare both approaches and verify the consistency of the results. Moreover, it will be executed a parametric study based on the damping and natural frequencies of the structure to measure the dependency of the response on these two characteristics.

The main idea driving to the development of the analysis with the two approaches is to take advantage from the features of both. The frequency domain analysis provides a faster assessment of the structural response compared with the time domain analysis. The former does not require the solution of several scenarios of simulated wind velocities as it is required by the latter. However, the time domain analysis provides a robust methodology to solve the equations of motion which is capable to handle non-linear problems.

4.1 Structure

A structural system as that shown in Figure 4-1 was studied under the action of a downburst wind which activates only the horizontal movement of the lumped mass.

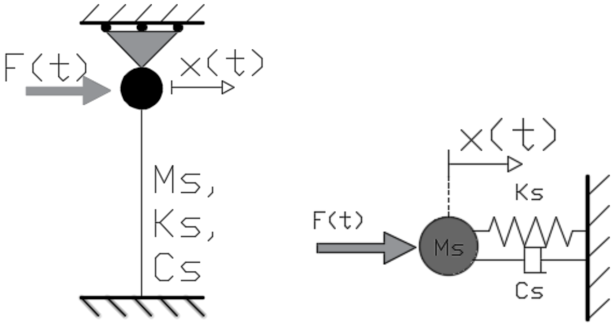

Figure 4-1: a) Simple Structure b) equivalent SDOF system

The equation describing the motion of a single degree of freedom, also known as *equation of motion*, gives the equilibrium of the dynamic forces to which the structure is submitted at any time and is given by the Equation 4-1.

Equation 4-1

$$m\ddot{x} + c\dot{x} + kx = F(t)$$

The first term of the left hand side of Equation 4-1 refers to inertia forces given by the product of the mass and the acceleration of the body, the second term refers to forces related to the viscous damping, the third to the elastic restoring forces given by the product of stiffness and the displacement. On the other hand, the right side of the equation contains the terms associated to the dynamic exciting force. For this case the exciting force is given by the pseudo-static and the buffeting effects of the thunderstorm downburst wind field acting on the structure.

4.2 Aerodynamic Forces

To compute the aerodynamic forces on the structure, an approach widely implemented for synoptic winds is that proposed by (Davenport 1962). The aerodynamic force (Equation 4-3) is given by the components of the wind velocities.

For a single point in the space (free to move only in one direction) the wind force (Equation 4-3) is given by means of the aerodynamic drag coefficient C_D and the relative velocity wind $V_{rel}(z,t)$ between the incoming wind and movement of the structure Equation 4-2.

Equation 4-2

$$V_{rel}(z,t) = [V(z,t) - \dot{x}(t)]$$

Equation 4-3

$$F(t) = \frac{1}{2}\rho C_D A[Vrel]^2$$

Where the density of the air is taken as ρ and the body reference area A.

The decomposition of wind field velocity is taken according to **§** 3.1**-** Equation 3-4, brought here for convenience:

Equation 4-4

$$V(z,t) = V_{max} * \alpha(z) * \gamma(t) + a(t)v'(t)$$

For the case of a fixed height, the dependence on z can be disregarded. Introducing the reference height of the observation point, Z_{ref}, it is possible to express the reference mean velocity, V_m, at the same point as:

Equation 4-5

$$V_m = V_{max} * \alpha(z)|_{z=z_{ref}}$$

And the Equation 4-4 becomes:

Equation 4-6

$$V(t) = V_m * \gamma(t) + a(t) * v'(t)$$

From **§** 3.6.4 it is possible to recall that the intensification function, $\gamma(t)$, and the amplitude modulating function, $a(t)$, can be taken as the same (see e.g.: Canor et al., 2016), i.e.:

Equation 4-7

$$\gamma(t) = a(t)$$

Regarding the square of the relative velocity:

Equation 4-8

$$V_{rel}(t)^2 = [V_m * \gamma(t) + a(t) * v'(t) - \dot{x}(t)]^2 \quad \text{(a)}$$

Or conversely:

$$V_{rel}(t)^2 = V^2(t) - 2V(t)\dot{x}(t) + \dot{x}^2(t) \quad \text{(b)}$$

Replacing Eq. 4-6 in (b):

$$V_{rel}(t)^2 = [V_m * a(t) + a(t) * v'(t)]^2 - 2[V_m * a(t) + a(t) * v'(t)]\dot{x}(t) + \dot{x}^2(t) \quad \text{(c)}$$

$$V_{rel}(t)^2 = a^2(t)[V_m + 2 * V_m * v'(t) + {v'}^2(t)] - 2a(t)[V_m + v'(t)]\dot{x}(t) + \dot{x}^2(t) \quad \text{(d)}$$

Since the turbulent component of the wind velocity and the body velocity are small compared with the mean velocity component it is possible to neglect the effect of the terms associated to their square, and approximate the relative velocity as:

Equation 4-9

$$V_{rel}(t)^2 = [V_m * a(t)]^2 + 2a(t)^2 V_m * v'(t) - 2a(t)V_m * \dot{x}(t)$$

The aerodynamic force is then given by:

Equation 4-10

$$F(t) = \frac{1}{2}\rho C_D A * [V_m * a(t)]^2 + \rho C_D A a(t)^2 V_m * v'(t) - \rho C_D A a(t) V_m * \dot{x}(t)$$

Dividing the force component according to their effect and nature it is possible to obtain three different forces. The force associated to the mean velocity component also taken as the *pseudo-*

static mean force, $F_s(t)$. The dynamic force or buffeting force coming from the turbulence of the wind field, $F_d(t)$.The effect of the body velocity creates an aerodynamic-damping, $F_r(t)$.

Equation 4-11

$$F_s(t) = \frac{1}{2}\rho C_D A * [V_m * a(t)]^2$$

Equation 4-12

$$F_d(t) = \rho C_D A a(t)^2 V_m * v'(t)$$

Equation 4-13

$$F_r(t) = \rho C_D A a(t) V_m * \dot{x}(t)$$

The dynamic exciting force is given by:

Equation 4-14

$$F(t) = F_s(t) + F_d(t) - F_r(t)$$

The problem could be solved as the contribution of two parts, one *pseudo-static* component produced by the mean wind field and giving rise to an equilibrium condition, $x_m(t)$ and the dynamic part x_d associated to the turbulent component of wind which will give rise to a vibration around the equilibrium condition. The problem is summarized in Equation 4-16.

The dynamic effect of the pseudo static component is negligible (in fact β<<1 as it will be explained **§** 4.7.3). Therefore, it is possible to approximate the aeroelastic damping component of Equation 4-13 to:

Equation 4-15

$$F_r(t) \cong \overbrace{\rho C_D A a(t) V_m}^{g(t)} * \dot{x}_d(t) = g(t)\dot{x}_d(t)$$

With $g(t)$ a function which encloses the time-variation of the aeroelastic component.

Equation 4-16

$$\begin{cases} x(t) = x_m(t) + x_d(t) \\ K\, x_m(t) = F_s(t)\ Pseudo-static \\ M * \ddot{x}_d(t) + [C + g(t)]\dot{x}_d(t) + K * x_d(t) = F_d(t)\ Dynamic \end{cases}$$

4.3 Time domain analysis

Basically, for the time domain analysis multiple time histories of the turbulent component of the wind speed were generated using a Monte Carlo algorithm based on the PSD of wind turbulent component. Then, those velocity times histories were transformed into dynamic exciting forces acting on the SDOF structure according to Equation 4-10.

With the dynamic forces and the computed structure parameters it was possible to define the equation of motion as shown in Equation 4-1 and divide its components as shown in Equation 4-16. Regarding the slowly varying mean, it was accounted with the solution of the *pseudo-static* problem which will give rise to an equilibrium position around which the wind turbulent component will vibrate.

The second part of Equation 4-16, corresponding to the solution for the turbulent wind force, was solved numerically by means of the direct integration of the equations of motion with the so-called Newmark method.

4.3.1 Generation of time histories

The generation of the velocity fields follows the same procedure explained and developed in the **§** 3.9.2.

4.3.2 Direct Integration of the equations of motion

In the previous developments it was explained how the multiple time histories of the turbulent component of the wind velocity field were generated, once again it is remarked that a huge amount of realizations was generated to be representative of the wind field. However, it is also required this effort to be done on the structural response identified on this step by the displacement of the top of the beam.

In other words, for every single realization of the turbulence it was performed the integration of the equations of motion to solve the part b of Equation 4-16 and to obtain the structural response of the system under the wind action as the summation of the *pseudo-static* equilibrium condition and the vibrations of the dynamic component.

To this purpose the method developed of direct integration of the equations of motion by Newmark (Chopra 2012) was implemented. This method computes numerically the structural response of a system by solving step by step on time the equations of motion of the system. The important aspects in the implementation of this method are the size of the time step, the selection of the β and γ

coefficients and the initial conditions. The selection of this parameters for the case of study will be explained in the following developments (Equation 4-20 and Equation 4-21).

- Initial conditions

The system is supposed to be at rest before the application of the wind field and therefore the homogeneous initial conditions can be indicated as follows:

Equation 4-17

$$\begin{cases} x(t=0)=0 \\ \dot{x}(t=0)=0 \end{cases}$$

The initial value of the acceleration and the external force is not necessarily equal to zero, the initial acceleration must be computed as follows:

Equation 4-18

$$\ddot{x}(t=0)=\frac{F(t=0)}{m}$$

- Selection of the β and γ coefficients

The selection of this coefficients defines the terms of the Taylor succession that will be considered to approximate the acceleration derivative within the time steps. In other words, they define the variation (or derivative) of the acceleration inside the discretized time step. From the practical point of view, for the case γ=1/2 and β=1/4 the acceleration is constant on each time step, and for the case γ=1/2 and β=1/6 the acceleration is linear on each time step.

To ensure the numerical stability of the algorithm, on the development of this study the case of constant acceleration was selected and therefore γ=1/2 and β=1/4. Because is unconditionally stable.

- Definition of the time step

This aspect is crucial for the convergence and accuracy of the method. Due numerical instability of the step by step methods for long time steps is possible to obtain unstable results giving rise to spurious data. The Newmark method is stable if:

Equation 4-19

$$\frac{t_{step}}{T_n}\leq\frac{1}{\pi\sqrt{2}}\frac{1}{\sqrt{\gamma-2\beta}}$$

With t_{step} representing the time step and T_n the natural period of the system.

For the case of constant acceleration, the ratio on the right-hand side of Equation 4-19 becomes infinity and therefore is unconditionally stable. However, this not occurs for the case in which the acceleration is linear inside the discretized time step.

Having all the structural parameters already defined and the set of method parameters, it is possible to extend the process given in (Chopra 2012) for the case of time-varying aeroelastic effects.

1. Initial Computations:

Equation 4-20

$$\left\{\begin{array}{c} a_1(t) = \dfrac{m}{\beta * {t_{step}}^2} + \dfrac{\gamma * [c + g(t)]}{\beta * t_{step}}; \qquad a_2(t) = \dfrac{m}{\beta * t_{step}} + \left(\dfrac{\gamma}{\beta} - 1\right)[c + g(t)] \\ a_3(t) = \left(\dfrac{1}{2\beta} - 1\right)m + \left(\dfrac{\gamma}{2\beta} - 1\right)[c + g(t)] \\ K = k + a_1(t) \end{array}\right.$$

2. Computations for the time step t_i:

Equation 4-21

$$\left\{\begin{array}{c} \widehat{F_d}(i+1) = F_d(i+1) + a_1(i)x_d(i) + a_2(i)\dot{x}_d(i) + a_3(i)\ddot{x}_d(i) \\ x_d(i+1) = \dfrac{\widehat{F_d}(i+1)}{\hat{k}} \\ \dot{x}_d(i+1) = \dfrac{\gamma}{\beta * t_{step}}[x_d\ (i+1) - x_d(i)] + \left(1 - \dfrac{\gamma}{\beta}\right)\dot{x}_d(i) + \left(1 - \dfrac{\gamma}{2\beta}\right)\ddot{x}_d(i) \\ \ddot{x}_d(i+1) = \dfrac{1}{\beta * {t_{step}}^2}[x_d(i+1) - x_d(i)] - \dfrac{1}{\beta * t_{step}}\dot{x}_d(i) - \left(\dfrac{1}{2\beta} - 1\right)\ddot{x}_d(i) \end{array}\right.$$

4.4 Aeroelastic Damping Study

To measure the effect of the aeroelastic damping on the overall response of the structure, it was studied the behavior of a SDOF system submitted to downburst wind velocity field. There were implemented four different strategies to simulate the aerodynamic damping of the system. The downburst wind velocity field used in the evaluation is described through the same 2.000 Monte Carlo generations that will be used in the parametric study to keep consistency between the data.

The following four strategies for the modelling of the aerodynamic damping will be considered in this work for comparison purposes:

1. Time varying aeroelastic damping. This strategy fully accounts for the non-stationarity of the wind velocity outflow as it is given in Equation 4-15 brought here for convenience.

Equation 4-22

$$F_r(t) = \rho CdAa(t)V_m * \dot{x}_d(t)$$

2. Constant-zero valued aeroelastic damping component. In this case the aeroelastic component of the wind is disregarded. Equation 4-23 is obtained from Equation 4-13 by imposing that *a*(*t*)=0 ∀ *t*, i.e:

Equation 4-23

$$F_r(t) = \rho CdAa(t)V_m * \dot{x}_d(t) \rightarrow a(t) = 0 \rightarrow 0$$

3. Constant-maximum valued aeroelastic damping component, referent to the extreme value obtained for a constant amplitude modulating function with unit value as given in Equation 4-24.

Equation 4-24

$$F_r(t) = \rho CdAa(t)V_m * \dot{x}_d(t) \rightarrow a(t) = 1 \rightarrow \rho CdAV_m * \dot{x}_d(t)$$

4. Constant-mean valued aeroelastic damping component, referent to the average value obtained for a constant amplitude modulating function with mean value as given in Equation 4-25.

Equation 4-25

$$F_r(t) = \rho CdAa(t)V_m * \dot{x}_d(t) \rightarrow \overline{a(t)} = Mean[a(t)] \rightarrow \rho CdA\overline{a(t)}V_m * \dot{x}_d(t)$$

The structural parameters used in the simulation are reported in Table 4-1: Structure simulation parameters.

Table 4-1: Structure simulation parameters

Parameter	Symbol	Value	Unit
Damping ratio	ζ	2	*[%]*
Mass	m	235	*[kg]*
Stiffness	k	$9.722x10^4$	*[N/m]*

Circular natural frequency	ω_n	20.831	*[rad/sec]*
Natural frequency	f_n	3.315	*[hz]*
Damping coefficient	c	196.228	*[kg/s]*
Drag coefficient	Cd	2.1	*[-]*

With the scope of giving a graphical representation only, in Figure 4-2 it is presented the *normalized time varying damping coefficient,* $g_n(t)$, associated to the wind coming from Equation 4-22 normalized with the structural damping coefficient, Equation 4-26. From the figure it is possible to observe that the maximum contribution of the wind associated damping is going to be equal to 60% of that coming from the structural components and by extracting the mean value of the same it is possible to observe an average contribution less than the 20%.

Equation 4-26

$$g_n(t) = \frac{g(t)}{C}$$

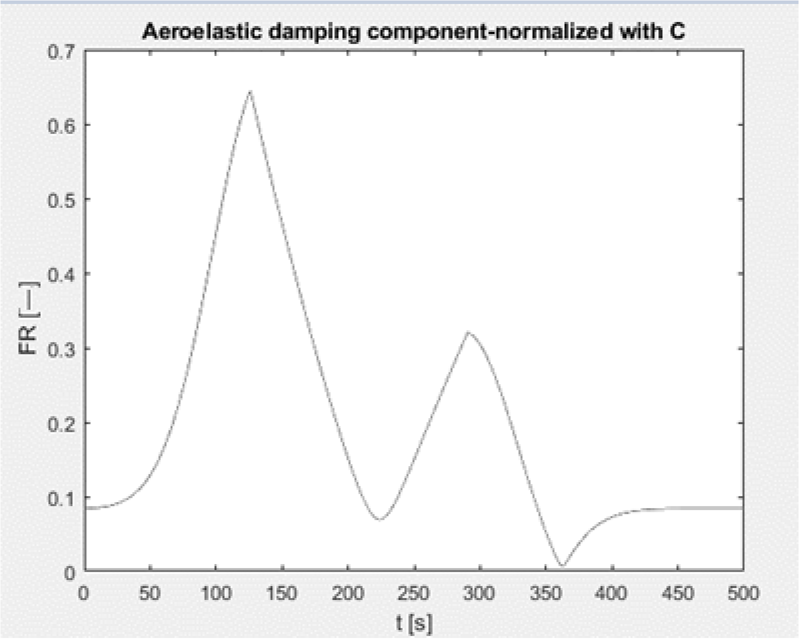

Figure 4-2: Normalized-Aeroelastic damping coefficient

4.4.1 Graphical Result Comparison

The analysis of the results is made based on their statistical properties. The outcomes were given from 2.000 Monte Carlo simulations of the wind velocity field. Therefore, it results attractive to verify the time varying spectral moments of the complete sample. However, and with the aim of providing a simple idea of the process, the comparison of a generic simulation is given in Figure 4-3.

From the graphical analysis of the picture it is not possible to distinguish a remarkable difference between the four approaches. Only possible to notice a slightly higher peak in the approach with disregarded aerodynamic damping (* symbol, a=0), as expected.

The time varying: maximum, mean and variance (Equation 4-27), from the *N=2.000* Monte Carlo simulations at each instant of time, t_i, are given from Figure 4-4 to Figure 4-6. From a qualitative and graphical point of view, the results of the four approaches fit on a same tendency. Relatively small discrepancies could be easily noticed; however, it is possible to appreciate the simulation with constant-maximum value of amplitude modulating function shows a lower response than the other approaches. In addition, the response neglecting the aeroelastic damping seems to follow closer the tendency of the actual response computed with the time varying aerodynamic damping.

With the graphical comparison it was possible to build a macro-structure of the behavior of the spectral moments and statistical properties of the response. However, in order to establish a complete comparison of the results it is necessary to check the numerical data.

Equation 4-27

$$\begin{cases} MaxX_d(t_i) = Max[x_d(N, t = t_i)] \\ MeanX_d(t_i) = Mean[x_d(N, t = t_i)] \\ VarX_d(t_i) = Var[x_d(N, t = t_i)] \end{cases}$$

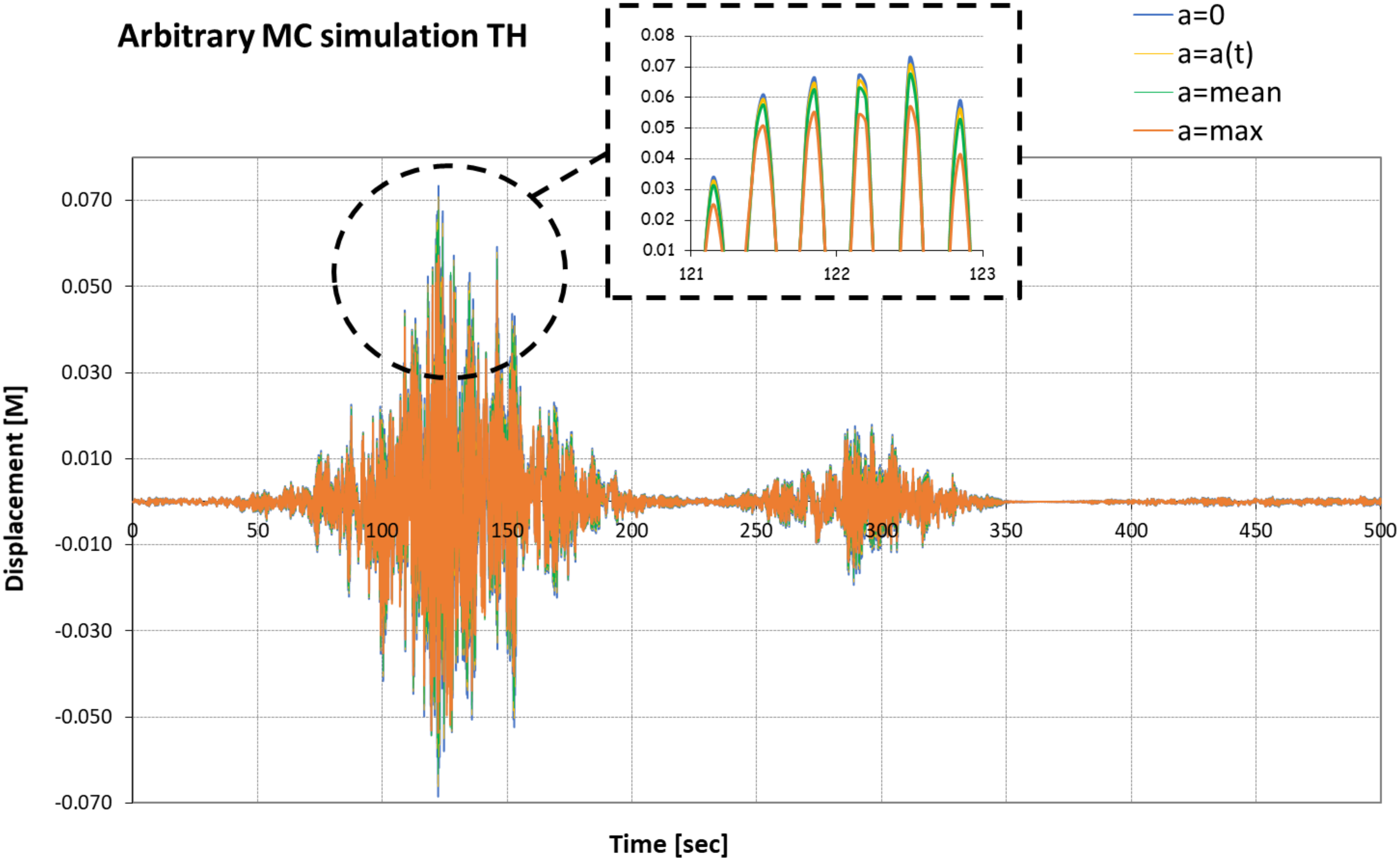

Figure 4-3: Generic simulation time history comparison

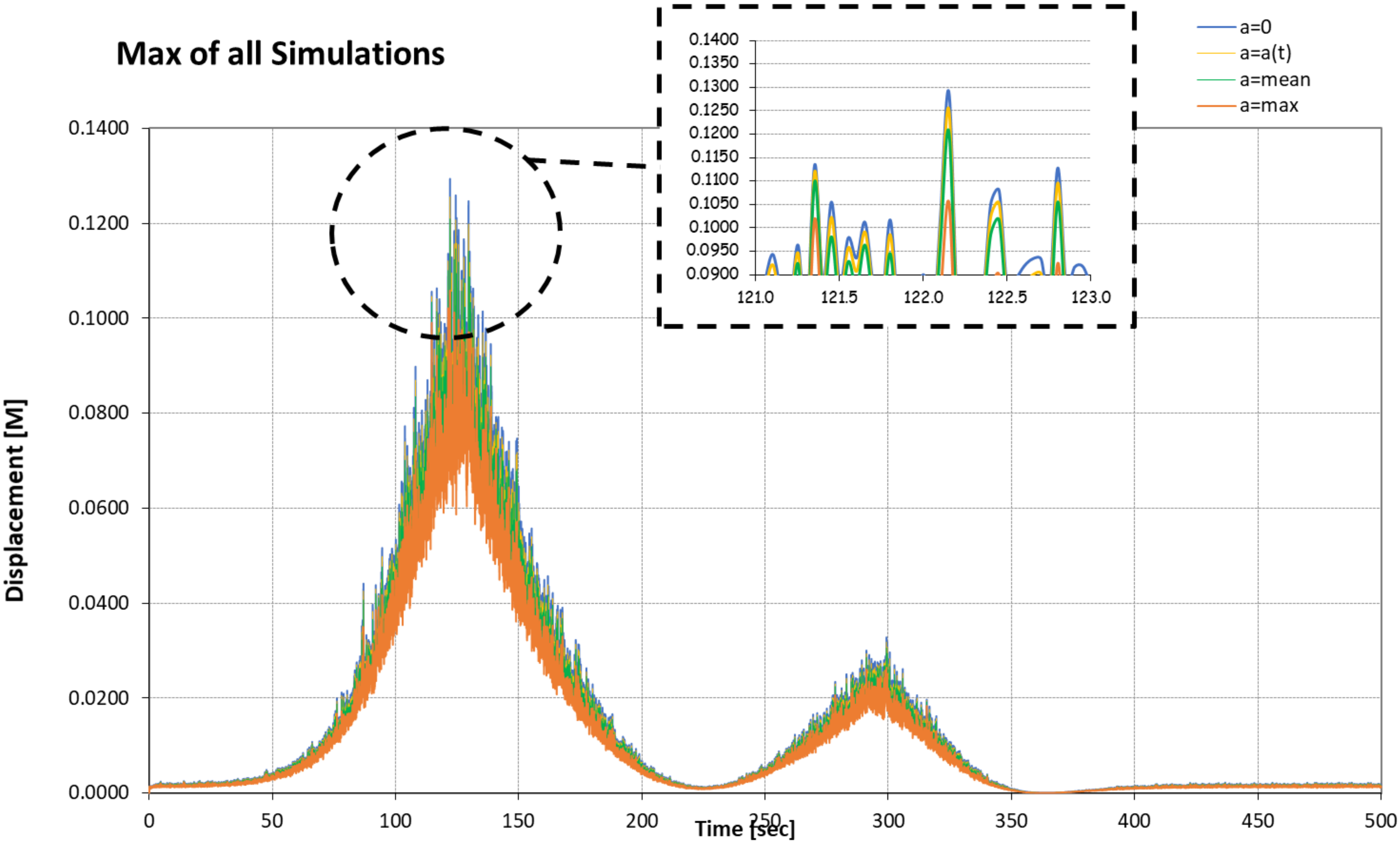

Figure 4-4: Comparison of Time varying maximum

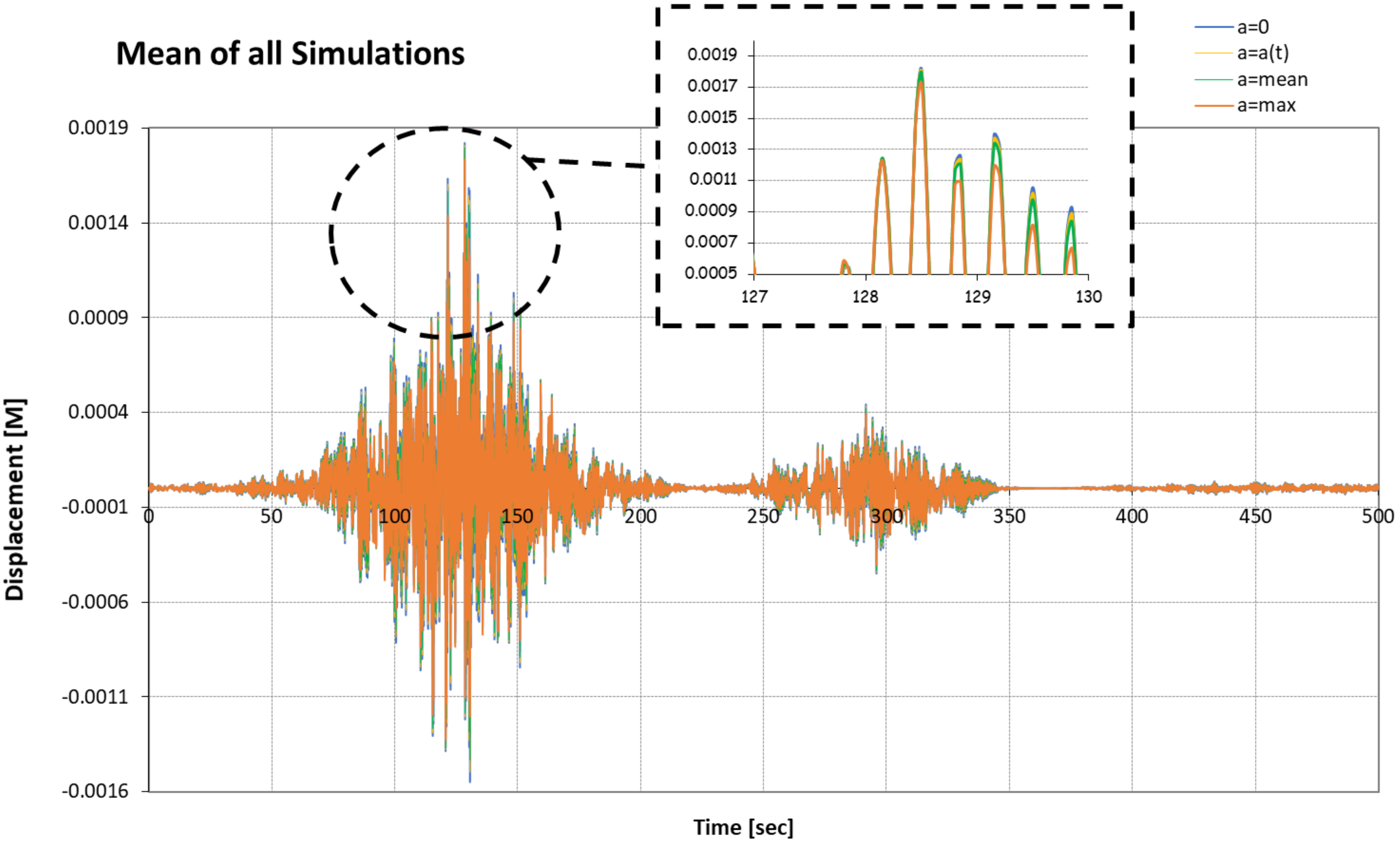

Figure 4-5: Comparison of Time varying mean

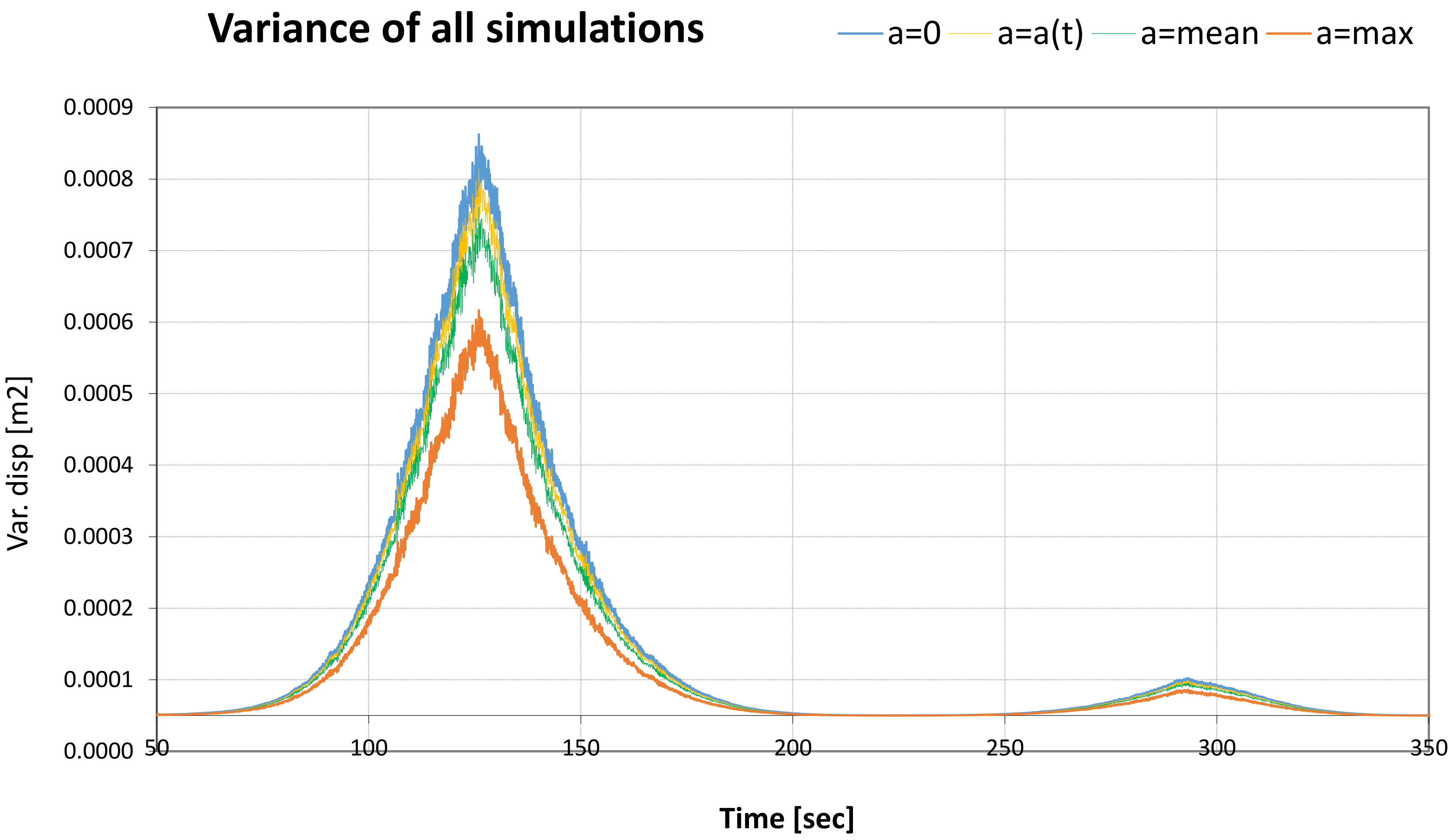

Figure 4-6: Comparison of Time varying variance

4.4.2 Numerical Result Comparison

The maximum fluctuating response for all the 10.000 simulated instants of time and 2.000 generated Monte Carlo histories are reported in Table 4-2. For the mean value Table 4-3 gives an analogous information.

Table 4-2: Maximum response

Approach	Value	Unit
1	0.1252	*[m]*
2	0.129	*[m]*
3	0.1055	*[m]*
4	0.1206	*[m]*

Table 4-3: Mean response

Approach	Value	Unit
1	2.0177e-6	*[m]*
2	2.0178e-6	*[m]*
3	2.0174e-6	*[m]*
4	2.0176e-6	*[m]*

The maximum value of the response computed with the full time-varying aeroelastic damping are closer to those computed neglecting its effect (approaches 1 and 2 respectively). Therefore, a final measure must be done in the error of these two approaches to verify the possibility of neglecting this effect. Regarding the mean, since its value is very small closer to zero it works as benchmarking test to proof the assumption of zero mean stochastic process.

4.4.3 Normalized Root Mean Squared Error

The root mean squared error, RMSE, is useful to determine how two signals are close to each other. it can be computed as shown in Equation 4-28. In which N is the length of the discretized signals, X_{ref} is the reference signal and X_i the signal to be verified.

Equation 4-28

$$RMSE = \sqrt{\frac{\sum_1^N (X_i - X_{ref})^2}{N}}$$

It is usually normalized with the *range* of the reference signal to give relative value to this parameter as shown in Equation 4-29.

Equation 4-29

$$NRMSE = \frac{RMSE}{Max\left(X_{ref}\right) - Min(X_{ref})} \quad (a)$$

$$NRMSE\ [\%] = \frac{RMSE}{Max\left(X_{ref}\right) - Min(X_{ref})} * 100 \quad (b)$$

To give a measure of how much the structural response is affected by neglecting the aeroelastic damping, it will be computed the NRMSE of the of complete statistical population of this signal (2.000 Monte Carlo Simulations) with those of the response with the time-varying aeroelastic damping effect.

Three different NRMSE will be computed to compare both responses:

- $NRMSE_{max}$: Obtained from the maximum response of the 2.000 simulations.

The reference signal $X_{ref,max}$ for this case, will be given by the maximum response from the complete population at each instant of time, t_i, coming from the response of approach 1.

Equation 4-30

$$X_{ref,max}(t = t_i) = \max[x_{d,apporach1}(t = t_i)]$$

The secondary signal $X_{i,max}$ for this case, will be given by the maximum response from the complete population at each instant of time, t_i, coming from the response of approach 2.

Equation 4-31

$$X_{i,max}(t = t_i) = \max[x_{d,apporach2}(t = t_i)]$$

The root mean squared error for this case will be given by:

Equation 4-32

$$RMSE_{max} = \sqrt{\frac{\sum_1^N (X_{i,max} - X_{ref,max})^2}{N}}$$

And the normalized expression:

Equation 4-33

$$NRMSE_{max} = \frac{RMSE_{max}}{Max\left(X_{ref,max}\right) - Min(X_{ref,max})} * 100$$

- $NRMSE_{mean}$: Obtained from the mean response of the 2.000 simulations.

The reference signal $X_{ref,meam}$ for this case, will be given by the mean response from the complete population at each instant of time, t_i, coming from the response of approach 1.

Equation 4-34

$$X_{ref,mean}(t = t_i) = \mathrm{mean}[x_{d,approach1}(t = t_i)]$$

The secondary signal $X_{i,mean}$ for this case, will be given by the mean response from the complete population at each instant of time, t_i, coming from the response of approach 2.

Equation 4-35

$$X_{i,mean}(t = t_i) = \mathrm{mean}[x_{d,approach2}(t = t_i)]$$

The root mean squared error for this case will be given by:

Equation 4-36

$$RMSE_{mean} = \sqrt{\frac{\sum_1^N (X_{i,mean} - X_{ref,mean})^2}{N}}$$

And the normalized expression:

Equation 4-37

$$NRMSE_{mean} = \frac{RMSE_{mean}}{Max(X_{ref,mean}) - Min(X_{ref,mean})} * 100$$

- $NRMSE_{var}$: Obtained from the variance of the response of the 2.000 simulations.

The reference signal $X_{ref,var}$ for this case, will be given by the variance of the response from the complete population at each instant of time, t_i, coming from the response of approach 1.

Equation 4-38

$$X_{ref,var}(t = t_i) = \mathrm{Var}[x_{d,approach1}(t = t_i)]$$

The secondary signal $X_{i,var}$ for this case, will be given by the variance of the response from the complete population at each instant of time, t_i, coming from the response of approach 2.

Equation 4-39

$$X_{i,var}(t = t_i) = Var[x_{d,approach2}(t = t_i)]$$

The root mean squared error in this case will be given by:

Equation 4-40

$$RMSE_{var} = \sqrt{\frac{\sum_{1}^{N}(X_{i,var} - X_{ref,var})^2}{N}}$$

And the normalized expression:

Equation 4-41

$$NRMSE_{var} = \frac{RMSE_{var}}{Max(X_{ref,var}) - Min(X_{ref,var})} * 100$$

The errors are reported in Table 4-4.

Table 4-4: Normalized Mean Squared Errors

Error	Value	Unit
$NRMSE_{max}$	0.7248	[%]
$NRMSE_{mean}$	0.2315	[%]
$NRMSE_{var}$	1.3090	[%]

The error computed between the two approaches confirms the similitude between the response of both signals already evidenced in the graphical assessment. Therefore, it is possible to state that for the specific problem herein studied the aeroelastic damping effect (coming from Equation 4-13) could be neglected in the computation of the structural response, and Equation 4-14 can be approximated to:

Equation 4-42

$$F(t) \cong F_s(t) + F_d(t)$$

It is now important to include the effect of the natural frequency into consideration since the model so far studied has fixed mechanical properties.

4.4.4 Study on Natural Frequency

The before studied system is referred to a single natural frequency as reported in Table 4-1. Therefore, in order to extend the conclusion to a more general case, it is necessary to study the behavior of the aeroelastic damping as function of the natural frequency of the oscillator.

For the analysis it will be used as reference signal the turbulent response of the oscillator with the time varying aeroelastic component (approach 1) Equation 4-22. The response of the system will be characterized by variable $\Delta_i(f_n)$ as function of the natural frequency, f_n(Equation 4-43). The index i, going from 2 to 4, denotes the approach for the aeroelastic damping determination.

Equation 4-43

$$\Delta_i(f_n) = \frac{\left|X_{ref}(f_n) - X_i(f_n)\right|}{X_{ref}(f_n)}$$

Where $X_{ref}(f_n)$ is the variance response of the system computed with approach 1 and $X_i(f_n)$ is the variance response of the system computed with the approach i.

The result of the study could be seen in Figure 4-7. It is possible to observe that for low natural frequency systems in range of 0.1 to 1 [Hz], as long structures (cables, tall buildings and bridges), the characteristic variable Δ has a peak evidencing a large difference between the time-varying aeroelastic damping and those assuming constants values. In addition, this difference is higher for the approaches 2 and 3 with a(t) equal to the extreme values (zero and maximum).

The results of the current study allow to conclude that the time-varying aeroelastic response is only negligible for structures with structural damping ratio of 2% and first natural frequencies greater than 1.5 [Hz]. For frequencies greater than this the characteristic variable Δ tends to a stabilize, showing a trustable response measured with the constant aeroelastic damping approaches.

For structures with natural frequencies in the range of Δ lower than 1.5 [Hz] the best approximation is to use a constant aeroelastic damping associated to the mean value of the modulating function a(t).

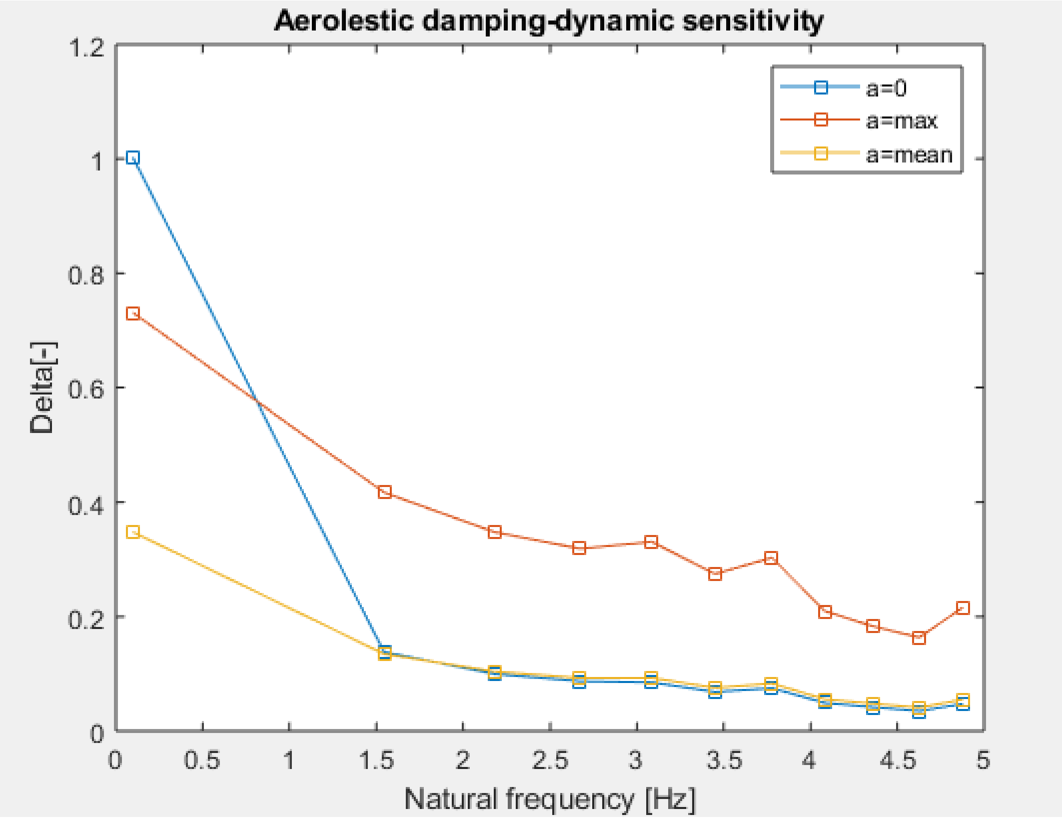

Figure 4-7: Dynamic effect on the aeroelastic damping behavior.

The results of the analysis allow to disregard the aeroelastic damping component in the analysis. With this option it will be possible to reduce the computational effort involved in the computation of the frequency response function H(f) **§** 4.6.1 for the Direct Frequency Domain Analysis that will be explained in the following developments.

Regarding the time domain analysis, in order to give a representation of the equations of motion compatible with the obtained results of the current paragraph, the effect of the aeroelastic damping will be disregarded and the Equation 4-16 is going to be simplified as follows:

Equation 4-44

$$\begin{cases} K\, x_m(t) = F_s(t)\ Pseudo-static \\ M * \ddot{x}_d(t) + C * \dot{x}_d(t) + K * x_d(t) = F_d(t)\ Dynamic \end{cases}$$

4.5 Direct frequency domain analysis

The direct frequency domain analysis is an alternative method for computing the structural response of a system subjected to a stochastic input. This approach computes the PSD of the response starting from the PSD of the aerodynamic force. From the practical point of view, it avoids the generation of huge amounts of data and reduces the computational effort related to the numerical evaluation of the equations of motion for every realization. Moreover, it allows for a deeper understanding of the physics of the problem.

On the other hand, this type of analysis may become very complex for MDOF systems as it requires to evaluate and invert the frequency response function matrix, as well as, the construction of the PSD including the Cross-PSD terms which considers the correlation between the excitation of the different degrees of freedom.

The non-stationarity of the problem is accounted for by exploiting the theory of the evolutionary spectra firstly developed by (Priestley 1965) and already described in in **§** 2.1.3.

4.5.1 Formulation of the Evolutionary Power Spectral Density (EVPSD)

The evolutionary PSD function according to **§** 2.1.3 for the uniformly modulated process depends on the stationary PSD function and the amplitude modulating function. In Equation 4-45 is reported the spectral representation of the turbulence.

Equation 4-45

$$EVS_{v'}(t,f) = |a(t)|^2 S_{v'}(f)$$

A graphical representation of the downburst EVPSD is reported in Figure 4-8.

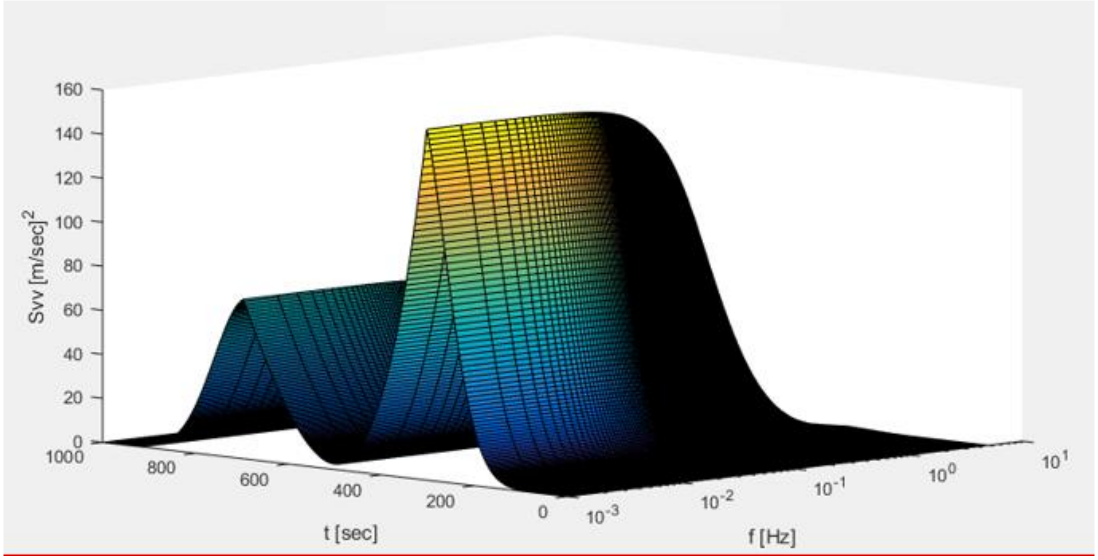

Figure 4-8:EVPSD of turbulent component

4.5.2 Structural frequency response function

The structure effect can be regarded as a filter. Therefore, to assess the structural response it will be used the procedure stablished in **§** Evolutionary frequency response function2.1.3.5. The structural frequency response function for the traditional stationary excitations is given in Equation 4-46 (noted as *H(f)* see **§**4.6.1) it can be also computed as the Fourier transform of the Impulse response function of the structure Equation 4-47 (noted as $H_1(f)$ see **§**4.6.1).

Equation 4-46

$$H(f) = [k + i2\pi fc - (2\pi f)^2 m]^{-1}$$

Alternatively,

Equation 4-47

$$H_1(f) = \int_{-\infty}^{+\infty} h(t-\tau) e^{-i2\pi ft} d\tau$$

With the impulse response function (Chopra 2012):

Equation 4-48

$$\begin{cases} h(t-\tau) = \dfrac{1}{m * \omega_D} e^{-\zeta\omega_n(t-\tau)} * \sin\big(\omega_D * (t-\tau)\big) \; for\; t \geq \tau, \\ \qquad h(t-\tau) = 0, \qquad elsewhere \end{cases}$$

Where, t is the current time and τ is the initial time of the impulse, therefore $t - \tau$ is the time window between the observation period and the impulse application. And ω_D is the damped circular frequency of the system, Equation 4-49.

Equation 4-49

$$\omega_D = -\omega_n \left(\zeta \pm i\sqrt{1 - \zeta^2} \right)$$

With ω_n, the circular natural frequency and ζ, the damping ratio.

4.5.3 EPSD of the structural response

The power spectrum associated to stationary input signal of the aerodynamic force, $S_p(f)$, can be computed as Equation 4-50.

Equation 4-50

$$S_p(f) = AD_0^2 S_{v'}(f)$$

Being $S_{v'}(f)$ the stationary power spectrum associated to the turbulent component of the wind velocity field.

The term AD_o stands for terms in the *pseudo-static* component of the aerodynamic force which allows to transform wind turbulent velocity into forces applied on the degrees of freedom of the structure. For this case and according to Equation 4-10, AD_o is going to be the terms multiplying the turbulent velocity:

$$AD_o = \rho \, Cd \, A \max(V_c)$$

The associated uniformly modulated non-stationary process is of the form:

Equation 4-51

$$p(t) = \int_{-\infty}^{+\infty} a(t) \, e^{i2\pi f t} d\varphi_p(f)$$

Where $d\varphi_p(f)$ is associated to $S_p(f)$ as defined in **§** 2.1.3.3 and Equation 4-51 is analogous to the before developed Equation 2-48.

Equation 4-52

$$E\left| d\varphi_p(f) \right|^2 = S_p(f) df$$

According to **§ 2.1.3.5 (**Equation 2-52**),** the response signal of a system (turbulent component of the displacement, in this case $x_d(t)$) is related to the input signal $p(t)$ by means of the following relation:

Equation 4-53

$$x_d(t) = \int_0^t p(\tau)h(t-\tau)d\tau$$

Replacing Equation 4-51 in Equation 4-53 it is possible to obtain:

Equation 4-54

$$x_d(t) = \int_0^t \int_{-\infty}^{+\infty} a(\tau)\, e^{i2\pi f\tau} d\varphi_p(f)\, h(t-\tau)d\tau$$

Analogously to **§ 2.1.3.5:** By squaring the quantities of Equation 4-54 and taking the average through all the realizations (Perotti 2017), it is possible to handle the problem in the frequency domain.

Equation 4-55

$$\begin{aligned}{\sigma_{x_d}}^2 = E\left[x_d^2(t)\right] &= E\left[\left|\int_0^t \int_{-\infty}^{\infty} a(\tau)e^{i2\pi ft} d\varphi_p(f)\, h(t-\tau)d\tau\right|^2\right] \\ &= \left|\int_0^t a(\tau)h(t-\tau)e^{i2\pi ft}d\tau \quad \right|^2 E\left[\left|d\varphi_p\right|^2\right]\end{aligned}$$

Hence, the evolutionary power spectrum of the response can be written as follows:

Equation 4-56

$$EVS_{x_d}(f,t) = |H_2(f,t)|^2 S_p(f)$$

Where the *generalized transfer function or evolutionary frequency response function EFRF,* $H2(f,t)$, with respect to the family of functions $a(t)$, is defined as (analogous to Equation 2-57) :

Equation 4-57

$$H_2\,(f,t) = \int_{-\infty}^{+\infty} a(t-\tau)h(\tau)e^{-2\pi f\tau}d\tau$$

Looking to the variation of $h(t)$ (for a reference structure with f_n=3.35Hz and ζ=2%) and $a(t)$, it is possible to state that while the former decays rapidly to zero as τ increases, the latter is almost constant in the range where $h(t)$ is not negligible. In Figure 4-9 a) the $h(t)$ function is plotted for a 10 second period, the function decays to zero in approximately 2 seconds, range of time for which

$a(t)$ on Figure 4-9 b) has change from 0.992 to 0.993 almost constant. Therefore, the process could be represented as a *slowly-varying uniformly modulated process.*

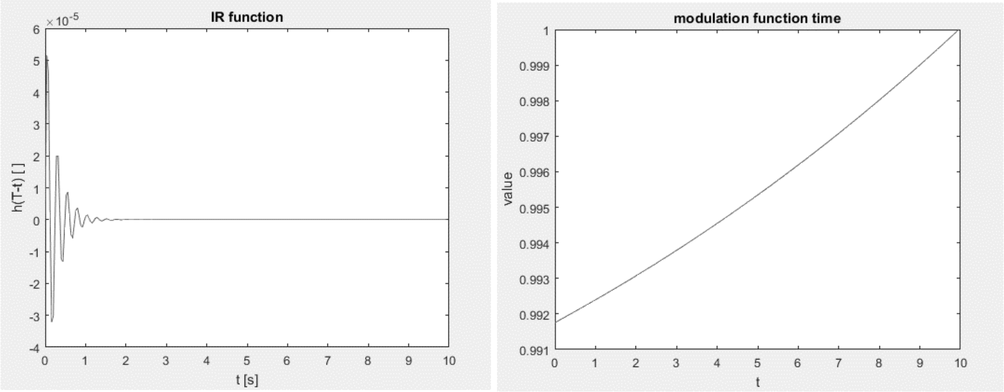

Figure 4-9: a) Impulse Response Function f_n=3.35hz ζ=2% b) amplitude modulating function

According to **§** Evolutionary frequency response function2.1.3.5, Equation 2-59**,**For *uniformly modulated process* the EVPSD of the response could be approximated to:

Equation 4-58

$$EVS_x(f,t) \cong |H(f)|^2 EVS_p(f,t)$$

Where $EVS_p(f,t)$

Equation 4-59

$$EVS_p(f,t) = |a(t)|^2 AD_o^2\, S_{v'}(f)$$

A typical spectrum of the response could be as that seen in the Figure 4-10.

The validity of the approximation for the *uniformly modulated process* (Equation 4-54) will be verified in **§** 4.6.1.

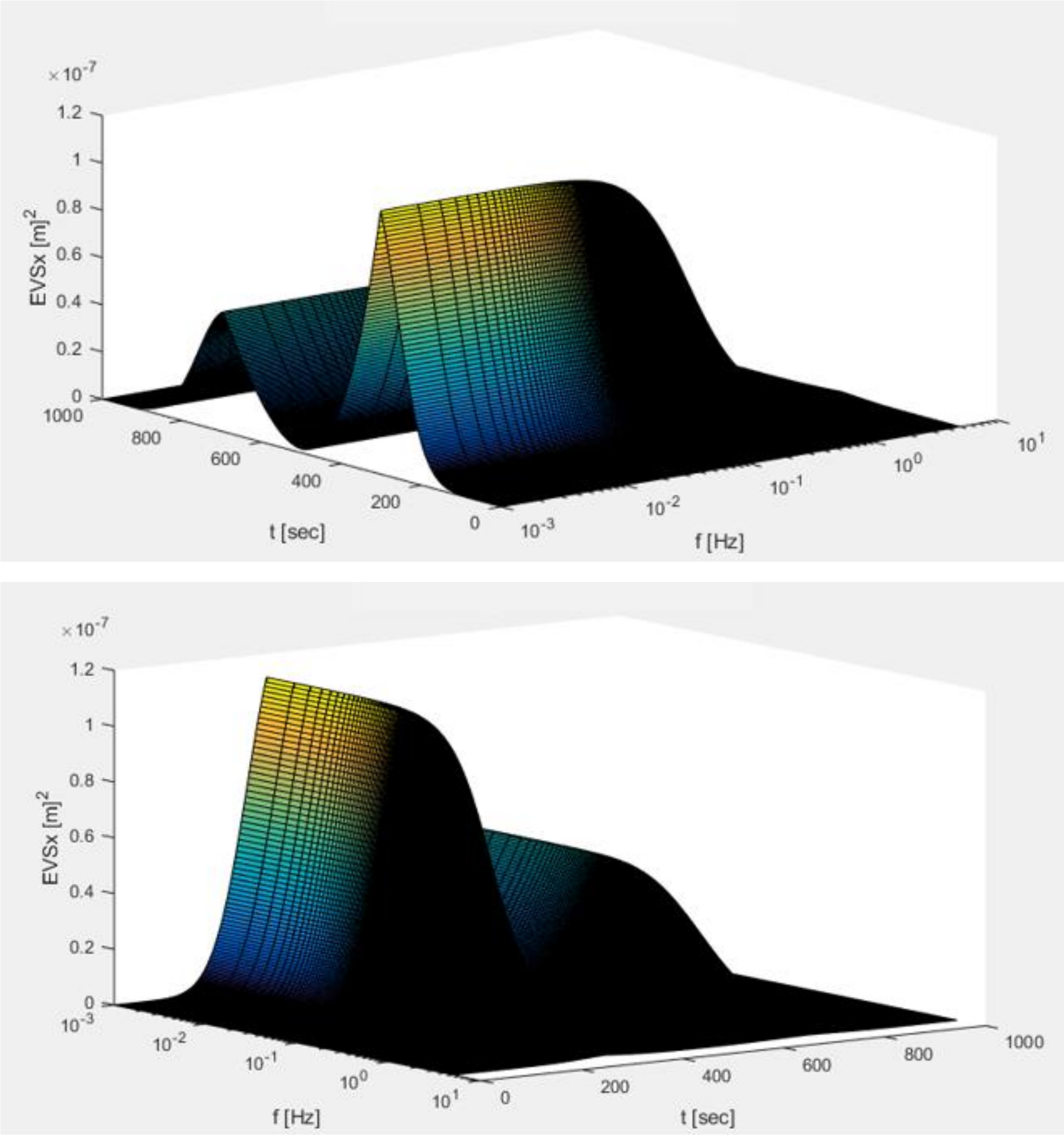

Figure 4-10: EVPSD of the displacement

4.6 Data consistency checks

4.6.1 Frequency response function

To verify the approximation introduced in Equation 4-58 a test was performed to check the validity of the same. The advantage of using the properties of the uniformly modulated process is to avoid the calculation of the convolution integral which can involve a huge computational effort, whenever numerically performed. It is important to clarify that the natural frequency of the system was set to be 0.5 [Hz] and the observation time within the test was set to be 200 [sec].

The test procedure consists in the comparison of the frequency response function computed with three different approaches. The objective is to highlight possible errors associated with the procedure, the algorithm and the numerical integration rule, to finally select the procedure which leads to the better description of the evolutionary frequency response function.

Approach 1

The first approach is the analytical evaluation of the frequency response function as provided in Equation 4-46. The evaluation of the *evolutionary frequency response function EFRF* is done according to **§** 2.1.3.5, Equation 2-60**,** for *slowly-varying uniformly modulated process.*

Equation 4-60

$$H(f,t) \cong |a(t)| * H(f)$$

Approach 2

The second approach consists in the numerical evaluation of the Fourier transform of the impulse response function as shown in Equation 4-47. Analogously, the time variance of the transfer function is added by taking the amplitude modulating function in the evaluation of it.

Equation 4-61

$$H_1\,(f,t) \cong |a(t)| * H_1(f)$$

Comparing the results of the two approaches, it is possible to evidence the error associated with the numerical evaluation of the integral Equation 4-47. Graphically the overlapping of both functions is given in Figure 4-11. The information shown in Figure 4-11 is a time section (t=152 sec) of the *EFRF* of the two approaches. The time interval used for the numerical evaluation of the integral (Equation 4-47) was 0.05 [sec]

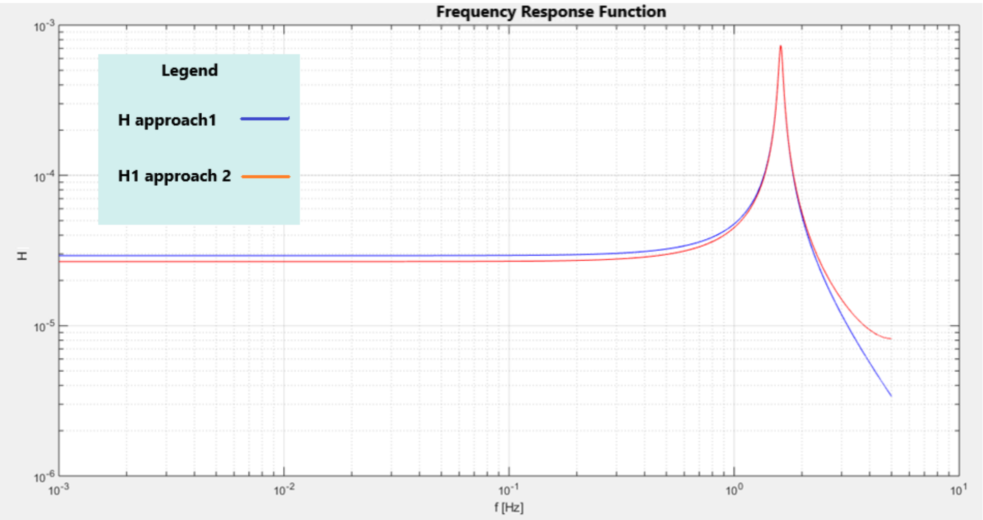

Figure 4-11. Graphic comparison of Transfer functions, t=152 [sec] dt=0.05[sec]

With the aim of reducing the numerical integration error in the process, the resolution of the analysis was incremented accounting for a time step of 0.01[sec]. This procedure leads to a more precise evaluation of the numeric integration. Once again there were plotted the evolutionary *EFRF* for both approaches in a fixed instant of time (t=152 sec), as expected the difference between both functions was considerably reduced. Therefore, it is possible to state that increasing the resolution reduces the difference between the EFRF, this property will be useful in a later step.

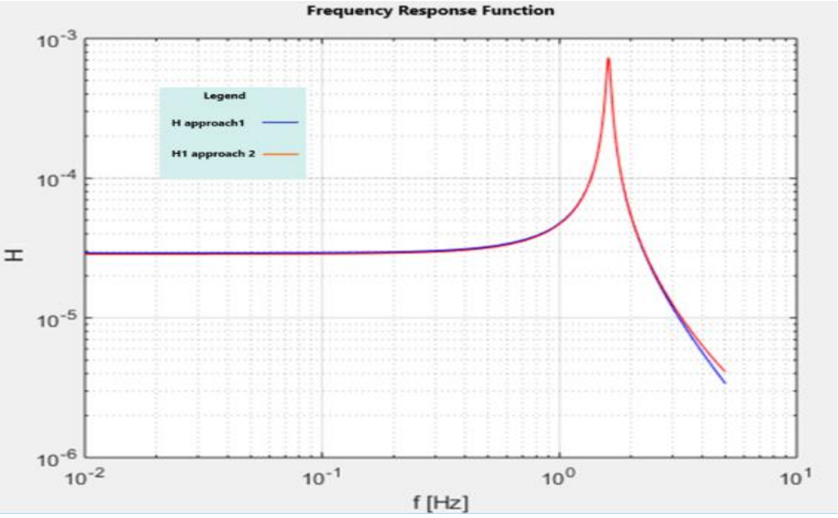

Figure 4-12: Graphical comparison, increased resolution, t=152 [sec]. dt=0.01[sec]

Approach 3

The third approach consists in a numerical evaluation of convolution integral between the impulse response function and the amplitude modulating function Equation 4-57.

The integral below was solved for every time and for every frequency.

Equation 4-62

$$H_2(f,t) = \left| \int_{-\infty}^{+\infty} a(t-\tau) * h(\tau) * e^{-i2\pi f\tau} d\tau \right|$$

In Figure 4-13 it is provide a graphical comparison of the three approaches for evaluating the *EFRF,* the time section plotted correspond to t=152 [sec] and the time step involved in the analysis was 0.2[sec].

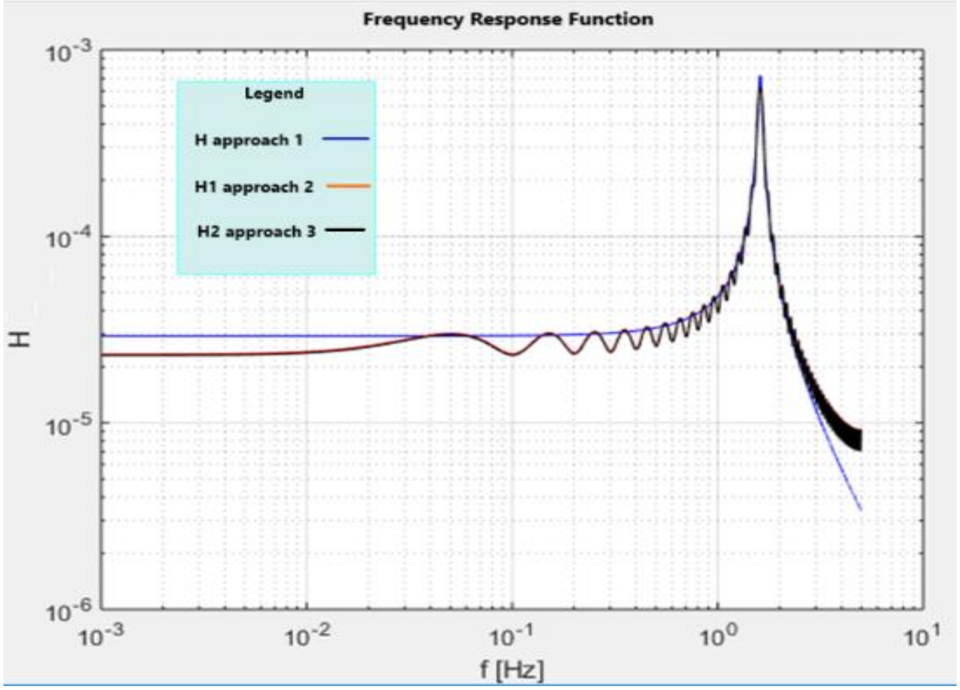

Figure 4-13: Comparison of FRF of the three approaches, t=152 [sec]. dt=0.2[sec]

Important comments must be done on the information shown in Figure 4-13. Since the *evolutionary-FRF* computed with approach 2 coincided with that of approach 3 there is an overlapping of the two functions and therefore it is possible to see only one of them. In addition, due to the computational effort involved in the process, the attempt shown in the figure was made with low frequency resolution.

Increasing the resolution to a time step of 0.1 [sec] it was possible to obtain the results reported in Figure 4-14.

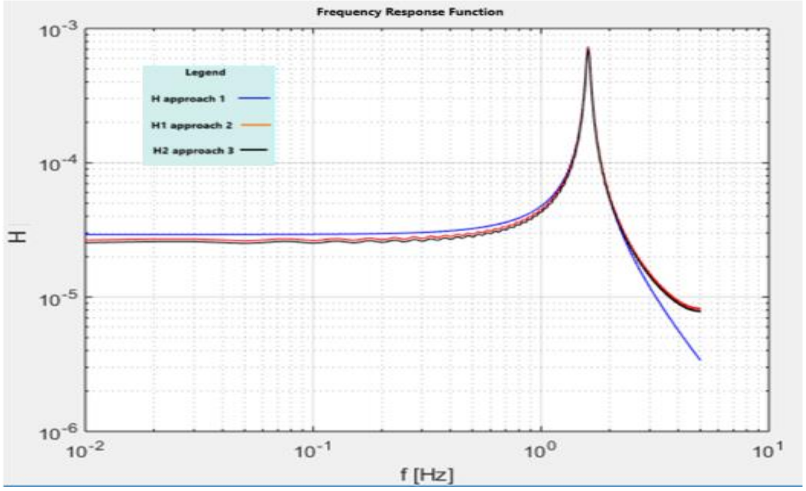

Figure 4-14: FRF comparison Increasing resolution, t=152 [sec] dt=0.1[sec]

Comparing the results of Figure 4-14 and Figure 4-13 is possible to see the tendency of reducing the error related to the numerical evaluation of the integrals i.e. there is convergence of the approaches associated with the increase in the resolution of the analysis.

It is possible to conclude that the evaluation of the *EFRF* with the three approaches, whether numerical or approximated gives similar results. Therefore, and for the sake of simplicity, it will be used in this study the approach #1 corresponding to the approximated evaluation of the *EFRF* by means of the properties of the *slowly-varying uniformly modulated process.*

Finally, it will be given the so-called surface plot of the *EFRF.* For both principal cases analytical (approach 1) and numerical (approach 3) the plots are registered in Figure 4-15 and Figure 4-16 respectively.

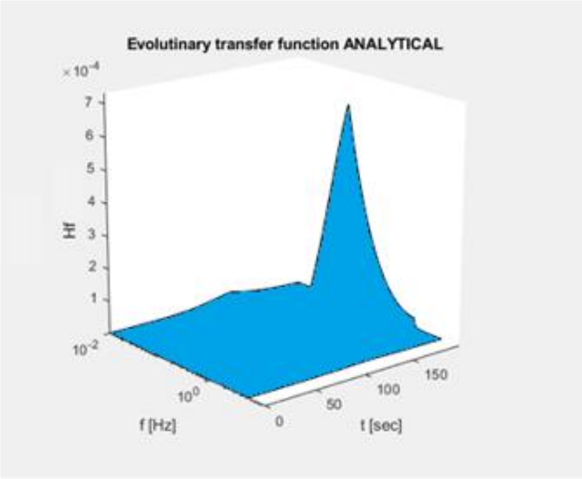

Figure 4-15: EFRF Analytical

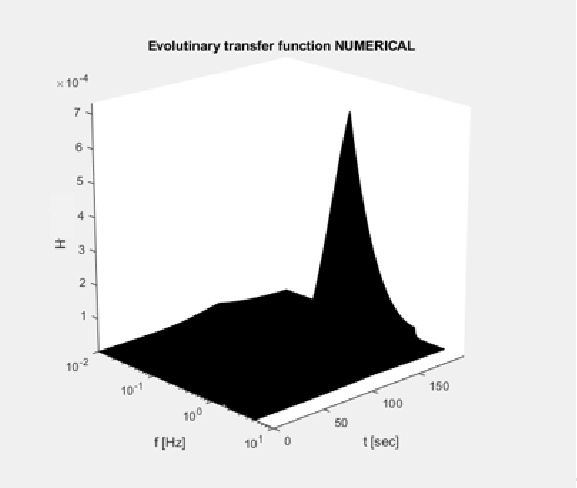

Figure 4-16: EFRF Function Numerical

Analyzing both images, it was possible to observe that the order of magnitude and the shape of both surfaces coincides.

4.7 Parametric Study: Rigid (High frequency) structures

4.7.1 Study of the variance

The frequency domain analysis is a useful tool for measuring the statistical spectral moments of the structural response. Therefore, a possible validation between time domain and frequency domain results can be done by the *study of variance* of the response computed with the two methods.

From the properties of the PSD function it is possible to obtain the RMS of a signal. Moreover, due to the definition made in the wind velocity decomposition, in which the slowly varying mean component was extracted from the signal leaving the turbulent component as a stochastic zero-mean process, it is possible to obtain directly the variance from the PSD.

The time-varying variance of the process could be computed for each time t_i, as follows:

Equation 4-63

$$\mathrm{\sigma f}^2_{x(t_i)} = \mathrm{RMS}_x - \mathrm{\mu}_x(=0) = \int_{-\infty}^{+\infty} EVS_x(f, t_i)df$$

On the other hand, the time domain analysis for the multiple Monte Carlo simulations give rise to a wide amount of data, that in general can be processed to obtain the statistical spectral moments of the response. Due to the non-stationarity and the loss of ergodicity in the random wind field, several realizations must be performed and integrated in the time domain by numerical approximations. To obtain an expression of the variance of the turbulent displacement response, comparable with that given in Equation 4-63 for frequency domain a procedure similar to than on Equation 4-64 was implemented for each step in the time domain. With N equal to the number of simulations, $\mathrm{\mu}_{(t_i,N)}$ the mean value of all the simulations at time instant t_i.

Equation 4-64

$$\mathrm{\sigma t}^2_{x(t_i)} = \sum_{i=1}^{N} \frac{(X_{(t_i,N)} - \mathrm{\mu}_{(t_i,N)})^2}{\mathrm{N}}$$

The results of the time-varying variance where compared after several examinations changing different parameters of the simulation. The study was aimed to highlight the difference between the two methods and its dependence on the structural and downburst features i.e. natural frequencies, stiffness and damping ratios and incoming wind fields.

4.7.2 Error Measurement

To define a metric or standardize the comparison on the variance of the structural response computed with the frequency domain and time domain analysis (Equation 4-63 and Equation 4-64 respectively), two different approaches were implemented. The first one is based on the difference of the peak response, while the second is based on the *normalized mean quadratic error* NRMSE.

The reference value for the SDOF analysis will be the frequency domain response since it was computed analytically. There was, however, the introduction of numerical integration for the evaluation of the variance since the computer code evaluates the integrals as discrete instead of continuous. On the other hand, the time domain analysis was performed numerically by means of the direct integration of the equations of motion.

The peak index provides a fast estimation of the comparison as it gives the ratio between the maximum value of the variance computed with the two analyses. The Equation 4-65 provides the computations needed to get this checking parameter. Due to its definition, this allows to obtain a target measure of the difference between the two approaches.

Equation 4-65

$$\text{Index} = \frac{max(\sigma \mathrm{t}_x{}^2)}{max(\sigma \mathrm{f}_x{}^2)}$$

The *root mean square error* RMSE was computed for each point inside the time discretization obtaining the total error involved in the numerical evaluation of the variance on time domain compared to that of the analytical variance of the response on the frequency domain. The error was computed as:

Equation 4-66

$$\text{RMSE} = \sqrt{\frac{\sum_1^N (\sigma \mathrm{f}_{x(ti)}{}^2 - \sigma \mathrm{t}_{x(ti)}{}^2)^2}{NT}}$$

With NT equal to the number of time discretization points.

The error was normalized with respect to the range of the reference variable i.e. the variance of the response computed in the frequency domain Equation 4-67.

Equation 4-67

$$\text{NRMSE} = \frac{RMSE}{Max\left(\sigma \mathrm{f}_{x(ti)}{}^2\right) - Min\left(\sigma \mathrm{f}_{x(ti)}{}^2\right)}$$

This type of error allows to measure how two signals differ from each other and therefore will give an accurate full measure of the comparison between the two approaches.

4.7.3 Canonical form of the equation of motion

To set the original parameters governing the equations of motion, the first step is to identify them. To do so, the equation of motion given in Equation 4-44 (*Dynamic*) should be taken into its canonic form to highlight the properties of its components. Starting from Equation 4-1 dividing by the mass.

Equation 4-68

$$\ddot{x}_d + \frac{c}{m}\dot{x}_d + \frac{k}{m}x_d = \frac{F(t)}{m}$$

Stablishing:

Equation 4-69

$$\begin{cases} F(t) = \overline{F_o} * f_t(t) \\ \overline{F_o} = \rho C_D A V_m \\ f_t(t) = a(t)^2 v'(t) \end{cases}$$

With $\overline{Fo}$ a *pseudo-static* component of the dynamic force and $f_t(t)$ a modulating function giving the time variation of the aerodynamic force.

The Equation 4-68 can be written as:

Equation 4-70

$$\ddot{x}_d + \frac{c}{m}\dot{x}_d + \frac{k}{m}x_d = \frac{\overline{F_o}}{m}f_t(t)$$

Replacing the expression of the natural frequency and damping coefficient from Equation 4-71 and Equation 4-72 on Equation 4-70 and taking into account that the associated *pseudo-static* component of the dynamic response is denoted as x_{do}. It is possible to write the canonical form of the equation of motion as Equation 4-73.

Equation 4-71

$$2\pi f_n = \omega_n = \sqrt{\frac{k}{m}}$$

Equation 4-72

$$c = 2 * \zeta * m * \omega_n$$

Equation 4-73

$$\ddot{x}_d + 2\zeta\omega_n\dot{x}_d + {\omega_n}^2 x_d = x_{do}\,{\omega_n}^2\, f_t(t)$$

With

$$x_{do} = \frac{\overline{F_o}}{k}$$

From the canonical form of the equation of motion Equation 4-73 it is possible to highlight that the governing variables are the damping ζ and the natural frequency ω_n.

4.7.4 Reference period of the downburst

A further development could be made for studying the dynamic sensitivity by introducing the reference period of the *slowly-varying mean* downburst. This reference period can be assessed from the mean velocity of the pointwise structure in the space already given in **§** 3.9.1 the downburst reference period T_{ref} will be given by the time window between the two peaks.

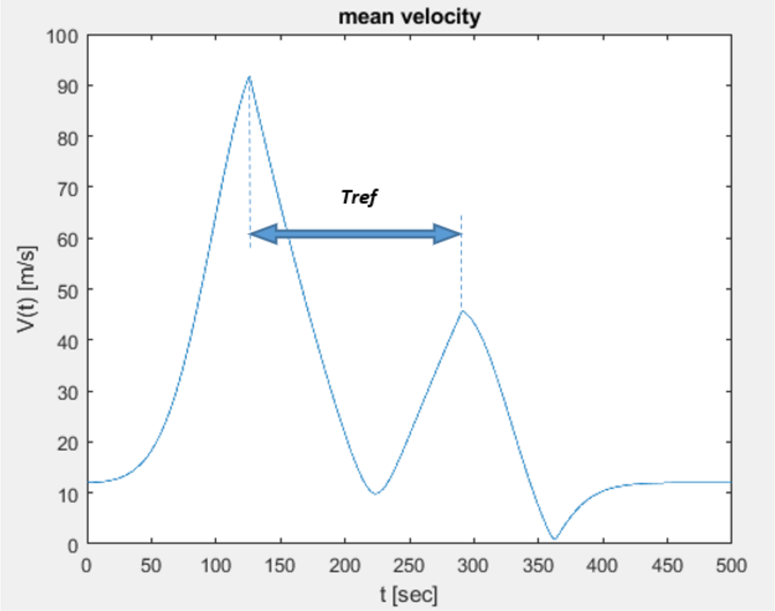

Figure 4-17: Mean velocity component

The dynamic sensitivity of the system is then given by the ratio of the natural period and the reference period:

Equation 4-74

$$\beta = \frac{T_n}{T_{ref}} << 1$$

Where T_n stands for the natural period:

Equation 4-75

$$T_n = \frac{2\pi}{\omega_n}$$

Supposing a fixed downburst wind velocity field the reference period will be constant and the dynamic sensitivity parameter β will be only function of the natural period. It is worth stressing that the slowly varying mean feature of the downburst is verified since the values that the β parameter can adopt are much lower than the unity.

4.7.5 Parameters and set

According to the latter definitions it is useful to parametrize the equation of motion based on the damping and the dynamic sensitivity. Therefore, two parameters will be introduced. C_m is going to be the parameter affecting the damping and C_b that of the dynamic sensitivity.

Equation 4-76

$$C_b = \frac{\beta}{\beta_b}$$

$$C_m = \frac{\zeta}{\zeta_b}$$

With $\beta_b \; and \; \zeta_b$ the basic values of the dynamic sensitivity and damping ratio for the analysis. Their values used for the analysis are given in Table 4-7.

For implementation reasons it will be used a Ck coefficient introduced directly on the stiffness of the system. Therefore, it is needed a relationship between the Ck stiffness coefficient and the Cb dynamic sensitivity coefficient.

Equation 4-77

$$C_k = \left[\frac{2\pi}{T_{ref}\; Cb\; \beta\; \omega_{n,b}}\right]^2 (a)$$

Replacing the β and $\omega_{n,b}$:

$$C_k = \left[\frac{1}{Cb}\right]^2 (b)$$

Where the base natural frequency, $\omega_{n,b}$ is that making C_k=1 when also C_b=1.

In total 2.000 Monte Carlo simulations for the downburst incoming wind field were performed, together with 10 variations of the C_b parameter and 9 variations of the C_m parameter. The equations of motion were numerically integrated 180.000 times and 90 analysis in frequency domain were performed to compare. The values of the parameters C_b and Cm are reported in Table 4-5 and Table 4-6 respectively.

The downburst reference period T_{ref} was 180 [sec], for the determination of the natural periods the structure data is given in **§** 4.7.6. It is important to highlight that the evaluation domain (natural periods and damping ratios) given in Table 4-5 and Table 4-6 was selected to test the methodology rather than provide a realistic application. A further study with structural parameters inside the reference values for flexible structures subject to wind actions will be provided in **§** 4.8.

Table 4-5: Values of the parameter Cb

Cb [-]	**Ck [-]**	**Natural period [sec]**	$\boldsymbol{\beta}$ **[-]**
0,0625	4	0,1546	0,000104
0,1875	2,30940	0,2034	0,000314
0,3125	1,7888	0,2312	0,000523
0,4375	1,5118	0,2514	0,000733
0,5625	1,3333	0,2678	0,000942
0,6875	1,20604	0,2815	0,001152
0,8125	1,10940	0,2935	0,001361
0,9375	1,03279	0,3042	0,001571
1,0625	0,97014	0,3139	0,001780
1,1875	0,917662	0,3228	0,001990

Table 4-6: Values of the parameter Cm

Cm [-]	**ζ [-]**
0,4	0,008
0,6	0,012
0,8	0,016
1	0,02
1,2	0,024
1,4	0,028
1,6	0,032
1,8	0,036
2	0,04

4.7.6 Structure input parameters

To develop the numerical values of the components in Equation 4-1, reference is herein made to the cross section shown in Figure 4-18, which corresponds to the structure on Figure 4-1. to obtain the values associated with the mass and the stiffness. The dynamic exciting force given by the wind filed can be computed according to Equation 4-10.

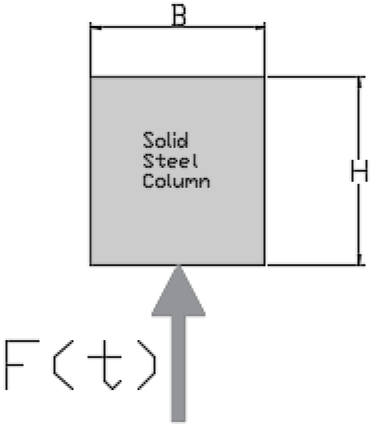

Figure 4-18: Cross section

The damping ratio is given in Equation 4-78, where Cm is a parameter controlling the damping ratio to control its effect over the response and ζ_b is the base damping ratio (given in Table 4-7).

Equation 4-78

$$\zeta = C_m * \zeta_b$$

The lumped mass is given by the half of the total mass of the system, computed as shown in Equation 4-79.

Equation 4-79

$$m = \frac{1}{2} * \rho_{steel} * B * H * L$$

With ρ_{steel} been the density of the material (7850 kg/m3) and B, H and L are the dimensions of the beam.

The stiffness on the other hand was computed as shown in Equation 4-80. Where the coefficient $C_{k,}$ will be used as control parameter for the development of a further parametric study and the base stiffness K_b will be that given by the horizontal movement of the beam.

Equation 4-80

$$k = C_k * K_b = C_k * 12\frac{EI}{L^3}$$

Where E is the elastic modulus of the material (210 Gpa) and I is the inertia of the square section.

The fundamental or natural frequency of the system correspond to the free vibration frequency of the structure and is computed according to Equation 4-81.

Equation 4-81

$$2\pi f_n = \omega_n = \sqrt{\frac{k}{m}} = 20.831\sqrt{C_k}[rad/s]\ or\ 3.315\sqrt{C_k}\ [hz]$$

The structural damping was determined in Equation 4-82.

Equation 4-82

$$c = 2 * \zeta * m * \omega_n$$

Table 4-7: Structure simulation parameters

Parameter	Symbol	Value	Unit
Base Damping ratio	ζ_b	2	*[%]*
Damping ratio	ζ	0.02 Cm	*[-]*
Mass	m	235	*[kg]*
Base Stiffness	k_b	$9.722x10^4$	*[N/m]*
Stiffness	k	$9.722x10^4\ Ck$	*[N/m]*
Circular natural frequency	ω_n	$20.831\sqrt{Ck}$	*[rad/sec]*
Natural frequency	f_n	$3.315\sqrt{Ck}$	*[hz]*
Base circular natural frequency	ω_{nb}	20.831	*[rad/sec]*
Damping coefficient	c	$196.228 * Cm * \sqrt{Ck}$	*[kg/s]*
Drag coefficient	C_D	2.1	*[-]*
Downburst reference period	T_{ref}	180	*[sec]*
Base Dynamic sensitivity	β_b	1.658x10^-3	*[-]*

4.7.7 Downburst input parameters

The parameters defining the downburst for this section of study will be the same as those used in **§** 3.9 for the generation of single point in space. Therefore, the slowly varying mean and the generic turbulent component are those already given in **§** 3.9.1 and **§** 3.9.2 respectively.

The input data for the downburst characteristics are given in Table 4-8.

Table 4-8: Downburst simulation parameters

PARAMETER	VALUE
Integral length scale L_v	34.6 [m]
Max. Radial velocity V_{max}	80 [m/s]
Track velocity Vt	12 [m/s]
Height of max velocity Z_{max}	67 [m]
Downburst diameter $D=r_{max}$	1000 [m]
Intial X_o	-2500 [m]
Initial y_o	150 [m]
Angle of tracking theta	0°

With a(t) defined as:

$$a(t) = \frac{\left|V_r(t)^2 + {V_t}^2 + 2 * V_r(t) * V_t * Cos\beta(t)\right|}{\max\left[V_r(t)^2 + {V_t}^2 + 2 * V_r(t) * V_t * Cos\beta(t)\right]}$$

With the provided input data and using the procedure of analysis in the time domain it was possible to evaluate the response. To give a graphical representation of the response, a generic output time history corresponding to a single generation can be seen in Figure 4-19. This contains the slowly varying equilibrium conditions and a random response to turbulent component.

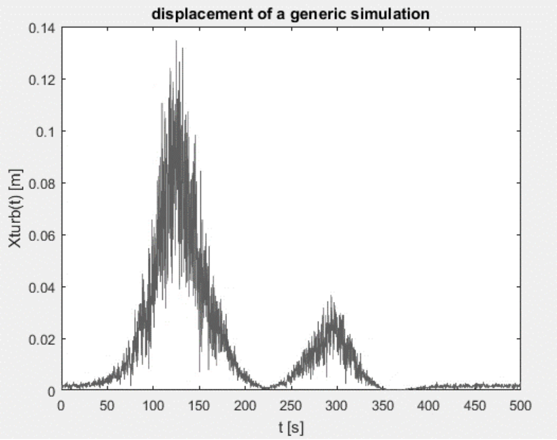

Figure 4-19: Displacement time history

4.7.8 Results

4.7.8.1 Peak Index of the variance

The peak index of the variance defined as **§** 4.7.2 Equation 4-65 is used to give a fast estimation of the difference between the variance computed by two approaches i.e. time domain approach and approximated frequency domain approach for slowly varying uniformly-modulated process. The results of this index evaluated for the complete set of parameters is given in Figure 4-20.

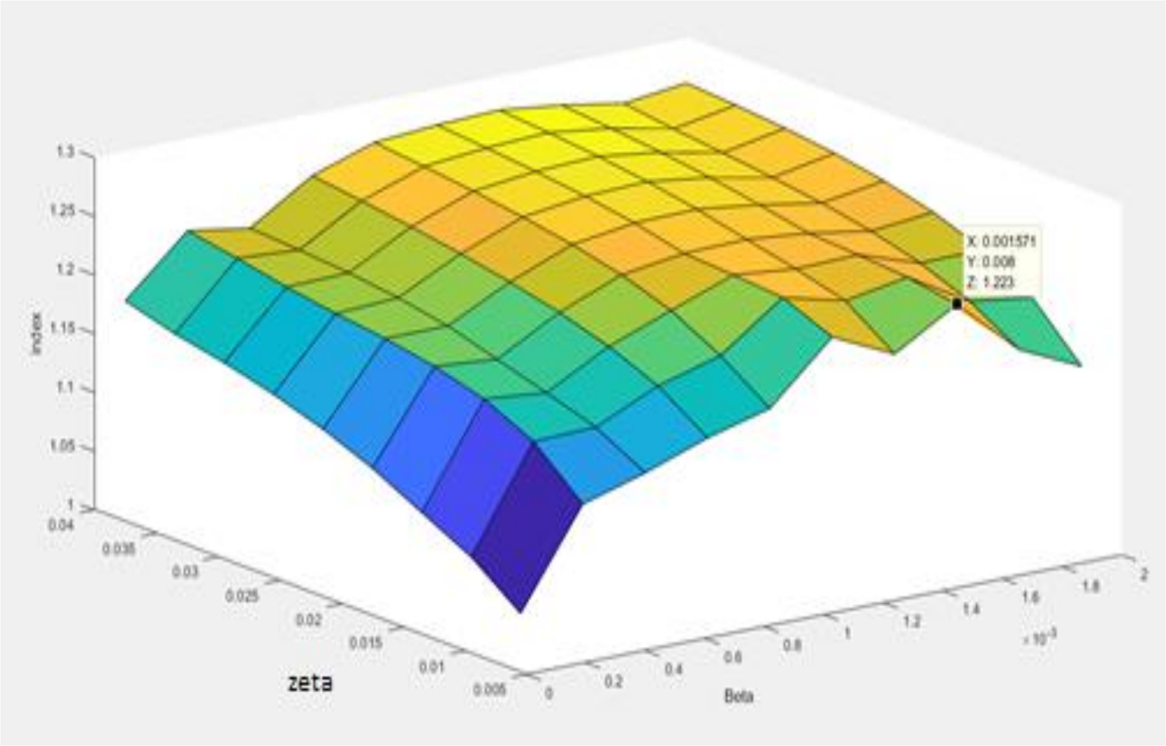

Figure 4-20: Peak Index of the variance comparison β(1.04x10-4 to 1.99x10-3) ζ(0.8 to 4 [%]).

The values that this indicator adopts vary between 1.0346 to 1.2709 for the pairs damping ratio and dynamic sensitivity of (0.8%, 1.04e-7) and (4%, 0.0014) respectively.

4.7.8.2 NRMSE of the variance

The *Normalized Root Mean Square* of the variance comparison defined as **§** 4.7.2 Equation 4-67 is used to give a full estimation of the difference between the variance computed by two approaches. The results of this index evaluated for the complete set of parameters is given in Figure 4-21.

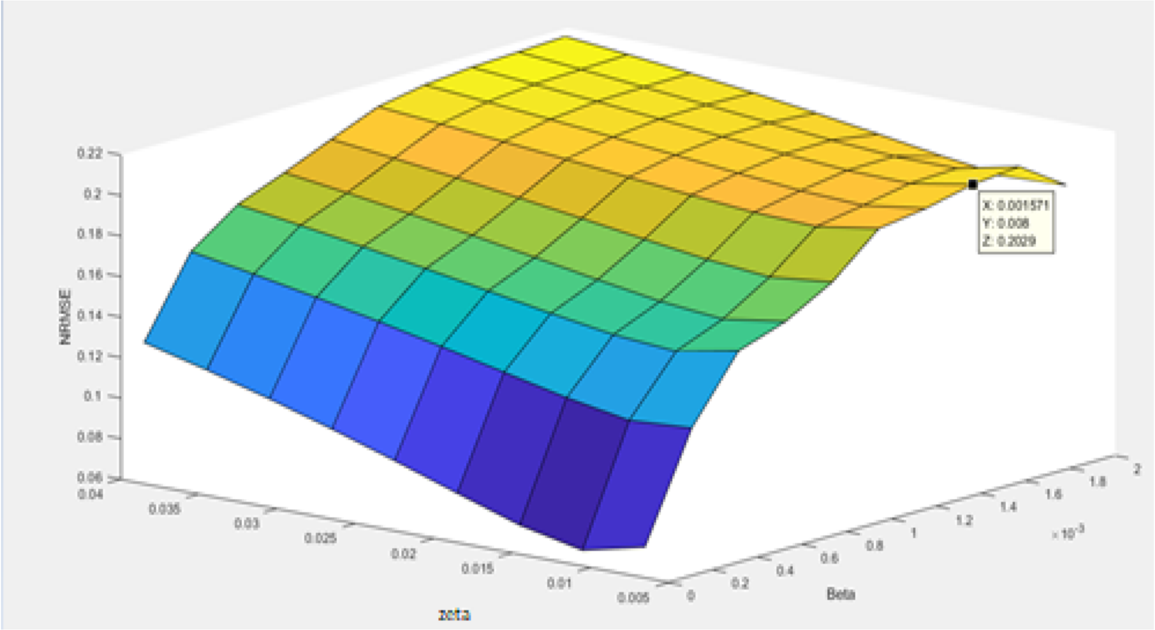

Figure 4-21: NRMSE of the variance comparison β(1.04x10-4 to 1.99x10-3) ζ(0.8 to 4 [%]).

The values that this indicator adopts vary between 0.0625 to 0.2162 for the pairs damping ratio and dynamic sensitivity of (1.2%, 1.04e-7) and (4%, 0.002) respectively.

4.7.8.3 Graphical comparison of the variance

The graphical representation of the case giving the lower value of the peak index is shown in Figure 4-22. It is possible to appreciate that both lines representing the variance computed in frequency domain (with the approximation for slowly varying uniformly modulated process) and in time domain show a very good agreement for this case. It can be observed that while the approximated frequency domain approach is characterized by a continuous smooth line in the variance, that one coming from the time domain shows a fluctuating behavior. It is worth to stress that the fluctuation in the latter approach is reduced by increasing the number of Monte Carlo simulations as explained in the section of the convergence check.

The graphical representation of the case giving the biggest value of the peak index is shown in Figure 4-23. It is possible to appreciate that even though both functions present a similar time structure i.e. time of the peaks and the minimums, the values of the variance of the time domain approach are greater than those coming from the approximated frequency domain. Showing a dependence of the peak index on the natural period and damping ratio.

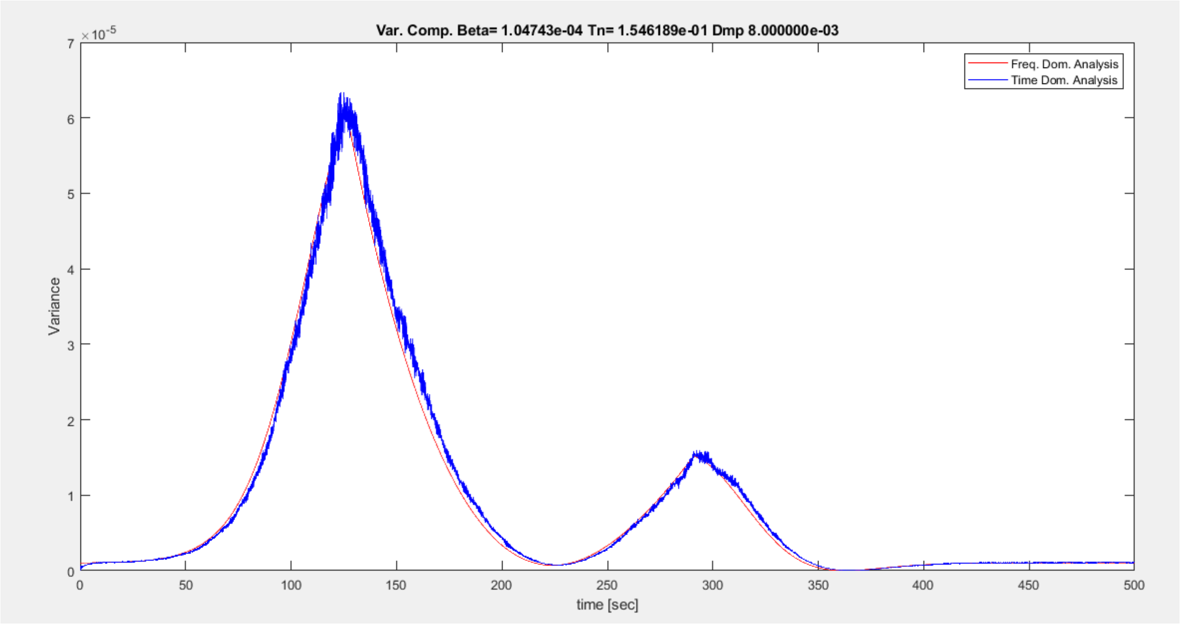

Figure 4-22: Graphical comparison of the variance β=1.04e-4 ζ=0.8%

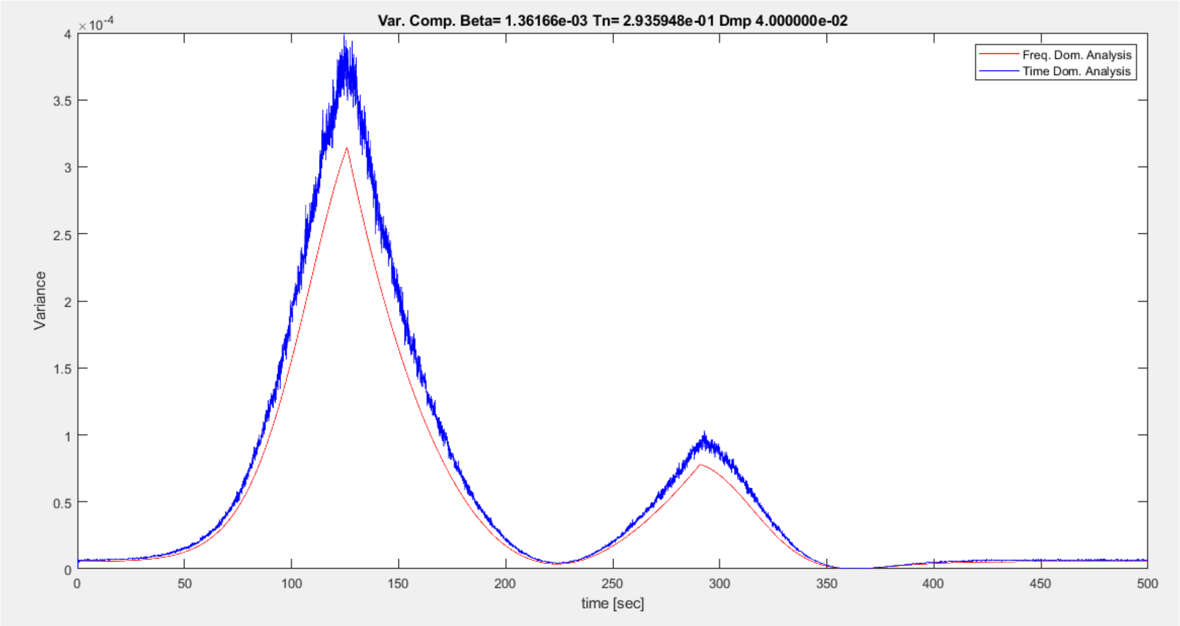

Figure 4-23: Graphical comparison of the variance β=1.36e-3 ζ=4%

The variation of the peak index inside the domain of study is close to 23%.

The graphical representation of the case giving the lower value of the *normalized root mean squared error* is shown in Figure 4-24. As in the case of Figure 4-22, the result of the analysis by the two approaches in time and frequency showed to be consistent evidencing a good matching between the variance calculated with the two methods. However, for the case giving the greatest value of the NRMSE (shown in Figure 4-25) the similarities of both responses differ, reporting an increase of the variance coming from the time domain approach compared with that of the aproximated frequency domain.

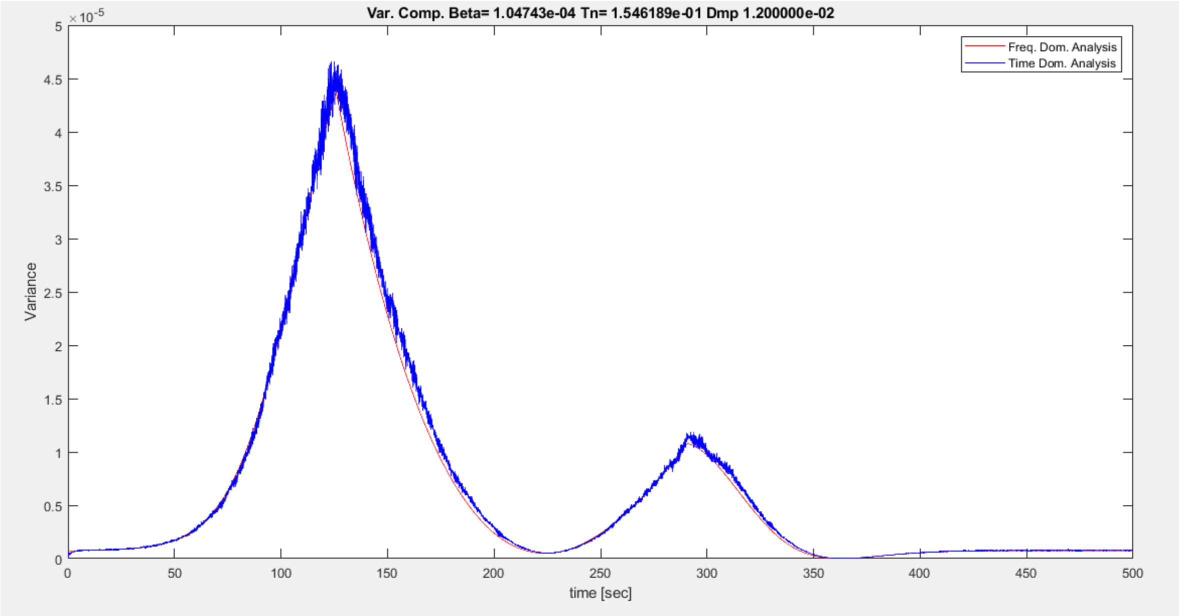

Figure 4-24: Graphical comparison of the variance β=1.04e-4 ζ=1.2%

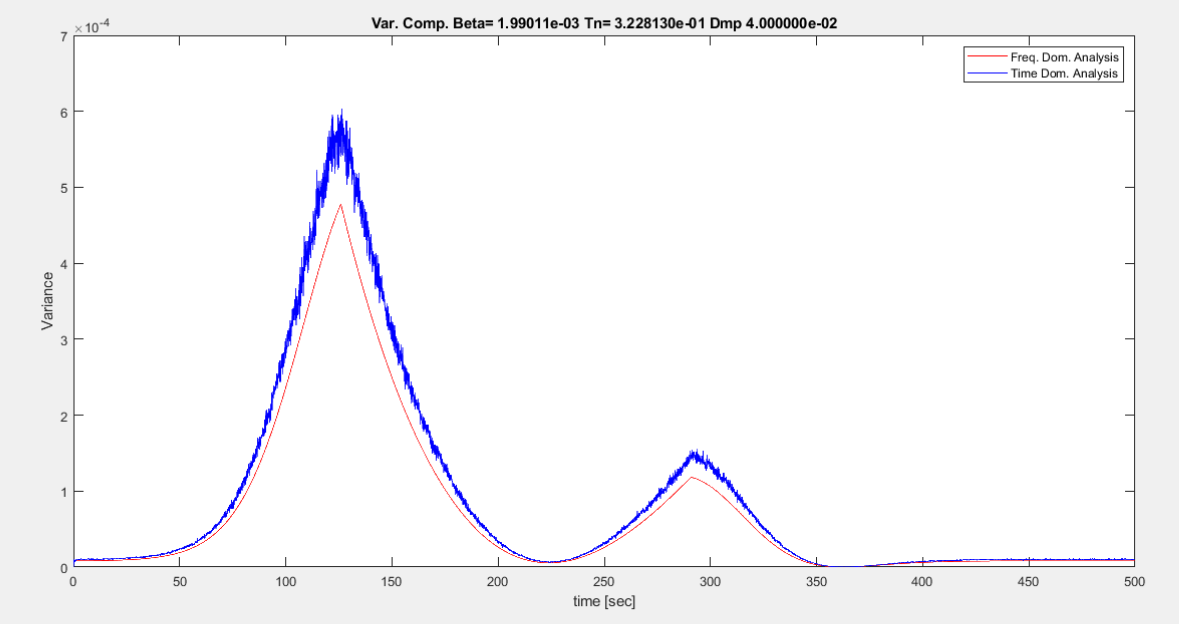

Figure 4-25: Graphical comparison of the variance β=1.99e-3 ζ=4%

The variation of the NRMSE inside the domain of study is close to 15%.

4.7.8.4 Monte Carlo Convergence Check

With the purpose of checking the consistency of the Monte Carlo simulations a convergence test was performed. The test consisted in the revision of the statistical properties of the response parameters obtained in the time domain by incrementing the number of simulations.

The value of peak of the variance by increasing the number of simulations with a fixed value of the natural period of 0.1546 [sec] and damping ratio ζ of 2% is shown in Figure 4-26.

From the figure it is possible to appreciate that the peak value of variance for this case is converging to a value of 3.268e-5 from 1.600 simulations.

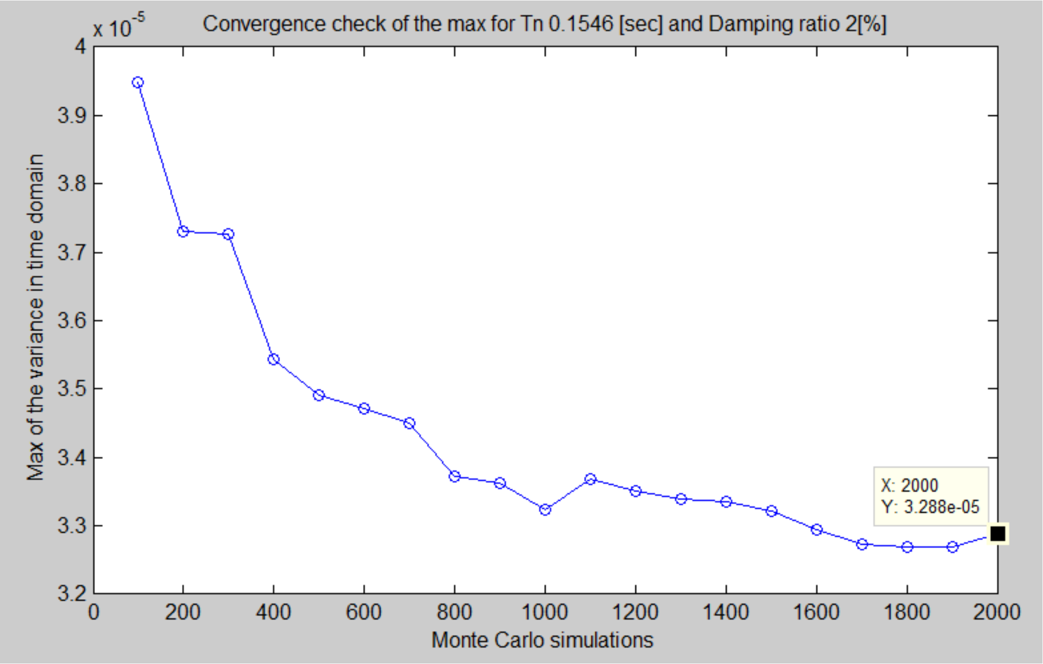

Figure 4-26: Convergence check for maximum value of variance in time domain

The value of the mean of the variance by increasing the number of simulations with a fixed value of the natural period of 0.1546 [sec]and damping ratio ζ of 2% is shown in Figure 4-27.

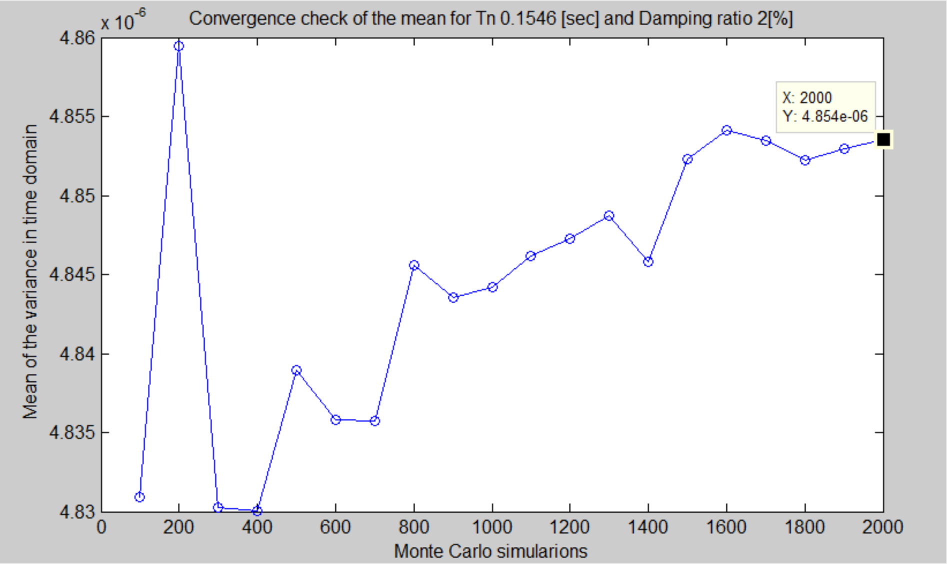

Figure 4-27: Convergence check for mean value of variance in time domain

From the figure it is possible to appreciate that the mean value of variance for this case has not yet converge at 2.000 simulations. However, the slope at the 2.000 simulations is close to be horizontal arriving to a value about 4.854e-6.

The value of the index parameter comparing the variance from the time domain analysis with that of the approximated frequency domain by increasing the number of simulations with a fixed value of the natural period of 0.1546 [sec]and damping ratio ζ of 2% is shown in Figure 4-28.

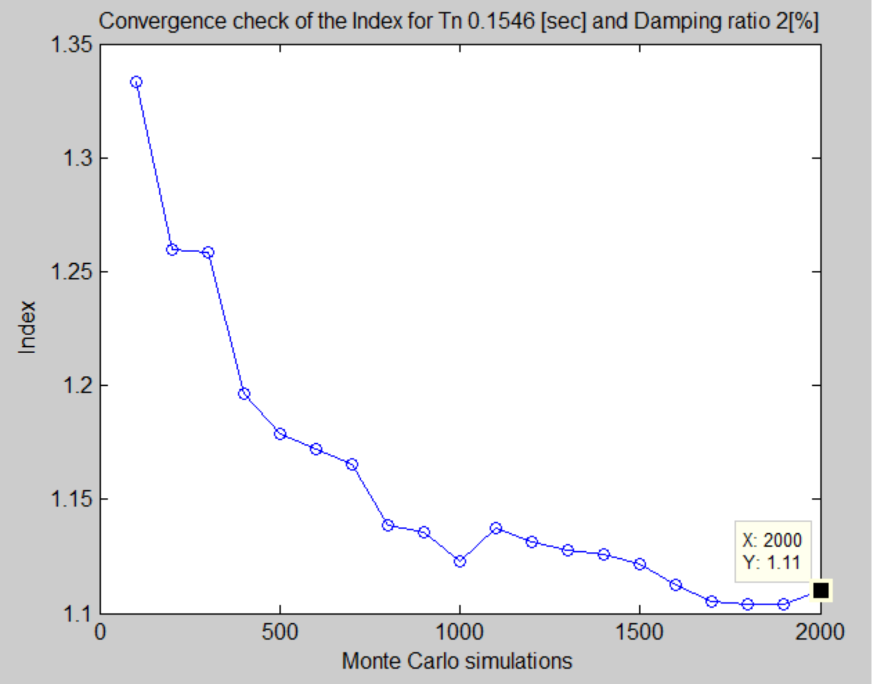

Figure 4-28: Convergence check for Index parameter of the comparison

From the figure it is possible to appreciate that the index parameter of the comparison for this case is converging to a value of 1.11 from 1700 simulations.

The value of the NRMSE comparing the variance from the time domain analysis with that of the approximated frequency domain by increasing the number of simulations with a fixed value of the natural period of 0.1546 [sec] and damping ratio ζ of 2% is shown in Figure 4-29.

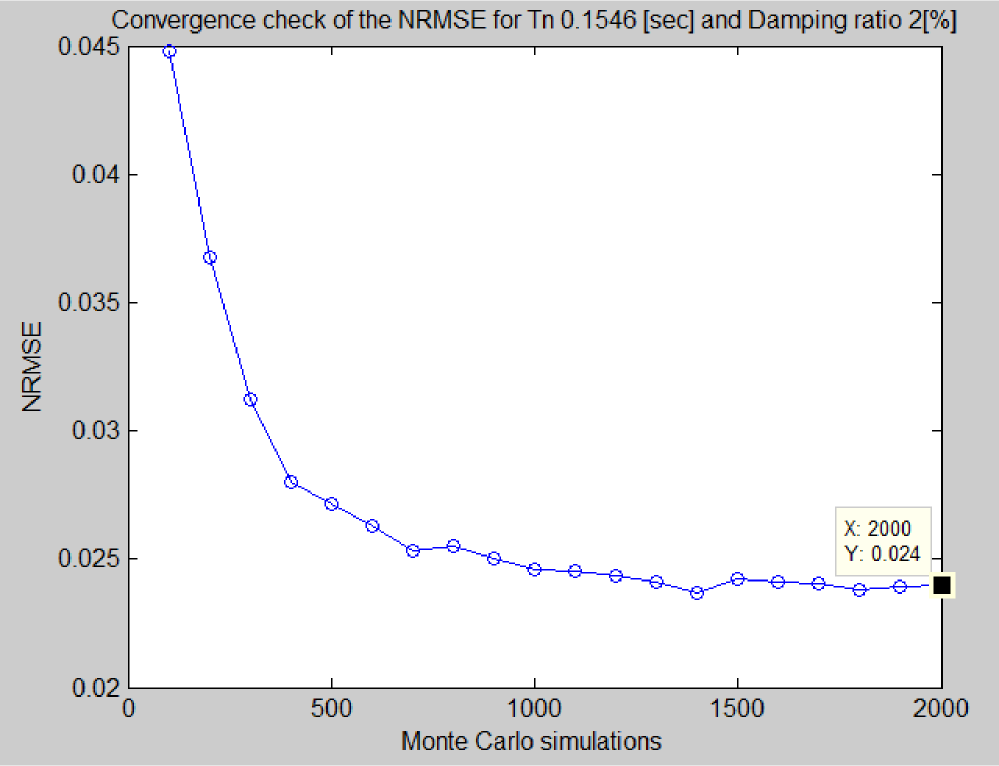

Figure 4-29: Convergence check for NRMSE of the comparison.

From the figure it is possible to appreciate that the NRMSE of the comparison for this case is converging to a value of 0.024 from 1.000 simulations.

4.7.9 Conclusions

The development of the parametric study showed a correspondence between the response coming from the time domain analysis and that coming from the approximated frequency domain analysis (for slowly varying uniformly modulated process) depend on the structural parameters i.e. natural frequencies (periods) and damping ratios.

Inside the domain of study, the ratio between the peak of the variance vary from 1.0346 to 1.2709 corresponding to a difference of 3 to 27%. On the other hand, the NMRSE went from 0.0625 to 0.2162 corresponding to 6 to 21%. It is worth stressing that both parameters agree in the order of magnitude of the difference between the two before-mentioned approaches.

The range of the peak index is close to 24%, while that of the NMRSE is 15%. This fact evidences that the incongruency in the variance of the response computed with the time domain method compared to that of the approximated frequency domain is concentered in the peaks rather than the entire development of the signals.

The possible explanations for the difference could be ascribed to the approximation of the evolutionary frequency response function for the *slowly varying uniformly modulated* process in the frequency domain approach. It is recommended to extend the study with the evaluation of the convolution integral for the *EFRF*. This case will be further developed in the section 4.8.3 of the present document.

This discrepancy, however, could not be attributed to the statistic population of the random variable. It is important to highlight that the convergence test of the Monte Carlo simulations showed that the maximum value of the variance coming from the time domain analysis, the peak index and the NMRSE are converging to 3.268e-5 [m2], 1.11 [-] and 0.024 [-] respectively.

The methodology was tested. However, to completely assess the comparison between the frequency and time domain approaches it is important to extend the study for structures with natural frequencies and damping ratios inside the reference values for flexible structures submitted to wind actions.

4.8 Parametric Study: Flexible (Low frequency) structures

With the aim of comparing the time domain approach (proposed in **§** 4.3 Time domain analysis) with the frequency domain approach (proposed in **§** 4.5) for the case of flexible structures subjected to downburst wind outflows, It will be performed a study similar to **§** 4.7 with different input parameters.

4.8.1 Parameter set

The parameters input data is given in Table 4-9 and table 4-10.

Table 4-9: Values of the parameter Cb

Cb [-]	**Ck [-]**	**Tn,Natural period [sec]**
6,839	0,382	0.5
109,322	0,095	1
68348	0,0038	5
1093546	0,000956	10

Table 4-10: Values of the parameter Cm

Cm [-]	**ζ [-]**
0,05	0,001
0,25	0,005
0,5	0,01
0.75	0,015

While the structural input parameters are reported in Table 4-11, the downburst parameters are reported in Table 4-12.

Table 4-11: Structure simulation parameters

Parameter	**Symbol**	**Value**	**Unit**
Base Damping ratio	ζ_b	2	*[%]*
Damping ratio	ζ	0.02 Cm	*[-]*
Mass	m	235	*[kg]*
Base Stiffness	k_b	$9.722x10^4$	*[N/m]*
Stiffness	k	$9.722x10^4\ Ck$	*[N/m]*
Circular natural frequency	ω_n	$20.831\sqrt{Ck}$	*[rad/sec]*
Natural frequency	f_n	$3.315\sqrt{Ck}$	*[hz]*
Base circular natural frequency	ω_{nb}	20.831	*[rad/sec]*
Damping coefficient	c	$196.228 * Cm * \sqrt{Ck}$	*[kg/s]*
Drag coefficient	C_D	2.1	*[-]*
Downburst reference period	T_{ref}	180	*[sec]*
Base Dynamic sensitivity	β_b	1.658x10^-3	*[-]*

Table 4-12: Downburst simulation parameters

PARAMETER	**VALUE**
Integral length scale L_v	34.6 [m]
Max. Radial velocity V_{max}	80 [m/s]
Track velocity Vt	12 [m/s]
Height of max velocity Z_{max}	67 [m]
Downburst diameter $D=r_{max}$	1000 [m]
Intial X_o	-2500 [m]
Initial y_o	150 [m]
Angle of tracking theta	0°

4.8.2 Results

4.8.2.1 *Peak Index of the variance*

The peak index of the variance defined as **§** 4.7.2 Equation 4-65 is used to give a fast estimation of the difference between the variance computed by two approaches, i.e. time domain approach and approximated frequency domain for slowly varying uniformly modulated process. The results of this index evaluated for the complete set of parameters is given in Figure 4-30.

The results of the peak index are in the order of 10 to 40% difference between the variances in the range of natural periods between 0.5 [sec] and 1 [sec]. For the cases of 5 [sec] and 10 [sec] of natural periods the peak of the variance in the frequency domain seems to be greater than that of the time domain.

4.8.2.2 *NRMSE of the variance*

The *Normalized Root Mean Square* of the variance comparison defined as **§** 4.7.2 Equation 4-67 is used to give a full estimation of the difference between the variance computed by two approaches. The results of this index evaluated for the complete set of parameters is given in Figure 4-31.

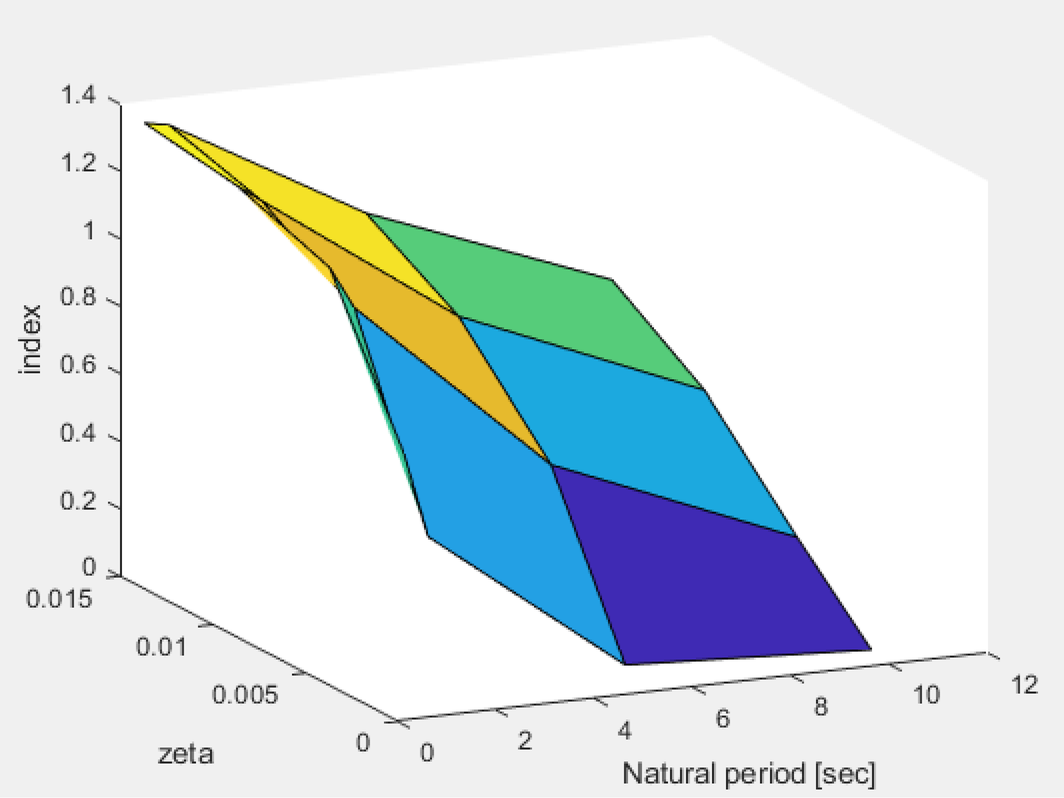

Figure 4-30: Peak Index of the variance comparison Tn(0.5 to 10) ζ(0.1 to 1.5 [%]).

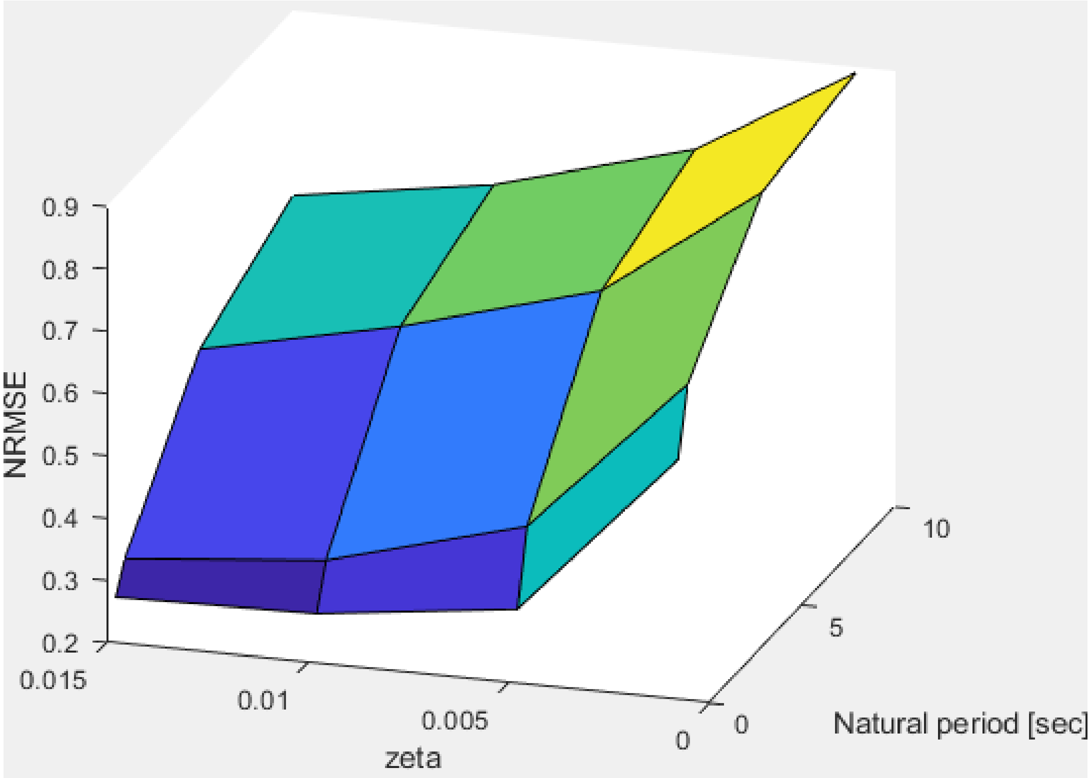

Figure 4-31: NRMSE of the variance comparison Tn(0.5 to 10) ζ(0.1 to 1.5 [%]).

The *NRMSE* seems to behave in the same order of magnitude of the peak index i.e. 10 to 40% for *Tn* between 0.5 and 1[sec]. In addition, it increases for natural periods of 5 and 10[sec], evidencing a remarkable difference between the two approaches when the resonant response is excited.

4.8.2.3 Graphical comparison of the variance

For natural periods of 0.5 [sec] there is remarkable difference between the two approaches for damping ratio of 0.1%. By increasing the damping ratio, it is possible to observe that the fit between both approaches improves, as it can be observed from Figure 4-32 to Figure 4-35.

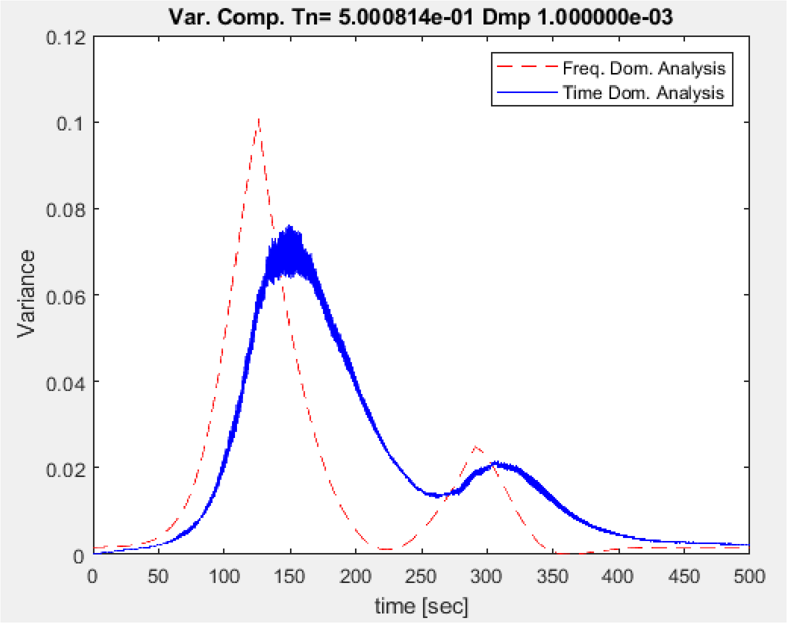

Figure 4-32:Var. Comp. Tn=0.5 sec ζ=0.1%

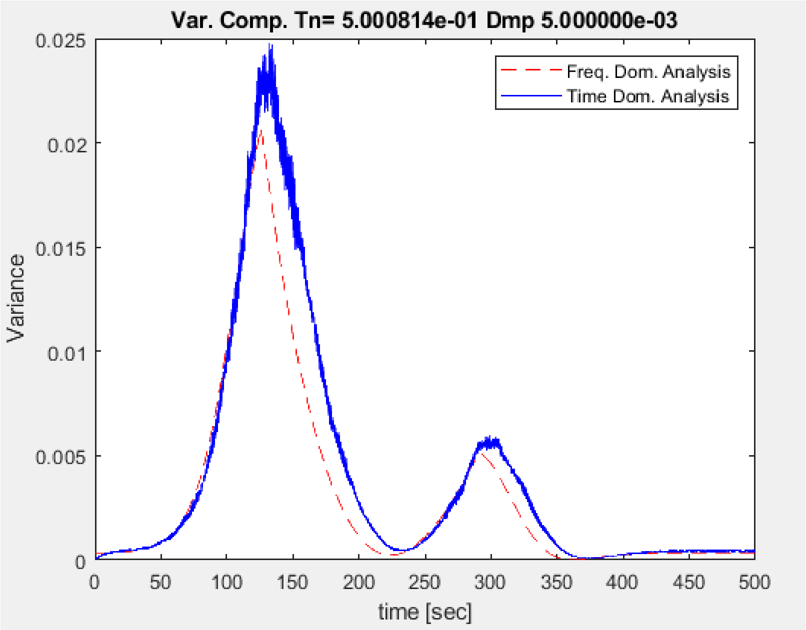

Figure 4-33:Var. Comp. Tn=0.5 sec ζ=0.5%

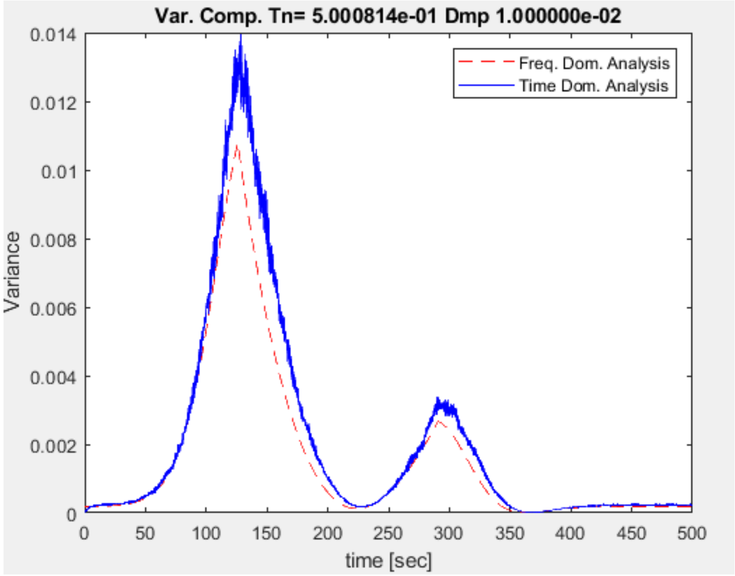

Figure 4-34:Var. Comp. Tn=0.5 sec ζ=1%

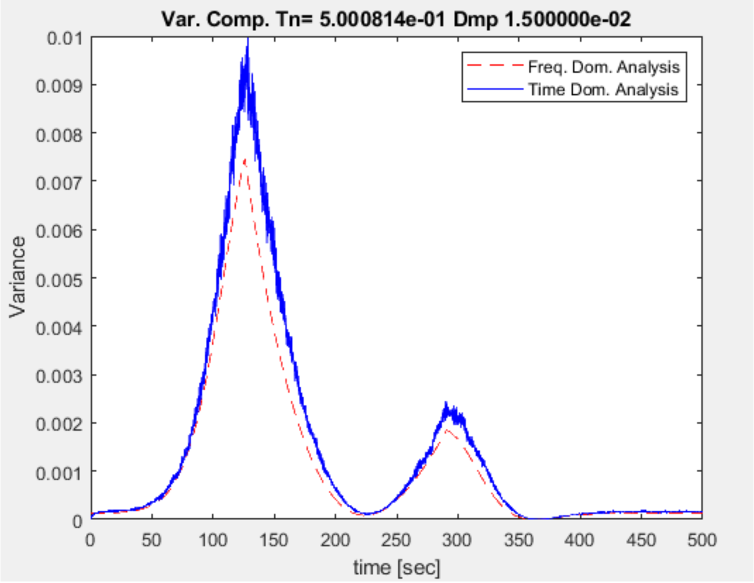

Figure 4-35:Var. Comp. Tn=0.5 sec ζ=1.5%

For natural period of 1 [sec] it is observed a similar behavior compared with 0.5 [sec] by increasing the damping ratio. The variance comparison for the different cases is given from Figure 4-36 to Figure 4-39.

It is important to state that the fit of the variance of the two approaches for both natural periods (1 and 0.5 sec) seems to be in the same order and it could be also verified with the analysis of the error indicators of Figure 4-30 and Figure 4-31 (peak index and NRMSE).

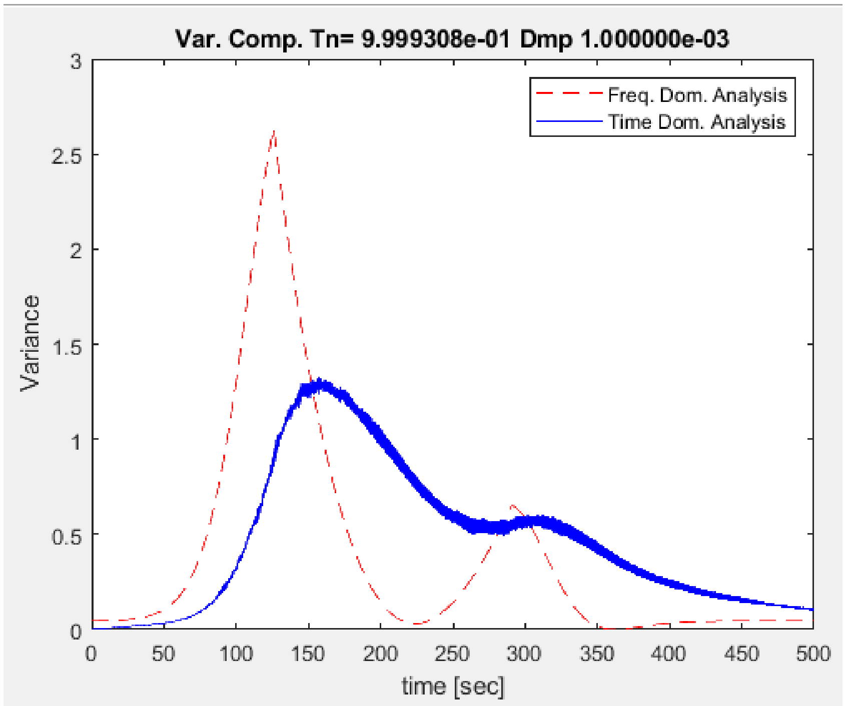

Figure 4-36:Var. Comp. Tn=1 sec ζ=0.1%

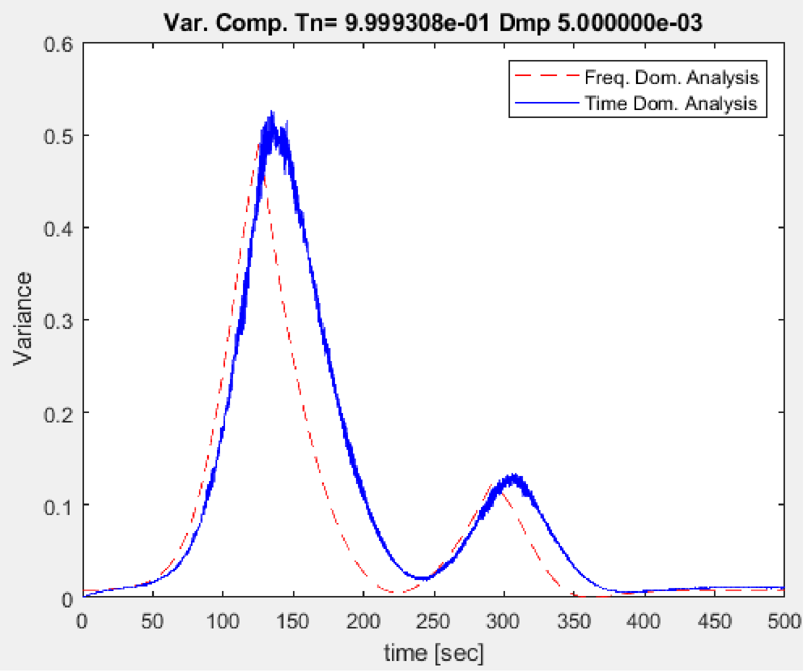

Figure 4-37:Var. Comp. Tn=1 sec ζ=0.5%

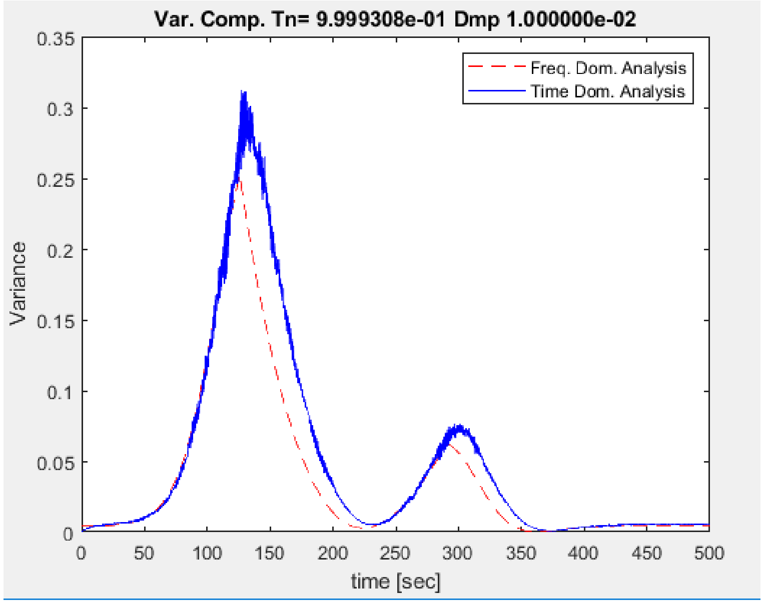

Figure 4-38:Var. Comp. Tn=1 sec ζ=1%

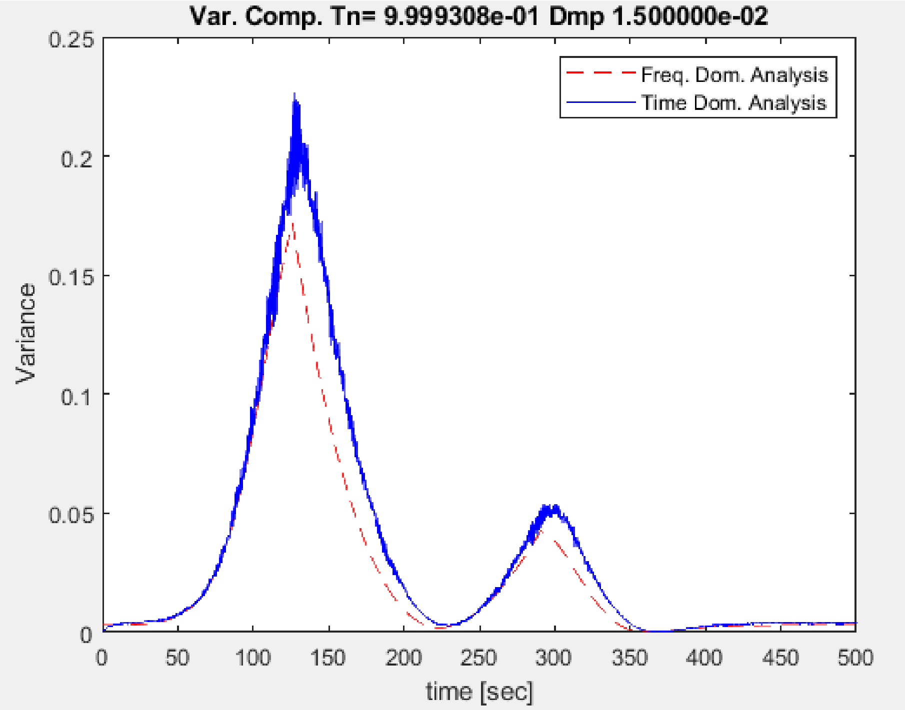

Figure 4-39:Var. Comp. Tn=1 sec ζ=1.5%

With the analysis of the first two natural periods it has been exposed the dependency of the results on the damping ratio. As it can be seen from the figures, for damping ratios of 0.5% and superior the variance computed with the approximate frequency domain approach coincides with that of the time domain. Therefore, it is possible to state that the reliability of the results obtained with the approximate frequency domain approach is not guaranteed for damping ratios close to 0.1%.

For natural periods of 5 and 10 [sec] the associated natural frequencies are 0.2 and 0.1 [Hz] respectively. If reference is made to the Von Karman spectrum in Figure 4-40, it possible to see that the natural frequencies fall inside the range where the wind turbulence signal has more associated energy. Therefore, the response is governed by the resonant component.

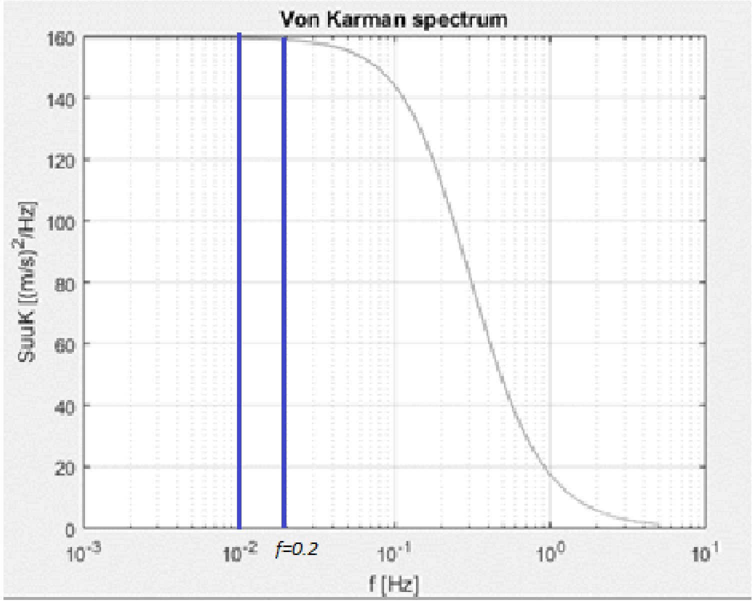

Figure 4-40:Von Karman spectrum

In Figure 4-41 and Figure 4-42 there are reported the cases of resonant response with low damping condition with natural periods of 5 and 10 [sec] respectively and damping ratio of 0.1%. From the figures it is possible to verify a remarkable difference between the two approaches (approximate frequency domain and time domain) as evidenced from the analysis of the error indexes (Figure 4-30 and Figure 4-31).

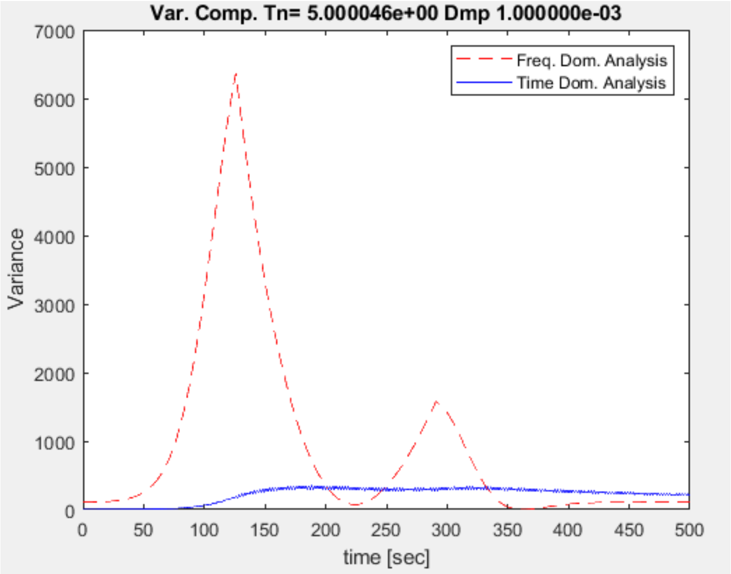

Figure 4-41:Var. Comp. Tn=5 sec ζ=0.1%

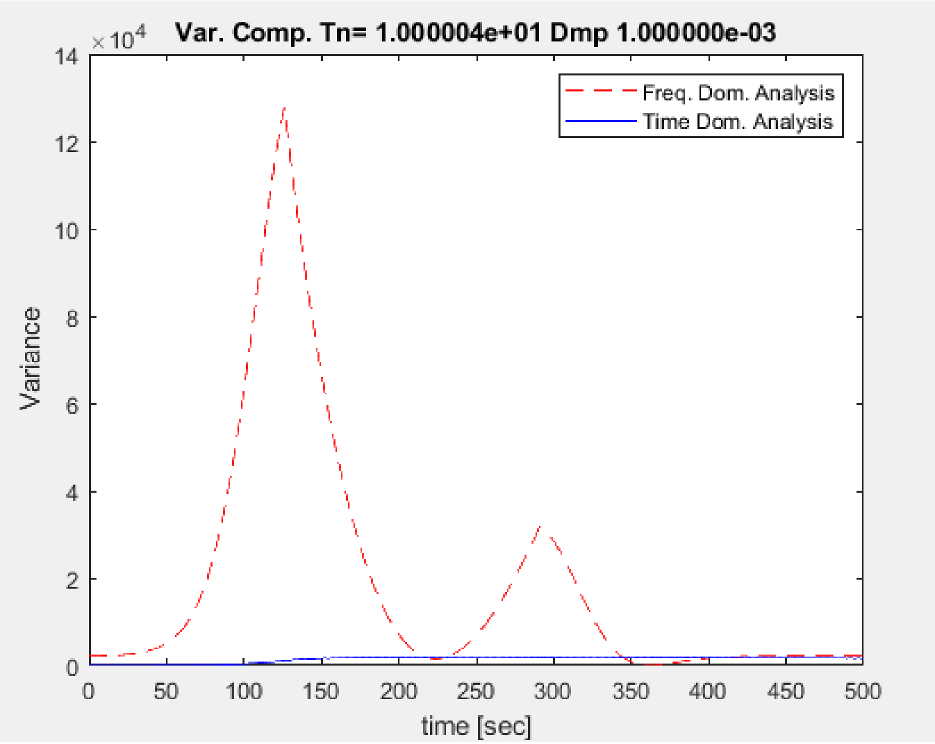

Figure 4-42:Var. Comp. Tn=10 sec ζ=0.1%

By increasing the damping, the difference of the two signals tend to reduce. The result can be seen from Figure 4-43 to Figure 4-46.

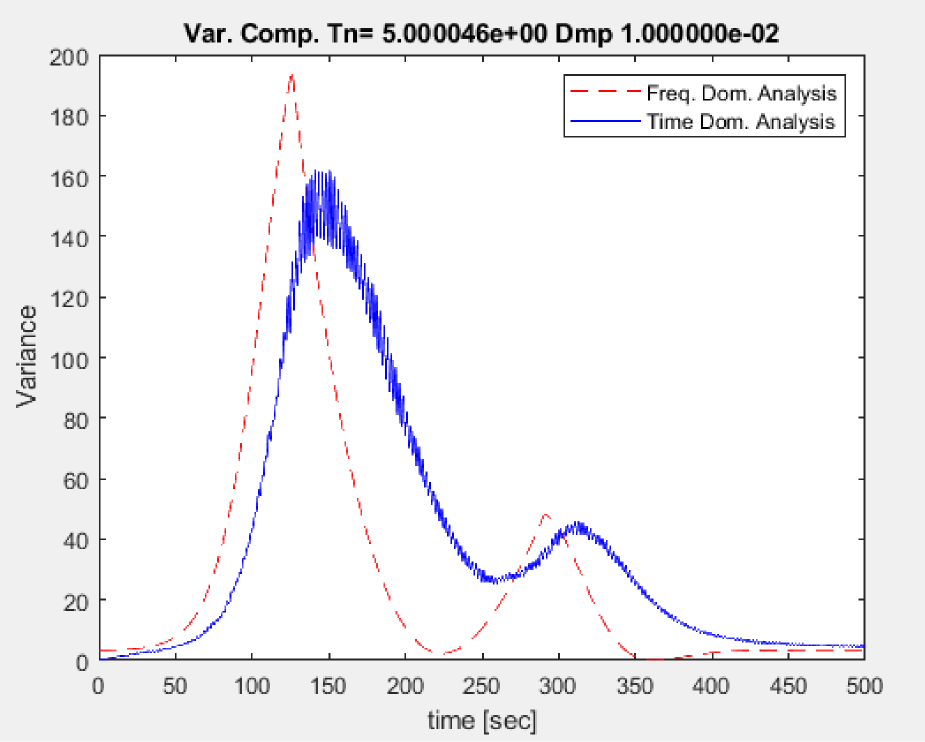

Figure 4-43:Var. Comp. Tn=5 sec ζ=1%

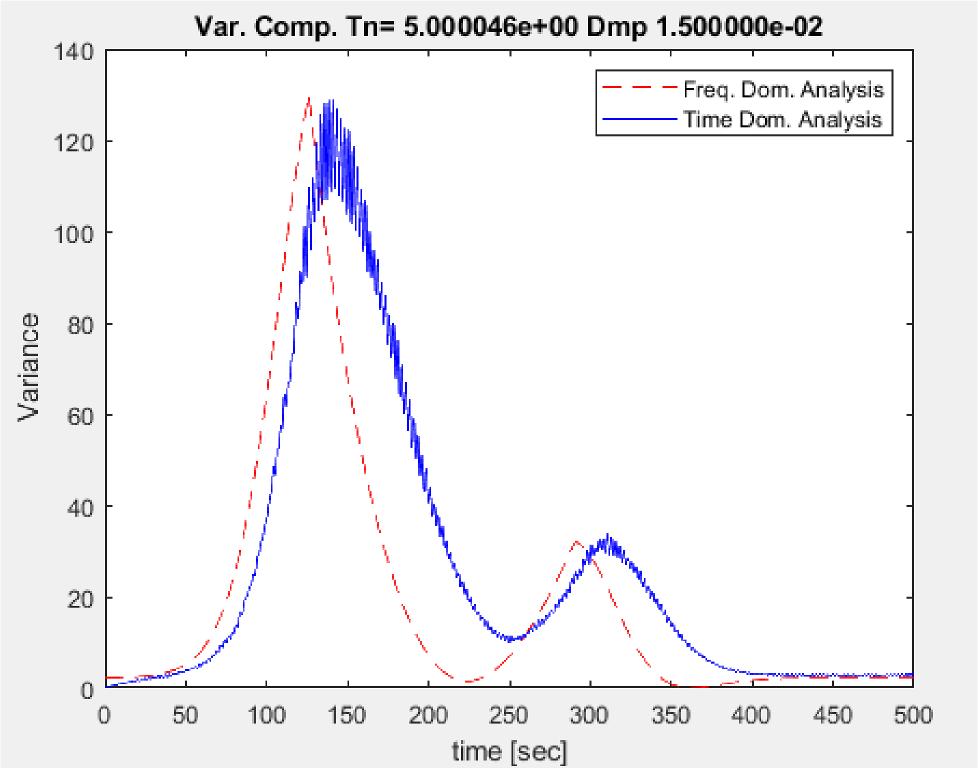

Figure 4-44:Var. Comp. Tn=5 sec ζ=1.5%

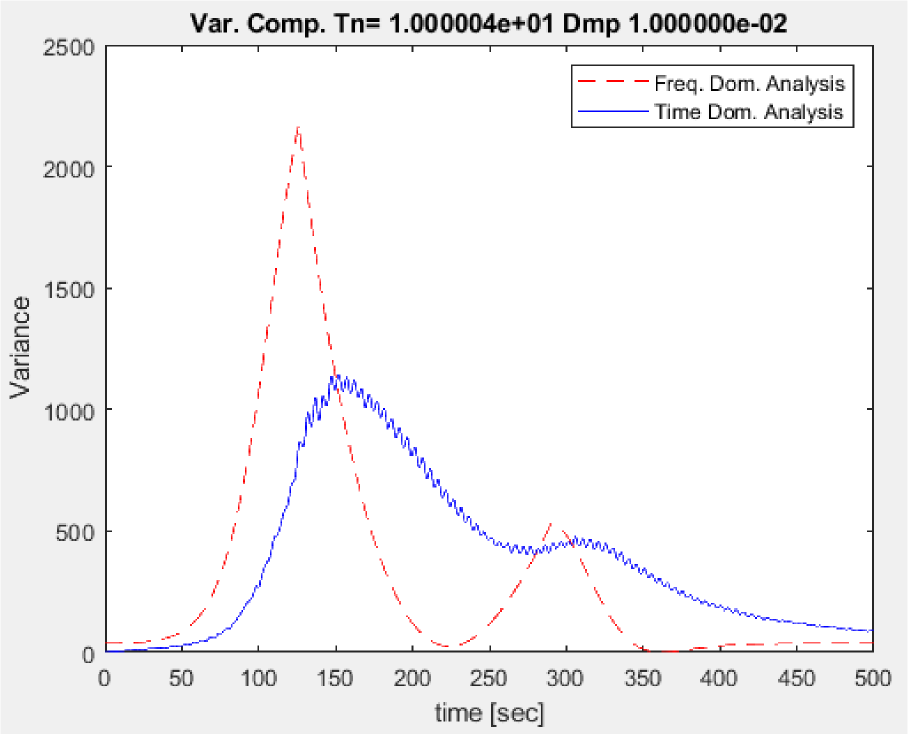

Figure 4-45:Var. Comp. Tn=10 sec ζ=1%

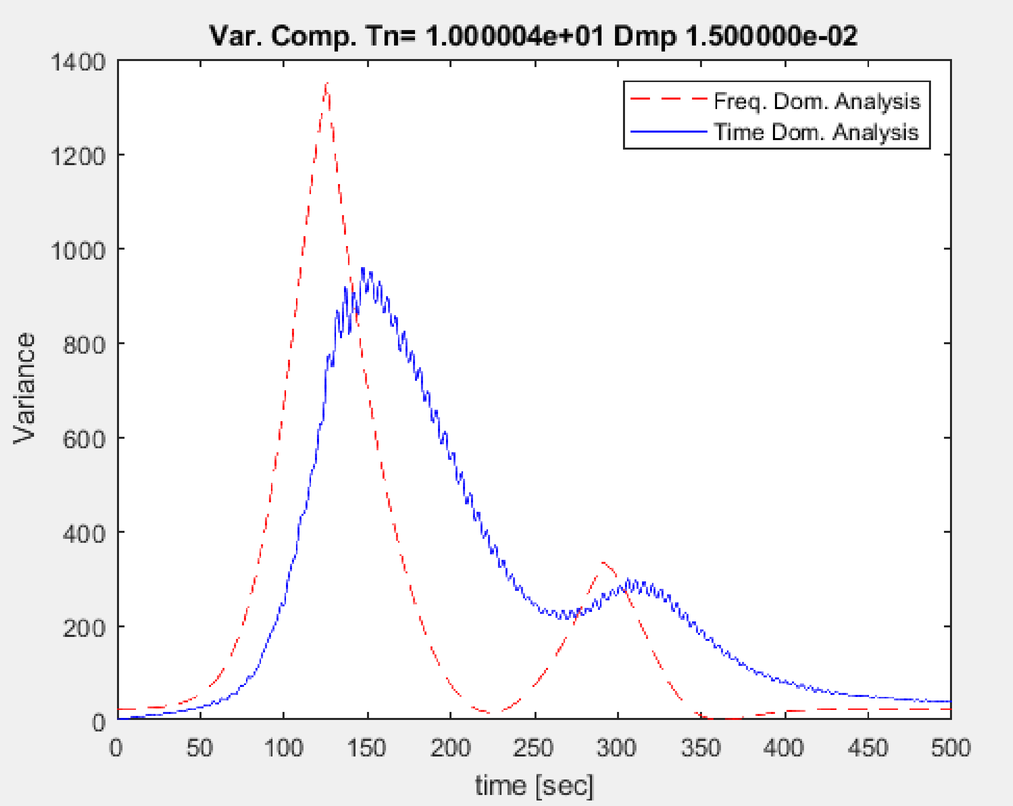

Figure 4-46:Var. Comp. Tn=10 sec ζ=1.5%

A possible explanation for this behavior lays on the assumption made of slowly varying *uniformly modulated* process. From (Priestley 1965) for this type of non-stationary process the amplitude modulating function of the spectral representation of the response is the same as the input signal, Equation 4-83 equivalent to Equation 2-59.

Equation 4-83

$$EVS_Y(f,t) \cong |H(f)|^2 EVS_X(f,t)$$

However, this assumption is valid if the amplitude modulating function a(t) is almost constant for the range in which the impulse response function h(t) is varying. This assumption was successfully verified for the case of structures with damping ratios of 2% and natural frequencies of 3.3 [Hz] in **§** 4.5.3 and **§** 4.6.1.

In order to extend the results to the case of low-damped flexible structures it will be computed the impulse response function for some of the cases within the parametric study. The results, given from Figure 4-48 to Figure 4-49 will be compared with the amplitude modulation function coming from the downburst outflow is given in Figure 4-47.

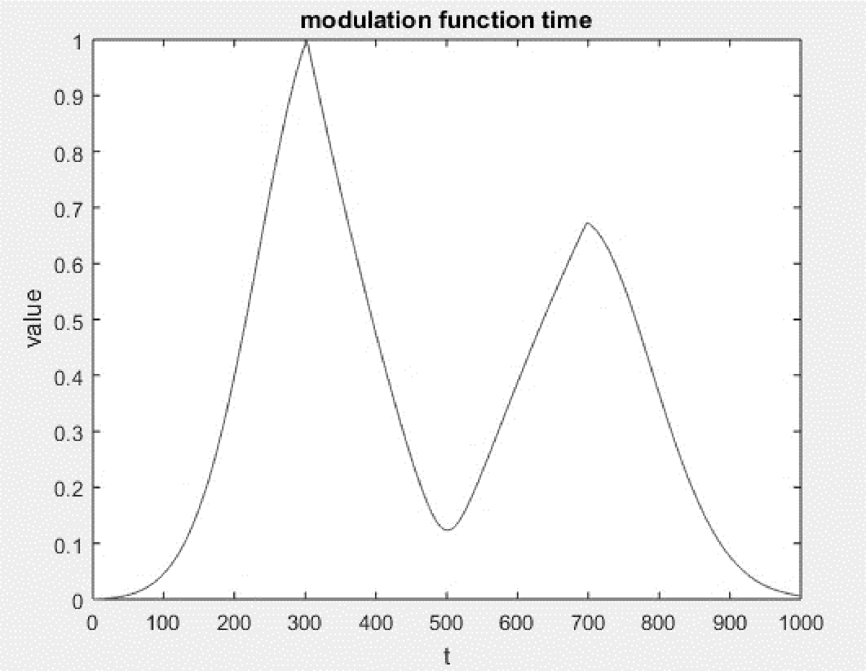

Figure 4-47:Amplitude modulating function

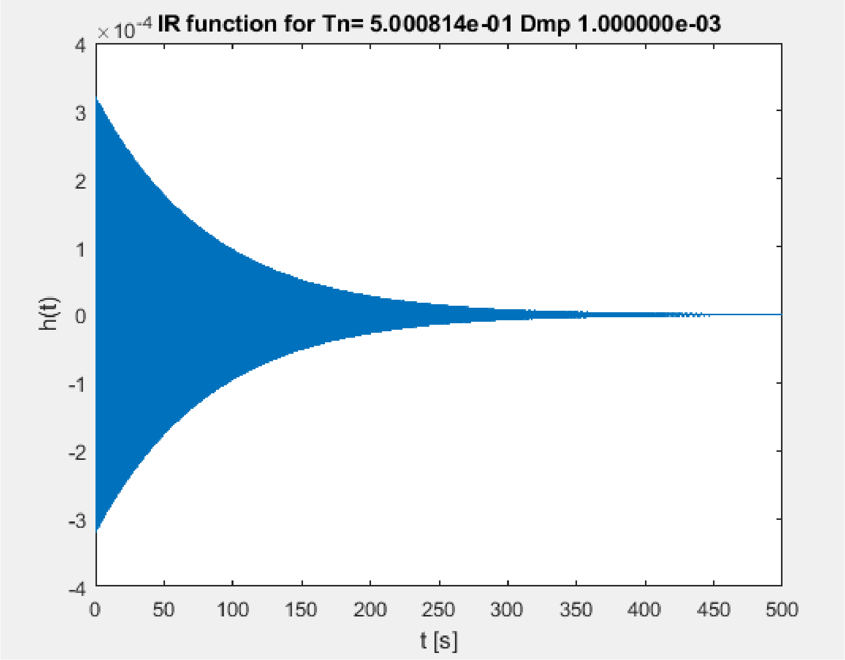

Figure 4-48:Impulse response function for Tn=0.5 sec ζ=0.1%

From Figure 4-48 it is possible to see that the period of oscillation of the low-damped system goes from 0 to 200 [sec]. Range in which the amplitude modulating function has reached the maximum and complete an oscillation cycle i.e. not constant. Therefore, it is possible to state that the assumption of *slowly varying uniformly modulated* process is not fulfilled in this case.

However, by increasing the damping from 0.1 to a 1% it is possible to see a remarkable improvement in the behavior of the approximate solution. In Figure 4-49 the period of oscillation goes from 0 to less than 50 [sec] range for which the amplitude modulating function is almost constant.

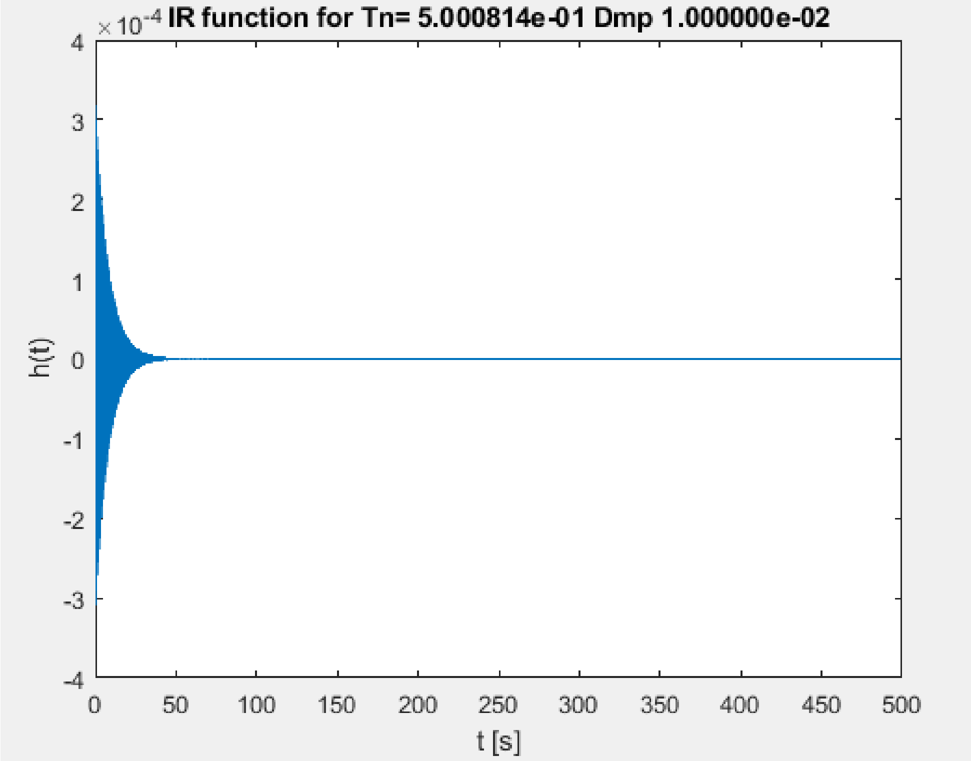

Figure 4-49:Impulse response function for Tn=0.5 sec ζ=1%

A different situation occurs when the resonant response is obtained. As it can be seen in Figure 4-50 and Figure 4-51. The oscillation period of the impulse response function covers the entire 500 [sec] time window. Therefore, the assumption of slowly varying uniformly modulated response cannot be verified for this type of systems.

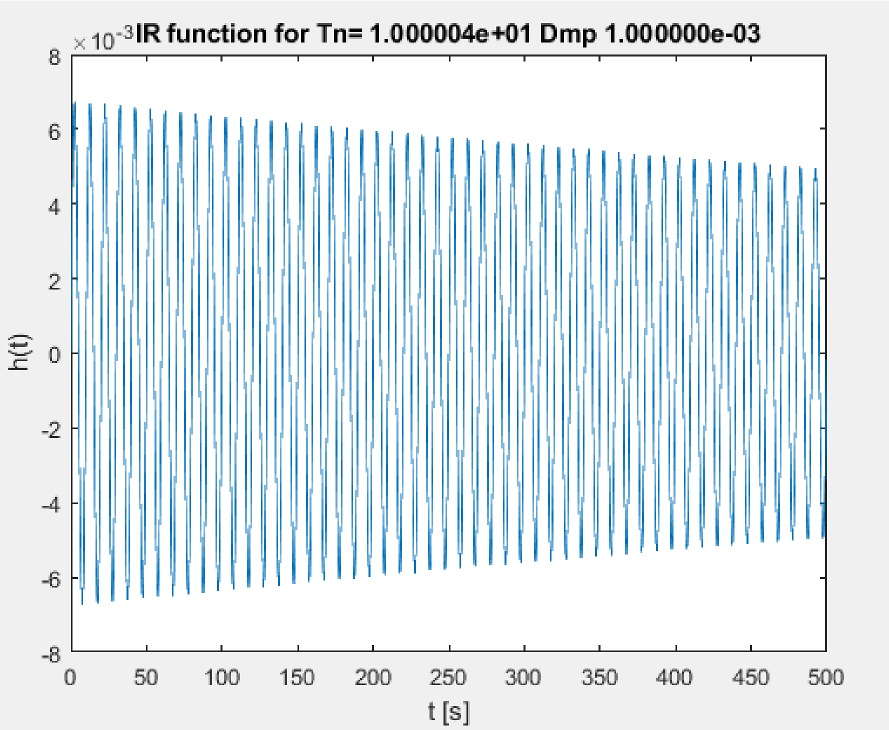

Figure 4-50:Impulse response function for Tn=10 sec ζ=0.1%

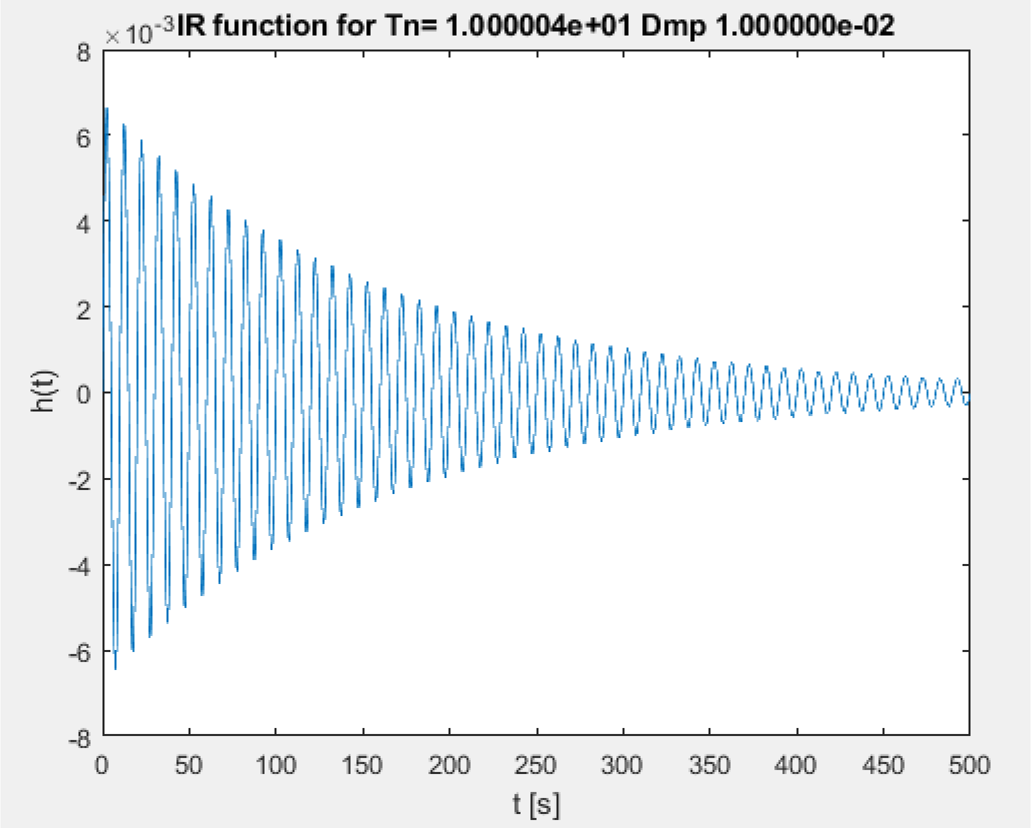

Figure 4-51:Impulse response function for Tn=10 sec ζ=1%

With the before-mentioned comparison between the amplitude modulating function and the impulse response function for low-damped flexible structures it is possible to state that the slowly varying uniformly modulated process assumption that was adopted to evaluate the system response is no longer valid. Therefore, the frequency domain analysis should be performed by evaluating the generalized transfer function (Equation 4-57) without approximations. As an example, the response of the system will be computed by numerically evaluating the convolution integral of Equation 4-57 in the “worst scenario” for the approximate frequency domain approach, i.e. T_n= 10[sec] and ζ=0.1%.

4.8.3 Numerical approach

In order to prove the validity of the methodology for the case of low-damped flexible structures, the response in frequency domain of oscillator with Tn= 10[sec] and ζ=0.1% will be computed using the full evaluation of the response i.e. evaluating the generalized transfer function $H_2(f,t)$ as it is given in Equation 4-57. Therefore, the evolutionary spectrum of the response will be computed with the full application as given in Equation 4-56.

The evaluation of Equation 4-57 is herein tackled by using a numerical integration rule. This is, of course, related to a quite huge computational effort, which, however, could be avoided at least reduced by adopting analytical or semi-analytical integration strategies.

The associated variance computed on the time domain for the case of study is that given in Figure 4-52.

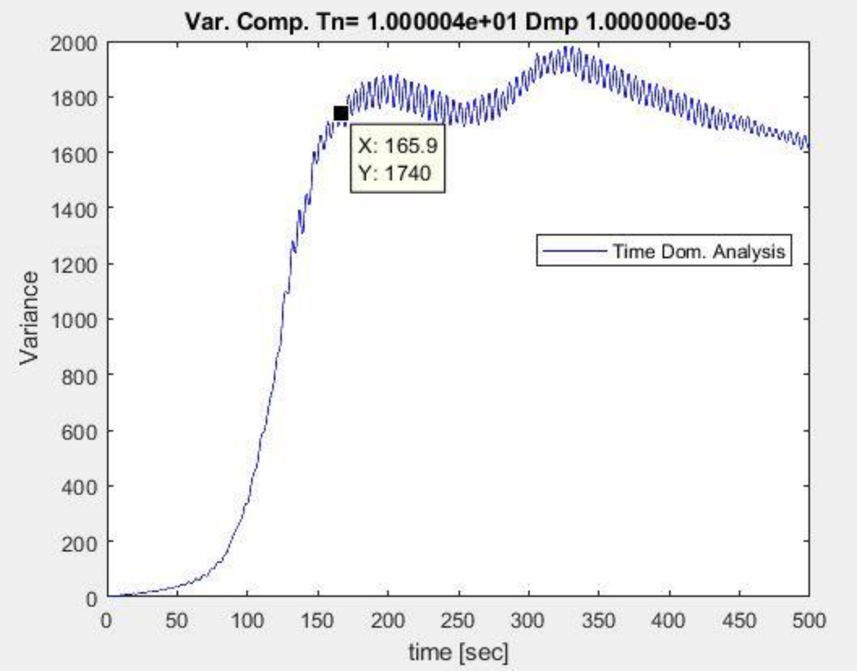

Figure 4-52: Variance computed for the time domain Tn=10[sec], ζ=0.1%

The variance of the frequency domain was computed according to Equation 4-63. And the superposition of the variance computed by the two approaches is given in the following figure:

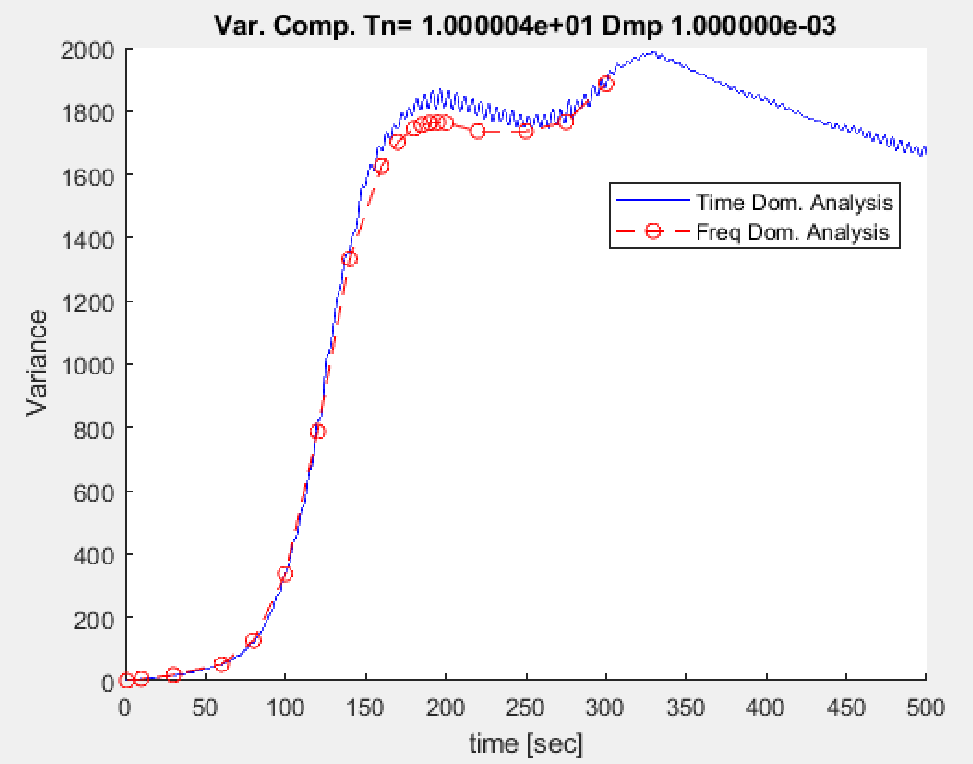

Figure 4-53: Comparison of the Variance computed for the time domain and frequency domain Tn=10[sec], ζ=0.1%

From the figure it is possible to see that the variance coming the two approaches match in behavior and order of magnitude. Therefore, the frequency domain methodology proposed herein is verified for the case of low-damped flexible structures.

4.8.4 Response evaluation on time domain

To extend the previous results, it will be performed a final check in the relation of: input / output signals computed with the time domain approach. It is important to remark that the assessment of the response in the time domain was tested and benchmarked with the examples given in the book (Chopra 2012) and with the commercial code Sap2000 - Annex A.

The test consists in verify the turbulent component of a generic response coming from the 2.000 Monte Carlo simulations and compare it with its correspondent turbulent force. The turbulent displacement is the $X_d(t)$ component of Equation 4-16 and its associated turbulent force is the $F_d(t)$ component of the Equation 4-12.

The scope of the test is to verify how much the amplitude modulating function of the input signal is transformed by the system in the output signal. The analysis is made by observation of the graphical representations given from Figure 4-54 to Figure 4-59.

Comparing the time histories of the response it is possible to observe the following:

For the value used in **§** 4.7 Tn=0.32 [sec] and ζ=2% reported in Figure 4-54. The envelope of both signals is the same.

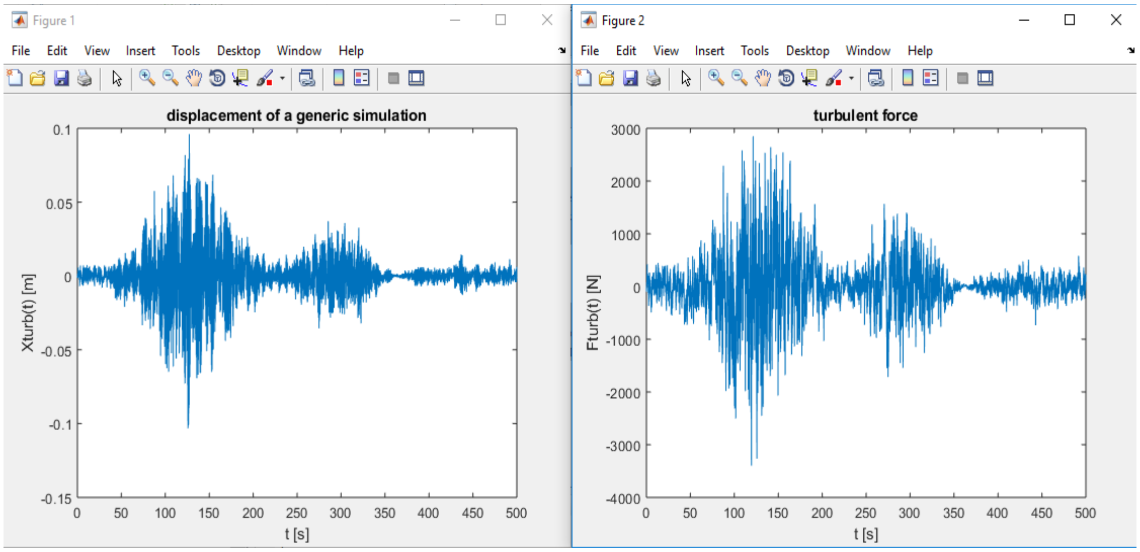

Figure 4-54: Input/output comparison. Tn=0.32 sec and ζ=2%.

Increasing the natural period to Tn=0.5 sec and ζ=2% as in Figure 4-55, the envelope of both signals do not substancially differ.

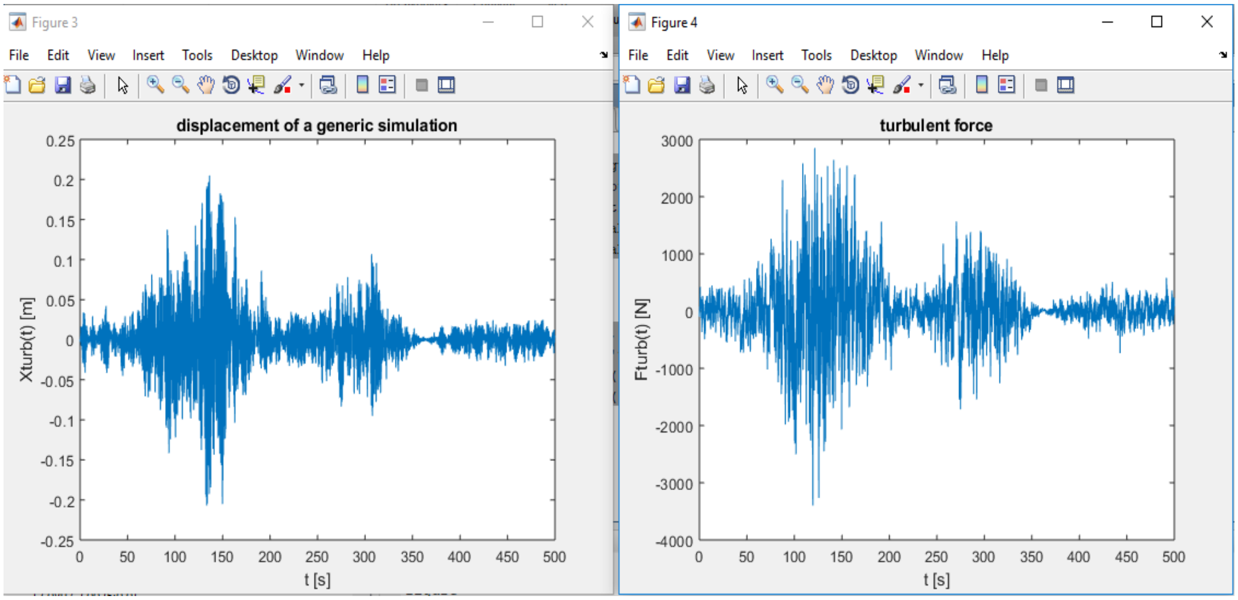

Figure 4-55: Input/output comparison. Tn=0.5 sec and ζ=2%.

However, if the damping ratio is decreased it starts to appear a difference between the modulating function of response compared with that of the input. In Figure 4-56 it is plotted the case of Tn= 0.5 [sec] and ζ=0.5%.

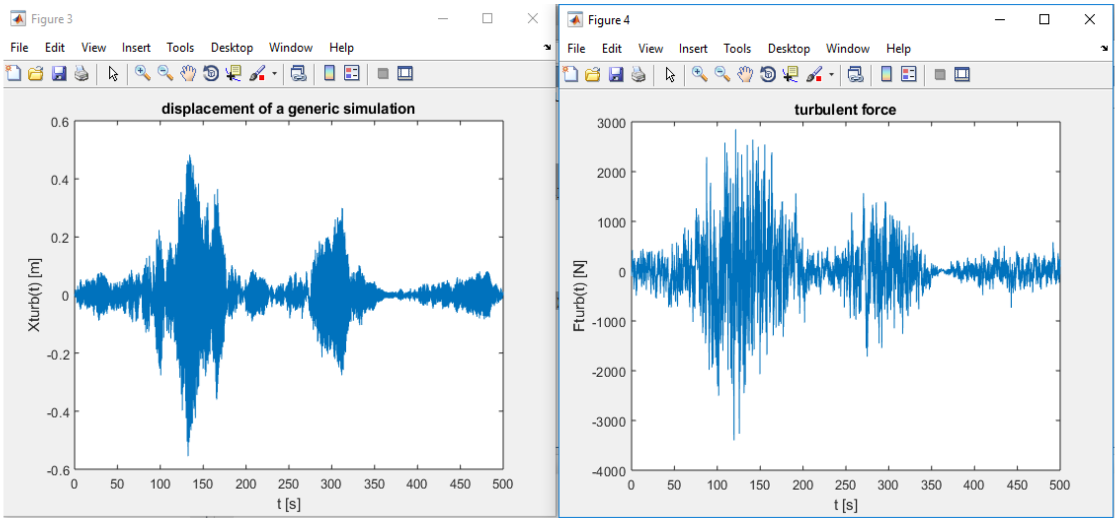

Figure 4-56: Input/output comparison. Tn=0.5 sec and ζ=0.5%.

If the damping ratio is decreased to very low values (0.1%) the difference starts to be more clear as it can be seen in Figure 4-57 for Tn= 0.5 [sec] and ζ=0.1%. Even though the similarity of modulating functions of both signals has been lost, some equalities could be seen.

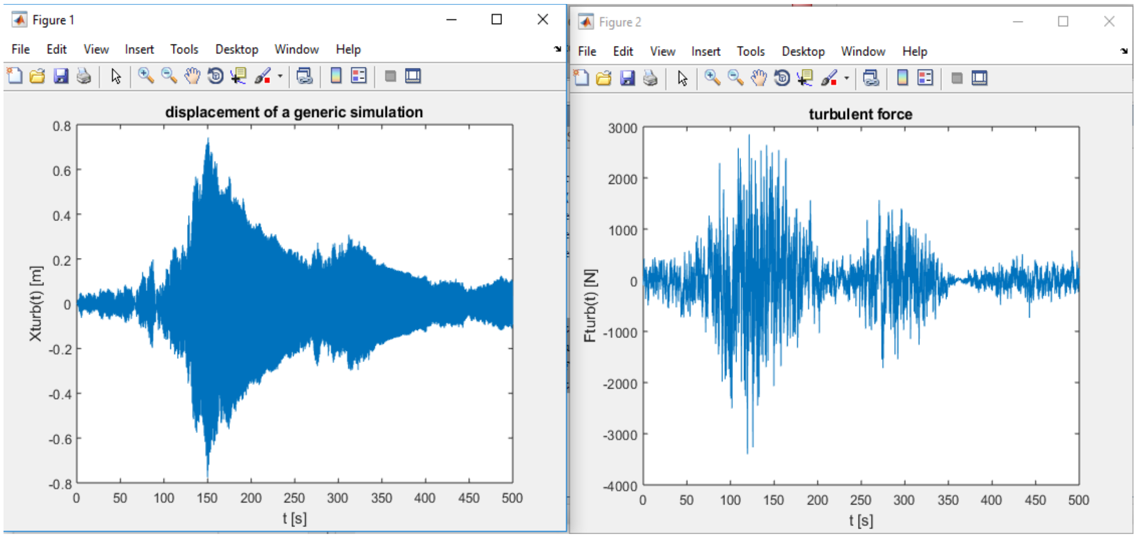

Figure 4-57: Input/output comparison. Tn=0.5 sec and ζ=0.1%.

Accounting for the effect of the resonant response, it is possible to see a complete difference between the two signals regardless the damping ratio. The relationship is as shown in Figure 4-58 and Figure 4-59.

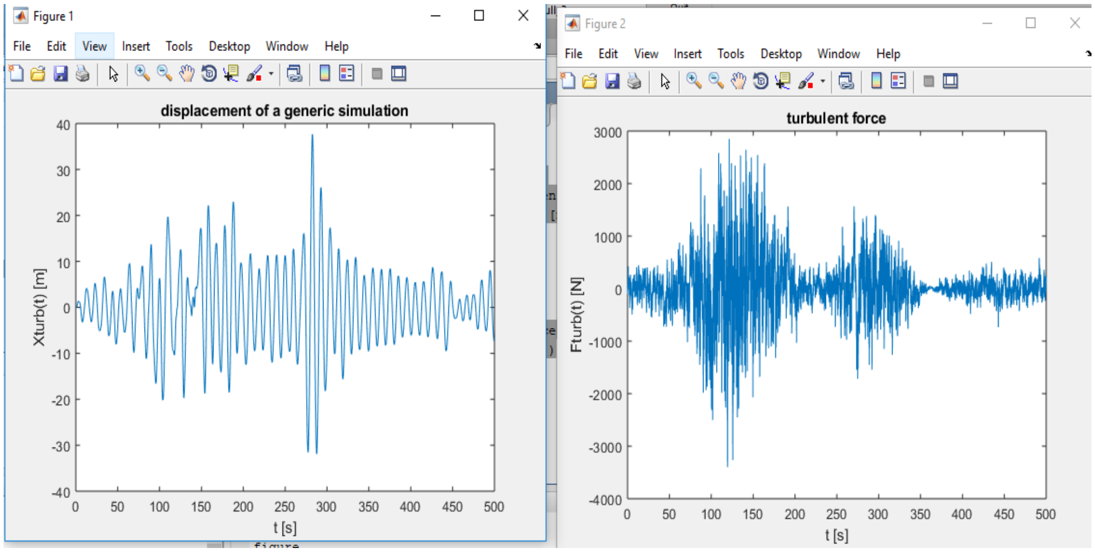

Figure 4-58: Input/output comparison. Tn=10 sec and ζ=2%.

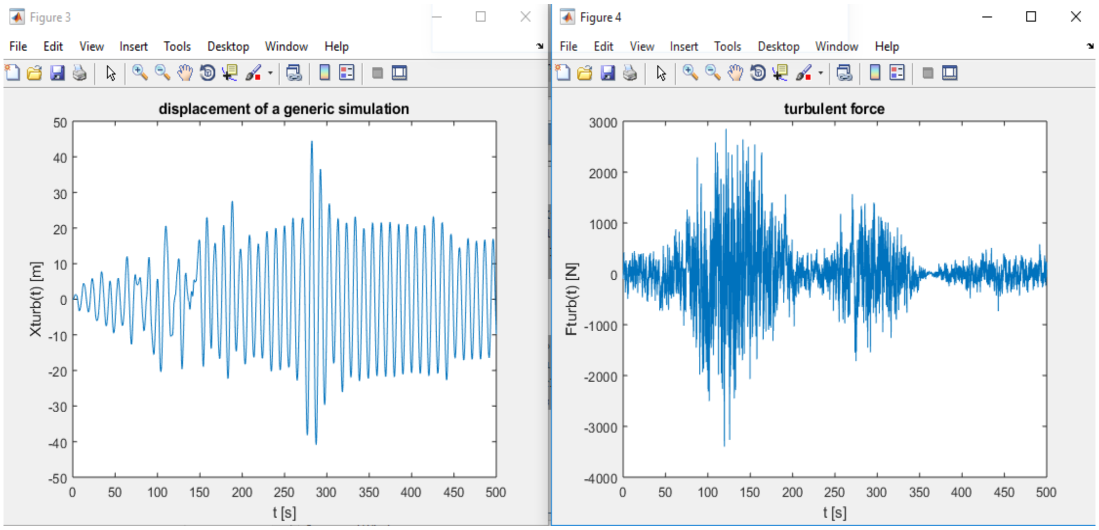

Figure 4-59: Input/output comparison. Tn=10 sec and ζ=0.1%.

With graphical analysis of the time histories, it is possible to verify that for structures associated to small damping ratios and low natural frequencies the amplitude modulating function of the response differs to that of the input signal. Therefore, the assumption of slowly varying uniformly-modulated process of the response cannot be fulfilled and for its assessment it must be implemented an approach as that of paragraph 4.8.3.

These results, hence, further strengthen the conclusion reached in the previous section (4.8.3): in the case of slightly damped flexible structures it is recommended to compute the convolution integral Equation 4-57 without introducing approximations.

4.8.5 Conclusions

To recall the response in the frequency domain of a system submitted to downburst outflow, the random process of the structural response can be catalogued as slowly varying *uniformly modulated* non-stationary process, if the resonant component has not a major contribution in the overall response and the system has a damping ratio of at least 0.5% according to the study developed herein.

For the case of slightly-damped flexible structures it was demonstrated that the approximation of uniformly modulated process for the evaluation of the response is no longer valid. Therefore, it is recommended to solve the problem by numerical evaluation of the generalized transfer function. The system response evaluated with the latter approach, indeed, showed a very good agreement with the results coming from the time domain approach.

CHAPTER 5. ASSESSMENT OF FAILURE PROBABILITY

5.1 Scope of the analysis

This study was made to compare the effects of the wind velocity fields computed with the traditional Atmospheric Boundary Layer model (ABL) and those of the downburst wind model. A simple reduced structure of one degree of freedom was first analyzed to obtain a representative description of the behavior. It is proposed to extend the results of the present study for more complex MDOF structures, in further step of the research.

To give a quantitative measurement for the comparison, the adopted criteria was related to the maximum velocities coming from both approaches (ABL & Downburst) and their associated failure probability. The latter can be associated to the overpassing of a certain limit state (even in elastic range) defined for the case of study. It is worth noting that the failure probability here is not necessarily related to a specific non-linear collapse mechanism.

5.2 Case of study

The first attempt for comparing both phenomena is the assessment of the failure probability of system of SDOF Figure 5-1(c). The system represents a tall chimney as that shown in Figure 5-1 (a). Due to the simple dynamic behavior of the structure, as an inverted pendulum, the structural response can be reduced, as a first approximation, to an equivalent SDOF as shown in Figure 5-1 (b).

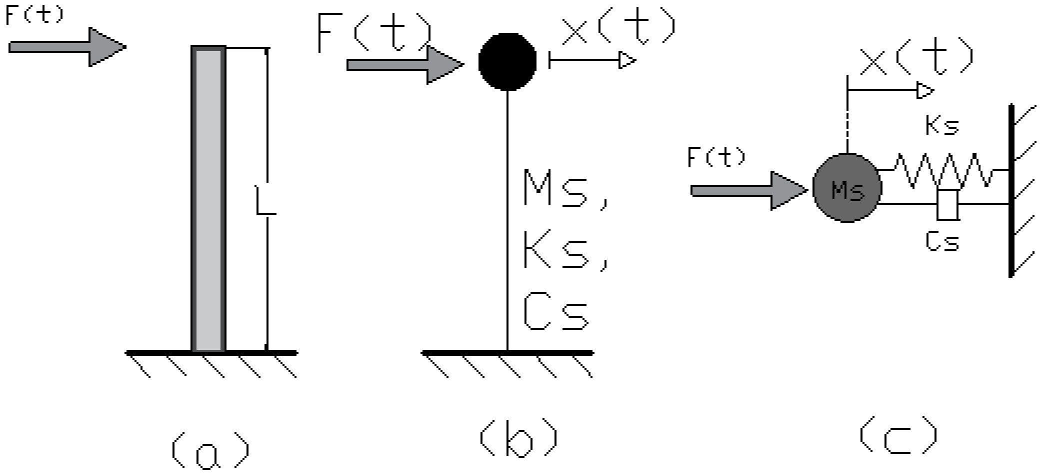

Figure 5-1 Structure reduced model a) Real structure b) equivalent 1mode structure c) equivalent 1dof system

5.3 Limit state

The failure probability in this study is related to the exceedance of limit displacement of the tip of the structure. The limit displacement is linked to the elastic limit of the moment at the base by means of the structural internal forces.

For the case of a square cross section the elastic limit bending moment, M_e, is given by:

Equation 5-1

$$M_e = \frac{F_{y'} * I_y}{h/2} \rightarrow F_{y'} * W_e$$

Where $F_{y'}$ is the effective yielding limit of the material and W_e the limit elastic section modulus, I_y is the section inertia and h the height.

For the cantilever beam the tip displacement δ_{tip} and bending moment M according to Figure 5-2 are given in Equation 5-2.

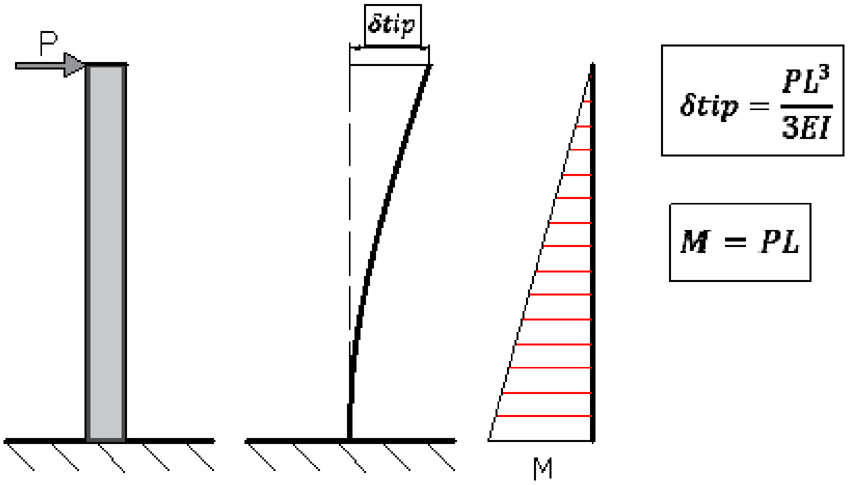

Figure 5-2: Structural behavior of cantilever beam

Equation 5-2

$$\delta_{tip} = \frac{PL^3}{3EI}\ , \quad M = PL \ \rightarrow \ \delta_{tip} = \frac{ML^2}{3EI}$$

For the elastic limit the tip displacement, $\delta tip_{,e}$ can be obtained as follows:

Equation 5-3

$$\delta_{tip,e} = \frac{M_e L^2}{3EI}$$

The limit displacement δLim for the analysis will be taken as fraction of the elastic limit, therefore Equation 5-3 becomes:

Equation 5-4

$$\delta_{lim} = \lambda * \delta_{tip,e}$$

With λ a multiplier lower than 1 used for test calibration.

5.4 Deterministic component (mean)

The pseudo-static component of the structural response computed as Equation 4-16 will be compared with the limit displacement. This will give a brief approximation (neglecting dynamic effects) of the stress state under the deterministic component of the wind velocity.

5.5 Failure Probability and Reliability Index

The probability of exceedance of the limit displacement δ_{Lim} is characterized by the variable $\theta_{,in}$ as shown in Equation 5-5 (Biondini 2018). The index in accounts for the generic Monte-Carlo simulation. The variables X_m and $X_{d,in}$ are respectively the pseudo-static and turbulent components of the displacement computed according to **§** 4.3 Time domain analysis**.**

Equation 5-5

$$\theta_{,in} = \frac{\delta_{lim}}{X_m + \max(X_{d,in})}$$

The probability of failure FP is defined as number of simulations exceeding the limit value (or analogously rend $\theta_{,in}$<1) divided over the total number of Monte-Carlo simulations, N, Equation 5-6.

Equation 5-6

$$FP = \frac{NF}{N}$$

With NF the number of simulations exceeding the limit value.

5.6 Atmospheric Boundary Layer Model

For the analysis it is first computed the failure probability for a reference ABL wind. It is supposed that the structure is located in the city of Genova Region of Liguria, Italy. No topographic effects will be introduced in the reference velocity at the tip of the structure. The terrain category will be chosen as 0 i.e. Sea or coastal area exposed to open sea. The parameters used for the simulation of ABL model are reported in Table 5-1.

Table 5-1: ABL model parameters

Parameter	Symbol	Value
Basic Velocity	V_b	30[m/s]
Roughness length	Zo	0.03 [m]
Integral length scale	L_v	111.81 [m]
Turbulence intensity	I_v	0.15
Height of point	Z	15 [m]
Reference velocity at tip	V_{ref}	32.51 [m/s]
Number of simulations	N	2.000 [und]

The vertical profile for the ABL model is following the logarithmic rule Equation 5-7. The profile is as that shown in Figure 5-3. In the figure it is highlighted the acting velocity at the reference height

Equation 5-7

$$V(z) = V_b * 0.19\left(\frac{zo}{0.05}\right)^{0.07} LN\left(\frac{z}{zo}\right)$$

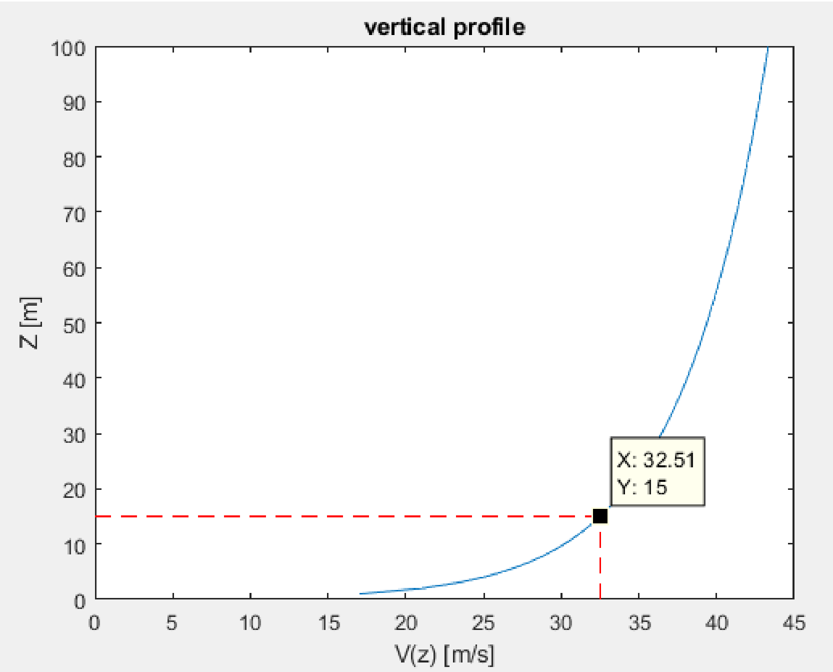

Figure 5-3: Vertical profile ABL model

5.7 Equivalent Downburst model

For the estimation downburst failure probability there were used different values of the maximum velocity of the downburst v_{max} (as defined in **§** 3.4). The *equivalent downburst outflow* is that giving the same failure probability of the reference ABL model.

The comparison is made in terms of the velocity of both wind fields and in their probability of occurrence. For this latter parameter, it is worth stressing that while for the case of the winds coming from the ABL it is possible to use the available aeolian maps, for the downburst the only accessible data base is that one reported on the WP (Wind and ports) and WPS (Wind Ports and Sea) projects in the zone of Liguria, Italy (Solari, et al. 2015).

It is important to remark that the characteristic velocity of downburst model defined in **§** 3.4 is the maximum radial velocity. This velocity is reached at the certain height, Z_{max}, not necessarily equal the reference height of the tip of the cantilever, Z_{ref}, therefore a modification according to the vertical profile should be included in the computations. In addition, there is also the effect of the tracking velocity of the mother storm which is vectorially added to the maximum radial component.

Finally, the maximum velocity of the downburst at the reference point must be computed for every velocity profile. The parameters used for the simulation of downburst outflow are reported in Table 5-2.

Table 5-2: Parameters to define downburst outflow

Parameter	Value
Integral length scale L_v	34.6 [m]
Turbulence intensity I_v	0.12
Max Radial velocity v_{max}	{25.0 27.5 28.5 30.0 32.5} [m/s]
Ref. radial velocity	{24.03 26.4 27.4 28.8 31.2} [m/s]
Track velocity Vt	12 [m/s]
Vmax*	{35.9 38.3 39.3 40.6 43.1} [m/s]
Height of max velocity Z_{max}	22.5 [m]
Downburst diameter $D=r_{max}$	1.000 [m]
Intial X_o	-2.500 [m]
Initial y_o	150 [m]
Number of simulations, N	2.000

From Figure 5-4 to Figure 5-13 it is possible to appreciate the vertical and radial diffusion profiles of the downburst models used in the current study. In the figures are highlighted the maximum radial velocity v_{max} and the maximum downburst velocity $V_{max}*$.

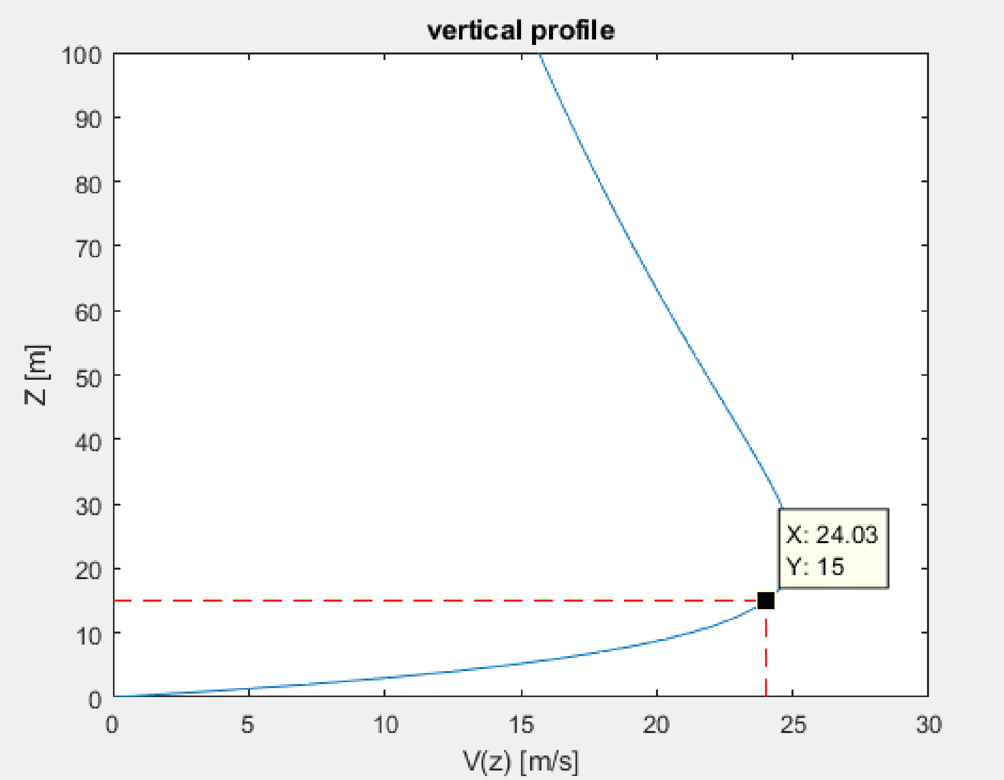

Figure 5-4: Vertical profile vmax=25 m/s

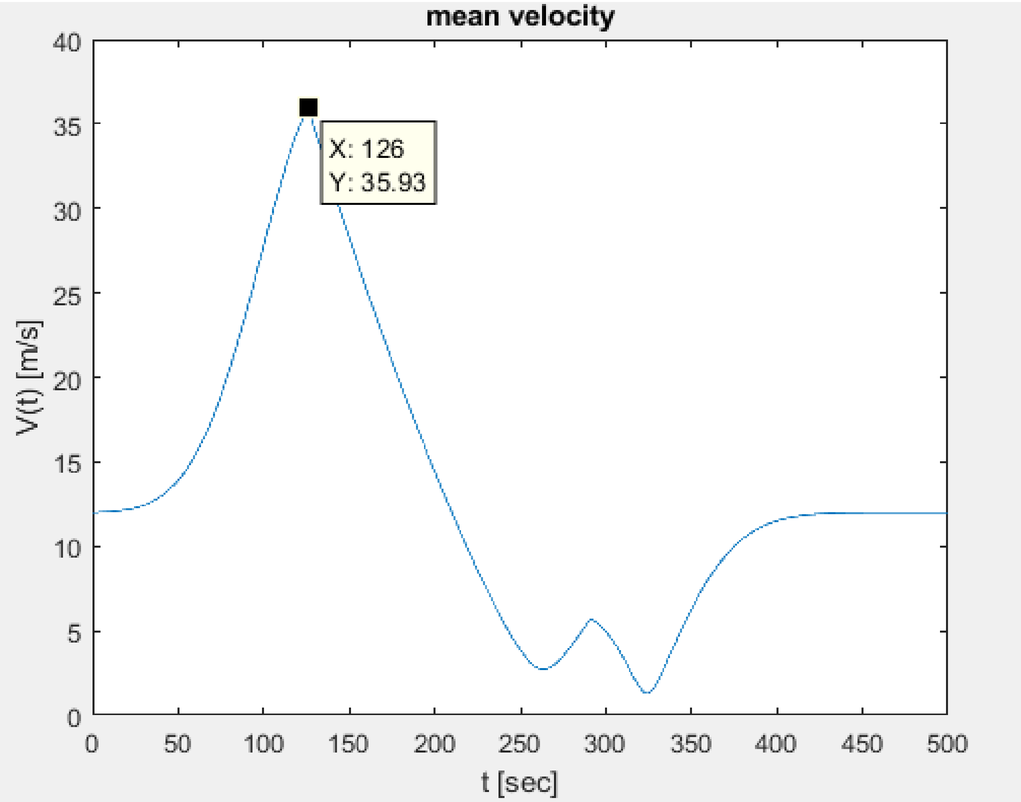

Figure 5-5: Mean velocity vmax=25 m/s

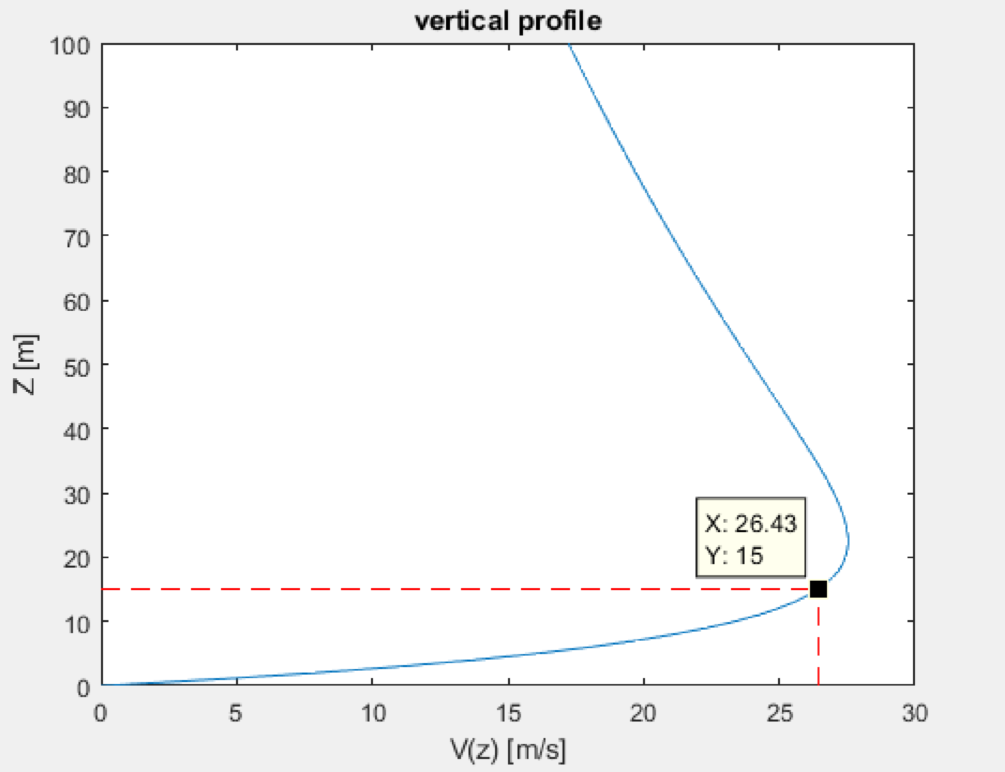

Figure 5-6: Vertical profile vmax=27.5 m/s

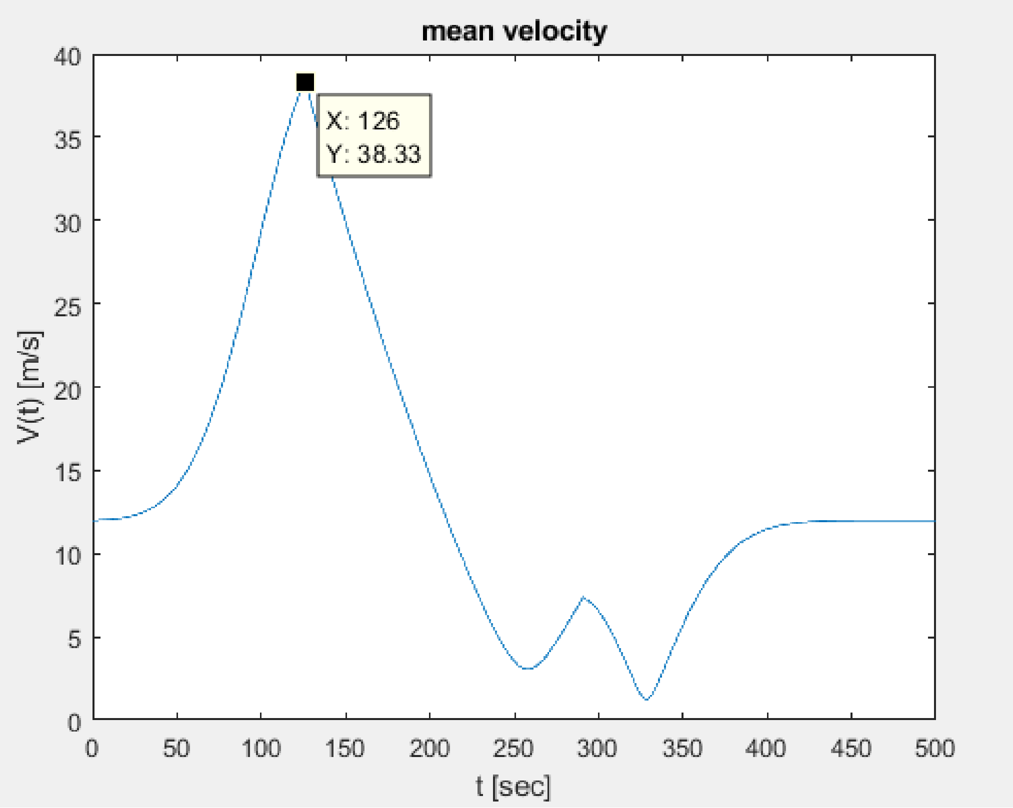

Figure 5-7: Mean velocity vmax=27.5 m/s

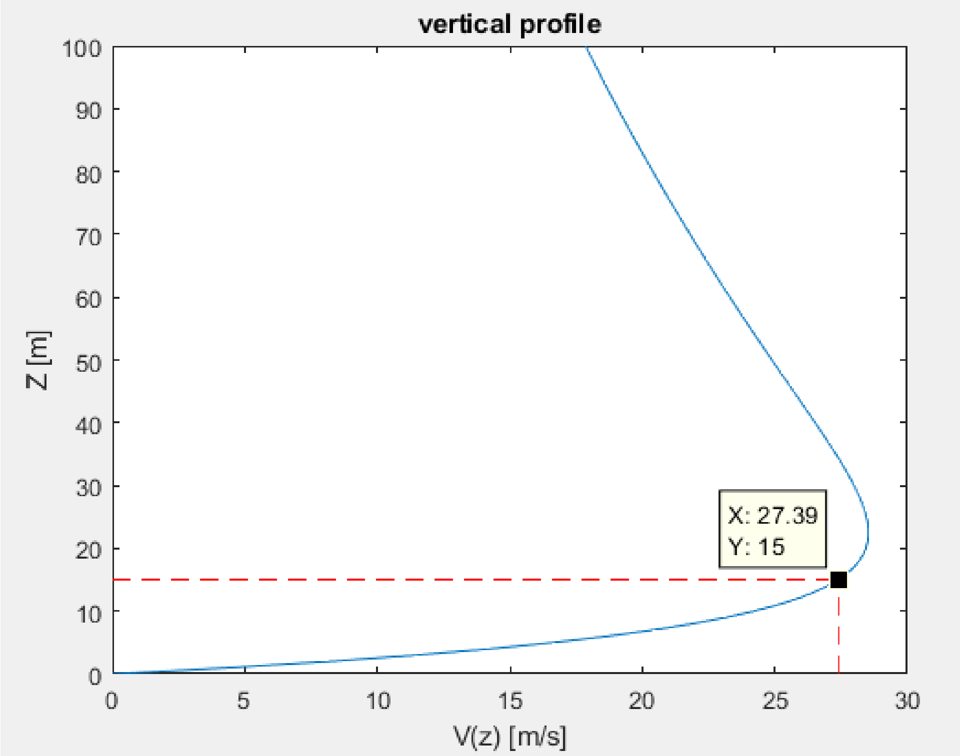

Figure 5-8: Vertical profile vmax=28.5 m/s

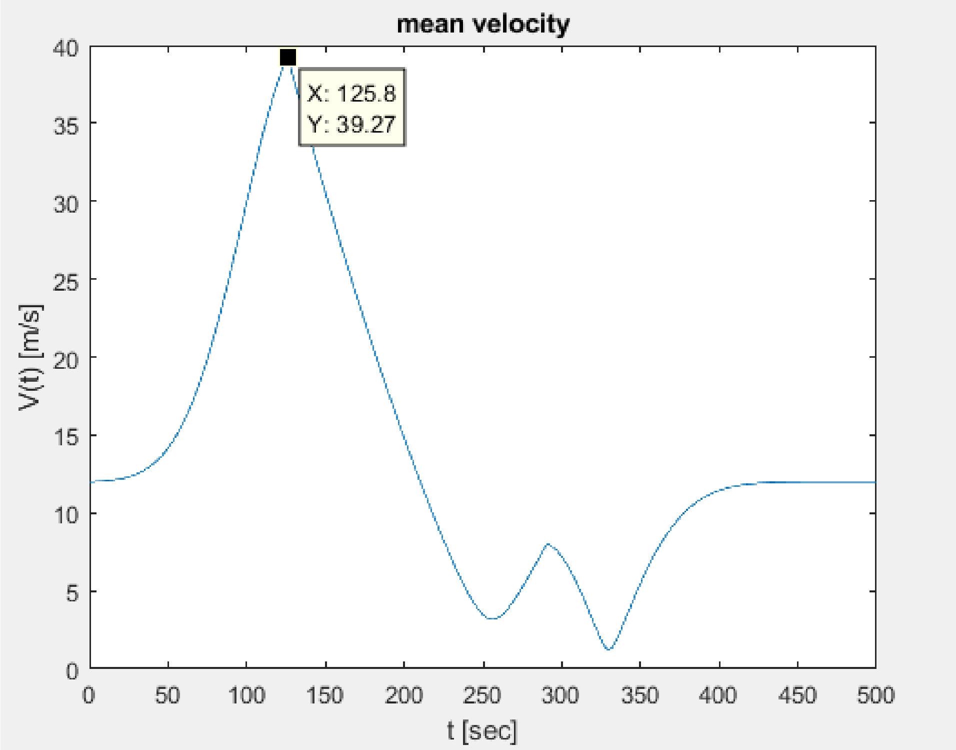

Figure 5-9: Mean velocity vmax=28.5 m/s

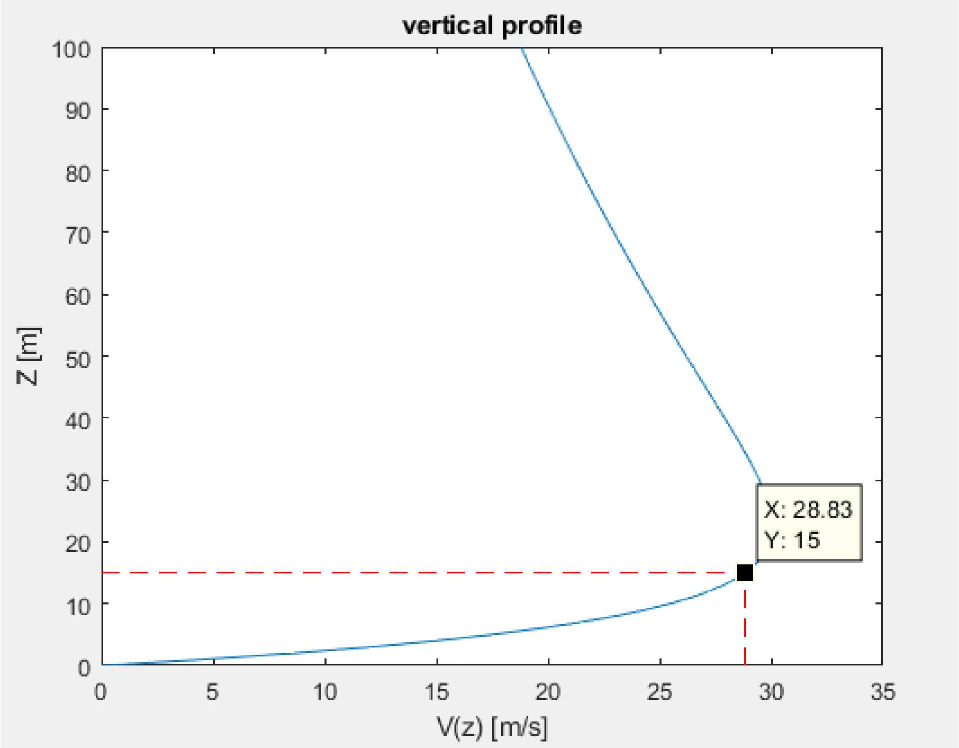

Figure 5-10: Vertical profile vmax=30 m/s

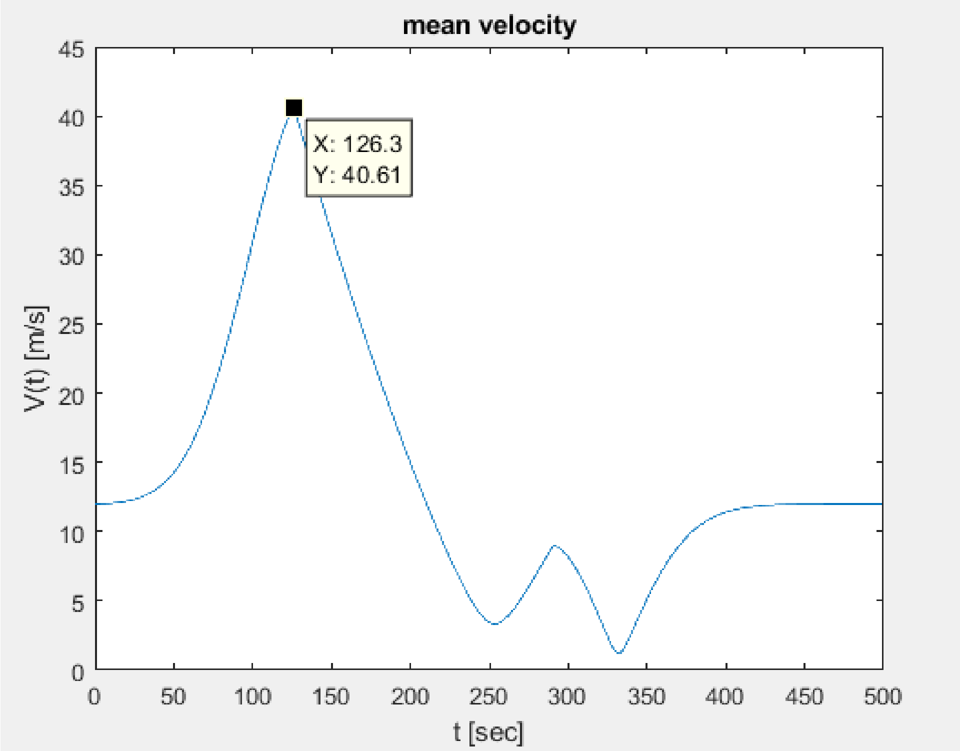

Figure 5-11: Mean velocity vmax=30 m/s

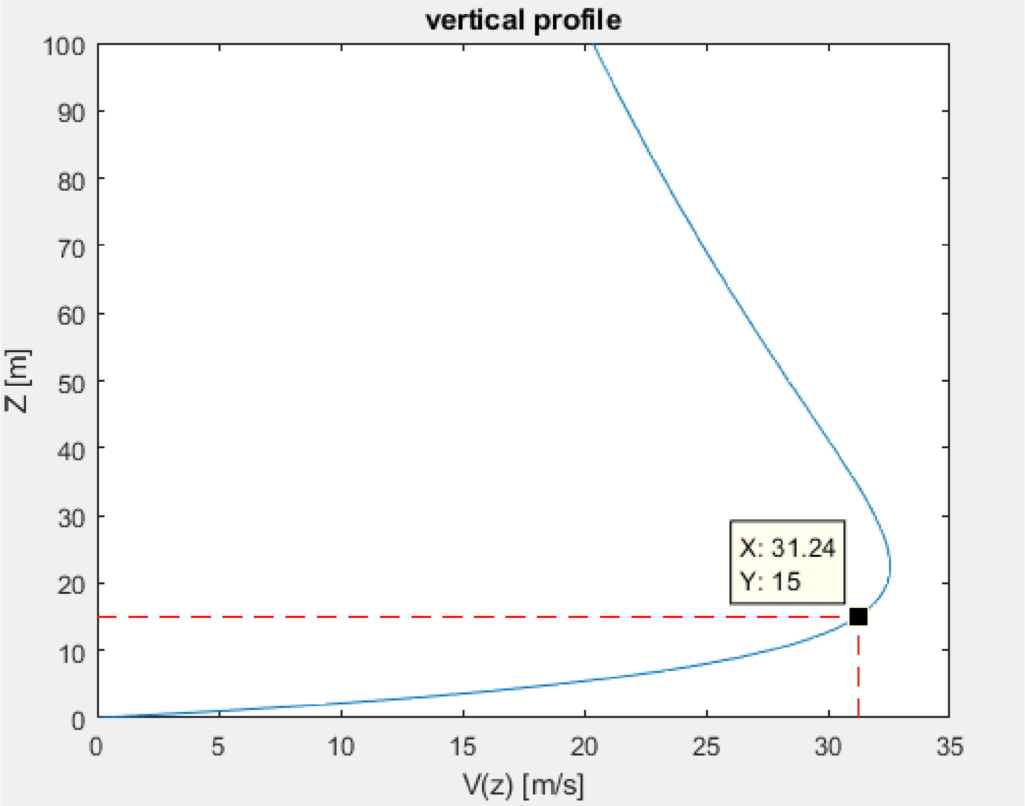

Figure 5-12: Vertical profile vmax=32.5 m/s

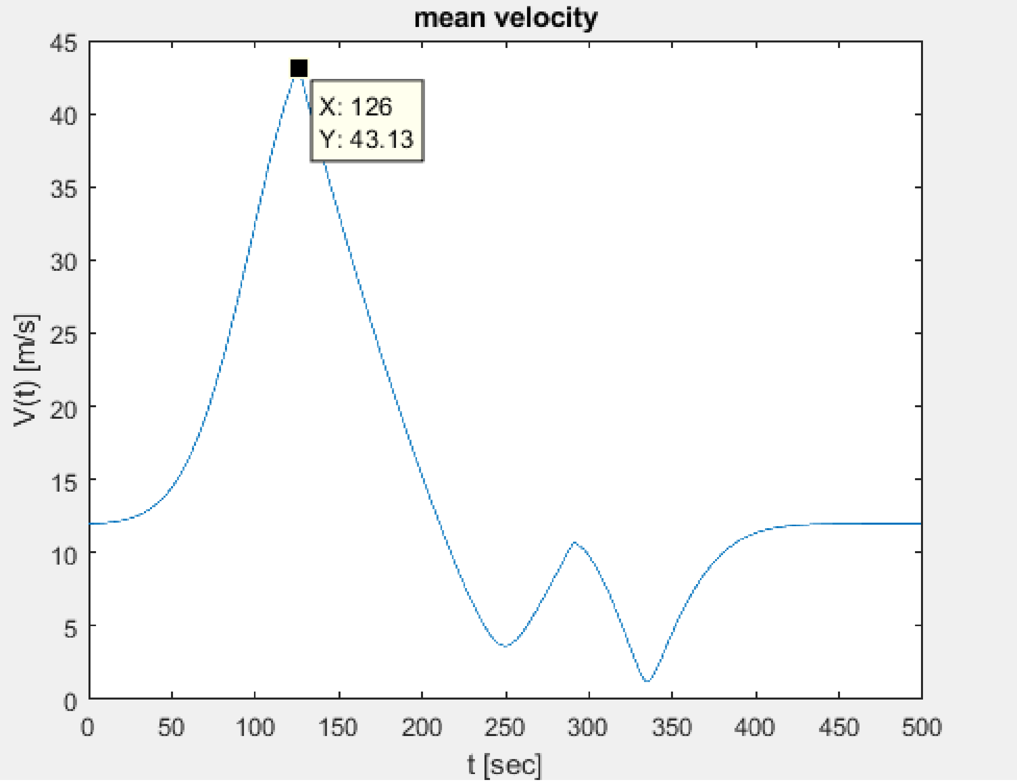

Figure 5-13: Mean velocity vmax=32.5 m/s

5.8 Test Setting

The material selected for the simulation is structural steel S235. The properties of the material are reported in Table 5-3. The damping ratio of the system is taken as 2%.

Table 5-3: Material simulation parameters

Parameter	Symbol	Value	Unit
Young Modulus	E	210	*[GPa]*
Poisson Ratio	ν	0.2	*[-]*
Density	ρ	7.850	*[kg/m3]*
Shear modulus	G	87,5	*[GPa]*
Effective Yield Limit	*Fy'=0.85*Fy*	199,750	*[MPa]*

The geometric properties of the system are reported in Table 5-4.

Table 5-4: Cross section simulation parameters

Parameter	Symbol	Value	Unit
Area	A	0.25	*[m2]*
Width	B	0.5	*[m]*
Height	H	0.5	*[m]*
Length	L	15	*[m]*
Inertia in y-y' direction	Iy	5.21e-3	*[m4]*
Inertia in z-z' direction	Iz	5.21e-3	*[m4]*
Elastic section modulus	W_e	2.08e-2	*[m3]*
Natural frequency	f_n	2.587	*[Hz]*

The limit displacement is reported in Table 5-5.

Table 5-5: Limit displacement

Parameter	Symbol	Value	Unit
Elastic limit moment	M_e	4161.458333	[kN*m]
Calibration multiplier	λ	0.0265	[-]
Limit displacement	δ_{lim}	0.0075	[m]

5.9 Results

Evaluating the response associated to the mean component of the velocity, the pseudo-static response, it is possible to get a measure of the safety coefficient of the defined limit displacement. The results are reported in the Table 5-6.

Table 5-6: Safety Coefficient

Model	Model Velocity	Max Mean Vel.	SF	Unit
ABL	30	32.5	0,349	[%]
DWB	25	35.9	0,427	[%]
DWB	27.5	38.3	0,486	[%]
DWB	28.5	39.3	0,510	[%]
DWB	30	40.6	0,548	[%]
DWB	32.5	43.1	0,615	[%]

Introducing the dynamic amplification factor, DYN, as the ratio between the turbulent component and the pseudo static. The failure probability For the different velocities is reported in Table 5-7 and graphically in Figure 5-14.

Table 5-7: Failure probability

Model	Model Velocity	Max Mean Vel.	DYN	Value	Unit
ABL	30	32.5	1,86	0,56	[%]
DWB	25	35.9	0,84	0,081	[%]
DWB	27.5	38.3	0,85	0,532	[%]
Range of the equivalent DWB model					
DWB	28.5	39.3	0,86	0,757	[%]
DWB	30	40.6	0,87	0,957	[%]
DWB	32.5	43.1	0,89	1	[%]

Comparing the dynamic amplification factor, DYN, of the synoptic winds computed with the ABL model with that of the DWB model is possible to see that the former is more than two times greater than the latter. A possible reason for this behavior lays inside the Von Karman PSD function which depends on the integral length scale and the turbulence intensity, as well as, on the mean velocity.

Even though the mean velocities of both models are in the same order of magnitude, the integral length scales of the ABL model are greater than those of the DWB and the turbulence intensity of the ABL model is 25% higher than that of the downburst.

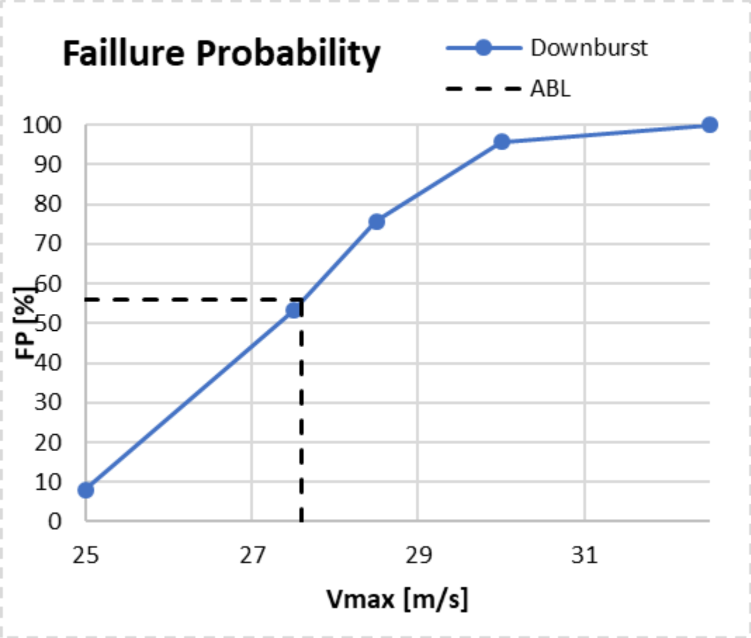

Figure 5-14: Downburst failure probability vs v_{max}

The equivalent downburst model will have a reference radial velocity of 27.7 [m/s] while the ABL model will be related to a basic velocity, Vb, of 30 [m/s]. While the maximum mean velocity at the reference point is 32.3 [m/s] for the ABL model, it is approximately 39 [m/s] for DWB model.

From (Solari, et al. 2015) it is possible to obtain the record of peak velocity measured in the same zone supposed for the development of the case of study; city of Genova Region of Liguria, Italy. The results are reported in Figure 5-15.

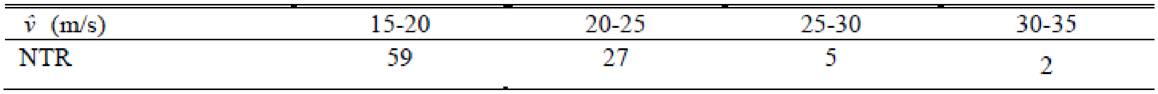

$\hat{v}$ (m/s)	15-20	20-25	25-30	30-35
NTR	59	27	5	2

Figure 5-15: Peaks of downburst wind fields from WP and WPS.Aadapted from (Solari, et al. 2015)

The maximum velocities reported on Figure 5-15 are in the range of 30 to 35 [m/s]. Since the maximum velocity of the equivalent DWB model is close to 39 [m/s], it is possible to notice none of the recorded DWB inside the framework of the WP and WPS projects exceed the maximum velocity of the so-defined equivalent downburst model. Two main reasons for this behavior can be explained. First is the associated return period of the aeolian maps considered in the design rules of Eurocode1 but not in the available records of downburst, it is recommended to perform a statistical analysis on this parameter for downburst models in a further step of the research. A second reason is the case of study, according to (Holmes and Oliver 2000) wind outflow of downburst has a greater impact over long structures because the acting diameter related to this phenomena ($\approx 4[km]$) is larger than the acting length of the winds coming from the ABL (≈200[m]).

CHAPTER 6. MDOF SYSTEM ANALYSIS

6.1 Wind Field Simulation

On CHAPTER 4 SDOF SYSTEM ANALYSIS, it was so far explained the procedure for the analysis of single degree of freedom structure. for the MDOF systems there must be introduced the relationships for analyzing spatial structures in 3-dimensions rather than point like structures.

The wind field description adopted will be that already described in **§** 3.10.

6.2 Structural Description

For the evaluation of the response of the MDOF system the space dimensions must be added to the SDOF reduced systems given in Numeral 4.3 Time domain analysis, therefore the scalar quantities of the mass, stiffness, damping, and natural frequency must be handled in matrix format. In the following, a brief introduction to the provisions and characteristics of the matrices will be explained together with the modal approach and the Newmark integration method of the equations of motion.

6.2.1 Mass matrix

The inertia forces fI_j acting on the structure components are function of the element mass and the acceleration $\ddot{x}(t)$. In Figure 6-1 it is shown a representation of the equilibrium condition of the structure, the coefficients m_{ij} are the inertia forces in the *node-j* due to the application of a unit acceleration at *node-i.*

Equation 6-1

$$\mathrm{fI_j} = \mathrm{m_{1j}} * \ddot{\mathrm{x}}_1 + \mathrm{m_{2j}} * \ddot{\mathrm{x}}_2 + \ldots + \mathrm{m_{nj}} * \ddot{\mathrm{x}}\ \mathrm{n}$$

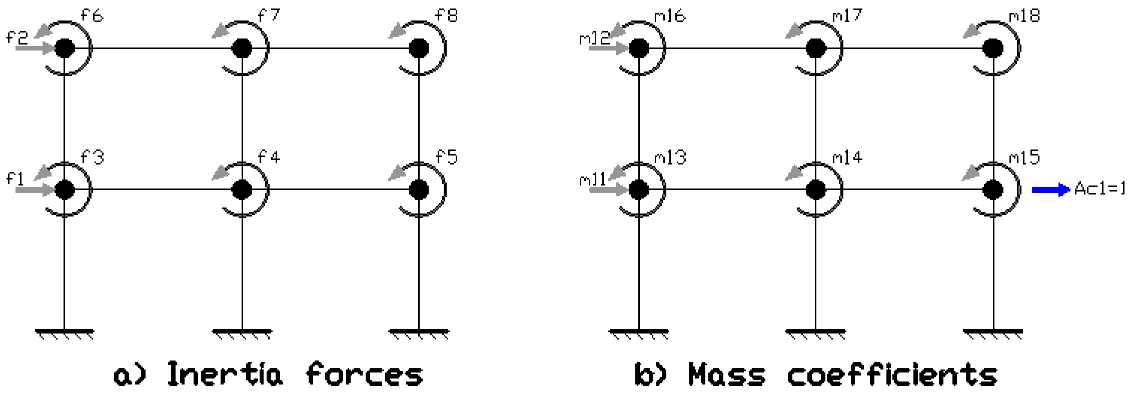

a) Inertia forces b) Mass coefficients

Figure 6-1 Inertia forces

Equation 6-1 could be represented in matrix form as:

Equation 6-2

$$\begin{bmatrix} f_1 \\ \vdots \\ f_j \end{bmatrix} = \begin{bmatrix} m_{11} & \cdots & m_{1n} \\ \vdots & \ddots & \vdots \\ m_{n1} & \cdots & m_{nn} \end{bmatrix} * \begin{bmatrix} \ddot{\mathrm{x}}_1 \\ \vdots \\ \ddot{\mathrm{x}}_\mathrm{n} \end{bmatrix} \quad (a)$$

$$\underline{\mathrm{fI}} = \underline{\underline{\mathrm{M}}} * \underline{\ddot{\mathrm{x}}} \quad (b)$$

The mass matrix is symmetric, therefore $m_{ij}=m_{ji}$.

There are two different approaches to define the mass of the structures, assumed mode method and lumped masses. While the former presents a more physical continuous mass distribution along the elements the latter represent a simplified discretized or point mass on the DOF's. While The assumed mass mode is more precise in the approximation of the mass system, the lumped mass approaches provides a simple definition of the mass from a practical point of view.

The two approaches were implemented in the development of the model for the MDOF analysis to profit of the advantages of one or the other according to structural necessities. Therefore, both methods will be explained herein.

6.2.1.1 Assumed mode method-Consistent mass matrix.

This method is based on an approximation (assumption) of the deformed shape of the structure with Hermite shape functions, supposing the velocities will follow the same shape of the displacements. Very briefly the idea of the method is to obtain the gradient of kinetic energy associated with the mass and the velocity. The mass matrix could be expressed as coefficient matrix of the quadratic form associated to the kinetic energy of the system.

Equation 6-3

$$\dot{\mathrm{u}}(\mathrm{x},\mathrm{t}) = \dot{\mathrm{u}}(\mathrm{t}) * \psi(\mathrm{x})$$

Equation 6-3 shows the decomposition of the velocity in space and time as a function of time and the ψ(x) shape function on space. The Kinect energy is therefore:

Equation 6-4

$$T(\dot{\mathrm{u}}) = 1/2\left\{\int \rho\,[\,\dot{\mathrm{u}}(\mathrm{t}) * \psi(\mathrm{x})] * [\,\dot{\mathrm{u}}(\mathrm{t}) * \psi(\mathrm{x})]\mathrm{dl}\right\} \qquad \text{(a)}$$

$$T(\dot{\mathrm{u}}) = 1/2\,\dot{\mathrm{u}}(\mathrm{t})\left\{\int \rho\,[\psi(\mathrm{x})^T * \psi(\mathrm{x})]\mathrm{dl}\right\}\,\dot{\mathrm{u}}(\mathrm{t}) \qquad \text{(b)}$$

$$\frac{\partial T(\dot{\mathrm{u}})}{\partial \dot{\mathrm{u}}(\mathrm{t})} = \int \rho\,[\psi(\mathrm{x})^T * \psi(\mathrm{x})]\mathrm{dl}\,\dot{\mathrm{u}}(\mathrm{t}) \qquad \text{(c)}$$

For the Lagragian equation it is need the gradient of the kinetic energy Equation 6-5 (a), and the consistent mass matrix Equation 6-5 (b).

Equation 6-5

$$\frac{d.}{dt}\left[\frac{\partial T(\,\dot{\mathrm{u}})}{\partial \dot{\mathrm{u}}(\mathrm{t})}\right] = \int \rho\,[\psi(\mathrm{x})^T * \psi(\mathrm{x})]\mathrm{dl}\dot{\mathrm{u}}(\mathrm{t}) \qquad \text{(a)}$$

$$\underline{\underline{M}} = \int \rho\,[\psi(\mathrm{x})^T * \psi(\mathrm{x})]\mathrm{dl} \qquad \text{(b)}$$

As it was explained before the consistency mass matrix is given by the quadratic form of the Hermite shape functions.

The definition of the previous ψ functions depends on the approximation of the displacement field according to the characteristics of the Finite Elements used in the model of the structure. for the case of Timoshenko elements, typical FE used for simulations of beams the shape functions are Hermite polynomial of third degree. The choose of this type of element instead of the Euler-Bernulli classical elements is the capability of the former to reproduce the shear deformability and the rotational inertia of the elements. Special considerations must be done in the case of shear locking for this type of elements, as the implementation of reduced integration scheme (Corigliano 2005).

The mass matrix adapted from (Gavin 2016) is the following:

Equation 6-6

$$M = \frac{\rho A L}{840}\begin{bmatrix} 280 & 0 & 0 & 140 & 0 & 0 \\ & 312+588\phi+280\phi^2 & \left(44+77\phi+35\phi^2\right)L & 0 & 108+252\phi+175\phi^2 & -\left(26+63\phi+35\phi^2\right)L \\ & & \left(8+14\phi+7\phi^2\right)L^2 & 0 & \left(26+63\phi+35\phi^2\right)L & -\left(6+14\phi+7\phi^2\right)L^2 \\ & & & 280 & 0 & 0 \\ & & SYM & & 312+588\phi+280\phi^2 & -\left(44+77\phi+35\phi^2\right)L \\ & & & & & \left(8+14\phi+7\phi^2\right)L^2 \end{bmatrix}$$

Where ϕ is a function considering the shear deformability, depends on the shear correction factor χ, a coefficient that allows accounts for the non-uniform shear distribution on the cross section allowing to approximate the integration scheme. The ϕ could be obtained as:

$$\phi = \frac{12EI}{G(A/\chi)L\hat{}2}$$

For rectangular sections χ is equal to 6/5 while for circular cross sections is equal to 10/9.

6.2.1.2 Lumped mass matrix

The lumped mass matrix provides a respectable and simple approximation for the mass distribution, Figure 6-1 Inertia forces shows a typical lumped mass scheme. It is worth noting that this is method is widely used for the implementation of commercial computer codes.

The important concept in the construction of a lumped mass matrix is the conservation of the momentum i.e. quantity of movement. Figure 6-2 shows a distribution of the masses of a beam element through its end nodes.

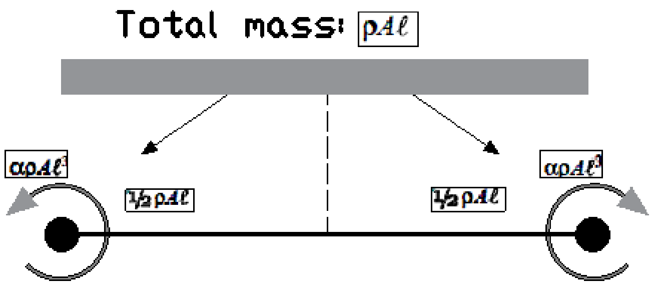

Figure 6-2: Lumped mass

The parameter α (Felippa 2013) accounts for the conservation of momentum. If the choice of this is taken to match the inertia of the element rotating on its midpoint, α will take values of -1/24. The best value for α is zero leading to a singular matrix already which, as told before, is not suitable for the structural analysis needing the inversion of the matrix (or use static condensation disregarding damping related to mass-less DOF's). To account for this problem, a possibility is to reduce the size of problem during the modal analysis stage disregarding an amount of modes greater or equal to the defect (size-rank) of the mass matrix.

6.2.2 Stiffness matrix

The elastic restoring forces are those equilibrating the applied forces relative to the resultant displacements x_j on the DOF's of the structure (Chopra 2012). Again, applying a unit displacement in the *DOF-j* while the others are restrained it is possible to recall the elastic restoring forces as:

Equation 6-7

$$\mathrm{fe_j} = \mathrm{k_{1j}} * \mathrm{x_1} + \mathrm{k_{2j}} * \mathrm{x_2} + \ldots + \mathrm{k_{nj}} * \mathrm{x_n}$$

Graphically the elastic forces could be represented as follows:

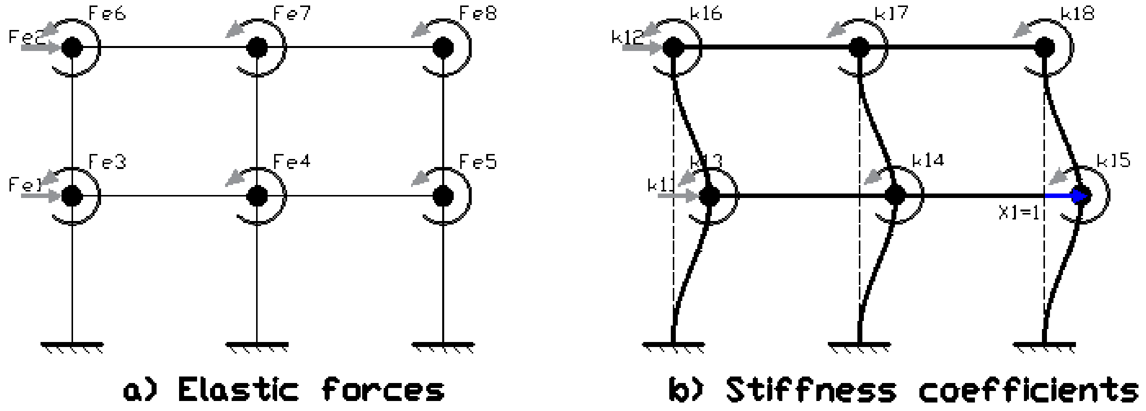

a) Elastic forces b) Stiffness coefficients

Figure 6-3: elastic restoring forces

The reaction force on the DOF j due to an application of a force in the DOF i is the stiffness coefficient k_{ij}. The matrix representation of the stiffness matrix is given in Equation 6-8.

Equation 6-8

$$\begin{bmatrix} fe_1 \\ \vdots \\ fe_j \end{bmatrix} = \begin{bmatrix} k_{11} & \cdots & k_{1n} \\ \vdots & \ddots & \vdots \\ k_{n1} & \cdots & k_{nn} \end{bmatrix} * \begin{bmatrix} \mathrm{x_1} \\ \vdots \\ \mathrm{x_n} \end{bmatrix} \; (a)$$

$$\underline{f}e = \underline{\underline{\mathrm{K}}} * \underline{x} \; (b)$$

The stiffness matrix of a structure is symmetric $k_{ij}=k_{ji}$ and positive definite, therefore non-singular and all the terms in the diagonal are positive.

For the description of structural scheme, the Finite Element Method was implemented i.e. the structural elements are subdivided and the space integration was computed numerically by approximating the displacement with Hermite functions. As was explained before, the select FE for the simulation of beams was the Timoshenko element since it can capture the shear deformability of the beam and the rotational inertia. The family of shape functions used according to (Felippa 2013) (Corigliano 2005) (Gavin 2016). For a 2D beam element the description of the DOF is given in Figure 6-4.

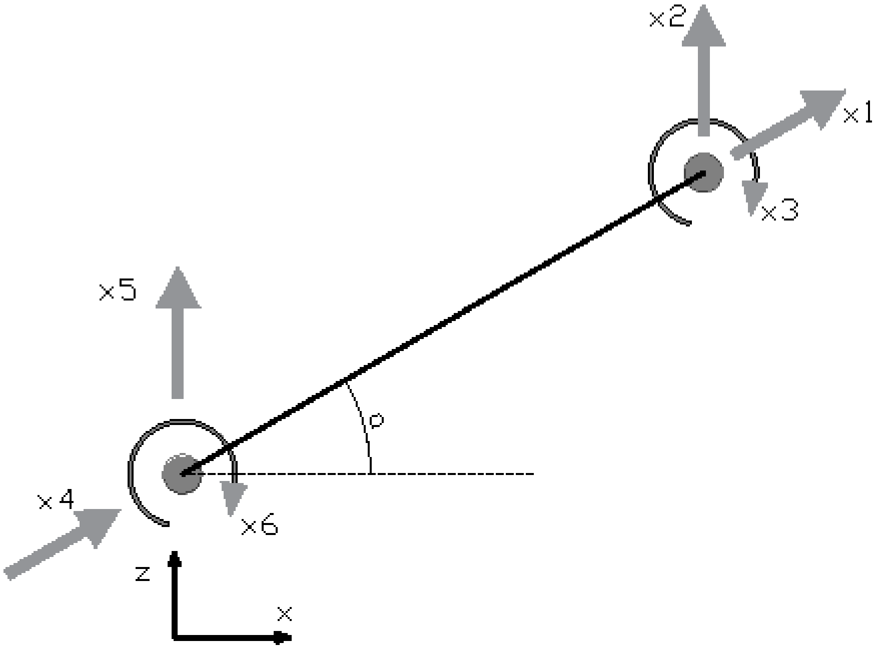

Figure 6-4: Reference frame for beam 2D DOF

The shape functions defining the displacement field are given in Equation 6-9 while the stiffness matrix is Equation 6-10.

Equation 6-9

$$\begin{aligned}
\psi_{(b)y2}(x) &= \frac{1}{1+\Phi}\left[1-3\left(\frac{x}{L}\right)^2+2\left(\frac{x}{L}\right)^3\right]\\
\psi_{(s)y2}(x) &= \frac{\Phi}{1+\Phi}\left[1-\frac{x}{L}\right]\\
\psi_{(b)y3}(x) &= \frac{L}{1+\Phi}\left[\frac{x}{L}-2\left(\frac{x}{L}\right)^2+\left(\frac{x}{L}\right)^3+\frac{1}{2}\left(2\frac{x}{L}-\left(\frac{x}{L}\right)^2\right)\Phi\right]\\
\psi_{(s)y3}(x) &= -\frac{L\Phi}{1+\Phi}\left[\frac{1}{2}\frac{x}{L}\right]\\
\psi_{(b)y5}(x) &= \frac{1}{1+\Phi}\left[3\left(\frac{x}{L}\right)^2-2\left(\frac{x}{L}\right)^3\right]\\
\psi_{(s)y5}(x) &= \frac{\Phi}{1+\Phi}\left[\frac{x}{L}\right]\\
\psi_{(b)y6}(x) &= \frac{L}{1+\Phi}\left[-\left(\frac{x}{L}\right)^2+\left(\frac{x}{L}\right)^3+\frac{1}{2}\left(\left(\frac{x}{L}\right)^2\right)\Phi\right]\\
\psi_{(s)y6}(x) &= -\frac{L}{1+\Phi}\left[\frac{1}{2}\frac{x}{L}\Phi\right]
\end{aligned}$$

Equation 6-10

$$\mathrm{K}=\begin{bmatrix}
\frac{EA}{L} & 0 & 0 & -\frac{EA}{L} & 0 & 0\\
 & \frac{12}{1+\phi}\frac{EI}{L^3} & \frac{6}{1+\phi}\frac{EI}{L^2} & 0 & -\frac{12}{1+\phi}\frac{EI}{L^3} & \frac{6}{1+\phi}\frac{EI}{L^2}\\
 & & \frac{4+\phi}{1+\phi}\frac{EI}{L} & 0 & -\frac{6}{1+\phi}\frac{EI}{L^2} & \frac{2-\phi}{1+\phi}\frac{EI}{L}\\
 & & & \frac{EA}{L} & 0 & 0\\
 & & SYM & & \frac{12}{1+\phi}\frac{EI}{L^3} & -\frac{6}{1+\phi}\frac{EI}{L^2}\\
 & & & & & \frac{4+\phi}{1+\phi}\frac{EI}{L}
\end{bmatrix}$$

Extending the case for 3D space elements a couple of modifications must be included. The scheme of degrees of freedom changes to that shown in Figure 6-5. The introduction of further angle of inclination.

The shape functions defining the displacement field are the same for the flexural and transversal displacements. For the torsional effects considering the uniform torsion theory (St Venant.) is enough by using the standard 6 DOF FE neglecting the warping effect (Vlasov theory) this approach is only valid because the structural cross section to be studied here in are double symmetric. Therefore, the shape functions of the axial behavior (ψ1 and ψ4 of 2D) could describe the behavior, considering only the change of E young modulus with G shear modulus.

The final scheme for stiffness matrix is given by (Biondini 2017). The same approach could be applied for the mass matrix, Equation 6-11 a) & b) shows the matrixes of stiffness and mass respectively for the 3D beam element.

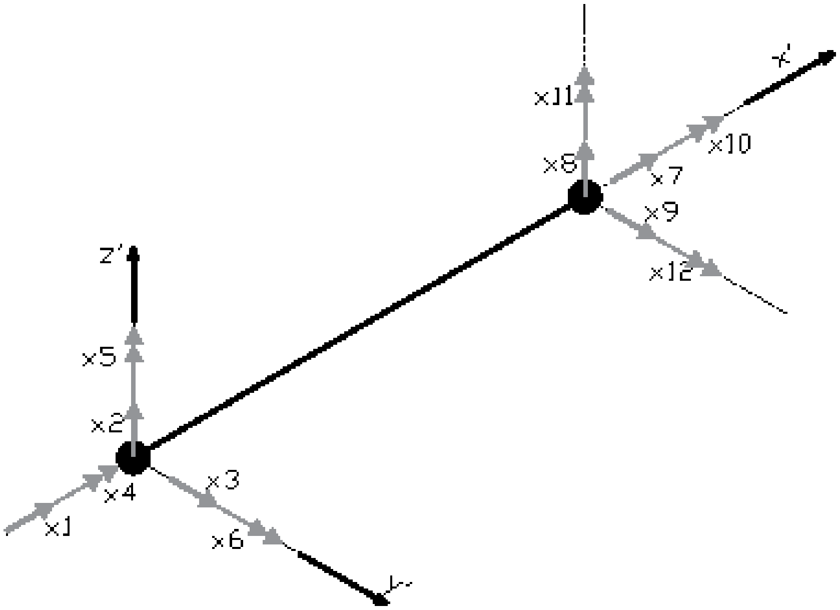

Figure 6-5: Reference frame for beam 3D DOF

Z-dof with the inertia in y and shear function in z. Y-dof with inertia along Z and shear function of y

Equation 6-11

$$
\mathrm{K}=\begin{bmatrix}
\frac{EA}{L} & 0 & 0 & 0 & 0 & 0 & -\frac{EA}{L} & 0 & 0 & 0 & 0 & 0 \\
 & \frac{12}{1+\phi z}\frac{EIy}{L^3} & 0 & 0 & 0 & \frac{6}{1+\phi z}\frac{EI}{L^2} & 0 & -\frac{12}{1+\phi z}\frac{EI}{L^3} & 0 & 0 & 0 & \frac{6}{1+\phi z}\frac{EI}{L^2} \\
 & & \frac{12}{1+\phi y}\frac{EIz}{L^3} & 0 & -\frac{6}{1+\phi y}\frac{EI}{L^2} & 0 & 0 & 0 & -\frac{12}{1+\phi y}\frac{EIz}{L^3} & 0 & -\frac{6}{1+\phi y}\frac{EI}{L^2} & 0 \\
 & & & \frac{GJ}{L} & 0 & 0 & 0 & 0 & 0 & -\frac{GJ}{L} & 0 & 0 \\
 & & & & \frac{4+\phi y}{1+\phi y}\frac{EI}{L} & 0 & 0 & 0 & \frac{6}{1+\phi y}\frac{EI}{L^2} & 0 & \frac{2-\phi y}{1+\phi y}\frac{EI}{L} & 0 \\
 & & & & & \frac{4+\phi z}{1+\phi z}\frac{EI}{L} & 0 & -\frac{6}{1+\phi z}\frac{EI}{L^2} & 0 & 0 & 0 & \frac{2-\phi z}{1+\phi z}\frac{EI}{L} \\
 & & & & & & \frac{EA}{L} & 0 & 0 & 0 & 0 & 0 \\
 & & & & & SYM & & \frac{12}{1+\phi z}\frac{EIy}{L^3} & 0 & 0 & 0 & -\frac{6}{1+\phi z}\frac{EI}{L^2} \\
 & & & & & & & & \frac{12}{1+\phi y}\frac{EIz}{L^3} & 0 & \frac{6}{1+\phi y}\frac{EI}{L^2} & 0 \\
 & & & & & & & & & \frac{GJ}{L} & 0 & 0 \\
 & & & & & & & & & & \frac{4+\phi y}{1+\phi y}\frac{EI}{L} & 0 \\
 & & & & & & & & & & & \frac{4+\phi z}{1+\phi z}\frac{EI}{L}
\end{bmatrix} \quad (a)
$$

$$
\begin{aligned}
&\mathrm{M}\\
&=\frac{\rho A L}{840}\begin{bmatrix}
280 & 0 & 0 & 0 & 0 & 0 & 140 & 0 & 0 & 0 & 0 & 0\\
 & 312+588\phi z+280\phi z^{2} & 0 & 0 & 0 & \left(44+77\phi z+35\phi z^{2}\right)L & 0 & 108+252\phi z+175\phi z^{2} & 0 & 0 & 0 & -\left(26+63\phi z+35\phi z^{2}\right)L\\
 & & 312+588\phi y+280\phi y^{2} & 0 & \left(26+63\phi y+35\phi y^{2}\right)L & 0 & 0 & 0 & 108+252\phi y+175\phi y^{2} & 0 & \left(44+77\phi y+35\phi y^{2}\right)L & 0\\
 & & & 280L2 & 0 & 0 & 0 & 0 & 0 & 140L2 & 0 & 0\\
 & & & & \left(8+14\phi y+7\phi y^{2}\right)L^{2} & 0 & 0 & 0 & -\left(26+63\phi y+35\phi y^{2}\right)L & 0 & -\left(6+14\phi y+7\phi y^{2}\right)L^{2} & 0\\
 & & & & & \left(8+14\phi z+7\phi z^{2}\right)L^{2} & 0 & \left(26+63\phi z+35\phi z^{2}\right)L & 0 & 0 & 0 & -\left(6+14\phi z+7\phi z^{2}\right)L^{2}\\
 & & & & & & 280 & 0 & 0 & 0 & 0 & 0\\
 & & & & & SYM & & 312+588\phi z+280\phi z^{2} & 0 & 0 & 0 & -\left(44+77\phi z+35\phi z^{2}\right)L\\
 & & & & & & & & 312+588\phi y+280\phi y^{2} & 0 & \left(44+77\phi y+35\phi y^{2}\right)L & 0\\
 & & & & & & & & & 280L2 & 0 & 0\\
 & & & & & & & & & & \left(8+14\phi y+7\phi y^{2}\right)L^{2} & 0\\
 & & & & & & & & & & & \left(8+14\phi z+7\phi z^{2}\right)L^{2}
\end{bmatrix}\quad(b)
\end{aligned}
$$

6.2.3 Transformation of coordinates

The stiffness and mass matrixes have been so far defined in the local reference frame of the elements. With the aim of giving a uniform definition of the full set of elements composing the structure, the structure itself has a reference frame of coordinates not necessarily equal to each element local reference. Therefore, a transformation rule uniform for every element must be implemented (Biondini 2017).

It is worth noting that the for the definition of an element in the space it is necessary to define the coordinates of three points. Points 1 and 2 correspond to the end nodes *i-point* and *j-point* already defined, while the point #3 stands for the giving the direction to the local axis in the global reference frame. The definition of this point inside the code, is automatically computed by the algorithm for every element.

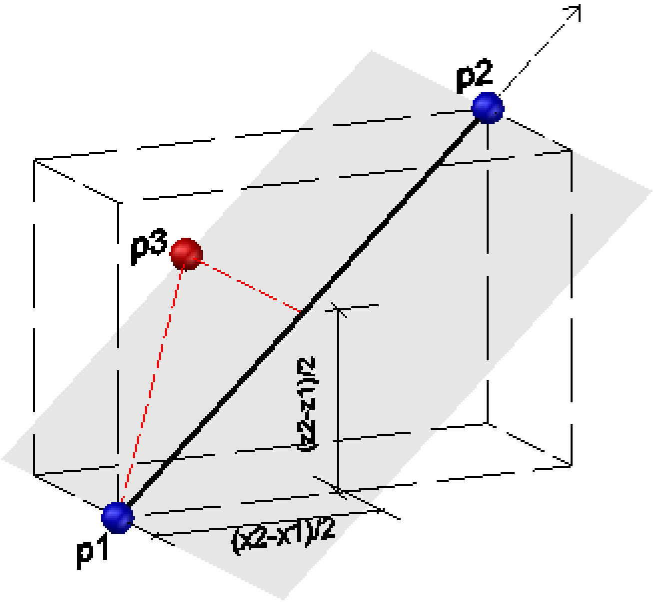

Figure 6-6: Generic element 3point definition

According to Figure 6-6 the *x-coordinate* and *z-coordinate* of point 3 are the those of the mid-point of the generic element. Regarding the *y-coordinate*, it can be any generic ordinate inside the orthogonal plane of the element shadowed in Figure 6-6. The definition of the latter is made inside the computer code by means of trigonometric relations.

Transformation matrix is based in the cosine directors.

Equation 6-12

$$\text{To} = [\text{Cx' Cy' Cz'}] = \begin{bmatrix} \text{Cx'x} & \text{Cy'x} & \text{Cz'x} \\ \text{Cx'y} & \text{Cy'y} & \text{Cz'y} \\ \text{Cx'z} & \text{Cy'z} & \text{Cz'z} \end{bmatrix}$$

To get the Cosine directors it is needed first to define the Euclidian metrics:

Equation 6-13

$$\begin{cases} \|X_{ij}\| = \sqrt{x_{ij}^2 + y_{ij}^2 + z_{ij}^2} = l_{ij} \\ \|x_{12} \wedge x_{13}\| = \sqrt{(y_{21}z_{31} - y_{31}z_{21})^2 + (z_{21}x_{31} - z_{31}x_{21})^2 + (x_{21}y_{31} - x_{31}y_{21})^2} = 2A_{123} \end{cases}$$

Equation 6-14

$$\text{Cx}' = \frac{X_{12}}{\|X_{12}\|} = \frac{1}{l_{12}} * \begin{bmatrix} x2 - x1 \\ y2 - y1 \\ z2 - z1 \end{bmatrix} \ (a)$$

$$\text{Cz}' = \frac{x_{12} \wedge x_{13}}{\|x_{12} \wedge x_{13}\|} = \frac{1}{2A_{123}} * \begin{bmatrix} y_{21}z_{31} - y_{31}z_{21} \\ z_{21}x_{31} - z_{31}x_{21} \\ x_{21}y_{31} - x_{31}y_{21} \end{bmatrix} \ (b)$$

$$\text{Cy}' = \text{Cz}' \wedge Cx' = \begin{bmatrix} Cz'yCx'z - Cx'yCz'z \\ Cz'zCx'x - Cz'xCx'z \\ Cz'xCx'y - Cx'xCz'y \end{bmatrix} \ (c)$$

Recalling the DOF’s distribution of the generic element of Figure 6-5 in the global reference frame, renaming those DOF’s in the local reference frame a representation as that shown in Figure 6-7 for displacement and forces is valid:

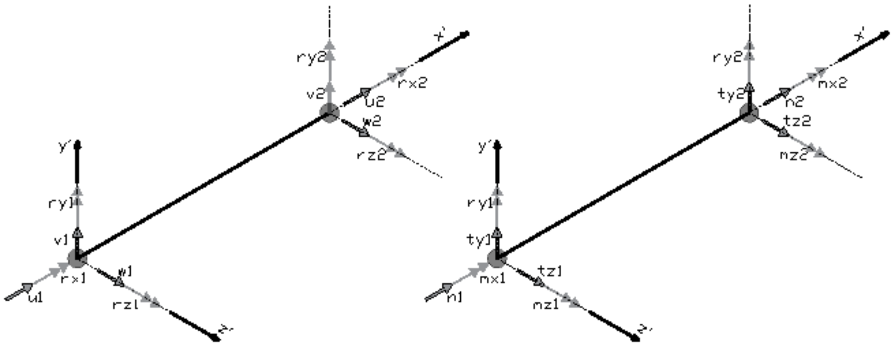

Figure 6-7: Displacements and forces on the degrees of freedom

The displacements and forces can be regarded as:

$$\begin{cases} S' = [u_1\ v_1\ w_1 | r_{x1}\ r_{y1}\ r_{z1} | u_2\ v_2\ w_2 | r_{x2}\ r_{y2}\ r_{z2}]^T\ in\ local\ R.F. \\ S = [x_1\ x_2\ x_3 | x_4\ x_5\ x_6 | x_7\ x_8\ x_9 | x_{10}\ x_{11}\ x_{12}]^T\ in\ global\ R.F. \end{cases}$$

$$\begin{cases} f' = [n_1\ t_{y1}\ t_{z1} | m_{x1}\ m_{y1}\ m_{z1} | n_2\ t_{y2}\ t_{z2} | m_{x2}\ m_{y2}\ m_{z2}]^T\ in\ local\ R.F. \\ \qquad F = [f_1\ f_2\ f_3 | f_4\ f_5\ f_6 | f_7\ f_8\ f_9 | f_{10}\ f_{11}\ f_{12}]^T\ in\ global\ R.F. \end{cases}$$

Introducing the full transformation matrix ***T*** as:

Equation 6-15

$$\boldsymbol{T} = \begin{bmatrix} \boldsymbol{To} & \mathbf{0} & \mathbf{0} & \mathbf{0} \\ \mathbf{0} & \boldsymbol{To} & \mathbf{0} & \mathbf{0} \\ \mathbf{0} & \mathbf{0} & \boldsymbol{To} & \mathbf{0} \\ \mathbf{0} & \mathbf{0} & \mathbf{0} & \boldsymbol{To} \end{bmatrix}$$

Where the $\mathbf{0}$ are matrixes of 3x3 the same size as ***To.*** The transformation matrix an orthonormal matrix. The transformation rule from local to global reference frame is:

Equation 6-16

$$\begin{cases} \boldsymbol{S} = \boldsymbol{T}\ \boldsymbol{s}' \\ \boldsymbol{F} = \boldsymbol{T}\ \boldsymbol{f}' \end{cases}$$

The stiffness matrix in terms of the global reference frame can be obtained as:

Equation 6-17

$$\boldsymbol{K} = \boldsymbol{T}\ \boldsymbol{K}'\ \boldsymbol{T}^T$$

6.2.4 Eigenvalue problem: free vibration

The movement of MDOF systems in free vibration is important for the description of the natural frequencies and the vibration shapes. The governing equation for the system is:

Equation 6-18

$$\mathbf{M}\ \ddot{\mathbf{x}} + \mathbf{K}\mathbf{x} = \mathbf{0}$$

The Equation 6-18 represent N homogenous differential equations assembled by means of the mass and the stiffness matrixes. N also represents the degrees of freedom of the structure. The Equation 6-18 could be handled as an eigenvalue problem of N equations as Equation 6-19 (a), the solution of which give the natural frequencies (ωn) and the modal shapes (**φ**n) (Equation 6-19 (b)).

Equation 6-19

$$[\mathbf{K} - \omega_n^2 \mathbf{M}]\boldsymbol{\varphi}_\mathrm{n} = 0 \text{ (a)}$$

$$\det[\mathbf{K} - \omega_n^2 \mathbf{M}] = 0 \text{ (b)}$$

In the expansion of the determinant (Equation 6-9b) of it is obtained a polynomial of order N and base ω_n. The solution of Equation 6-19 (b) has N roots all positive since the mass and the stiffness matrixes are positive definite. Moreover, the N roots define the natural frequencies of the structure. Once the ω_n values are known it could be possible to obtain the modal shape $\boldsymbol{\varphi}_n$ related to each natural frequency by means of Equation 6-19 (a). The ω_n^2 values are known as eigenvalues while the $\boldsymbol{\varphi}_n$ are known as eigenvectors.

It is worth noting that the eigenvalues and eigenvectors associated to Equation 6-18 could be a grouped in matrix format. The assemble of the mode shapes is a square matrix known as *The Modal Matrix* Equation 6-20 (a) contains the eigenvectors organized coherently with the eigenvalues, by its way the assemble of the eigenvalues is a diagonal matrix known as *The Spectral Matrix* Equation 6-20 (b).

Equation 6-20

$$\boldsymbol{\phi} = [\varphi_{\mathrm{jn}}] = \begin{bmatrix} \varphi_{11} & \cdots & \varphi_{1\mathrm{n}} \\ \vdots & \ddots & \vdots \\ \varphi_{\mathrm{n}1} & \cdots & \varphi_{\mathrm{nn}} \end{bmatrix} \text{ (a)}$$

$$\boldsymbol{\Omega}^2 = \begin{bmatrix} \omega_1^2 & & \\ & \ddots & \\ & & \omega_\mathrm{n}^2 \end{bmatrix} \text{ (b)}$$

It has been so far proved (Chopra 2012) that the modes have the property of create an orthogonal base then, the multiplication of different two mode vectors will give zero as result Equation 6-21. In a further step and due to the above-mentioned property, the multiplication of the stiffness and mass matrixes with the modal matrix will give rise to diagonal matrixes.

Equation 6-21

$$\boldsymbol{\varphi}_\mathrm{n}^T * \boldsymbol{\varphi}_\mathrm{r} = 0, n \neq r$$

Equation 6-22

$$\mathbf{K} = \boldsymbol{\phi}^{\boldsymbol{T}} \mathbf{k}\, \boldsymbol{\phi} \qquad \mathbf{M} = \boldsymbol{\phi}^{\boldsymbol{T}} \mathbf{m}\, \boldsymbol{\phi}$$

The diagonal terms inside the matrixes are given by:

Equation 6-23

$$\mathrm{K}_{\mathbf{n}} = \boldsymbol{\varphi}_{\mathrm{n}}^{T}\,\mathbf{k}\,\boldsymbol{\varphi}_{\mathrm{n}} \qquad \mathbf{M}_{\mathbf{n}} = \boldsymbol{\varphi}_{\mathrm{n}}^{T}\,\mathbf{m}\,\boldsymbol{\varphi}_{\mathrm{n}}$$

The solution of Equation 6-19 (a) giving the eigenvectors finds the relative shape values, therefore any proportional value to $\varphi\mathrm{n}$ stills being an eigenvector of the system because the equation is still being satisfied. This allows to scale the modal shapes such that a particular term in the equations has a certain control value, this process is known as normalization. For the present document the normalization process will be performed such that the modal mass matrix becomes an identity, unless a particular problem requires a different definition.

Equation 6-24

$$\mathrm{M}\mathbf{n} = [\alpha_{\mathrm{n}} * \boldsymbol{\varphi}_{\mathrm{n}}^{T}]\,\mathbf{m}\,[\alpha_{\mathrm{n}} * \boldsymbol{\varphi}_{\mathrm{n}}] \ = \mathbf{1} \qquad \mathbf{M} = [\boldsymbol{\alpha} * \boldsymbol{\phi}^{T}]\,\mathbf{m}\,[\boldsymbol{\alpha} * \boldsymbol{\phi}] = \ \mathbf{I}$$

It might be useful to introduce a scale factor (α) to rend the mass terms in Equation 6-22 and Equation 6-23 as the desired normalization Equation 6-24. To do so the scale factor must be:

Equation 6-25

$$\alpha_{\mathrm{n}} = \frac{1}{\sqrt{M_n}}; \ \ \boldsymbol{\alpha} = \begin{bmatrix} \alpha_1 \\ \vdots \\ \alpha_{\mathrm{n}} \end{bmatrix}$$

Using the normalized modal matrix is then possible to recall the stiffness matrix in the *mass normalized form* as the *spectral matrix.* Equation 6-26.

Equation 6-26

$$\mathbf{K} = [\boldsymbol{\alpha} * \boldsymbol{\phi}^{T}]\,\mathbf{k}\,[\boldsymbol{\alpha} * \boldsymbol{\phi}] = \boldsymbol{\Omega}^{2}$$

6.2.5 Damping matrix

There are many mechanisms providing energy dissipation inside the structures such as the frictional forces of the connections, the hysteretic behavior of the material, the interaction between soil and foundations or the contact with a viscous material (aerodynamic or hydrodynamic damping) and of course the addition of damping devices. All of those could be idealized as an equivalent viscous damping. With this hypothesis, it is possible to relate the external forces associated to the velocity vj of a structure with the damping forces needed to equilibrate the system as shown in Figure 6-8: Damping forces.

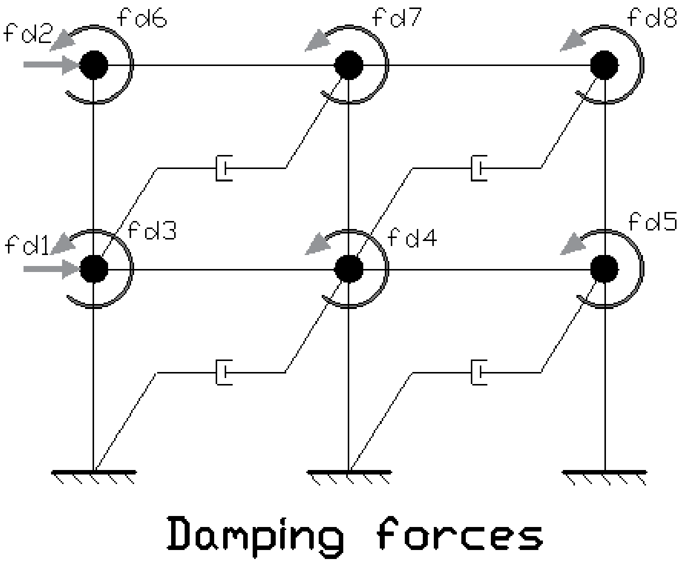

Figure 6-8: Damping forces

The damping forces could be represented as given in Equation 6-27. Then, the coefficient cij represent the reaction force in the node i for the application of a unit velocity at node j.

Equation 6-27

$$\mathrm{fd_j} = \mathrm{C_{1j}} * \mathrm{v_1} + \mathrm{C_{2j}} * \mathrm{v_2} + \ldots + \mathrm{C_{nj}} * \mathrm{v_n}$$

In matrix format

Equation 6-28

$$\begin{bmatrix} fd_1 \\ \vdots \\ fd_j \end{bmatrix} = \begin{bmatrix} C_{11} & \cdots & C_{1n} \\ \vdots & \ddots & \vdots \\ C_{n1} & \cdots & C_{nn} \end{bmatrix} * \begin{bmatrix} \mathrm{v_1} \\ \vdots \\ \mathrm{v_n} \end{bmatrix} \ (a)$$

$$\underline{f}d = \underline{\underline{\mathrm{C}}} * \underline{v} \ (b)$$

To define the damping matrix in the structures there are many accepted methods as the Rayleigh damping or the Caughey damping. All of those always inside the classical damping reference frame. Herein it will be explained the procedure adopted in this document for the definition of the damping which is the well-known modal approach also classical.

The modal approach for the definition of the damping is based on the damping ratios ζ. It starts from the definition of the modal damping matrix as:

Equation 6-29

$$\mathbf{C} = \boldsymbol{\phi}^{\boldsymbol{T}} \mathbf{c}\, \boldsymbol{\phi}$$

Due to the orthogonality of the modes C is diagonal and the generic term inside the matrix could be computed as:

Equation 6-30

$$\mathrm{C_n} = \zeta_\mathrm{n}(2\mathrm{M_n}\omega_\mathrm{n})$$

The damping ratios could be computed from experimental data, however a common practice in engineering is to use fixed values according with the type structure (Newmark 1982) i.e. for buildings composed by steel frames with welded connection ζ is 2-3% (Frictional behavior) and for those composed by reinforced concrete (with remarkable cracking) ζ varies from 3-5% (hysteretic dissipation). For the long structures subjected to wind actions such as bridges and cables for power line systems (and other structures with flexible dynamic behavior), the values that ζ can adopt are much lower in a range less than 0.5%.

Taking advantages of the properties of modal vectors and inverting the Equation 6-29 is possible then to write a pragmatic expression for the computation of the damping matrix as (Chopra 2012):

Equation 6-31

$$\mathbf{c} = \mathbf{m}\left(\sum_{n=1}^{N} \frac{2\zeta_n\omega_n}{M_n} \varphi_n\varphi_n^T\right)\mathbf{m}$$

This approach ensures that damping ratio for all the modes is going the be kept constant

6.2.6 Modal coordinates and superposition

The modal matrix is composed by N independent vectors that could be used as base to define any other vector of size N. Therefore, any displacement vector **x** could be expressed in terms of its modal expansion as:

Equation 6-32

$$\mathbf{x} = \sum_{r=1}^{N} \boldsymbol{\varphi_r} * \boldsymbol{q_r} = \boldsymbol{\phi q}$$

The terms q_r are scalar multipliers called modal coordinates and the vector **q** is the assemble of the coordinates.

The modal coordinates are relative to the so-called Lagragian coordinates arising when the dynamic problem is derived from the energy conservation rather than an equilibrium approach.

In the case of classical damping the modal analysis allows to solve the equations of motion as N decupled SDOF equations of the form given in Equation 6-33 . The modal coordinates are then found for each single system and with Equation 6-32 is possible to recall the displacement vector in natural coordinates.

Equation 6-33

$$\mathrm{M_n}\,\ddot{\mathrm{q}}_\mathrm{n} + \mathrm{C_n}\,\dot{\mathrm{q}}_\mathrm{n} + \mathrm{K_n}\,\mathrm{q_n} = \mathrm{P_n(t)}$$

In the case of the aeroelastic phenomena there are some cases in which the link between the damping of the structure and the damping of wind effects gives rise to a coupling of the equations of motion in modal coordinates not allowing to write the systems as Equation 6-33. Therefore, the modal analysis will only act as a tool for reducing the size of the problem from the N DOF in natural coordinates to the M<N dynamic degrees of freedom in modal coordinates.

6.3 Aeroelastic effects on slender structures

The wind effects over bluff bodies are governed by the buffeting force, i.e. the aerodynamic component of the wind force due to the turbulent fluctuations in the incoming flow. This action is produced by the impinging of the turbulent wind particles with the body, giving rise also to a turbulent force component dependent of the body shape and the wind velocity characteristics.

For the case of slender bodies, the effect of the turbulent wind could be remarkably important due to the dynamic components of the wind actions that could not be approximated by the equivalent static force methods. Moreover, a coupling between the aeroelastic components with the damping and stiffness may arise for this type of structures, suggesting a highly dynamic effect that must be carefully studied. Considering the cross section of a deformable-slender body submitted to wind actions as shown in Figure 6-9, some important facts could be highlighted: the aerodynamic action applied to the *j-th* sectional model (Equation 6-54 to Equation 6-61) could be easily extended to the global behavior with the correct assembly procedure, the quantities actually acting on the structure depend on the incoming wind velocities and the approximation angle $\beta(t)$ given by Equation 3-17. The action will be first derived in the wind reference system and then translated to the structure reference system. Calling the turbulent wind components u(t) aligned with the mean wind vector (along wind) and v(t) the cross-wind component orthogonal to the mean velocity vector, it is possible to write the expression for the instantaneous forces acting on the body as:

Equation 6-34

$$\begin{cases} F_D(z,t) = 0.5\rho B(z) C_D(\psi) V_{rel}^2 \quad (a) \\ F_L(z,t) = 0.5\rho B(z) C_l(\psi) V_{rel}^2 \quad (b) \end{cases}$$

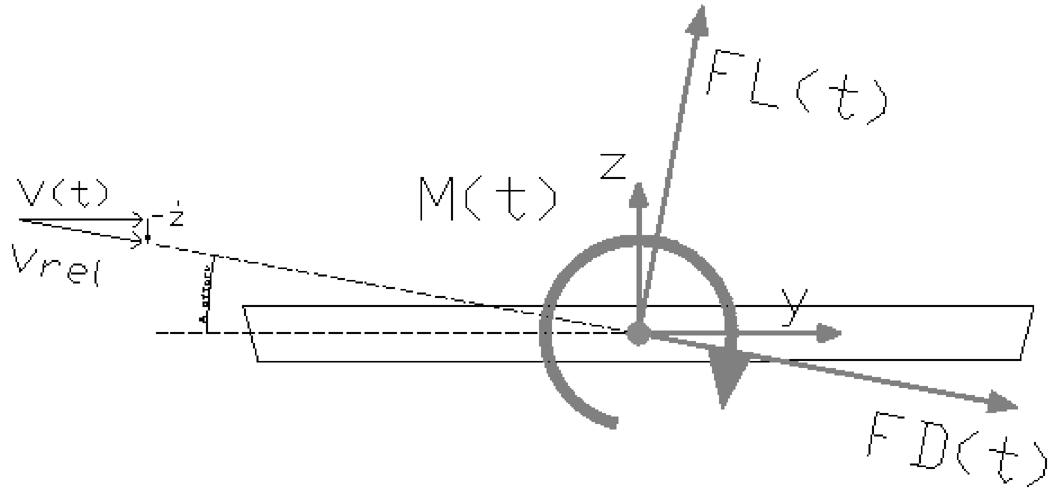

Figure 6-9 Slender body with wind actions

The term V_{rel} stands for the relative velocity between the incoming wind flow and the body motion, is this component actual velocity giving rise to aeroelastic effects, could be compute as Equation 6-35. On the other hand, the instantaneous angle of attack ψ represents the wind velocity components on the reference frame of the structure motion which gives the direction of the relative velocity. The latter could be computed from trigonometric relations as Equation 6-36.

Equation 6-35

$$V_{rel}^2 = (\mathrm{V(t)} + \mathrm{u(t)} - \dot{\mathrm{x}})^2 + (v(t) - \dot{y})^2$$

Equation 6-36

$$\psi(\mathrm{z,t}) = \mathrm{atan}[\frac{v(t) - \dot{y}}{\mathrm{V(t)} + \mathrm{u(t)} - \dot{\mathrm{x}}}]$$

The forces of Equation 6-34 could be represented for convenience in the wind reference frame as:

Equation 6-37

$$\begin{cases} F_u(z,t) = 0.5\rho B(z) V_{rel}^2 [C_D(\psi) Cos\psi \; - \; C_l(\psi) sin\,\psi] \;\; (a) \\ F_v(z,t) = 0.5\rho B(z) V_{rel}^2 \; [C_D(\psi) sin\psi + C_l(\psi) cos\,\psi] \;\; (b) \end{cases}$$

The wind actions are not necessary passing through the centroid of the cross section therefore a moment action also arises.

Equation 6-38

$$\mathrm{F_m}(\mathrm{z,t}) = 0.5\rho B^2(z)C_m(\psi)V_{rel}^2$$

The forces acting in the structure are given in Figure 6-10.

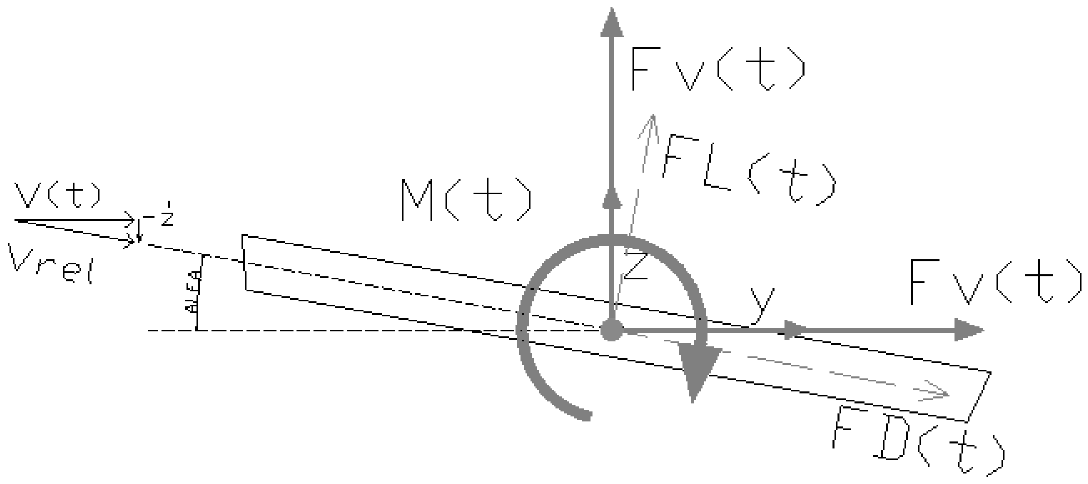

Figure 6-10:Aerodynamic forces acting in a bluff body in body reference system

Considering the rotation of the body:

Equation 6-39

$$\begin{cases} F_u(z,t) = 0.5\rho B(z)V_{rel}^2[C_D(\alpha)Cos\psi\ -\ C_l(\alpha)sin\,\psi]\ \ (a) \\ F_v(z,t) = 0.5\rho B(z)V_{rel}^2\ [C_D(\alpha)sin\psi + C_l(\alpha)cos\,\psi]\ \ (b) \\ F_m(z,t) = 0.5\rho B^2(z)C_m(\alpha)V_{rel}^2 \end{cases}$$

With the relative angle of attack

$$\alpha(\mathrm{t}) = \theta(\mathrm{t}) + \psi(\mathrm{t})$$

The aerodynamic coefficients defining the transformation rule between wind velocities and forces must be measured in experimental test. Those coefficients give a relationship between the associated forces and the wind velocity components. However, their non-linear dependence on the angle of attack α (accounting for ψ and the body rotation) couples them with the turbulent components and the body configuration. With the aim of providing a suitable approach to define buffeting forces, a linearization approach by means of the Queasy Steady Theory will be introduced herein as its widely used for this type of applications. A foreword: the QST is valid for reduced velocities greater than 15 (Diana 2018).

The linearized QST approach supposes a linear variation of the aerodynamic coefficients over a static equilibrium condition Equation 6-40. Therefore, the aerodynamic forces acting in a generic section of the body become linear. All of this based on the hypothesis of small oscillations over the equilibrium configuration which allows to approximate the variation of the coefficients by means of the Taylor expansion of the coefficients as expressed in Equation 6-41.

Equation 6-40

$$\begin{cases} \bar{x} = x - x_o \\ \bar{y} = y - y_o \\ \bar{\theta} = \theta - \theta_o \end{cases}$$

With yo, zo and θo representing the equilibrium condition.

Equation 6-41

$$\mathrm{C_D}(\alpha) = \mathrm{C_D}(\alpha = 0) + \frac{\partial \mathrm{C_D}}{\partial \alpha}|_0 \alpha = \mathrm{C_{Do}} + K_d \alpha \qquad (a)$$

$$\mathrm{C_l}(\alpha) = \mathrm{C_l}(\alpha = 0) + \frac{\partial \mathrm{C_l}}{\partial \alpha}|_0 \alpha = C_{lo} + K_l \alpha \qquad (b)$$

$$\mathrm{C_m}(\alpha) = \mathrm{C_m}(\alpha = 0) + \frac{\partial \mathrm{C_m}}{\partial \alpha}|_0 \alpha = C_{mo} + K_m \alpha \quad (c)$$

Supposing then, that the mean velocity component is greater than the turbulent is possible also to approximate Eq. 3-36 as follows:

Equation 6-42

$$\psi(\mathrm{z,t}) = \frac{\mathrm{v} - \dot{\bar{\mathrm{y}}} - \mathrm{B_1(z)}\dot{\bar{\theta}}}{V} \quad (a)$$

$$\sin\psi = \psi \qquad (\mathrm{b})$$

$$\cos\psi = 1 \qquad (\mathrm{c})$$

Equation 6-43

$$V_{rel}^2 = \mathrm{V^2(t)} + 2\mathrm{V\,u(t)} - 2\mathrm{V}\,\dot{\bar{\mathrm{x}}}$$

A further comment must be done with respect to the reference width $B_1(z)$, it represents the characteristic dimension of the cross section, its definition is referred to empirical and experimental data and its trustful implementation must be done inside the approach of Corrected Quasi Steady Theory (Diana 2018), leading to different values for the three dimensions B_1y B_1z and $B_1\theta$. In case the CQST is not implemented or the experimental test are not available a good approximation is to leave B1y and B_1z as zero and $B_1\theta$ as B(z)

The forces could be expressed as:

Equation 6-44

$$\begin{cases} F_u(z,t) = 0.5\rho B(\mathrm{V}^2(\mathrm{t}) + 2\mathrm{V}\,\mathrm{u(t)} - 2\mathrm{V}\,\dot{\bar{\mathrm{x}}})[(C_{Do} + K_d\alpha\,) - \;(C_{lo}\; + K_l\alpha)\psi] \;\; (a) \\ F_v(z,t) = 0.5\rho B(\mathrm{V}^2(\mathrm{t}) + 2\mathrm{V}\,\mathrm{u(t)} - 2\mathrm{V}\,\dot{\bar{\mathrm{x}}})\;[(Cl_o + K_l\alpha)\psi + (C_{lo}\; + K_l\alpha)] \;\; (b) \\ F_m(z,t) = 0.5\rho B^2(\mathrm{V}^2(\mathrm{t}) + 2\mathrm{V}\,\mathrm{u(t)} - 2\mathrm{V}\,\dot{\bar{\mathrm{x}}})[C_{mo}\; + K_m\alpha] \qquad\qquad (c) \end{cases}$$

Developing the algebraic expression and neglecting the second order terms in angle of attack it is possible to obtain a set of expression that could be grouped by their behavior and characteristics.

The terms associated with the mean velocity are the equilibrium components, normally for synoptic winds with constant mean value of velocity gives rise to static components associated with the mean wind speed, for the case of downburst the mean gives rise to instantaneous equilibrium positions.

Equation 6-45

$$\begin{cases} F_{uq}(z,t) = 0.5\rho B\mathrm{V}^2(\mathrm{t})C_{Do} \;\; (a) \\ F_{vq}(z,t) = 0.5\rho B\mathrm{V}^2(\mathrm{t})C_{lo} \quad (b) \\ F_{mq}(z,t) = 0.5\rho B^2\mathrm{V}^2(\mathrm{t})C_{mo} \;\; (c) \end{cases}$$

The terms associated with the turbulence wind component gives rise to the aerodynamic forces,

Equation 6-46

$$\begin{cases} F_{ud}(z,t) = \rho B\;\mathrm{V}\,[\mathrm{u(t)}C_{Do} - 0.5v(t)C_{lo}\,] \;\; (a) \\ F_{vd}(z,t) = \rho B\mathrm{V}\,[\mathrm{u(t)}C_{lo}\; + 0.5v(t)C_{lo}\,] \;\; (b) \\ F_{md}(z,t) = \rho B\mathrm{V}\,[\mathrm{u(t)}C_{mo}\; + 0.5BK_m] \;\; (c) \end{cases}$$

Those terms associated with the rotation (in general displacement) of the body, give rise to an aerodynamic stiffness. Special care must be done to this part of the equation since its effect over the global stiffness matrix leads to a non-symmetrical matrix which for very particular cases could produce 2 degree of freedom instability (flutter instability) (e.g. when the slope of the moment coefficient is positive making the associated frequency of torsional mode equals to the vertical for a certain wind speed level, then the movement of one degree of freedom is in resonance with the other introducing energy to the system).

Equation 6-47

$$\begin{cases} F_{uk}(z,t) = 0.5\rho B\,\mathrm{V}^2\,[\mathrm{K_d}\,\bar{\theta}]\ \ (a) \\ F_{vk}(z,t) = 0.5\rho B\,\mathrm{V}^2\,[\mathrm{K_l}\,\bar{\theta}]\ \ (b) \\ F_{mk}(z,t) = 0.5\rho B\,\mathrm{V}^2\,[\mathrm{BK_m}\,\bar{\theta}]\ \ (c) \end{cases}$$

The terms associated with the velocity of the body are known as damping forces. As well as for the stiffness coefficients, the damping ones could produce instability. The one degree of freedom instability associated with this force arises when the lift or the moment coefficient have a negative slope and their associated terms are higher (in absolute value) than those of the structural damping giving rise to a negative damping coefficient which could be translated into a vibration with increasing amplitude rather than dissipation of energy. A foreword: since the drag coefficient is always positive it is not possible to have 1 dof instability for the horizontal motion.

Equation 6-48

$$\begin{cases} F_{ur}(z,t) = -0.5\rho BV(t)[2\,C_{Do}\,\dot{\bar{\mathrm{x}}} + (K_d - C_{lo})\dot{\bar{y}} \ + \ B1x\,(K_d - C_{lo})\,\dot{\bar{\theta}}\,] \quad (a) \\ F_{vr}(z,t) = -0.5\rho BV(t)[2\,C_{lo}\,\dot{\bar{\mathrm{x}}} + (K_l + C_{Do})\dot{\bar{y}} \ + \ B1y\,(K_l + C_{Do})\,\dot{\bar{\theta}}\,]\ (b) \\ F_{mr}(z,t) = -0.5\rho BV(t)[2\,C_{mo}\,\dot{\bar{\mathrm{x}}} + BK_m\dot{\bar{y}} \ + \ B1\theta\,K_m\,\dot{\theta}\,] \quad (c) \end{cases}$$

The previous derivations allows to define the forces given from Equation 6-45 to Equation 6-48 in the wind reference frame aligned with the mean velocity component, however in order to perform the structural analysis it is better to use the forces oriented in the structural reference frame assigned at the correspondent degrees of freedom. To this aim, a couple of relations between the two reference systems must be introduced Equation 6-49-Equation 6-50 .

Equation 6-49

$$\mathrm{F_{jx}} = \mathrm{F_u}\cos\beta_\mathrm{j}(\mathrm{t}) - \mathrm{F_v}\sin\beta_\mathrm{j}(\mathrm{t})\ \ (\mathrm{a})$$

$$\mathrm{F_{jy}} = \mathrm{F_u}\sin\beta_\mathrm{j}(\mathrm{t}) + \mathrm{F_v}\cos\beta_\mathrm{j}\,(\mathrm{t})\ (\mathrm{b})$$

Equation 6-50

$$\dot{\bar{\mathrm{x}}} = \dot{\mathrm{X}}\cos\beta_\mathrm{j}(\mathrm{t}) \ + \dot{\mathrm{Y}}\sin\beta_\mathrm{j}(\mathrm{t})\ \ (\mathrm{a})$$

$$\dot{y} = -\dot{\mathrm{X}}\ \sin\beta_{\mathrm{j}}(\mathrm{t})\ + \dot{\mathrm{Y}}\cos\beta_{\mathrm{j}}(\mathrm{t})\quad (\mathrm{b})$$

Further and for the sake of simplicity, the matrix notation will be introduced in the above defined relations. The aerodynamic force could be written as the assemble of its components Equation 6-51. The array of the turbulent wind velocity components Equation 6-52.

Equation 6-51

$$\mathbf{FA} = \begin{bmatrix} F_x \\ F_y \\ F_\theta \end{bmatrix}$$

Equation 6-52

$$\mathbf{b} = \begin{bmatrix} u \\ v \end{bmatrix}$$

With respect to the structures movements a further comment must be done, the equations provided herein correspond to an effective section of the complete structure that could be easily extended to the global application by means of simple rules that will be explained afterward. For frame bodies analyzed with FEM tools its necessary to define the vector of equivalent nodal forces which includes the acting force in its respective degree of freedom, in the case of three-dimensional structures for every point there are 6 degrees of freedom as shown in Figure 6-5. However, due to hypothesis of wind action over a plane 3.3.1 there will be only three force components for the wind action: transversal, longitudinal and torsional; the flexural (bending only) and axial equivalent nodal forces will not be directly excited by the wind action. Finally, the movement vectors of the structure will be Equation 6-53.

Equation 6-53

$$\bar{\boldsymbol{X}} = \begin{bmatrix} \bar{x} \\ \bar{y} \\ \bar{z} \\ \overline{\varphi_x} \\ \overline{\varphi_y} \\ \overline{\varphi_z} \end{bmatrix}; \qquad \dot{\bar{\mathbf{X}}} = \begin{bmatrix} \dot{\bar{\mathrm{x}}} \\ \dot{\bar{\mathrm{y}}} \\ \dot{\bar{\mathrm{z}}} \\ \dot{\overline{\varphi_{\mathrm{x}}}} \\ \dot{\overline{\varphi_{\mathrm{y}}}} \\ \dot{\overline{\varphi_{\mathrm{z}}}} \end{bmatrix}; \quad \boldsymbol{X_o} = \begin{bmatrix} x_o \\ y_o \\ z_o \\ \varphi_{xo} \\ \varphi_{yo} \\ \varphi_{zo} \end{bmatrix}; \quad with\, \theta = \varphi_x$$

The contribution to the global aerodynamic forces of the structure’s *j-th* sectional division (or node of the FEM mesh) on the structural reference frame are then:

- Pseudo-static force for equilibrium configuration:

Equation 6-54

$$\mathbf{Fq}, \mathrm{j} = \mathbf{Qs}, \mathrm{j}\, \mathbf{X}_{\mathrm{o}}$$

Equation 6-55

$$\mathbf{Qs},\mathrm{j} = 0.5\mathrm{\rho BjLjV(t)}_j^2\begin{bmatrix} C_D\,cos -\ C_l\ sin \\ C_D\,sin\ +\ C_l\ cos \\ 0 \\ 0 \\ 0 \\ B_j\,C_m \end{bmatrix}$$

- Aerodynamic forces turbulent component:

Equation 6-56

$$\mathbf{Fd},\mathrm{j} = \mathbf{A}\mathrm{m},\mathrm{j}\ \mathbf{b}$$

Equation 6-57

$$\mathbf{A}\mathrm{m}_{,\mathrm{j}} = \mathrm{\rho B_jV_j\ (t)\ L_j}\begin{bmatrix} C_D\,cos -\ C_l\,sin & -0.5[C_l - K_d]cos + [C_D + K_l]sin \\ C_D\,sin\ +\ C_l\,cos & -0.5[C_l - K_d]sin + [C_D + K_l]cos \\ 0 & 0 \\ 0 & 0 \\ 0 & 0 \\ B_j\,C_m & 0.5\,B_j\,C_m \end{bmatrix}$$

- Aerodynamic stiffness:

Equation 6-58

$$\mathbf{Fk}_{,\mathrm{j}} = \boldsymbol{K}\mathrm{a}_{,\mathrm{j}}\ \overline{\boldsymbol{X}}$$

Equation 6-59

$$\boldsymbol{K}\mathrm{a}_{,\mathrm{j}} = 0.5\mathrm{\rho B_jL_jV(t)}_j^2\begin{bmatrix} 0 & 0 & 0 & K_d\,cos - K_l\,sin & 0 & 0 \\ 0 & 0 & 0 & K_d\,sin + K_l\,cos & 0 & 0 \\ 0 & 0 & 0 & 0 & 0 & 0 \\ 0 & 0 & 0 & 0 & 0 & 0 \\ 0 & 0 & 0 & 0 & 0 & 0 \\ 0 & 0 & 0 & B_j\,K_m & 0 & 0 \end{bmatrix}$$

- Aeroelastic damping:

Equation 6-60

$$\mathbf{Fr}_{,\mathrm{j}} = \boldsymbol{C}\mathrm{a}_{,\mathrm{j}}\ \dot{\overline{\mathbf{X}}}$$

$\boldsymbol{C}\mathrm{a}_{,\mathrm{j}} = 0.5\mathrm{\rho B_jV_j(t)L_j}{*}$

$$\begin{bmatrix} \begin{gathered} 2C_D\, cos^2 + (C_l + K_d)cos\, sin + \\ (C_D - K_l)sin^2 \end{gathered} & \begin{gathered} -2C_l\, sin^2 + (C_D + K_l)cos\, sin - \\ (Cl - Kd)cos^2 \end{gathered} & 0 & 0 & 0 & \begin{gathered} B1x\,(K_d - C_{lo})cos\, - \\ B1y\,(K_l + C_{Do})\, sin \end{gathered} \\ \begin{gathered} 2Cl\, cos^2 + (C_D + K_l)cos\, sin + \\ (C_l - K_d)sin^2 \end{gathered} & \begin{gathered} -2C_D\, sin^2 + (Cl + Kd)cos\, sin - \\ (C_D - Kl)cos^2 \end{gathered} & 0 & 0 & 0 & \begin{gathered} B1x\,(K_d - C_{lo})\, sin + \\ B1y\,(K_l + C_{Do})\, cos \end{gathered} \\ 0 & 0 & 0 & 0 & 0 & 0 \\ 0 & 0 & 0 & 0 & 0 & 0 \\ 0 & 0 & 0 & 0 & 0 & 0 \\ B(2C_m\, cos\, - K_m\, sin) & B(2C_m\, sin\, - K_m\, cos) & 0 & 0 & 0 & B1\theta\, K_m \end{bmatrix}$$

Equation 6-61

$$\mathbf{Fa}\,\mathrm{dyn}_{,j} = \mathbf{Am}_{,j}\,\mathbf{b_j} - \boldsymbol{C}\mathrm{a}_{,}\mathrm{j}\,\dot{\mathbf{X}}_{,}\mathrm{j} - \boldsymbol{K}\mathrm{a,j}\,\overline{\boldsymbol{X}}_{,j}$$

The final scheme of the equations of motion:

$$\mathbf{M}\,\ddot{\mathbf{X}} + [\mathbf{C} + \boldsymbol{C}\mathrm{a}]\dot{\mathbf{X}} + [\mathbf{K} + \boldsymbol{K}\mathrm{a}]\overline{\boldsymbol{X}} = \mathbf{Am}\,\mathbf{b}$$

6.4 Time domain analysis

The structural response in time domain is computed by means of the direct integration of the equations of motion. To this aim the same approach exposed for scalar quantities in §4.3.2 is extended to matrix notation in modal coordinates in the following.

To ensure the accuracy and numerical stability of the method the same provisions explained in §4.3.2 for the time step apply for MDOF systems, as well as, the prescription of the values for β and γ.

1. Modal transformation:

Equation 6-62:

$$(q_n)_0 = \frac{\phi_n^T \mathbf{m}\,\mathbf{u}_0}{\phi_n^T \mathbf{m}\,\phi_n}; \qquad (\dot{q}_n)_0 = \frac{\phi_n^T \mathbf{m}\,\dot{\mathbf{u}}_0}{\phi_n^T \mathbf{m}\,\phi_n}$$

$$\mathbf{q}_0^T = \langle (q_1)_0, \ldots, (q_J)_0 \rangle \qquad \dot{\mathbf{q}}_0^T = \langle (\dot{q}_1)_0, \ldots, (\dot{q}_J)_0 \rangle.$$

$$\mathbf{P}_0 = \mathbf{\Phi}^T \mathbf{p}_0.$$

$$\text{Solve } \mathbf{M}\,\ddot{\mathbf{q}}_0 = \mathbf{P}_0 - \mathbf{C}\,\dot{\mathbf{q}}_0 - \mathbf{K}\,\mathbf{q}_0 \Rightarrow \ddot{\mathbf{q}}_0.$$

With the suffix 0 denoting the initial value for *t=0.*

2. Initial Computations:

Equation 6-63:

$$\begin{cases} \boldsymbol{a1} = \dfrac{\boldsymbol{M}}{\beta * t_{step}^{2}} + \dfrac{\gamma * \boldsymbol{C}}{\beta * t_{step}}; \qquad \boldsymbol{a2} = \dfrac{\boldsymbol{M}}{\beta * t_{step}} + \left(\dfrac{\gamma}{\beta} - 1\right)\boldsymbol{C} \\ \boldsymbol{a3} = \left(\dfrac{1}{2\beta} - 1\right)\boldsymbol{M} + \left(\dfrac{\gamma}{2\beta} - 1\right)C \\ \widehat{\boldsymbol{K}} = \boldsymbol{K} + \boldsymbol{a1} \end{cases}$$

3. Computations for every time step:

Equation 6-64

$$\begin{cases} \widehat{\boldsymbol{P}}(i+1) = \boldsymbol{P}(i+1) + \boldsymbol{a1}\boldsymbol{q}(i) + \boldsymbol{a2}\dot{\boldsymbol{q}}(i) + \boldsymbol{a3}\ddot{\boldsymbol{q}}(i) \\ \boldsymbol{q}(i+1) = \dfrac{\widehat{\boldsymbol{P}}(i+1)}{\widehat{\boldsymbol{K}}} \\ \dot{\boldsymbol{q}}(i+1) = \dfrac{\gamma}{\beta * tstep}[\boldsymbol{q}(i+1) - \boldsymbol{q}(i)] + \left(1 - \dfrac{\gamma}{\beta}\right)\dot{\boldsymbol{q}}(i) + \left(1 - \dfrac{\gamma}{2\beta}\right)\ddot{\boldsymbol{q}}(i) \\ \ddot{\boldsymbol{q}}(i+1) = \dfrac{1}{\beta * tstep^{2}}[\boldsymbol{q}(i+1) - \boldsymbol{q}(i)] - \dfrac{1}{\beta * tstep}\dot{\boldsymbol{q}}(i) - \left(\dfrac{1}{2\beta} - 1\right)\ddot{\boldsymbol{q}}(i) \end{cases}$$

The computer code was benchmarked with sap2000 and the examples of (Chopra 2012).

6.1 Direct frequency domain analysis

In the current study the frequency domain analysis was not fully implemented for the case of MDOF systems because of the computational effort involved in the construction of the Frequency Response Function accounting for the time-varying aeroelastic effects. Therefore, it is strongly recommended to perform this analysis in a further step of the research.

The non-linear behavior of the problem does not allow to completely apply the frequency domain approach. To perform this type of analysis is necessary to linearize the problem and proceed as shown by (Canor, et al. 2016)

6.2 Numerical Application

To give an example of the structural response of MDOF system submitted to the action of the downburst 3D- outflows and of the numerical procedure implemented in the present work, a simple application will be presented in this section. The structure to analyze is that already introduced in §3.10 and brought here for convenience in Figure 6-11.

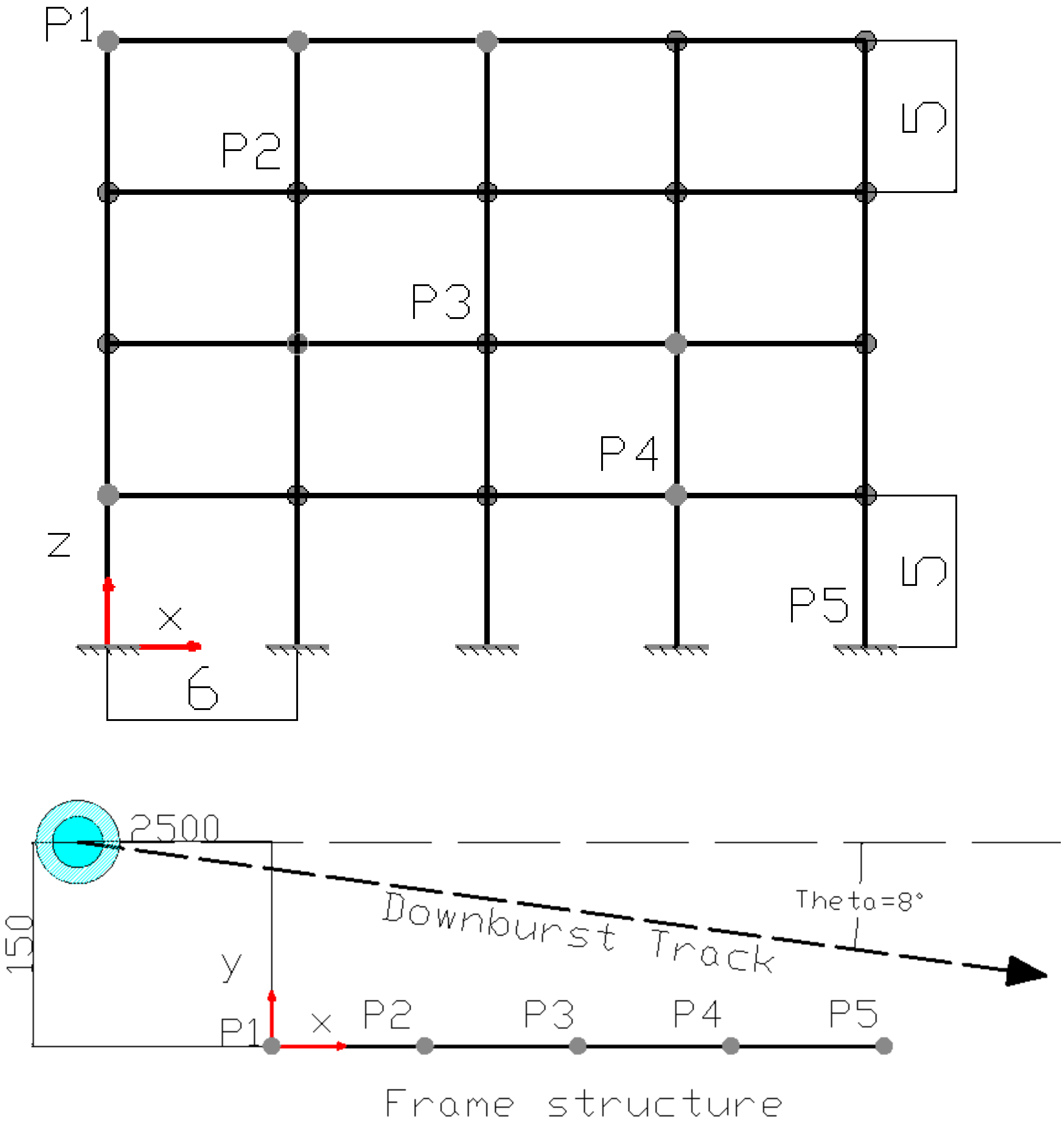

Figure 6-11: 2D frame with 3D downburst. a) Front view. b) Plan view

6.2.1 Structure parameters

The structure is idealized to be a square section made of solid steel. The material parameters Table 6-1.

Table 6-1: Material simulation parameters

Parameter	Symbol	Value	Unit
Young Modulus	E	210	*[GPa]*
Poisson Ratio	ν	0.2	*[-]*
Density	ρ	7.850	*[kg/m3]*
Shear modulus	G	87,5	*[GPa]*

All the elements of the structure are composed by the same cross section, a picture of the same could be seen in Figure 6-12.

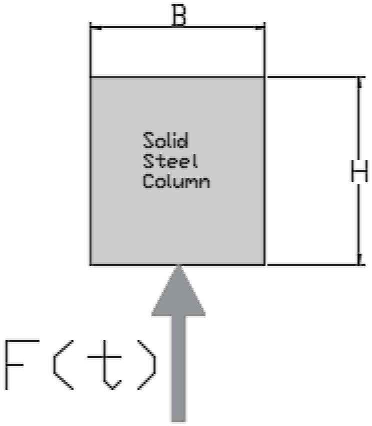

Figure 6-12: Cross section

The geometric properties of the section are reported in Table 6-2.

Table 6-2: Cross section simulation parameters

Parameter	Symbol	Value	Unit
Area	A	0.25	*[m2]*
Inertia in y-y’ direction	I_y	0.0052	*[m4]*
Inertia in z-z’ direction	I_z	0.0052	*[m4]*
Shear coefficient	χ	$5/6$	*[-]*
Shear correction factor	ϕ_y	0.0199	*[-]*
Shear correction factor	ϕ_z	0.0199	*[-]*

The stiffness and the mass of the elements is computed in local reference frame considering the stiffness and mass matrixes provided in Equation 6-11. With the structural matrixes it is possible then to perform the modal analysis and build the modal damping matrix as explained in **§**6.2.4 **§**6.2.5. The damping ratio ζ is taken as 2% for accepted value for steel structures.

6.2.2 Aerodynamical Properties

The cross sections are assumed to be squared. The drag coefficients were taken from the study of (Carassale, et al. 2012). It is worth noting that while the time-varying approximation angle of the downburst β(t) will induce changes in the angle of attack, the small rotations of the cross section will not induce a significant change in the same. Therefore, it is important to include the variation of the drag coefficient with the angle of attack as function of the approximation angle β(t) only since the former varies in time faster than the structural associated rotation.

On Figure 6-13 there are reported the values of the Strouhal number for square cross section with rounded corner. The drag and lift coefficients are given in Figure 6-14 and Figure 6-15. For the case of study where no rounding corners were included the r/b ratio is equal to zero.

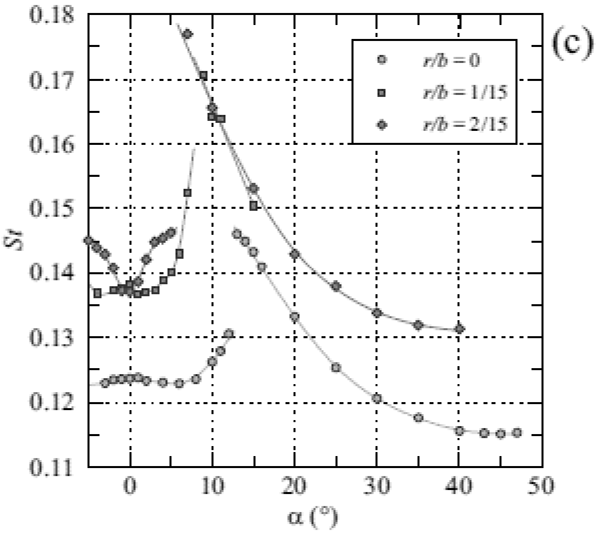

Figure 6-13: Strouhal Number. Adapted from (Carassale, et al. 2012)

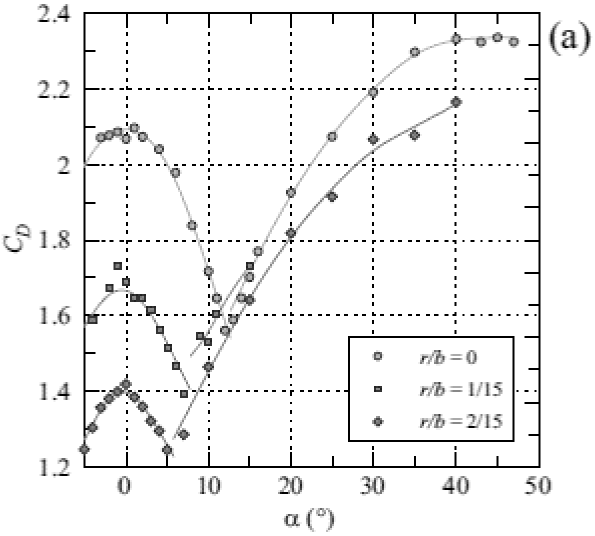

Figure 6-14: Drag coefficient for square section. Adapted from (Carassale, et al. 2012).

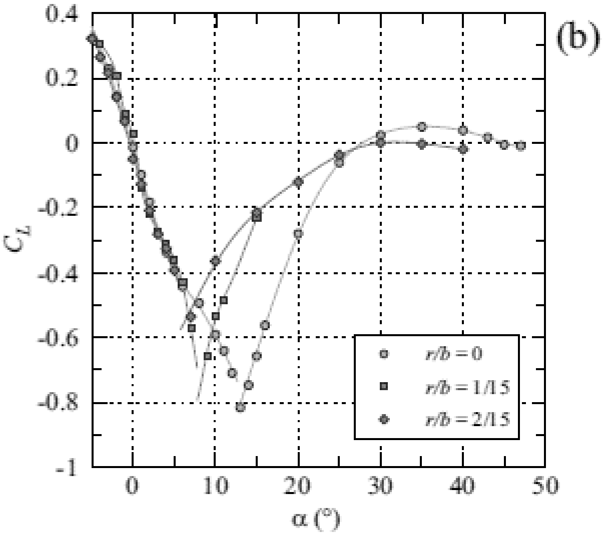

Figure 6-15: Lift coefficient. Adapted from (Carassale, et al. 2012).

6.2.3 Downburst Properties

The parameters of the downburst outflow implemented in this section are the same already provided in **§** 3.10. Therefore, the mean velocity and the approximation angle together with the downburst parameters are those from **§**3.10.1 while the random turbulent components are those coming from the Monte Carlo simulation given in **§**3.10.2.

6.2.4 Response

The structural response was computed according to **§** 6.4.

The generic turbulent displacement could be seen Figure 6-16.

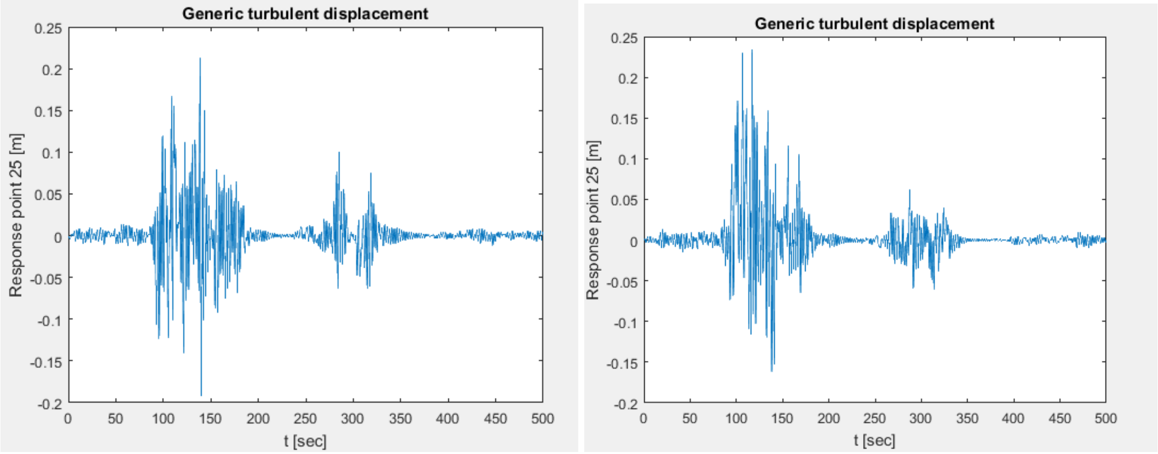

Figure 6-16: Turbulent component of the displacement

To consider the pseudo-static displacement in the response, it must be included the solution for the slowly varying mean force coming from Equation 6-55. The pseudo-static force depends strongly in the approximation angle. Therefore, the oscillatory nature of the cosine of the approximation angle produces an oscillatory response in the pseudo-static force. A generic response (displacement in the y-direction of a point in the right-hand superior corner) computed with beta angle Figure 6-17. A graphical representation of the structural response taking out the variation of the approximation angle is given in Figure 6-18 i.e. a response that could be compared with that one of the SDOF.

6.1 Conclusions

The computational tool developed to solve the dynamic problem is capable to account for the aeroelasticity phenomenon in time domain. The developed computer tool can generate the multi-point three-dimensional wind structure of the downburst outflow using the strategy explained in **§** 3.10. Further developments must be done to account also for the frequency domain analysis.

In order to extend the developments of this chapter it is recommended to apply the definitions here exposed to a large structure and evaluate its response. Furthermore, it can be suggested to apply and generalize the methodology proposed in **§** CHAPTER 5 ASSESSMENT OF FAILURE PROBABILITY to evaluate the capabilities of a structure projected with the current design rules to resist the downburst wind velocity outflows.

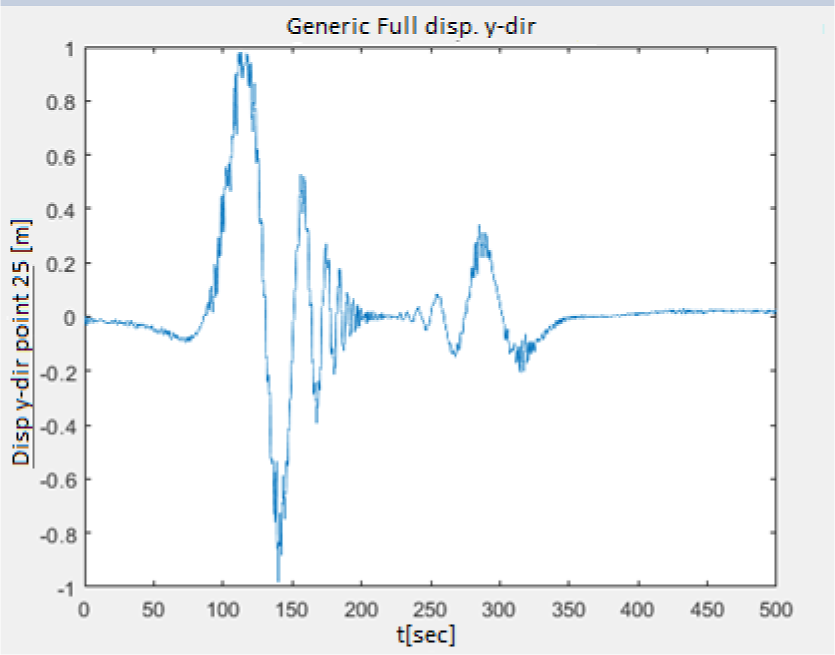

Figure 6-17: Full displacement in y-direction with beta computed.

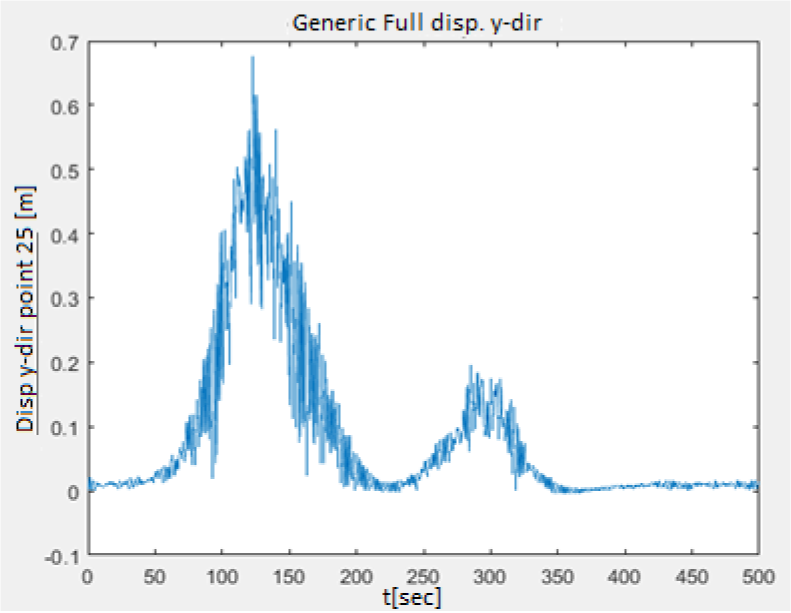

Figure 6-18: Full displacement in y-direction with beta equal zero.

CONCLUSIONS

After the developments of the current research it was possible to fully create a downburst wind velocity model. The mentioned model is capable to reproduce the three-dimensional structure of the outflow and apply its action to civil engineering structures. In addition, the model for the single point in space was successfully extended to more realistic multi-point structures.

The model for single points in space is capable to analyze SDOF reduced systems, it can reproduce the available records of the downburst. It was so far explained in the chapter 3 of the present study how a generic simulation made with the current model can capture the behavior of the record Andrews Airforce Base (AFB) including the two peaks of the wind velocity field and the zero crossing of the mother storm. This study provides a solid benchmark to the model proving the accuracy of the same.

For the case of MDOF systems the model is capable to fully reproduce the three-dimensional wind field for all the points of the structure. However, it shall be remarked that the since the hypothesized tracking path of the downburst affects the approximation angle, the outflow radial diffusion and the aeroelastic effects over the structure. It is recommended to perform a study on the latter parameter before starting a further step of analysis for MDOF structures.

The study over the aeroelastic damping revealed that for the case of study, with 2% of structural damping ratio and natural frequency of 3.35 [Hz], the assumption of neglecting the aeroelastic effect is not only, the most conservative option, but also, the closest to the real aeroelastic effect.

It is important to comment, however, that for the case of structures with associated natural frequencies lower than 1.5 [Hz] the aeroelastic component plays an important role and should not be neglected. For those cases even though it can be recommended to use the time-varying aeroelastic damping. A possible approximation can be to use a constant aeroelastic damping with value equal to the mean of the effect.

The wind velocity field of the downburst of this study was artificially generated using a Monte Carlo algorithm. A test on the convergence of the Monte Carlo simulations was made to verify if sample composed by 2.000 realizations was enough to describe the phenomena. The results of the test show to be acceptable since the statistical properties tend to specific values between the analysis.

From the parametric study in 4.7, it is possible to conclude that the two methods of analysis made in the frequency-domain and in the time-domain are in good agreement. Discrepancies between the two approaches can be found, depending on damping and natural period of the structure if an approximate generalized transfer function based on the slowly varying uniformly modulated process assumption is considered in the computations. The results reported in sections 4.7 and 4.8 showed that while the approximation assumption can be considered as valid for relatively rigid and damped structures, it fails in reproducing the behavior of lightly damped and flexible systems. In the latter case, hence, the convolution integral involved in the evaluation of the generalized transfer function should be evaluated without introducing approximations. This largely reconciles the prediction of the time domain and frequency domain approaches, as has been shown in section 4.8.3.

It was also possible to successfully compare the effect of the downburst model with the traditional atmospheric boundary layer model. The scope of this comparison was to attempt a first step towards the definition of a methodology for checking if a structure correctly projected with the standard design rules for wind loads is capable to resist a probable scenario of a downburst outflow. In general terms it should be highlighted the dynamic factor of the response for synoptic winds seems, for the cases considered in this work, to be higher than that of the downburst because of the difference in the size of the integral length scales and the turbulence intensities.

For the case of study of a tall structure (natural frequency of 2.58 Hz and damping ratio of 2%,) located in Genova and with basic velocity for the definition of the ABL model equal to 30 [m/s], it has been shown that the equivalent downburst producing the same effect has a model velocity of 27.7 [m/s] with a tracking velocity of 12 [m/s]. The maximum velocities reached by the ABL and DWB models were 32.5 [m/s] and 39 [m/s] respectively. While useful to introduce a methodology, the application example, however, should be extend in a future research to cover a wider set of case of study. It could be in particular interesting to check the effects of the downburst on both lightly damped flexible structures and large structures (e.g. over-head power lines, bridges).

For the MDOF systems it was possible to successfully develop a computational tool able to evaluate the dynamic response of a three-dimensional structure subjected to a multi-point downburst wind velocity outflow. The code works in time domain analysis by solving the equations of motion using a Newmark integration scheme. For the given case of study, it was possible to verify the three-dimensional structure of the wind velocity field and asses the response of the system under the downburst action.

Finally, it is recommended to extend the failure probability assessment to the case of study of MDOF structures to which the features of the downburst wind velocity field become critical compared with the ABL model.

References

AS/NZS 7000. 2010. *Overhead line design- detailed procedure.* Australian/New Zeland Standard.

Biondini, F. 2017. "Class notes of Computational Structural Analysis." *Stiffness matrix of Beam Elements.* MIlano, Lombardia.

Biondini, F. 2018. "Lecture Notes Relaibility class." *Politecnico di Milano.*

Byers, HR, and RR Braham. 1949. "The Thunderstrom: final report of the thunderstrom project." *US goverment pritning office.*

Canor, T, V Denoël, and L Caracoglia. 2016. "Perturbation methods in evolutionary spectral analysis for linear dynamics and equivalent statistical linearization." *ELSEVIER, Probabilistic Engineering Mechanics Vol46* 1-17.

Caracoglia, L, and T Le. 2017. "Computer-based model for the transient dynamics of a tall building during digitally simulated Andrews AFB thunderstrom." *ELSEVIER, Computers and Structures Vol 193* 44-72.

Carassale, L, A Freda, M Marrè Brunenghi, G Piccardo, and G Solari. 2012. "Experimental Investigation on the aerodynamic behavior of square cylinders with round corners." *The seventh colloquim on bluff body aerodynamics and applications BBAA7.*

Chay, MT, and CW Letchford. 2002. "Pressure distributuons on a cubue in a simulated thunderstrom downburst-PartA: stationary donwburst observations." *Journal of Wind Engineering and Industrial Aerdynamics* 90:711-32.

Chen, L, and C Letchford. 2004. "A deterministic-sthocastic hybrid model of downburst and its imparc on a cantilevered structure." *ELSEVIER, Engineering Structures Vol 26* 619-629.

Chopra, Anil K. 2012. *Dynamic of Structures 4th Edition.* Berkeley: Pearson Education, Inc.

Corigliano, A. 2005. *Meccanica Computazzionale- Soluzione del problema elastico lineare.* Bologna: Esculapio.

Davenport, A. 1962. "Buffeting of a Suspension Bridge by Strom Winds." *Journal of the Structural Division vol 88 ACSE* 233-270.

Davenport, A. 1968. "The dependance of the wind load upon meteorological parameters." *Proceedings of International Seminar on Wind Effects on Buildings and Structures* p.19-82.

Denoël, V. 2004. *Application des méthodes d'analyse stochastique à l'étude des effets du vent sur les structures du génie civil.* Liege: Universite de Liege.

Deodatis, G. 1989. "Simulation of ergodic multivariate stochastic process." *Journal of Enginerring Mechanics ASCE Vol 122* 778-787.

Di Paola, M., and I. Gullo. 2001. "Digital generation of multivariate wind field processes." *Probabilistic Engineering Mechanics ELSEVIER Vol 16* 1-10.

Diana, G. 2018. "Lecture Notes in Wind Engineering." In *Chapter 4: Immersed Bodies*. Politecnico di Milano.

—. 2018. "Lecture Notes: Wind Effects On Bridges." *Wind Engineering lessons.* Milano.

Elawady, A. 2016. *Development of Design Loads for Transmission Line Structures Subjected to Downburst Using Aeroleastic Testing and Numercial Modeling.* London, Canada: PhD Thesis.

Eurocode1. n.d. "Eurocode1 1991 1-4(1991): Actions on Structures Part 1-4: General Actions: Wind actions, CEN."

Felippa, C. 2013. "Chapter 18 Matrix Finite Element Methods in Dynamics." *(Course in Preparation) - Date TBA* Chapter 18.

Fujita, T. 1990. "Downburst: Meteorological features and wind field characteristics." *J Wind Eng Ind Aerodyn* 36:75-86.

Fujita, T. 1985. "Downburst: microburst and macroburst." *University of Chicago Press.*

Gavin, H. 2016. "Structural Element Stiffness, Mass, and Damping Matrices." *CEE541 Structural dynamics Duke University.*

Hangan, H, D Roberts, Z Xu, and . 2003. "Downburst simulation, experimental an numerical challenges." *11th International Conference on Wind Engineering.*

Hawes, H, and D Dempsey. 1993. "Review of recent Australian transmission line failures due to high intensity winds." *Porceedings of the task Force of High Intesnsity Winds on Transmission Lines, Buenos Aires* 19-23.

Hjelmfelt, MR. 1998. "Structure and lufe cycle of microburst outflows observerd in Colorado." *Journal of Applied Meteorology Vol 27.*

Holmes, JD, and SE Oliver. 2000. "An empirical model of a downburst." *ELSEVIER, Engineering Structures Vol 22* 1167-1172.

HYDRO ONE NETWORKS INC. 2006. *Failur of towers 610 and 611, circuit X503-500kV guyed towers near the township of Waybaushene".* Ontario: Faillure Investigation Report, Line Engineering.

Ivan, M. 1986. "A ring-vortex downburst model for fligth simulations." *Journal of Aricraft 23* 232-236.

Kaimal, JC. 1972. "Spectral charactersitics of surface-layer turbulence." *Journal of the Royal Meteorological Society, London Vol 98* 563-89.

Kanak, J. 2007. "Case of study of the 9 May 2003 windstrom in southwestern Slovakia." *Atmos. Resm 83* 162-175.

Kwon, D, and A Kareem. 2009. "Gust-front factor: New framework for wind load effects on structures." *Journal of structural engineering ASCE Vol 135* 712-732.

Mason, M, G Wood, and D Fletcher. 2009. "Numerical simulation of downburst winds." *Journal of Wind Engineering and Industrial Aerodynamics, ELSEVIER Vol 97* 523-539.

Mason, M, G Wood, and D Fletcher. 2009. "Numerical simulation of downburst winds." *Journa of Wind Engineering and Industrial Aerodynamics Vol 97* 523-539.

McCarthy, P, and M Melness. 1996. "Severe weather elements associated with the september 5, 1996 hydro tower failures near Grosee Isle, Manitoba, Canda." *Manitoba Environmental Services Centre, Enviroment Canda.*

Newmark. 1982. "Earthquake Spectra and Design." *Earthquake Engieering Research Institute.*

Oliver, SE. 1992. "Severe wind in New South Wales." *Report prepared for Pacific Power by Bureau of Meteorology, Special Services Unit.*

Osegura, RM, and RL Bowles. 1988. "A simple analytic 3-dimensional downburst model based on boundary layer stagnation flow." *NASA Technical Memorandum 100632.*

Perotti, F. 2017. "AN INTRODUCTION TO RANDOM VIBRATION OF STRUCTURES:Non – stationary models." *Class notes.*

Perotti, F. 1990. "Structural Response to non-stacionary multi-support random excitation." *Earthquake Engineering and strucutral dynamics VOL 19* 513-527.

Poreh, M, and JE Cermak. 1959. "Flow characteristics of a circular submerged jet impinging normally on a smooth boundary." *Sixth annual conference on fluid mechanics, Austin Texas.*

Priestley, M. 1965. "Evolutionary Spectra and Non-stacionary Processes." *Journal of the Royal Statistical Society. Series B(Methodological) Vol 27* 204-237.

Shehata, A, A El Damatty, and E Savory. 2005. "Finite Element modeling of transmission line under downburst loading." *Finite Elements in Analysis and Design ELSEVIER Vol 42* 71-89.

Shinozuka, M, and G Deodatis. 1991. "Simulation of stochastic process by Spectral Representation." *Applied Mechanis reviews Vol 44* 191-204.

Solari, G, and Piccardo. 2001. "Probabilistic 3-D turbulence modeling for gust buffeting of structures." *ELSEVIER, Probabilistic Engineering Mechanics Vol 16* 73-86.

Solari, G, D Rainisio, and P De Gaetano. 2017. "Hybrid simulation of thunderstorm outflows and wind excited response of structures." *Springer Scinece+Buisness Media Vol 52.*

Solari, G, M Burlando, P De G, and M Repetto. 2015. "Characteristics of thunderstorms relevant to the wind loading of structures." *Eng Ind Aerodyn 143* 62-77.

Solari, M Burlando, P. De Gaetano, and MP. Repetto. 2015. "Characteritics of thunderstorms relevant to the wind of structures." *Wind Structures Vol 20* 763-791.

University of Western Ontario UWO. n.d. https://www.eng.uwo.ca/windeee/research_publications.html .

Van der Hooven. 1957. "Power Sprecturm of horizontal wind speed in frequency range 0.0007 to 900 cycles per hour." *Journal of meteorology Vol 14* 160-164.

Vermire, B, O Leigh, and E Savory. 2011. "Improved modelling of donwburst outflows for wind engineering applications using cooling source apporach." *Journal of Wind Engineering and Industrial Aerodynamics Vol 99* 801-814.

Vicroy, D. 1992. "Assesment of microburst models for downdraft estimation." *Journal of Aircraft Vol 29.*

Wilson, JW, and Roger Wakimoto. 2001. "The discrovery of donwburst: T.T. Fujita's Contribution." *International Glosary of Hidrology Vol 82* 49-62.

Wilson, JW, RD Roberts, C Kessinger, and J McCarthy. 1984. "Microburst wind structure and evaluation of Doppler radar for airport wind shear detection." *J Clim App Met Vol 23* 898-915.

Wood, GS, and KCS Kwok. 1998. "An emperically derived estimate for the mean velocity profile of a thunderstrom downburst." *7th AWES Workshop, Auckland.*

Yang, SC, and HP Hong. 2016. "Nonlinear inelastic responses of transmission tower-line system under downburst wind." *ELSEVIER, Engineering Structures Vol 123* 490-500.

APPENDIX A: Code benchmarking

The first two benchmarks provided in the following are aimed to certify the effectiveness of the function *MODAL1* which computes for a given mass matrix, stiffness matrix and damping ratio the eigenvalues, eigenmodes and the modal damping matrix.

1. Eigenvalue Problem: From Pag. 432-Chopra DOS 4th Edition

The structure reported in Image 1 is provided as an example of the modal analysis inside (Chopra 2012). The masses and stiffnesses for the given shear frame are those showed, the term $m = 0.259\ kip - s2/plug$ and $k = \ 168\ kips/plug$

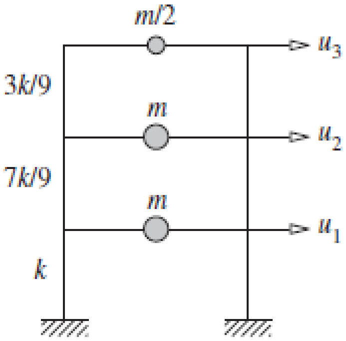

Image 1: Structure for modal analysis. Adapted from Chopra 4th edition

The structural matrixes of the system are:

Expression 1

$$\boldsymbol{M} = m\begin{bmatrix} 1 & & \\ & 1 & \\ & & 1/2 \end{bmatrix} \quad \boldsymbol{K} = \frac{k}{9}\begin{bmatrix} 16 & -7 & 0 \\ -7 & 10 & -3 \\ 0 & -3 & 3 \end{bmatrix}$$

The input data for solving the problem with the function MODAL1 of the computer code is given in

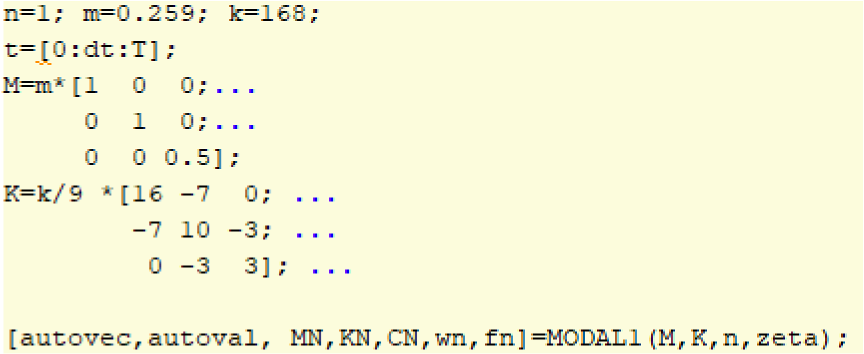

```
n=1; m=0.259; k=168;
t=[0:dt:T];
M=m*[1  0  0;...
     0  1  0;...
     0  0 0.5];
K=k/9 *[16 -7  0; ...
        -7 10 -3; ...
         0 -3  3]; ...

[autovec,autoval, MN,KN,CN,wn,fn]=MODAL1(M,K,n,zeta);
```

Image 2: Structure input for modal Test

The first eigenvalue and eigenvector of the system reported in Chopra's book are given in Expression 2 and those computed by the code are reported in Expression 3.

Expression 2

$$\omega 1 = \sqrt{\lambda 1} = \sqrt{144.14} = 12.006 \quad \boldsymbol{\varphi} 1 = \begin{bmatrix} 0.6377 \\ 1.2752 \\ 1.9122 \end{bmatrix}$$

Expression 3

$$\omega 1^{*} = \sqrt{\lambda 1^{*}} = \sqrt{144.1441} = 12.006 \quad \boldsymbol{\varphi} 1^{*} = \begin{bmatrix} 0.6375 \\ 1.2750 \\ 1.9125 \end{bmatrix}$$

Parameter	Chopra	Code	Error[%]
$\boldsymbol{\varphi}1(1)$	0.6377	0.6375	*0.03*
$\boldsymbol{\varphi}1(2)$	1.2752	1.2750	*0.015*
$\boldsymbol{\varphi}1(3)$	1.9122	1.9125	*0.015*

Comparing both approaches and taking as reference the value from (Chopra 2012) it is possible to verify the capability of the computer code to solve the eigenvalue problem showing an error less than 0.03%.

2. Damping Matrix Construction From: Pag. 463 ex 11.4-Chopra DOS 4th edition

To test the construction of the modal damping matrix, it was developed the given example in the topic of Chopras's book. The structure to analyze is given in Image 3.

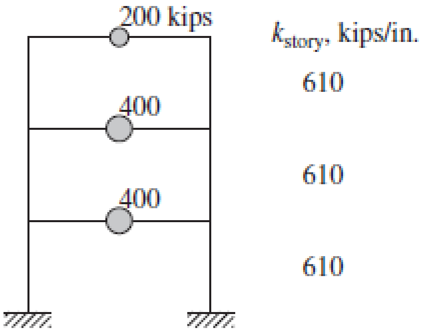

Image 3:Structure for Damping benchmark

The structural matrixes of the system

Expression 4

$$\boldsymbol{M} = \frac{1}{386}\begin{bmatrix} 400 & & \\ & 400 & \\ & & 200 \end{bmatrix} \quad \boldsymbol{K} = 610\begin{bmatrix} 2 & -1 & 0 \\ -1 & 2 & -1 \\ 0 & -1 & 1 \end{bmatrix}$$

The modal information was reported in the example and compared with that computed by the code

Expression 5

$$\boldsymbol{\omega} n = \begin{bmatrix} 12.57 \\ 34.33 \\ 46.89 \end{bmatrix} \quad \boldsymbol{\phi} = \begin{bmatrix} 0.401 & 0.803 & 0.401 \\ 0.695 & 0 & -0.695 \\ 0.803 & -0.803 & 0.803 \end{bmatrix}$$

Expression 6

$$\boldsymbol{\omega} n^{*} = \begin{bmatrix} 12.5590 \\ 34.3118 \\ 46.8708 \end{bmatrix} \quad \boldsymbol{\phi}^{*} = \begin{bmatrix} 0.401 & 0.8021 & 0.401 \\ 0.6946 & 0 & -0.6946 \\ 0.8021 & -0.8021 & 0.8021 \end{bmatrix}$$

For the computation of the modal damping matrix it was prescribed a non-dimensional damping ratio of 5%

The modal matrix reported in the book for the three modes is that given in Expression 7 and that computed by the code Expression 8.

Expression 7

$$\boldsymbol{C1} = \begin{bmatrix} 0.217 & 0.376 & 0.217 \\ & 0.651 & 0.376 \\ & & 0.217 \end{bmatrix} \quad \boldsymbol{C2} = \begin{bmatrix} 2.37 & 0 & 0.969 \\ & 0 & 0 \\ & & 0.593 \end{bmatrix} \quad \boldsymbol{C3} = \begin{bmatrix} 0.89 & -1.40 & 0.81 \\ & 2.43 & -1.4 \\ & & 0.811 \end{bmatrix}$$

$$\boldsymbol{C} = \begin{bmatrix} 3.4 & -1.03 & -0.159 \\ & 3.08 & -1.03 \\ & & 1.62 \end{bmatrix}$$

Expression 8

$$\boldsymbol{C}^{*} = \begin{bmatrix} 3.3968 & -1.0264 & -0.1588 \\ & 3.0793 & -1.0264 \\ & & 1.6190 \end{bmatrix}$$

Parameter	Chopra	Code	Error[%]
C11	3.4	3.3968	0.09411765
C12	-1.03	-1.0264	-0.34951456
C13	-0.159	-0.1588	-0.12578616
C22	3.08	3.0793	0.02272727
C23	-1.03	-1.0264	-0.34951456

C33	1.62	1.619	0.0617284

Comparing both approaches and taking as reference the value from (Chopra 2012) it is possible to verify the capability of the computer code to compute the modal damping matrix showing an error less than 0.35% in each component and 1.41% summing all components.

The values computed for the modal analysis and the modal damping matrix from both approaches match. Therefore, it is verified that the *MODAL1* function is correctly describing the behavior of the structure. The function code is given in the following:

```
function [phi,lambda, MN,KN,CN,wn,fn]=MODAL1(m,k,n,zeta)

[autoveco,autovalo]=eig(k,m);
%mode organization
[N,r1]=size(autoveco);
incidence=zeros(N,2);
autoval=zeros(N,N);
autovec=zeros(N,N);
LB1=zeros(N,1);
for i=1:N
   incidence(i,1)=i;
   LB1(i)=autovalo(i,i);
end
LB2=sort(LB1);
for i=1:N

   for j=1:N
       if LB1(i)==LB2(j)
       index=j;
       end
    end
   incidence(i,2)=index;
end
for i=1:N
   ind=incidence(i,2);
   autoval(ind,ind)=autovalo(i,i);
   autovec(:,ind)=autoveco(:,i);

end
%Mass normalization

 nautovec=zeros(size(autovec));
 for i=1:N
     nautovec(:,i)=autovec(:,i)/sqrt(autovec(:,i)'*m*autovec(:,i));
 end
 %%%%%%%%%%%%%%%%%%%%%%%%%%%%%%%%%%

 %HOW MANY MODES TO CONSIDER?

 %%%%%%%%%%%%%%%%%%%%%%%%%%%%%%%%

phi=zeros(N,n);
lambda=zeros(n,n);
for i=1:n
    phi(:,i)=nautovec(:,i);
    lambda(i,i)=autoval(i,i);
end
wn=(lambda.^(0.5));
fn=(lambda.^(0.5))/(2*pi);
MN=(phi'*m)*phi;
KN=(phi'*k)*phi;
Ms=zeros(3,3);
tol=10^(-4);
```

```
%modal damping superposition benchmark pag 463 chopra
c=zeros(N,N);

for i=1:n
    c=c+(2*zeta*wn(i,i)/MN(i,i))*(m*(phi(:,i)*phi(:,i)'))*m;

end
CN=phi'*c*phi;
for i=1:n
    for j=1:n
       Mij=MN(i,j);
       Kij=KN(i,j);
       Cij=CN(i,j);
       if Mij<tol
           MN(i,j)=0;
       end
       if Kij<tol
           KN(i,j)=0;
       end
       if Cij<tol
           CN(i,j)=0;
       end
    end
end
end
```

The following benchmarks test the capability of the *Newmark* function to solve the equations of motion by means of the direct integration scheme of the so-called Newmark's method.

3. Newmark Method for SDOF from: Pag 178 Chopra DOS 4th edition

A dynamic force as that given in Image 4 is applied to a single degree of freedom system Image 5.

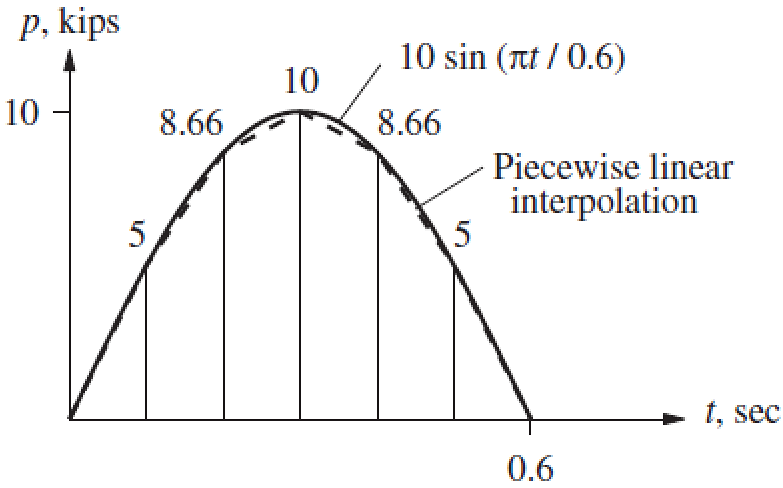

Image 4: Dynamic force for Newmark benchmark. Adapted from (Chopra 2012)

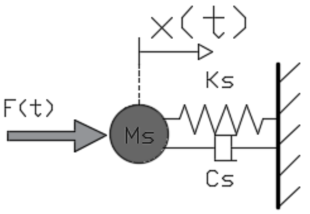

Image 5: SDOF structure

The structural parameters were set according to the provisions of (Chopra 2012).

Parameter	**Symbol**	**Value**	**Unit**
Mass	m	0.2533	*[kip-sec2/in]*
Stiffness	k	10	*[kip/in]*
Circular natural frequency	ωn	6.283	*[rad/sec]*
Damping ratio	ζ	5	*[%]*
Time step	Δt	0.1	*[sec]*

The initial conditions of the problem:

Expression 9

$$uo = 0 \qquad \dot{u}o = 0 \qquad Po = 0$$

Following the procedure explained in **§** 4.3.2, the solution of the problem given inside the text book for constant acceleration (β=1/4 γ=1/2) is reported in Image 6 while that for linear acceleration (β=1/6 γ=1/2) in Image 7.

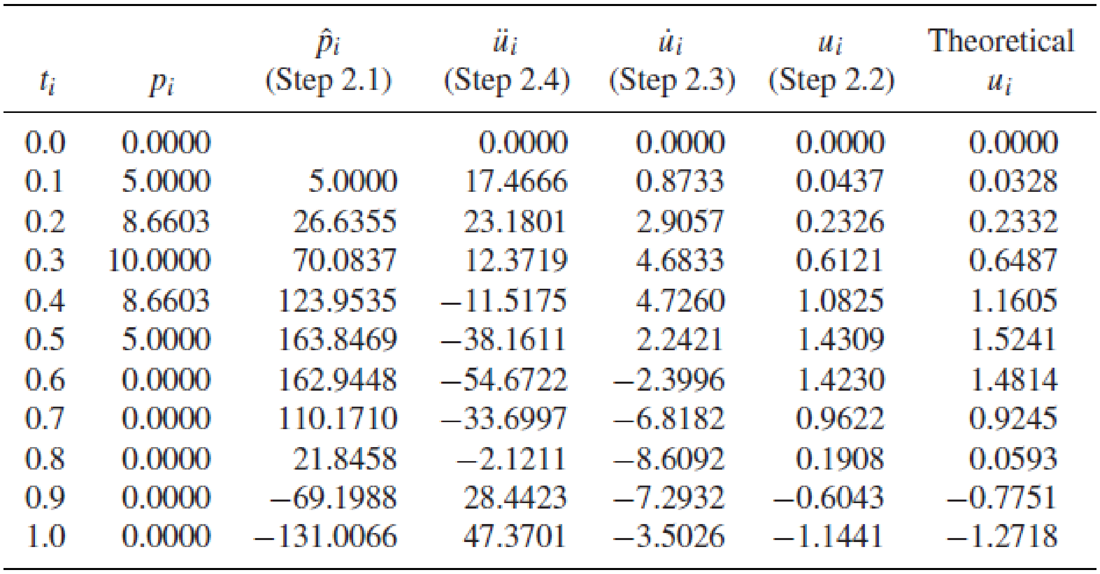

t_i	p_i	$\hat{p}_i$ (Step 2.1)	$\ddot{u}_i$ (Step 2.4)	$\dot{u}_i$ (Step 2.3)	u_i (Step 2.2)	Theoretical u_i
0.0	0.0000		0.0000	0.0000	0.0000	0.0000
0.1	5.0000	5.0000	17.4666	0.8733	0.0437	0.0328
0.2	8.6603	26.6355	23.1801	2.9057	0.2326	0.2332
0.3	10.0000	70.0837	12.3719	4.6833	0.6121	0.6487
0.4	8.6603	123.9535	−11.5175	4.7260	1.0825	1.1605
0.5	5.0000	163.8469	−38.1611	2.2421	1.4309	1.5241
0.6	0.0000	162.9448	−54.6722	−2.3996	1.4230	1.4814
0.7	0.0000	110.1710	−33.6997	−6.8182	0.9622	0.9245
0.8	0.0000	21.8458	−2.1211	−8.6092	0.1908	0.0593
0.9	0.0000	−69.1988	28.4423	−7.2932	−0.6043	−0.7751
1.0	0.0000	−131.0066	47.3701	−3.5026	−1.1441	−1.2718

Image 6: Response for constant acceleration. Adapted from (Chopra 2012)

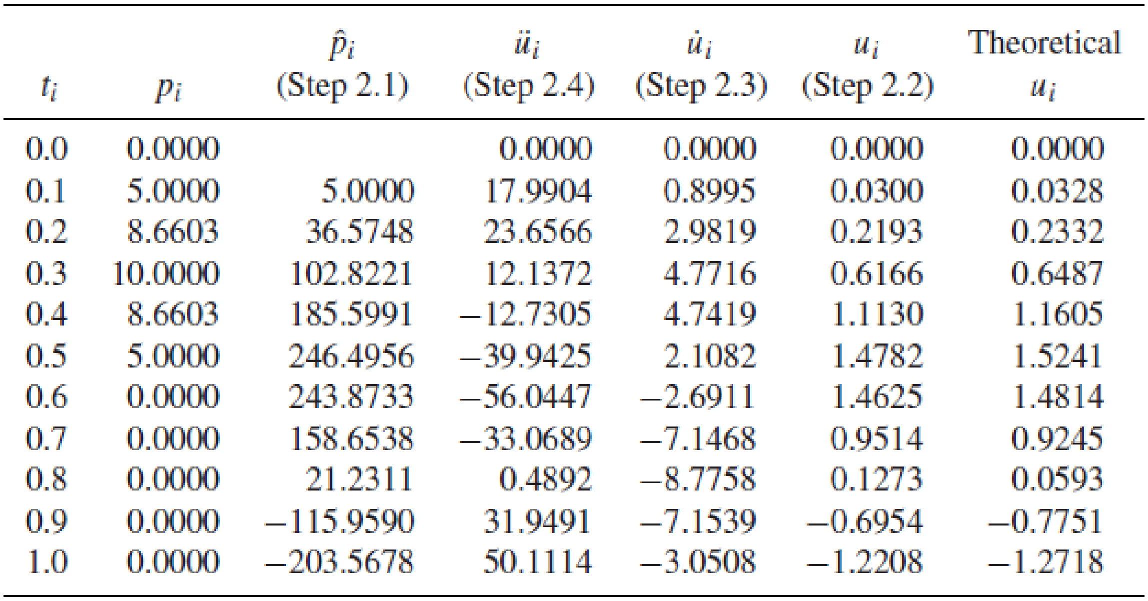

t_i	p_i	$\hat{p}_i$ (Step 2.1)	$\ddot{u}_i$ (Step 2.4)	$\dot{u}_i$ (Step 2.3)	u_i (Step 2.2)	Theoretical u_i
0.0	0.0000		0.0000	0.0000	0.0000	0.0000
0.1	5.0000	5.0000	17.9904	0.8995	0.0300	0.0328
0.2	8.6603	36.5748	23.6566	2.9819	0.2193	0.2332
0.3	10.0000	102.8221	12.1372	4.7716	0.6166	0.6487
0.4	8.6603	185.5991	−12.7305	4.7419	1.1130	1.1605
0.5	5.0000	246.4956	−39.9425	2.1082	1.4782	1.5241
0.6	0.0000	243.8733	−56.0447	−2.6911	1.4625	1.4814
0.7	0.0000	158.6538	−33.0689	−7.1468	0.9514	0.9245
0.8	0.0000	21.2311	0.4892	−8.7758	0.1273	0.0593
0.9	0.0000	−115.9590	31.9491	−7.1539	−0.6954	−0.7751
1.0	0.0000	−203.5678	50.1114	−3.0508	−1.2208	−1.2718

Image 7: Response for linear acceleration. Adapted from (Chopra 2012)

The data introduced in the computer code is given in Image 8.

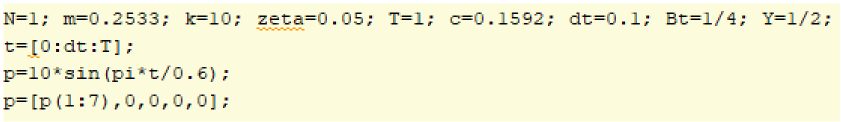

```
N=1; m=0.2533; k=10; zeta=0.05; T=1; c=0.1592; dt=0.1; Bt=1/4; Y=1/2;
t=[0:dt:T];
p=10*sin(pi*t/0.6);
p=[p(1:7),0,0,0,0];
```

Image 8: Input parameters for SDOF benchmark

The dynamic force could be seen in Image 9

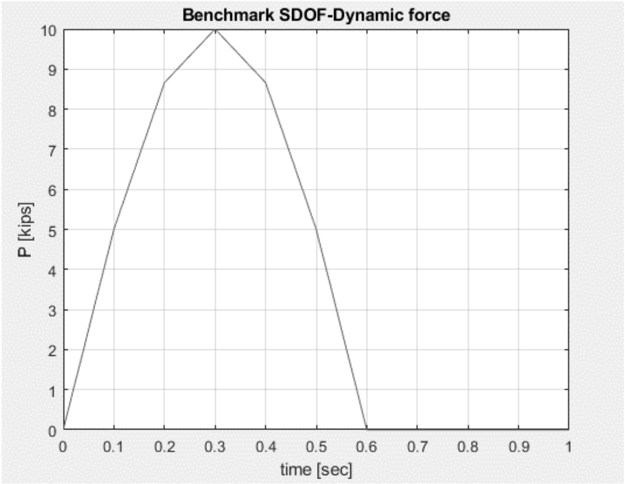

Image 9: Input force

The solution is given in Image 10 and Image 11.

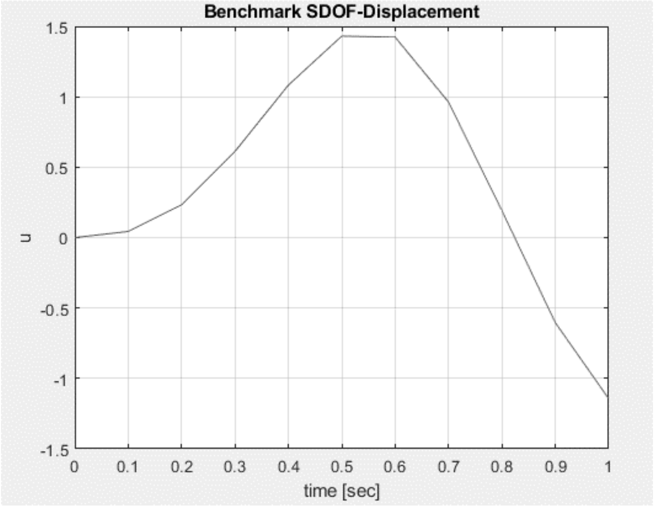

Image 10: Response for SDOF benchmark-constant acceleration

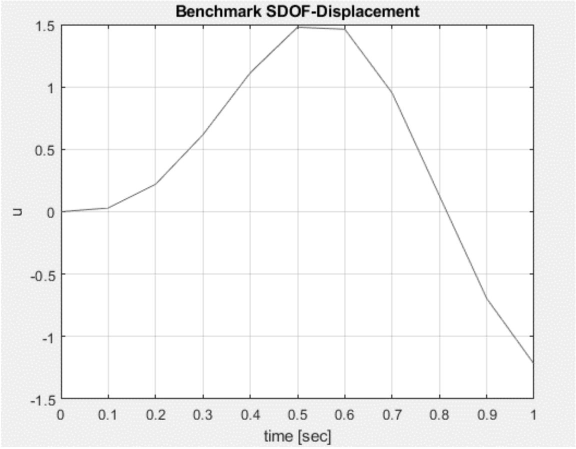

Image 11: Response for SDOF benchmark-linear acceleration

Time	u-constant acc	u-linear acc
0	0	0
0,1	0,0436665968001118	0,0299839286142628
0,2	0,232616513636352	0,219331309427338
0,3	0,612062958627255	0,616602191668912
0,4	1,08252521764122	1,11299781370026
0,5	1,43092707443901	1,47818122356363
0,6	1,42304922080044	1,46245569277727
0,7	0,962158348751629	0,951412864283085
0,8	0,190785913815418	0,127318087078159
0,9	-0,604335358601955	-0,695381429463452
1	-1,14412278585381	-1,22075244478284

The error is of the time steps of the response is shown in the following:

Time	**u-constant acc**			**u-linear acc**		
	Code	**Chopra**	**Error[%]**	**Code**	**Chopra**	**Error[%]**
0	0	0	0	0	0	0
0,1	0.0437	0.0437	0.0765	0.0300	0.0300	0.0536
0,2	0.2326	0.2326	0.0071	0.2193	0.2193	0.0143
0,3	0.6121	0.6121	0.0061	0.6166	0.6166	0.0004
0,4	1.0825	1.0833	0.0670	1.1130	1.1130	0.0002
0,5	1.4309	1.4309	0.0019	1.4782	1.4782	0.0013
0,6	1.4230	1.4230	0.0035	1.4625	1.4625	0.0030
0,7	0.9622	0.9622	0.0043	0.9514	0.9514	0.0014
0,8	0.1908	0.1908	0.0074	0.1273	0.1273	0.0142
0,9	-0.6043	-0.6043	0.0059	-0.6954	-0.6954	0.0027
1	-1.1441	-1.1441	0.0020	-1.2208	-1.2208	0.0039
		Total	**0.182**		Total	**0.095**

The error computed is less than 0.2% therefore the capability of the code to assess the response by means of the integration of the equations of motion of SODF systems is verified.

4. Newmark Method for MDOF from: Pag 678-679 Chopra DOS 4th edition

A structure as that given in Image 12 a) submitted to a uniform dynamic force with time variation as that shown in Image 12 b) was analyzed using the numerical scheme of the Newmark method. The result reported by (Chopra 2012) was compared with that coming from the computer code analysis.

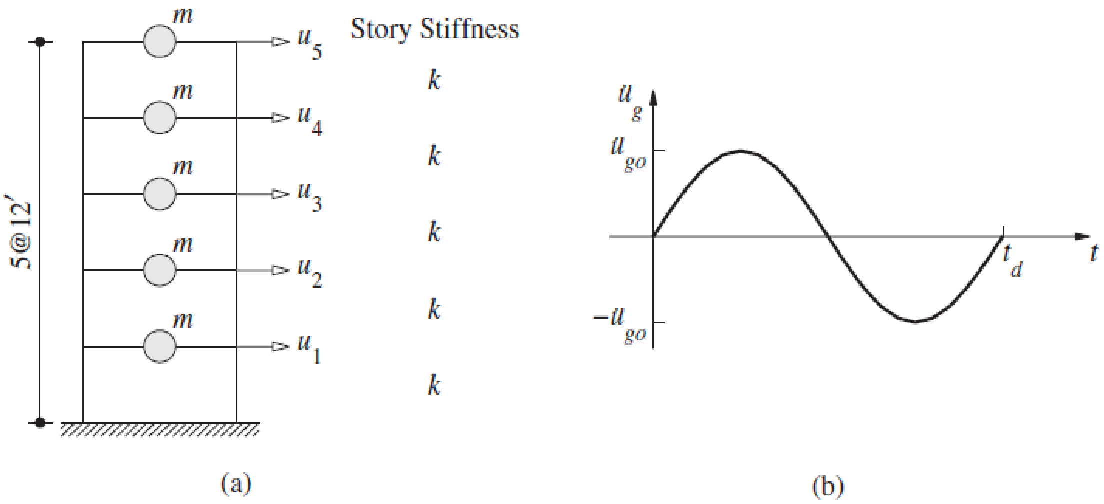

(a) (b)

Image 12: Structure for MDOF Newmark method. Adapted from (Chopra 2012)

The structural matrixes and the dynamic force distribution vector are:

$$\mathbf{m} = m\begin{bmatrix} 1 & & & & \\ & 1 & & & \\ & & 1 & & \\ & & & 1 & \\ & & & & 1 \end{bmatrix} \quad \mathbf{k} = k\begin{bmatrix} 2 & -1 & & & \\ -1 & 2 & -1 & & \\ & -1 & 2 & -1 & \\ & & -1 & 2 & -1 \\ & & & -1 & 1 \end{bmatrix} \quad \mathbf{p}(t) = -m\begin{bmatrix} 1 \\ 1 \\ 1 \\ 1 \\ 1 \end{bmatrix} \ddot{u}_g(t) \tag{a}$$

Parameter	Symbol	Value	Unit
Mass	m	100	*[kips/g*]*
Stiffness	k	100	*[kip/in]*
Dynamic excitation	$\ddot{u}0$	0.5	*[g*]*
Damping ratio	ζ	5	*[%]*
Time step	*Δt*	0.1	*[sec]*
Cut Time	*td*	1	*[sec]*

* the term g stands for the gravity constant

Solving for the first two modes of the structure it is possible to obtain:

$$\Omega = \begin{bmatrix} 5.592 & \\ & 16.32 \end{bmatrix} \qquad \Phi = \begin{bmatrix} 0.334 & -0.895 \\ 0.641 & -1.173 \\ 0.895 & -0.641 \\ 1.078 & 0.334 \\ 1.173 & 1.078 \end{bmatrix}$$

Image 13: Modal quantities. Adapted from (Chopra 2012)

Normalizing the structural quantities to the modal coordinates.

$$\mathbf{M} = \begin{bmatrix} 1 & \\ & 1 \end{bmatrix} \qquad \mathbf{K} = \begin{bmatrix} 31.27 & \\ & 266.4 \end{bmatrix} \qquad \mathbf{P}(t) = \begin{bmatrix} -1.067 \\ 0.336 \end{bmatrix} \ddot{u}_g(t)$$

And the modal damping matrix:

$$\mathbf{C} = \begin{bmatrix} 0.559 & \\ & 1.632 \end{bmatrix}$$

The solution in modal and natural coordinates using linear acceleration can be seen in graphically in Image 14 and numerically in Image 15.

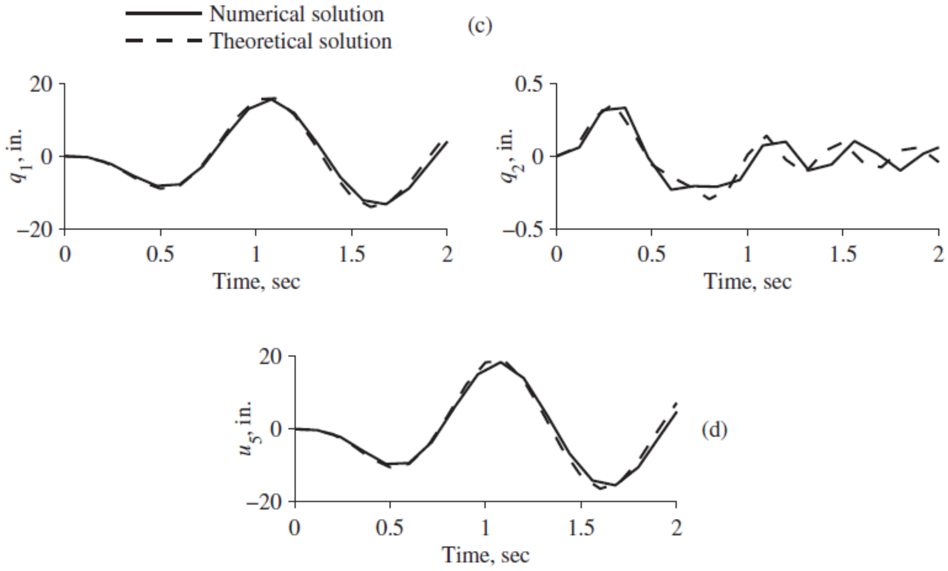

Image 14: Graphical Response of MDOF benchmark Adapted from (Chopra 2012)

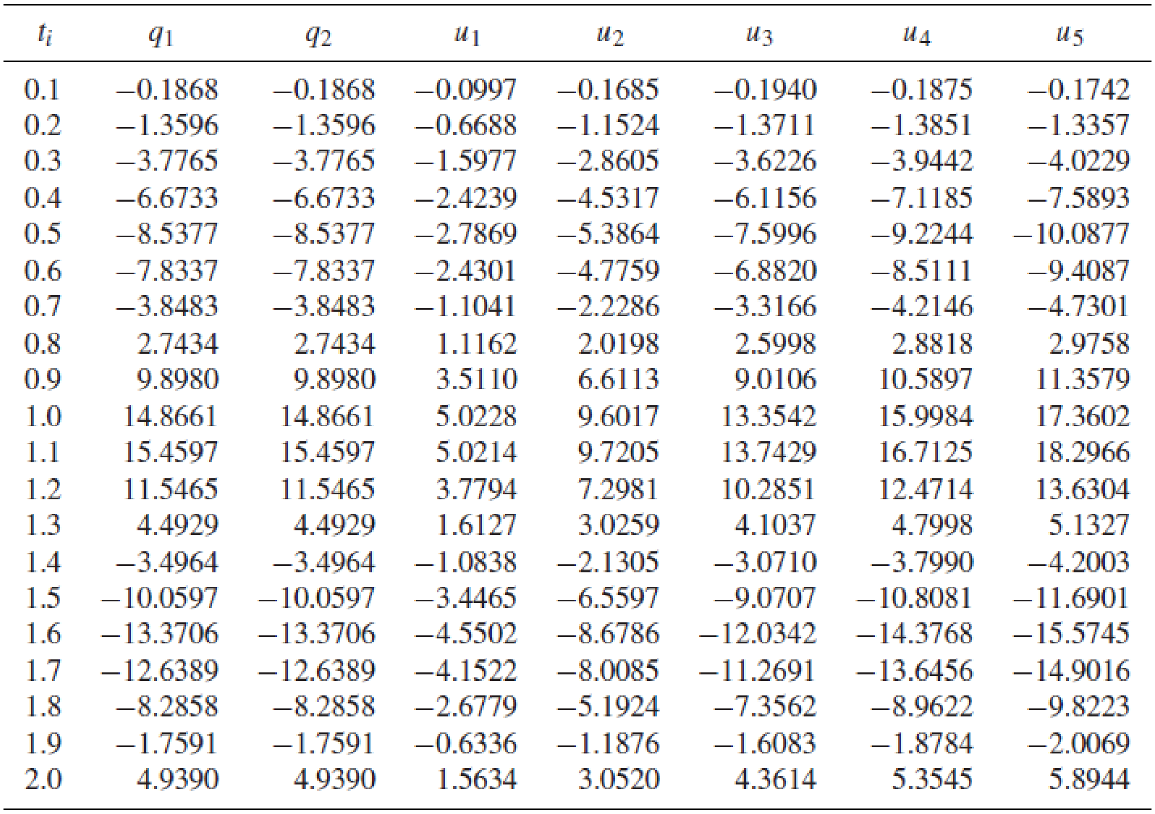

t_i	q_1	q_2	u_1	u_2	u_3	u_4	u_5
0.1	−0.1868	−0.1868	−0.0997	−0.1685	−0.1940	−0.1875	−0.1742
0.2	−1.3596	−1.3596	−0.6688	−1.1524	−1.3711	−1.3851	−1.3357
0.3	−3.7765	−3.7765	−1.5977	−2.8605	−3.6226	−3.9442	−4.0229
0.4	−6.6733	−6.6733	−2.4239	−4.5317	−6.1156	−7.1185	−7.5893
0.5	−8.5377	−8.5377	−2.7869	−5.3864	−7.5996	−9.2244	−10.0877
0.6	−7.8337	−7.8337	−2.4301	−4.7759	−6.8820	−8.5111	−9.4087
0.7	−3.8483	−3.8483	−1.1041	−2.2286	−3.3166	−4.2146	−4.7301
0.8	2.7434	2.7434	1.1162	2.0198	2.5998	2.8818	2.9758
0.9	9.8980	9.8980	3.5110	6.6113	9.0106	10.5897	11.3579
1.0	14.8661	14.8661	5.0228	9.6017	13.3542	15.9984	17.3602
1.1	15.4597	15.4597	5.0214	9.7205	13.7429	16.7125	18.2966
1.2	11.5465	11.5465	3.7794	7.2981	10.2851	12.4714	13.6304
1.3	4.4929	4.4929	1.6127	3.0259	4.1037	4.7998	5.1327
1.4	−3.4964	−3.4964	−1.0838	−2.1305	−3.0710	−3.7990	−4.2003
1.5	−10.0597	−10.0597	−3.4465	−6.5597	−9.0707	−10.8081	−11.6901
1.6	−13.3706	−13.3706	−4.5502	−8.6786	−12.0342	−14.3768	−15.5745
1.7	−12.6389	−12.6389	−4.1522	−8.0085	−11.2691	−13.6456	−14.9016
1.8	−8.2858	−8.2858	−2.6779	−5.1924	−7.3562	−8.9622	−9.8223
1.9	−1.7591	−1.7591	−0.6336	−1.1876	−1.6083	−1.8784	−2.0069
2.0	4.9390	4.9390	1.5634	3.0520	4.3614	5.3545	5.8944

Image 15: Response of MDOF benchmark Adapted from (Chopra 2012)

The data introduced in the computer code is given in Image 16.

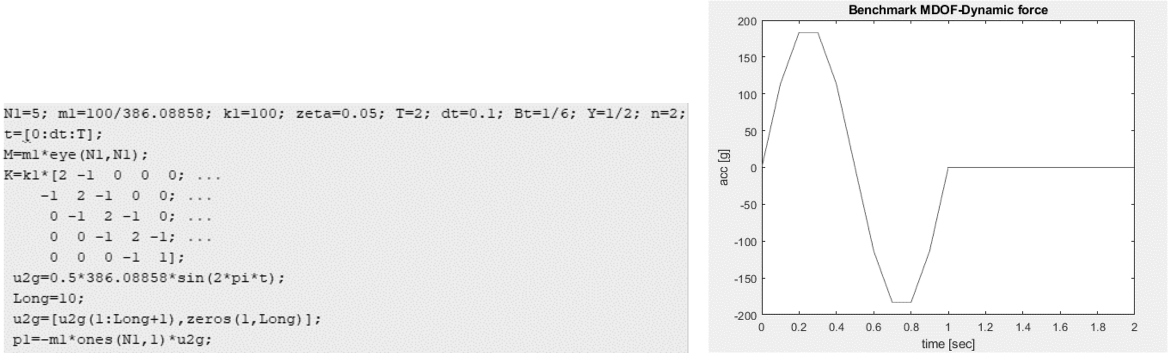

```
N1=5; m1=100/386.08858; k1=100; zeta=0.05; T=2; dt=0.1; Bt=1/6; Y=1/2; n=2;
t=[0:dt:T];
M=m1*eye(N1,N1);
K=k1*[2 -1  0  0  0; ...
    -1  2 -1  0  0; ...
     0 -1  2 -1  0; ...
     0  0 -1  2 -1; ...
     0  0  0 -1  1];
 u2g=0.5*386.08858*sin(2*pi*t);
 Long=10;
 u2g=[u2g(1:Long+1),zeros(1,Long)];
 p1=-m1*ones(N1,1)*u2g;
```

Image 16: Input parameters for MDOF benchmark

The solution is given in Image 17.

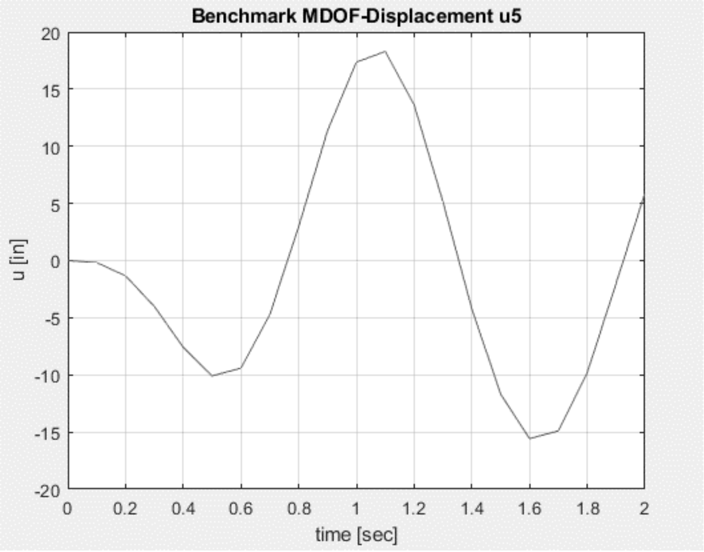

Image 17: Response for MDOF benchmark

Time	q1	q2	u5
0	0	0	0
0,1	-0,186865633807604	0,0416455532978688	-0,174275016382209
0,2	-1,35975819055173	0,240060246107161	-1,33602151950221
0,3	-3,77678463008510	0,376504092889729	-4,02371484055991
0,4	-6,67357391080269	0,219284639272090	-7,59060073381859
0,5	-8,53757607672224	-0,0701660360523685	-10,0887262678436
0,6	-7,83265253540952	-0,206090269174448	-9,40847355976412
0,7	-3,84614443873849	-0,201465161633760	-4,72800387785398
0,8	2,74639268324389	-0,224006115223162	2,97960734413175
0,9	9,90087734148697	-0,231434849516072	11,3625739848454
1	14,8675125368108	-0,0677936695531881	17,3639526485609
1,1	15,4583388920794	0,155106900328850	18,2971346259484
1,2	11,5419718815220	0,0832374414465396	13,6264515670801
1,3	4,48593966817822	-0,126331145050207	5,12507038829085
1,4	-3,50382044617911	-0,0928179966700731	-4,20941584990312
1,5	-10,0651950680919	0,0992322500763592	-11,6977797628692
1,6	-13,3720289852520	0,0974080392820531	-15,5780903161438

1,7	-12,6352119189265	-0,0743610786516145	-14,8990660510939
1,8	-8,27749983008625	-0,0978675093239892	-9,81355877012316
1,9	-1,74833806772110	0,0520837179273239	-1,99436181093077
2,0	4,94904734015376	0,0950179096727110	5,90678819305177

The error computed for the displacement of the 5th DOF is as reported in the following:

Time	Chopra	Code	Error [%]
0	0	0	0
0,1	-0.1742	-0.1742750	0.0430634
0,2	-1.3357	-1.3360215	0.0240712
0,3	-4.0229	-4.0237148	0.0202551
0,4	-7.5893	-7.5906007	0.0171390
0,5	-10.0877	-10.0887263	0.0101735
0,6	-9.4087	-9.4084736	0.0024067
0,7	-4.7301	-4.7280039	0.0443145
0,8	2.9758	2.9796073	0.1279435
0,9	11.3579	11.3625740	0.0411518
1	17.3602	17.3639526	0.0216164
1,1	18.2966	18.2971346	0.0029220
1,2	13.6304	13.6264516	0.0289678
1,3	5.1327	5.1250704	0.1486471
1,4	-4.2003	-4.2094158	0.2170285
1,5	-11.6901	-11.6977798	0.0656946
1,6	-15.5745	-15.5780903	0.0230525
1,7	-14.9016	-14.8990661	0.0170045
1,8	-9.8223	-9.8135588	0.0889937
1,9	-2.0069	-1.9943618	0.6247541
2,0	5.8944	5.9067882	0.2101689
		Total	**1.779**

The results reported in (Chopra 2012) coincide with those computed by the code. Therefore, it is verified that the function *Newmark* performs the numerical integration of the equations of motion. The function is given in the following:

```
function [u,v,ac]=newmark(m,k,c,Bt,Y,p,T,dt,t,N,uo,vo)
% all quantities must enter whether in modal or natural coordinates
% if input in MODAL ouput in MODAL, if input NATURAL output NATURAL
% solution vectors
 u=zeros(N,T/dt);
 v=zeros(N,T/dt);
 ac=zeros(N,T/dt);
%intial conditions
if uo==0
 u(:,1)=zeros(N,1);
else
  u(:,1)=uo;
end
if vo==0
 v(:,1)=zeros(N,1);
else
  v(:,1)=vo;
end
 %adapted from page 678 chopra 4th edition
 ac(:,1)=m\(p(:,1)-c*v(:,1)-k*u(:,1));
 a1=1/(Bt*dt^2)*m+Y/(Bt*dt)*c;
 a2=1/(Bt*dt)*m+(Y/Bt-1)*c;
 a3=(1/(2*Bt)-1)*m+dt*(Y/(2*Bt)-1)*c;
 Kn=k+a1;

  for i=2:length(t)
       Pi=p(:,i);
       Pni=Pi+a1*u(:,i-1)+a2*v(:,i-1)+a3*ac(:,i-1);
       u(:,i)=Kn\Pni;
       v(:,i)=Y/(Bt*dt)*(u(:,i)-u(:,i-1))+(1-Y/Bt)*v(:,i-1)+dt*(1-
Y/(2*Bt))*ac(:,i-1);
       ac(:,i)=1/(Bt*dt^2)*(u(:,i)-u(:,i-1))-1/(Bt*dt)*v(:,i-1)-(1/(2*Bt)-
1)*ac(:,i-1);

 end

end
```

APPENDIX B: SAP 2000 Dynamic testing

1. Sap2000 control model for SDOF

A sap2000 model was built to test the direct integration of the equations of motion, the results were successful obtaining the same result in terms of shape, maximum and minimum displacement.

The model consists in a lumped mass with linked with a spring as shown in Figure 0-1 representing the structure shown already in Figure 4-1b. no further details of the modeling could be included since was a very simple one.

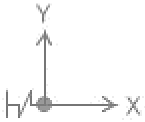

Figure 0-1: Sap2000 model

The values of mass are those provide in Equation 4-79 and stiffness Equation 4-80, the test was performed used a stiffness parametric coefficient Ck of 0.5. The damping was simulated as constant damping ratio of 2% for all modes (even though there is only one). While the acting acceleration introduced in the Sap model corresponds to force of a white noise signal which was generated according to 4.3 divided by the mass of the system (Figure 0-2), the input signal for the time domain analysis was the white noise signal itself.

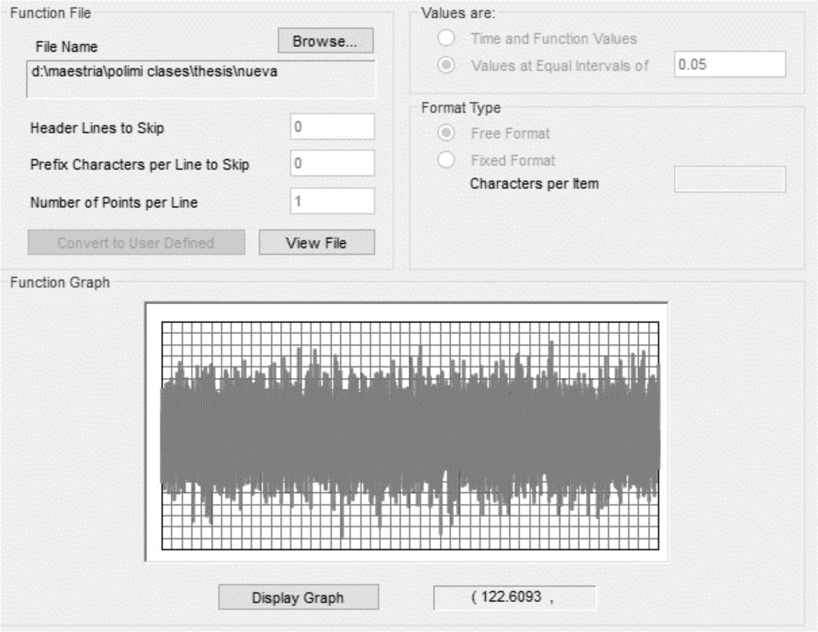

File Name: d:\maestria\polimi clases\thesis\nueva

Header Lines to Skip: 0

Prefix Characters per Line to Skip: 0

Number of Points per Line: 1

○ Time and Function Values

● Values at Equal Intervals of: 0.05

● Free Format

○ Fixed Format

Characters per Item:

(122.6093 ,

Figure 0-2: Acceleration time history Sap2000 model

The result of the Sap model is given in Figure 0-3. The maximum displacement $7.023\text{x}10^{-4}$ and the minimum $-7.305\text{x}10^{-4}$. Regarding the built-up code for the integration of equation motion, the result is given in Figure 0-4 with the maximum 7.0226e-04 and a minimum 7.3049e-04.

The error involved between the two approaches could be computed as:

$$error = \frac{MaxSap - MaxTDA}{MaxSap} = \frac{7.023 - 7.0226}{7.023} = 0.005\%$$

This error could be given by the approximation of the scientific notation. In addition, comparing the shape of the responses is possible to see a complete match of both representations. Therefore, is possible to state that the algorithm of generation of equations of motion is fully calibrated and not error in the final response could come from this.

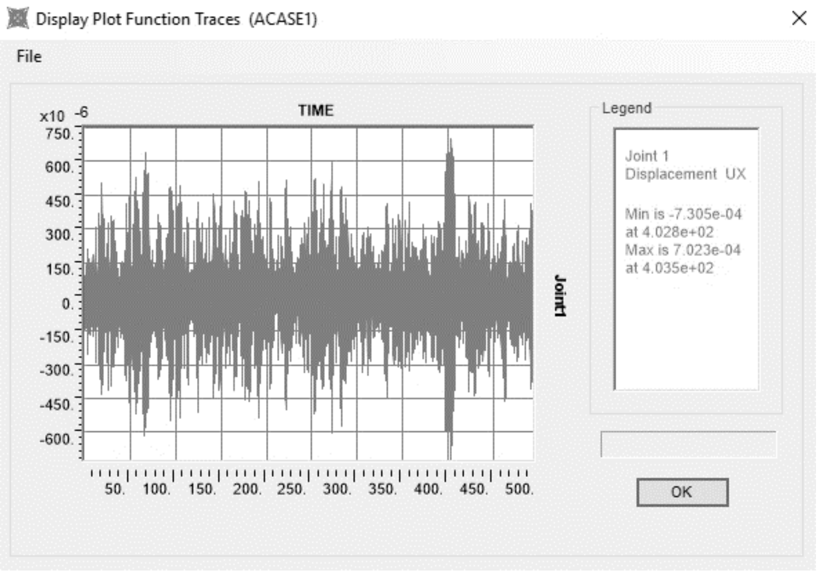

Joint 1
Displacement UX

Min is -7.305e-04
at 4.028e+02
Max is 7.023e-04
at 4.035e+02

Figure 0-3: Response displacement time history Sap2000 model

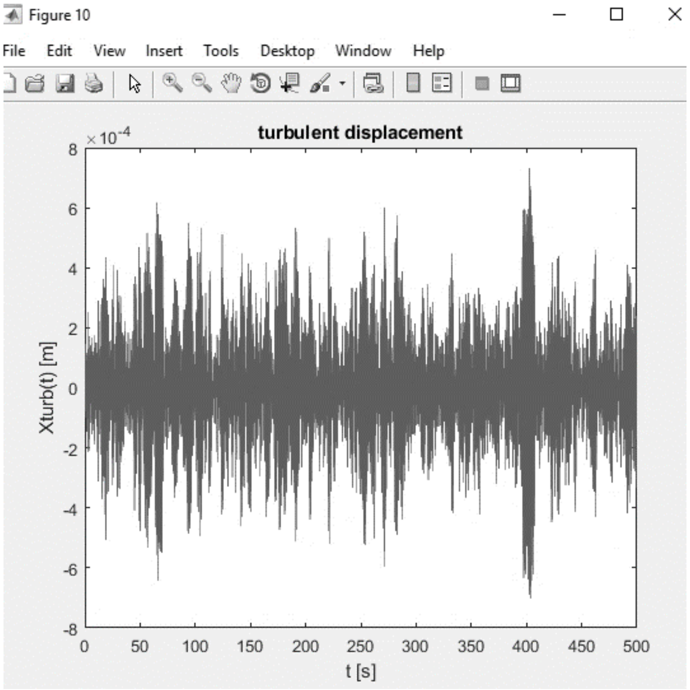

Figure 0-4: Response displacement time history TDA_SDOF model

2. Sap2000 control model for MDOF

Computer Code Simulation

A 3D frame structure as that shown in Image 18 submitted to harmonic dynamic force was analyzed using the computer code and the results were compared with those obtain with the commercial code Sap2000.

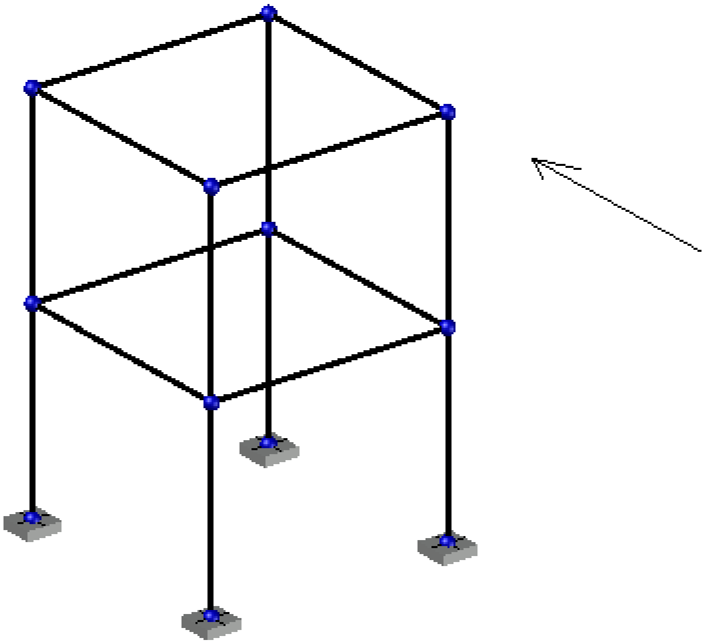

Image 18: 3D frame for MDOF benchmark

The structure nodes can be seen in Image 19 and the element Image 20.

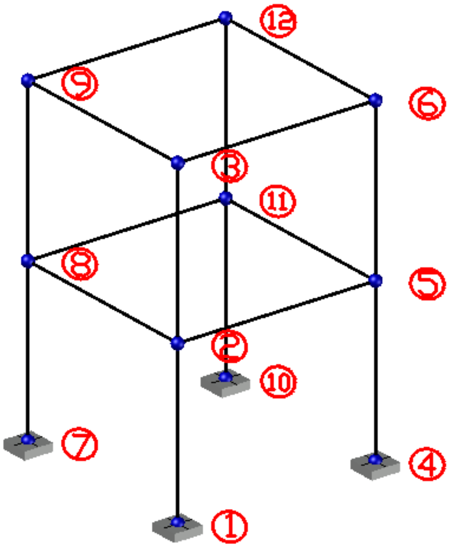

Image 19: Node id-3D frame for MDOF benchmark

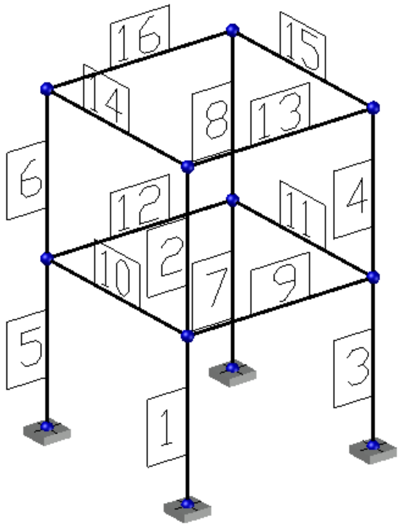

Image 20: Elements id-3D frame for MDOF benchmark

The structure is idealized to be a square section made of solid steel. The material parameters are reported as follows:

Parameter	Symbol	Value	Unit
Young Modulus	E	210.000.000	*[kPa]*
Poisson Ratio	ν	0.2	*[-]*
Density	ρ	7.850	*[kg/m3]*
Shear modulus	G	87.500.000	*[kPa]*

All the elements of the structure are composed by the same cross section, a picture of the same could be seen in Image 21

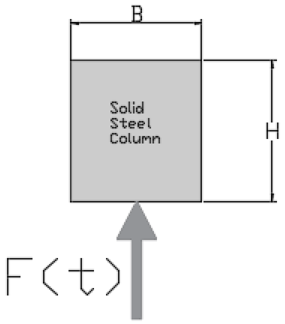

Image 21 Cross section

The geometric properties of the section are reported in the following:

Parameter	Symbol	Value	Unit
Area	A	0.25	*[m2]*
Inertia in y-y' direction	Iy	0.0052	*[m4]*
Inertia in z-z' direction	Iz	0.0052	*[m4]*
Shear coefficient	χ	5/6	*[-]*
Shear correction factor	ϕy	0.0199	*[-]*
Shear correction factor	ϕz	0.0199	*[-]*

The damping ratio is taken as 2% for accepted value for steel structures.

The dynamic force is applied in the node 6 in the positive *y-direction,* the time varying trend is as shown in Image 22.

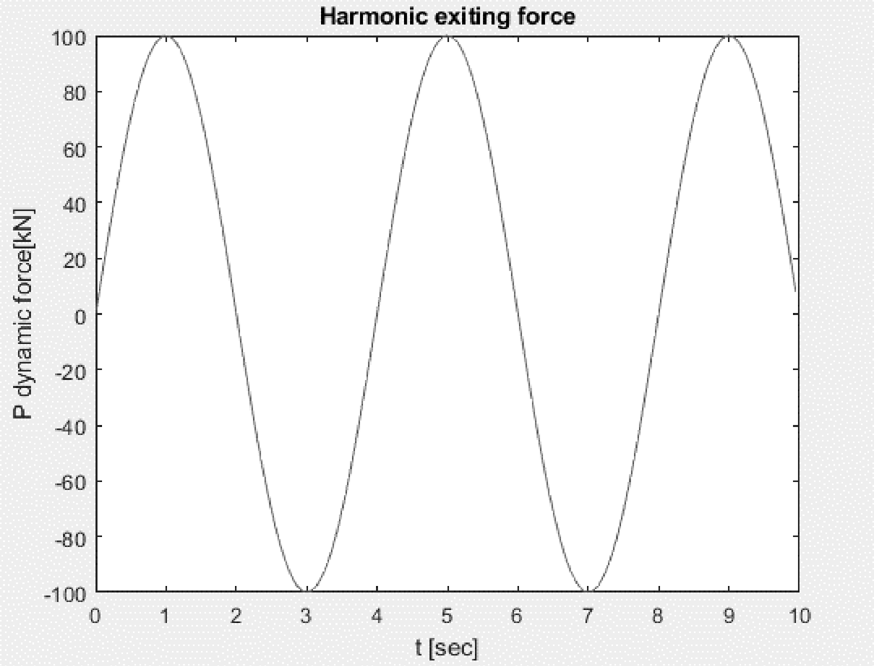

Image 22: Dynamic Force-3D frame for MDOF benchmark

$$P = 100 * sin\left(\frac{1}{2} * pi * t\right)[kN]$$

The structural model introduced in the computer code could be seen in Image 23

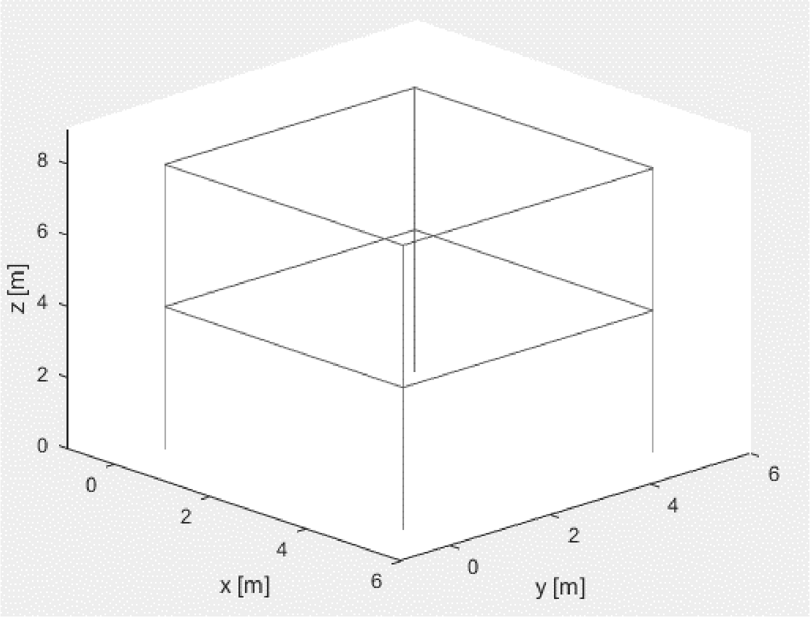

Image 23: Structure in MATLAB

Solving the Eigenvalue problem for the first 10 modes it was possible to recall the natural frequencies as:

Mode	Frequency	Period
1	7,82660044864517	0,127769394459520
2	7,82660044864577	0,127769394459510
3	8,86521981053036	0,112800361567140
4	20,5544087005782	0,0486513630514639
5	24,1125819211889	0,0414721245227269
6	24,1125819211889	0,0414721245227269
7	25,6222644248781	0,0390285567043420
8	30,3182497217688	0,0329834343729278
9	60,7037435312858	0,0164734486182819
10	71,4746144212041	0,0139909813868591

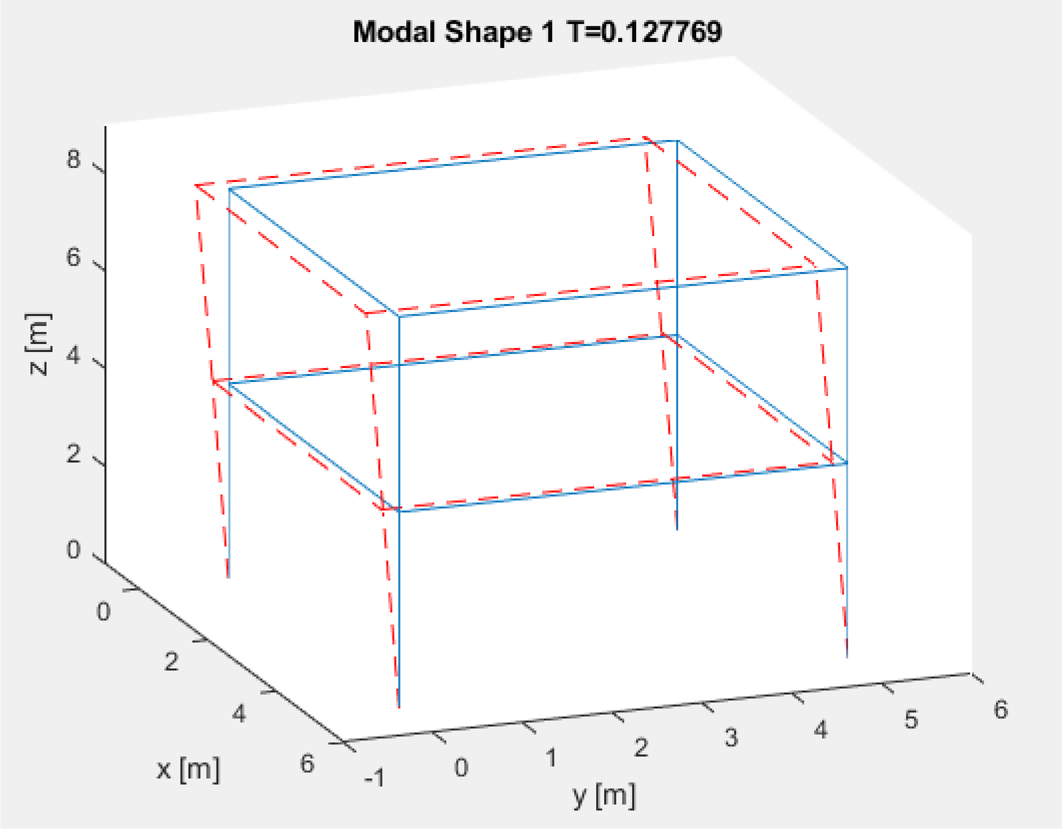
Modal Shape 1 T=0.127769
z [m]
8
6
4
2
0
x [m]
0
2
4
6
y [m]
-1
0
1
2
3
4
5
6

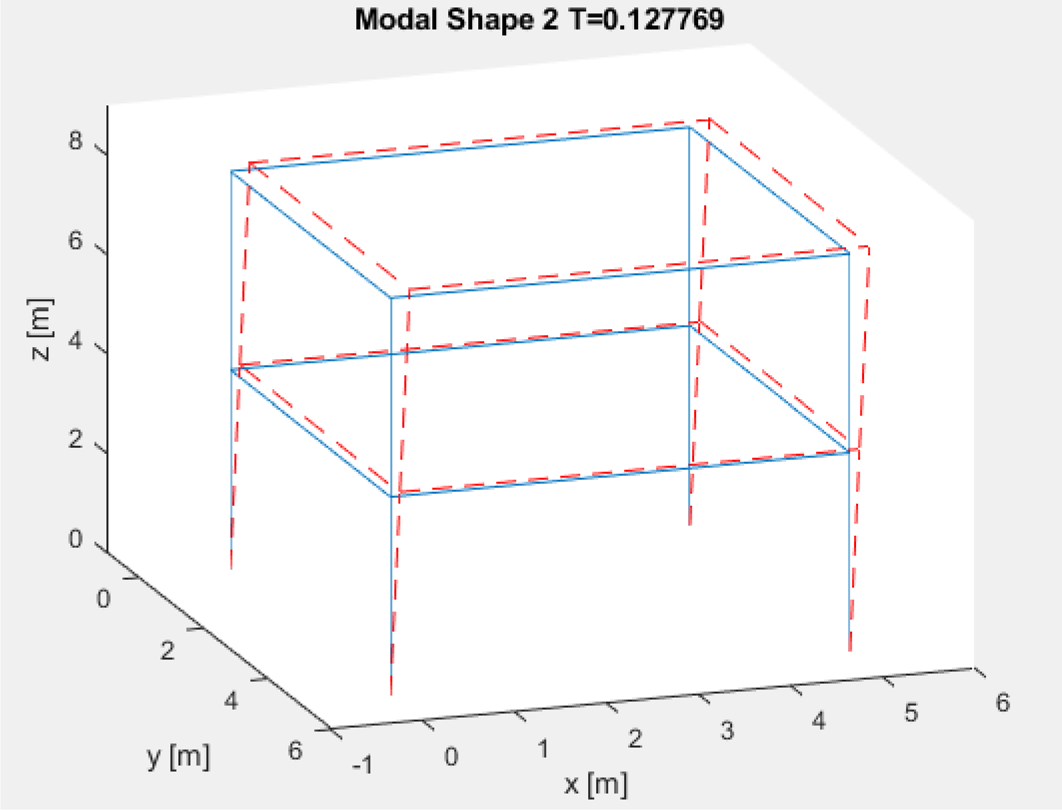
Modal Shape 2 T=0.127769
z [m]
8
6
4
2
0
y [m]
0
2
4
6
x [m]
-1
0
1
2
3
4
5
6

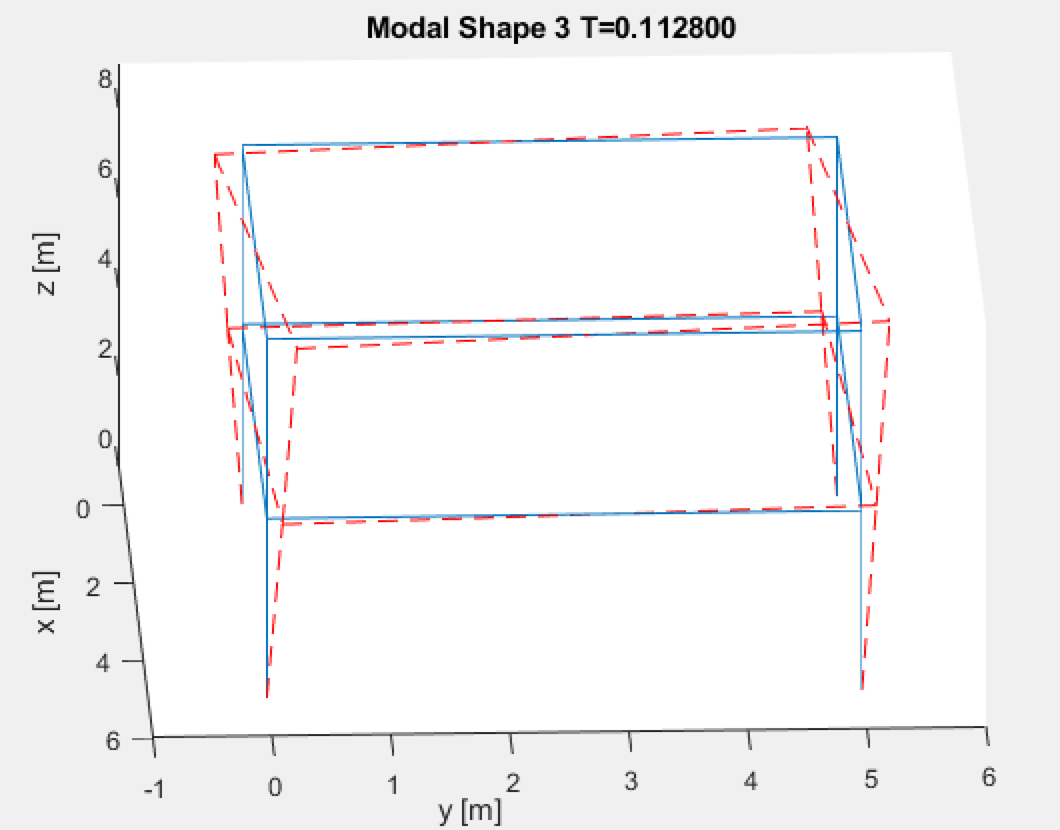
Modal Shape 3 T=0.112800
z [m]
8
6
4
2
0
x [m]
0
2
4
6
y [m]
-1
0
1
2
3
4
5
6

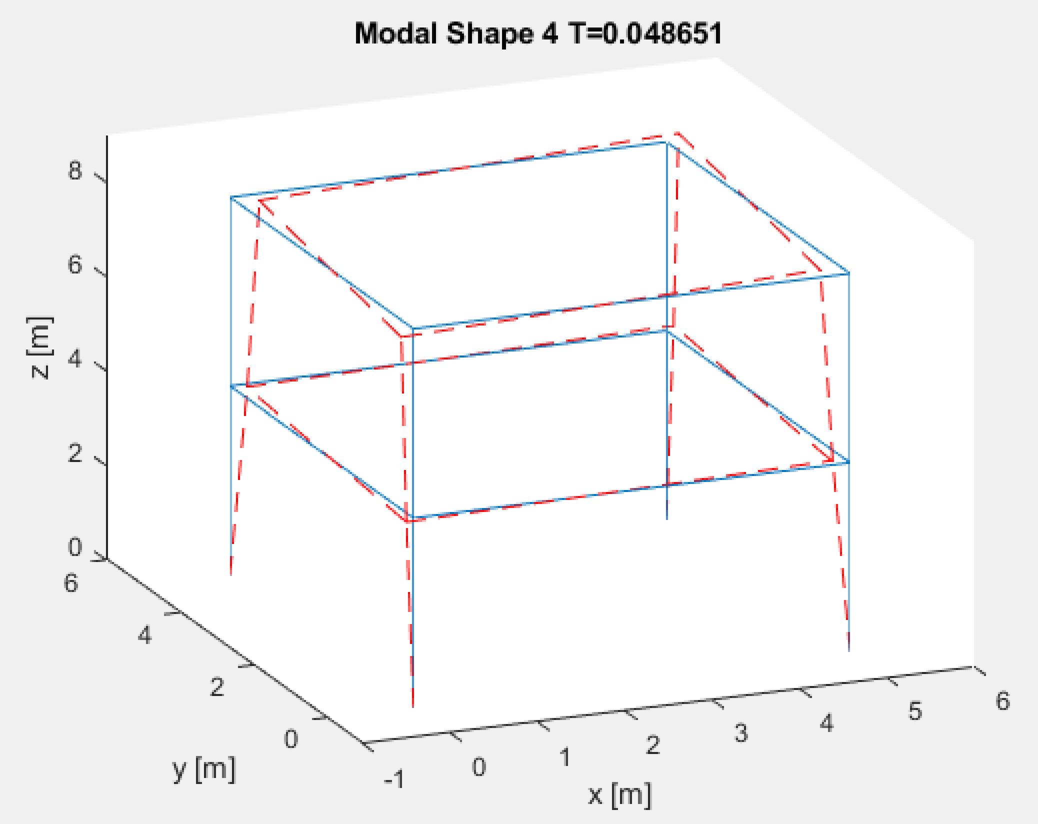
Modal Shape 4 T=0.048651
z [m]
8
6
4
2
0
y [m]
6
4
2
0
x [m]
-1
0
1
2
3
4
5
6

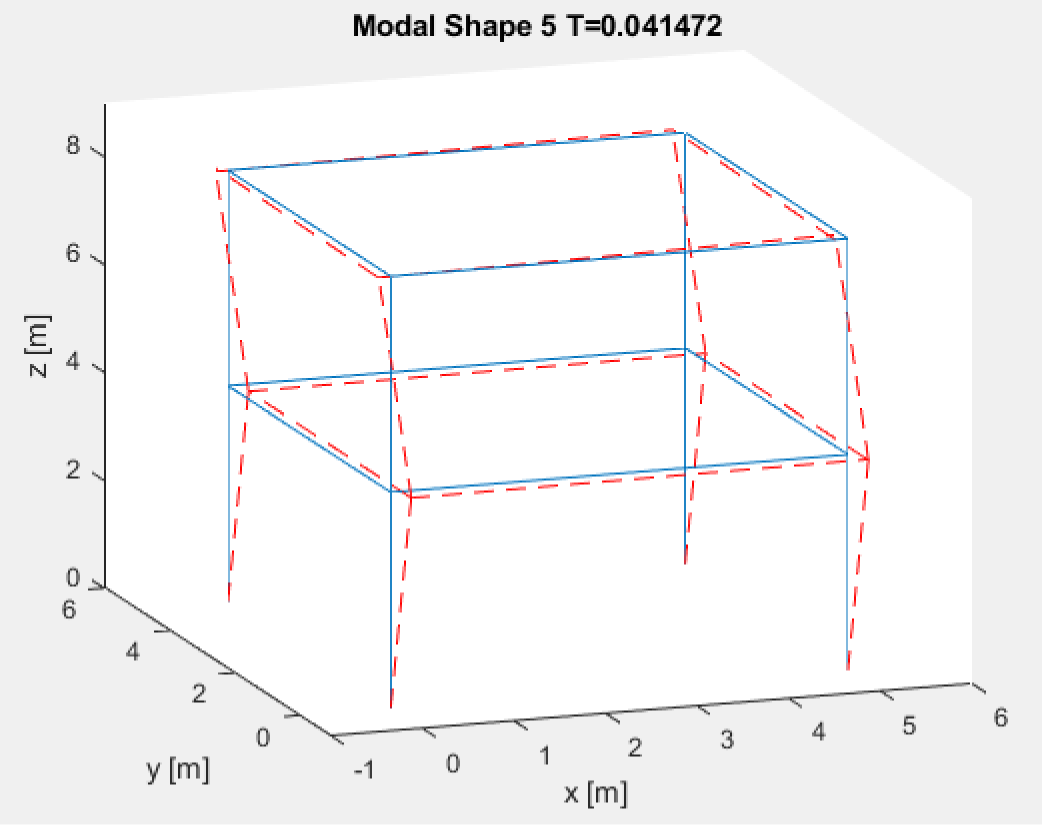
Modal Shape 5 T=0.041472
z [m]
8
6
4
2
0
y [m]
6
4
2
0
x [m]
-1
0
1
2
3
4
5
6

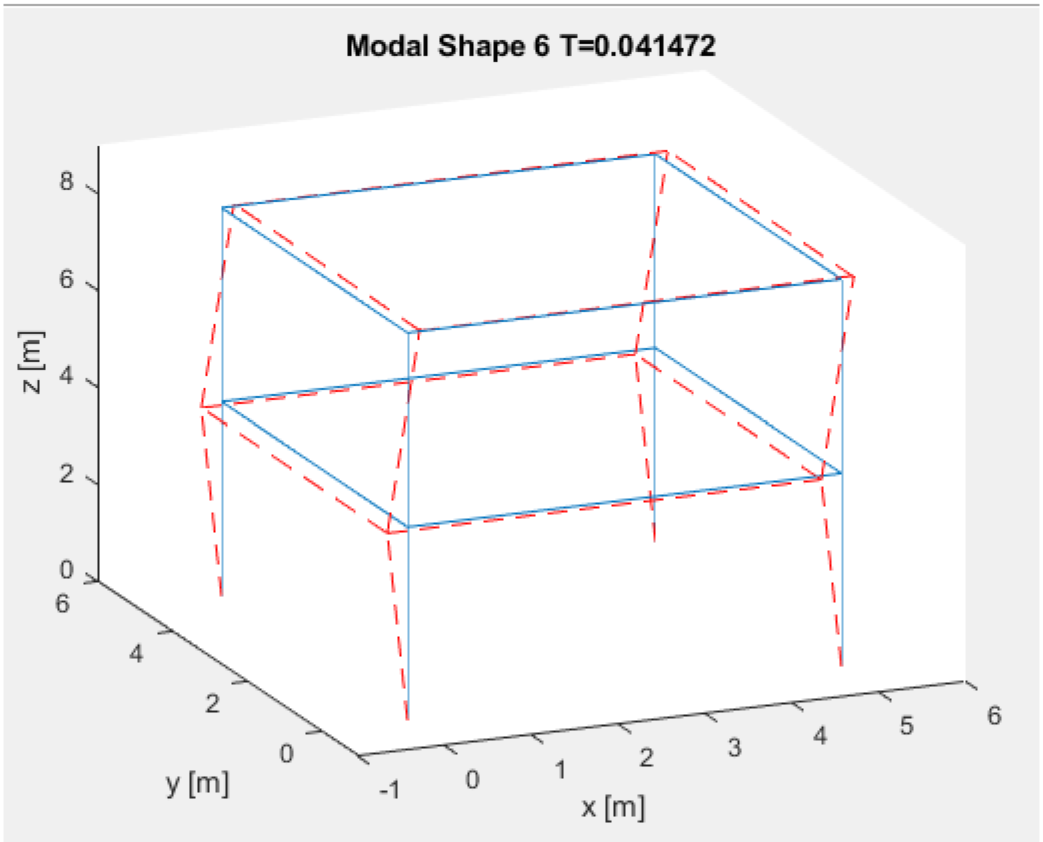
Modal Shape 6 T=0.041472
z [m]
8
6
4
2
0
y [m]
6
4
2
0
x [m]
-1
0
1
2
3
4
5
6

The displacement at the 20th DOF corresponding to the y-direction of the 6th node is given in Image 24.

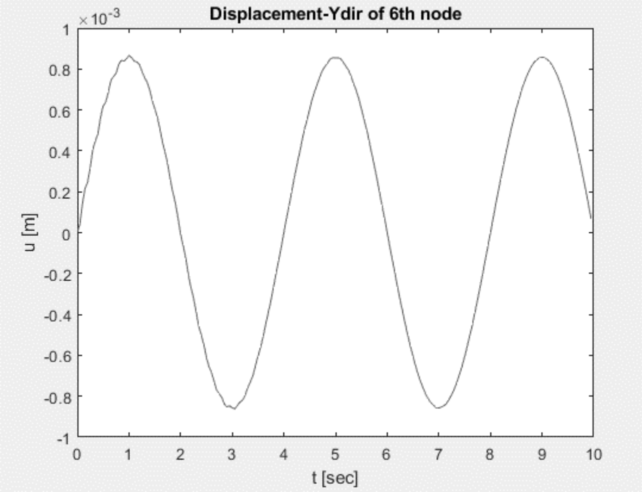

Image 24: Displacement 20th DOF.

Model in Sap2000

The material properties are those given in Image 25.

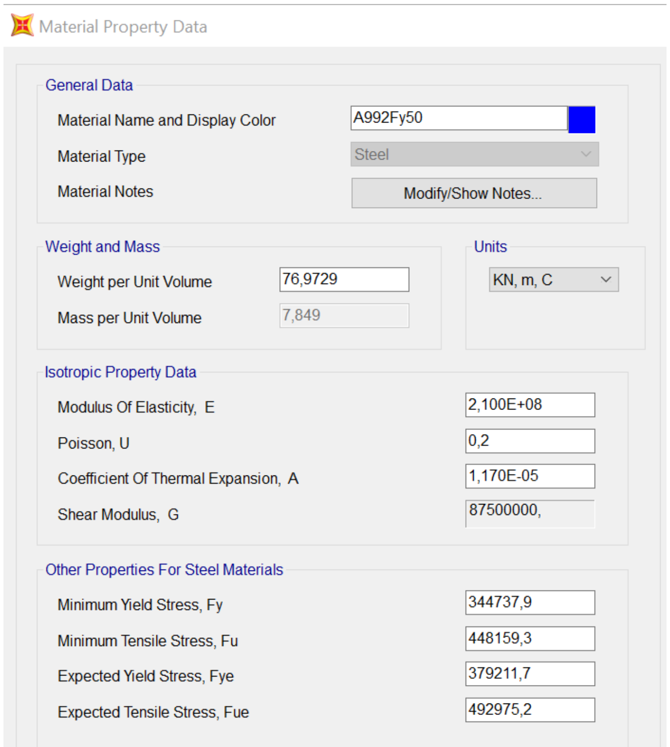
Material Property Data

General Data

Material Name and Display Color: A992Fy50

Material Type: Steel

Material Notes: Modify/Show Notes...

Weight and Mass

Weight per Unit Volume: 76,9729

Mass per Unit Volume: 7,849

Units: KN, m, C

Isotropic Property Data

Modulus Of Elasticity, E: 2,100E+08

Poisson, U: 0,2

Coefficient Of Thermal Expansion, A: 1,170E-05

Shear Modulus, G: 87500000,

Other Properties For Steel Materials

Minimum Yield Stress, Fy: 344737,9

Minimum Tensile Stress, Fu: 448159,3

Expected Yield Stress, Fye: 379211,7

Expected Tensile Stress, Fue: 492975,2

Image 25: Material properties Sap2000

The sections properties are given in Image 26.

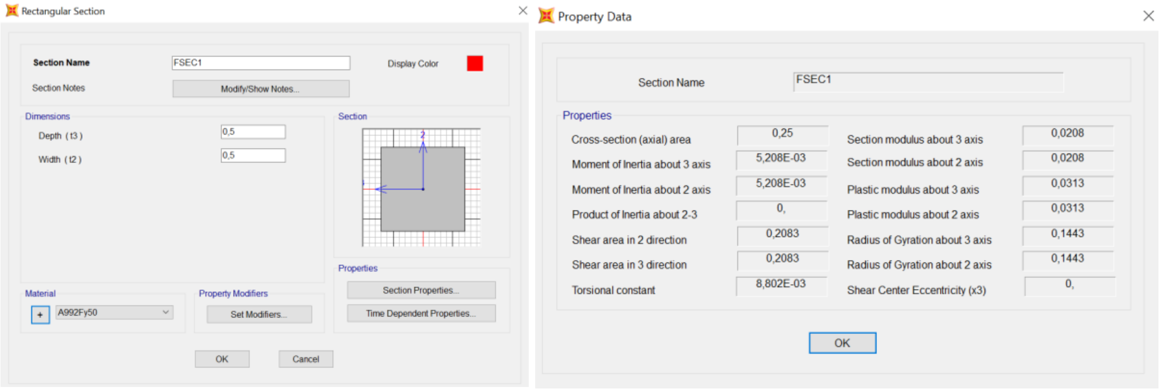

Section Name: FSEC1

Section Notes

Display Color: 🟥

Depth (t3): 0,5

Width (t2): 0,5

Material: A992Fy50

Section Name: FSEC1

Cross-section (axial) area	0,25	Section modulus about 3 axis	0,0208
Moment of Inertia about 3 axis	5,208E-03	Section modulus about 2 axis	0,0208
Moment of Inertia about 2 axis	5,208E-03	Plastic modulus about 3 axis	0,0313
Product of Inertia about 2-3	0,	Plastic modulus about 2 axis	0,0313
Shear area in 2 direction	0,2083	Radius of Gyration about 3 axis	0,1443
Shear area in 3 direction	0,2083	Radius of Gyration about 2 axis	0,1443
Torsional constant	8,802E-03	Shear Center Eccentricity (x3)	0,

Image 26: Section properties Sap2000

The structural scheme is that shown in Image 27 a). The dynamic excitation is placed in the positive *y-direction,* as shown in Image 27 b).

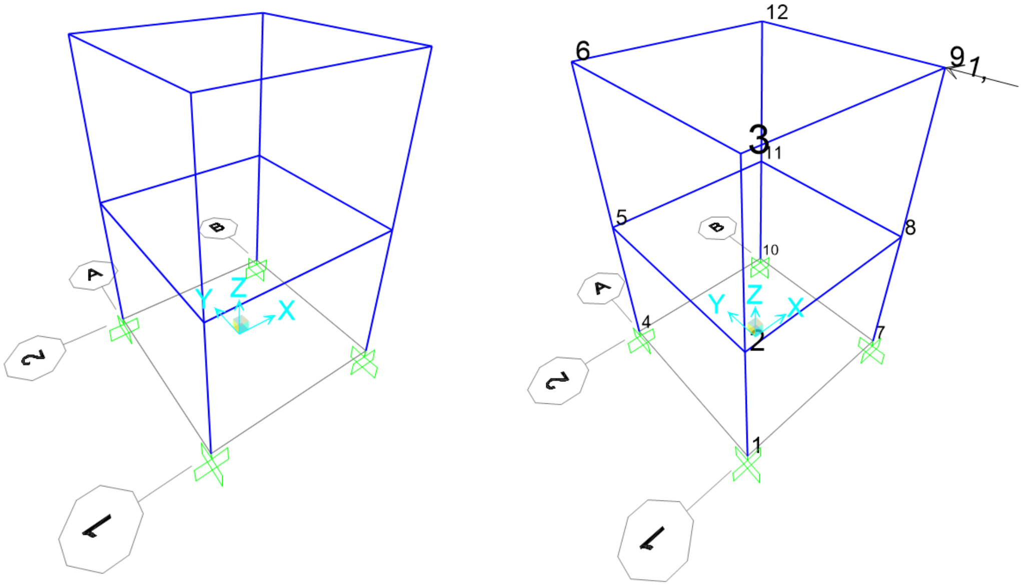

Image 27: Structure Sap2000

The dynamic force is as shown in Image 28.

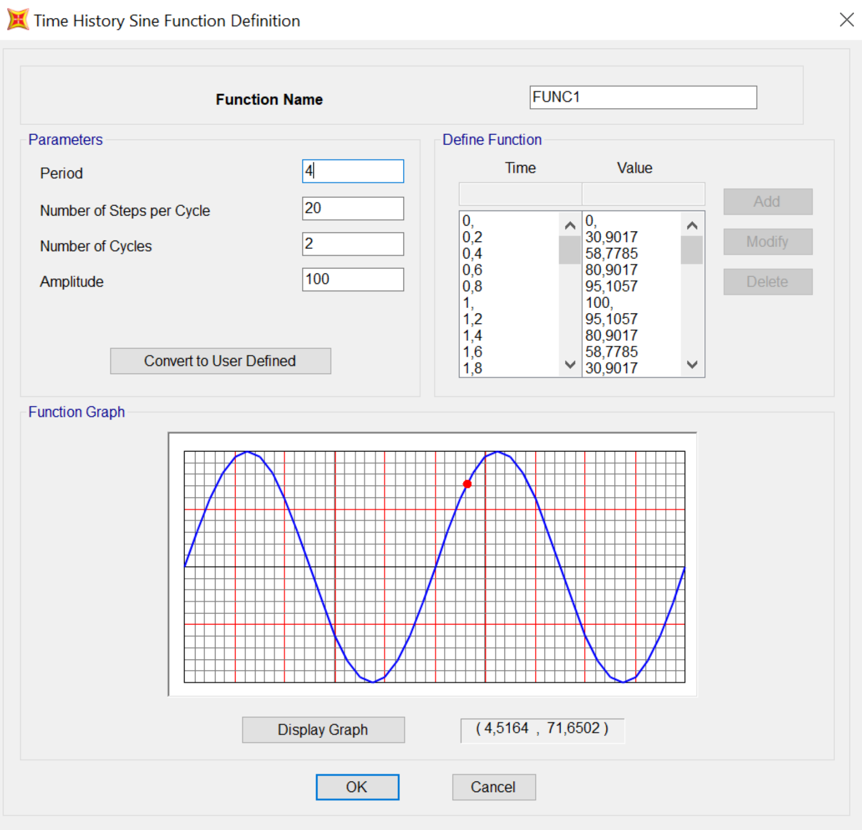

Function Name FUNC1

Period 4

Number of Steps per Cycle 20

Number of Cycles 2

Amplitude 100

Time	Value
0,	0,
0,2	30,9017
0,4	58,7785
0,6	80,9017
0,8	95,1057
1,	100,
1,2	95,1057
1,4	80,9017
1,6	58,7785
1,8	30,9017

(4,5164 , 71,6502)

Image 28: Dynamic force Sap2000

The modal information computed with Sap2000 are as follows:

MODE	Period	Frequency
1	0.1280	7.8125
2	0.1280	7.8125
3	0.1131	8.8403
4	0.0488	20.4900
5	0.0413	24.2252
6	0.0413	24.2252
7	0.0388	25.7679
8	0.0329	30.3647
9	0.0108	92.4531
10	0.0107	93.5302
11	0.0107	93.5302
12	0.0106	94.7475

And the modal shapes:

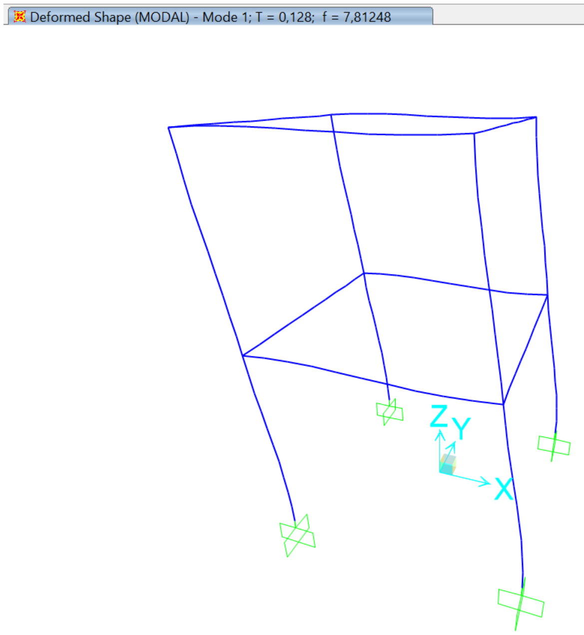
Deformed Shape (MODAL) - Mode 1; T = 0,128; f = 7,81248

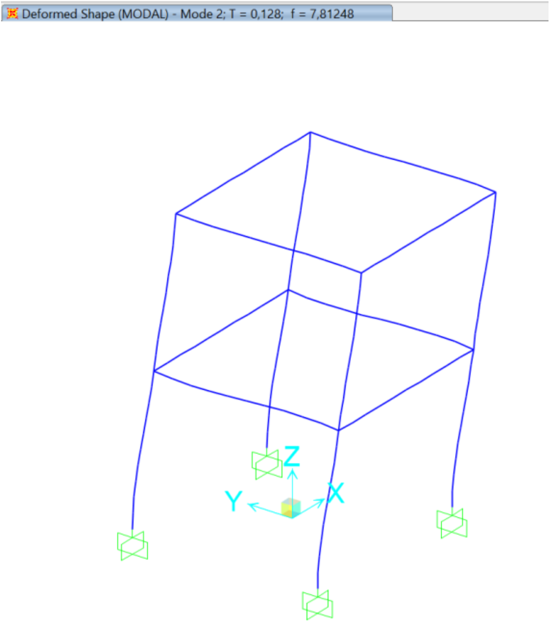
Deformed Shape (MODAL) - Mode 2; T = 0,128; f = 7,81248

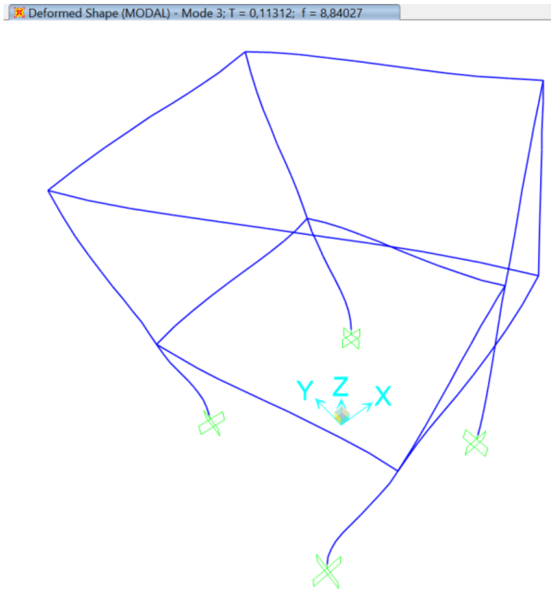
Deformed Shape (MODAL) - Mode 3; T = 0,11312; f = 8,84027

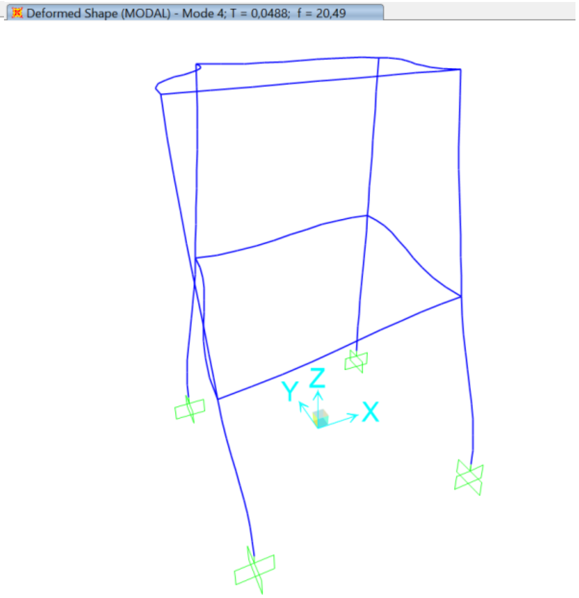
Deformed Shape (MODAL) - Mode 4; T = 0,0488; f = 20,49

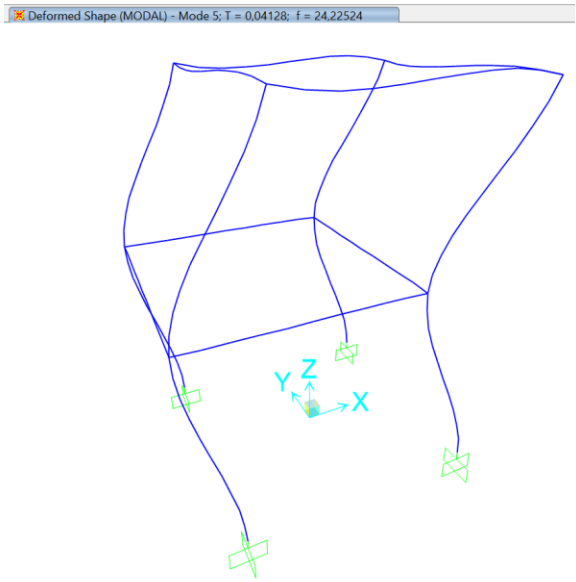

Deformed Shape (MODAL) - Mode 5; T = 0,04128; f = 24,22524

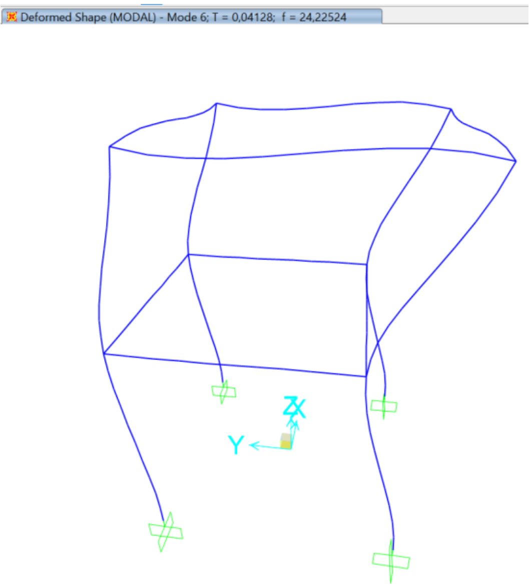

Deformed Shape (MODAL) - Mode 6; T = 0,04128; f = 24,22524

The response computed with the direct integration of motion Image 29.

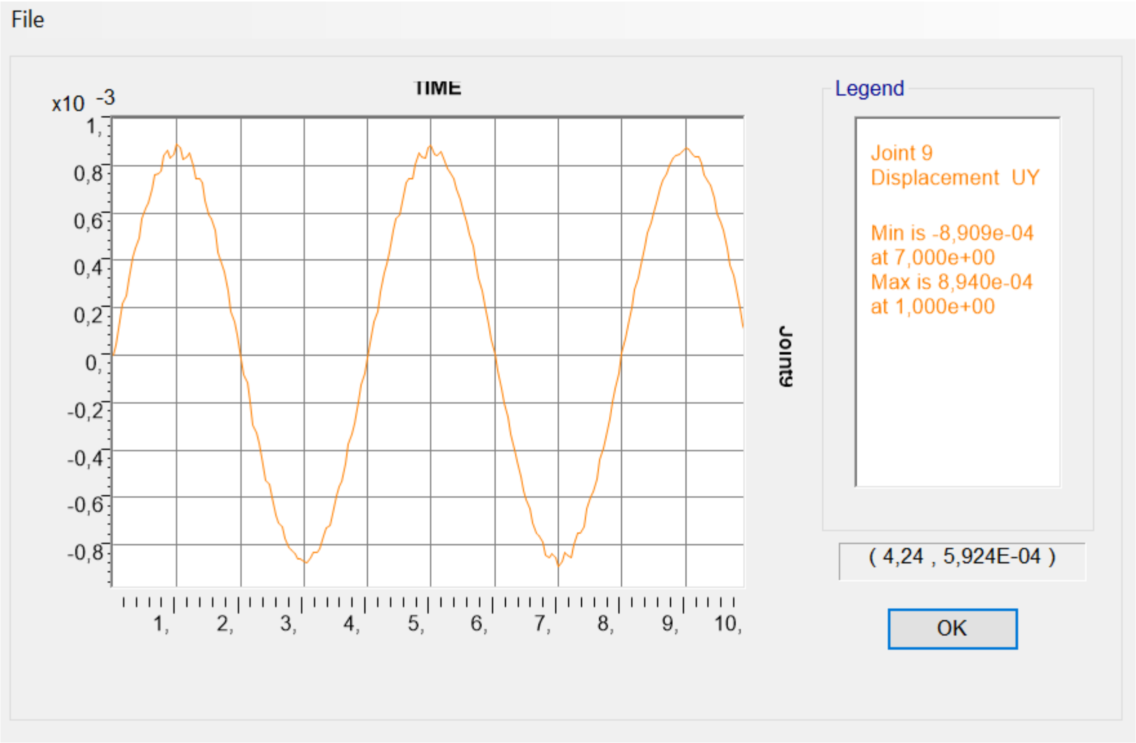

Joint 9
Displacement UY

Min is -8,909e-04
at 7,000e+00
Max is 8,940e-04
at 1,000e+00

(4,24 , 5,924E-04)

Image 29:Displacement of the 9th point in y-direction

The error computed for the first 8 modes is reported in the following:

mode	Sap2000	Code	Error [%]
1	0.128	0.12776939	0
2	0.128	0.12776939	0.1801606
3	0.1131	0.11280036	0.2649323
4	0.0488	0.04865136	0.3045839
5	0.0413	0.04147212	0.4167664
6	0.0413	0.04147212	0.4167664
7	0.0388	0.03902856	0.5890637
8	0.0329	0.0329834	0.2535999
		Total	**2.426**

The capability of the code to reproduce the dynamic response by means of the integrations of motion and to assess the modal information by solving the eigenvalue problem for 3D frames is verified as the error comparing the results of the code with the commercial code Sap2000 is less than 2.5%.

APPENDIX C: VARIANCE ANALYSIS GRAPHICS

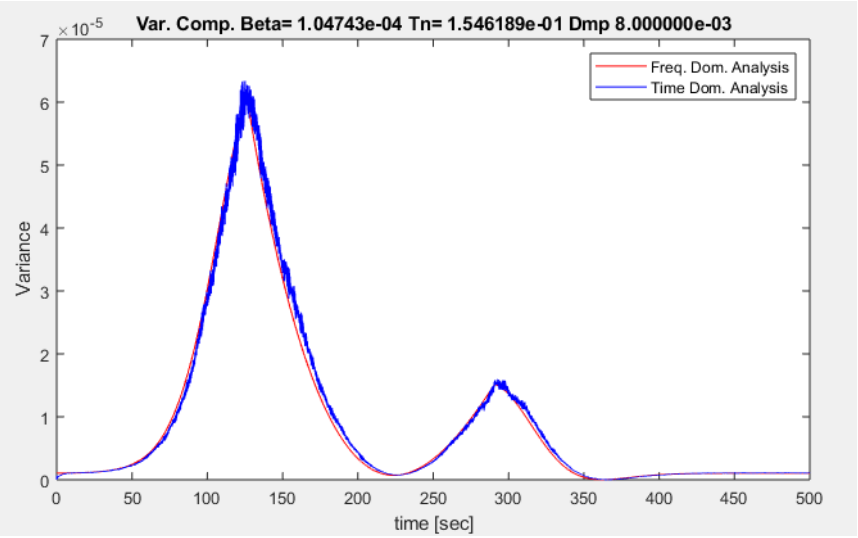
Var. Comp. Beta= 1.04743e-04 Tn= 1.546189e-01 Dmp 8.000000e-03
×10⁻⁵
7
6
5
4
3
2
1
0
Variance
0
50
100
150
200
250
300
350
400
450
500
time [sec]
Freq. Dom. Analysis
Time Dom. Analysis

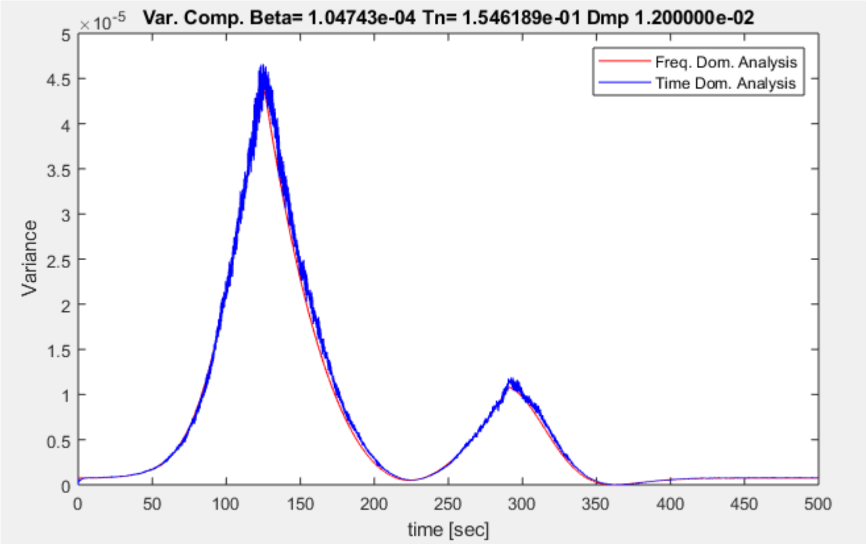
Var. Comp. Beta= 1.04743e-04 Tn= 1.546189e-01 Dmp 1.200000e-02
×10⁻⁵
5
4.5
4
3.5
3
2.5
2
1.5
1
0.5
0
Variance
0
50
100
150
200
250
300
350
400
450
500
time [sec]
Freq. Dom. Analysis
Time Dom. Analysis

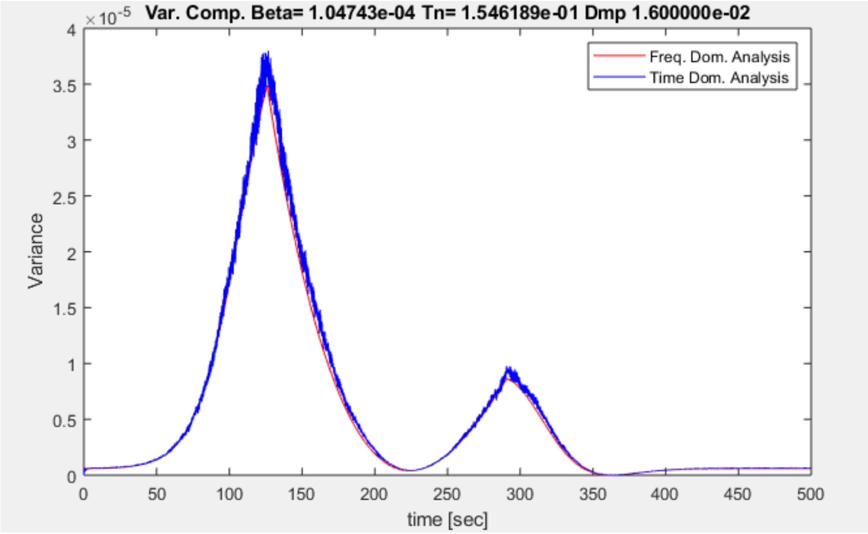
Var. Comp. Beta= 1.04743e-04 Tn= 1.546189e-01 Dmp 1.600000e-02
×10⁻⁵
4
3.5
3
2.5
2
1.5
1
0.5
0
Variance
0
50
100
150
200
250
300
350
400
450
500
time [sec]
Freq. Dom. Analysis
Time Dom. Analysis

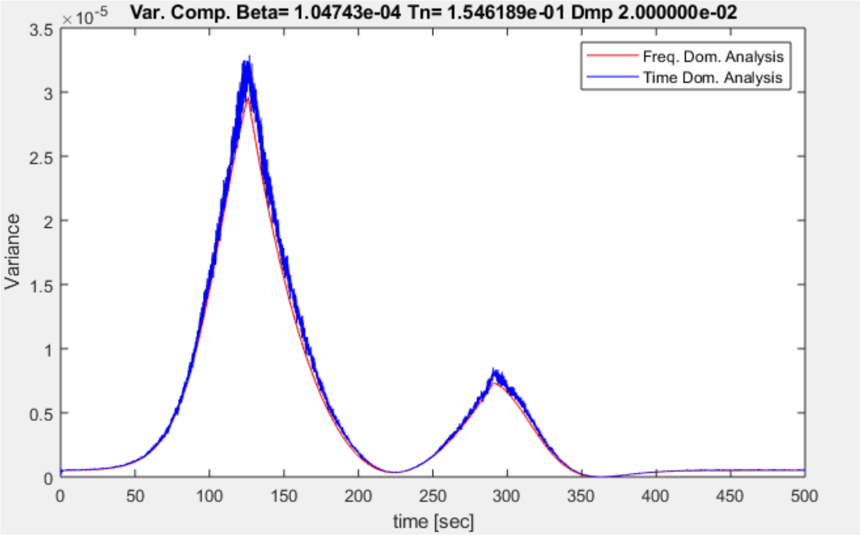
Var. Comp. Beta= 1.04743e-04 Tn= 1.546189e-01 Dmp 2.000000e-02
×10⁻⁵
3.5
3
2.5
2
1.5
1
0.5
0
Variance
0
50
100
150
200
250
300
350
400
450
500
time [sec]
Freq. Dom. Analysis
Time Dom. Analysis

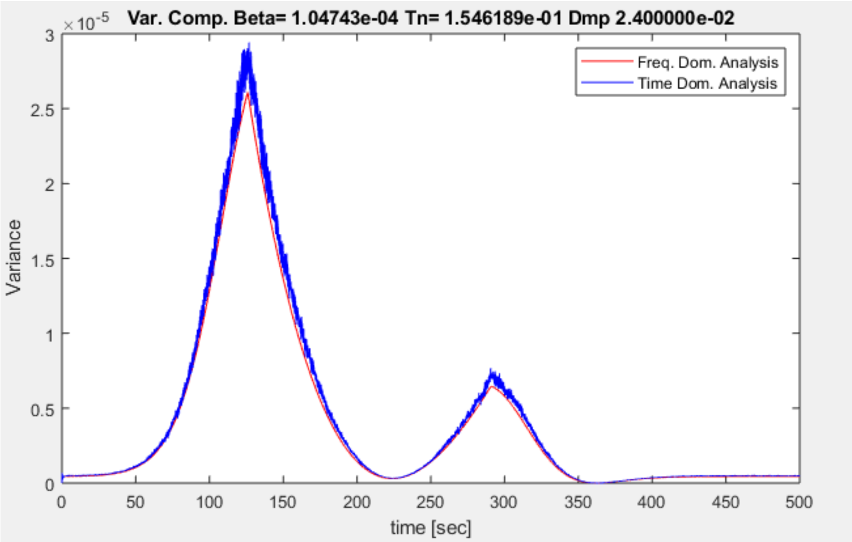
Var. Comp. Beta= 1.04743e-04 Tn= 1.546189e-01 Dmp 2.400000e-02
×10^-5
Freq. Dom. Analysis
Time Dom. Analysis
Variance
time [sec]
0
0.5
1
1.5
2
2.5
3
0
50
100
150
200
250
300
350
400
450
500

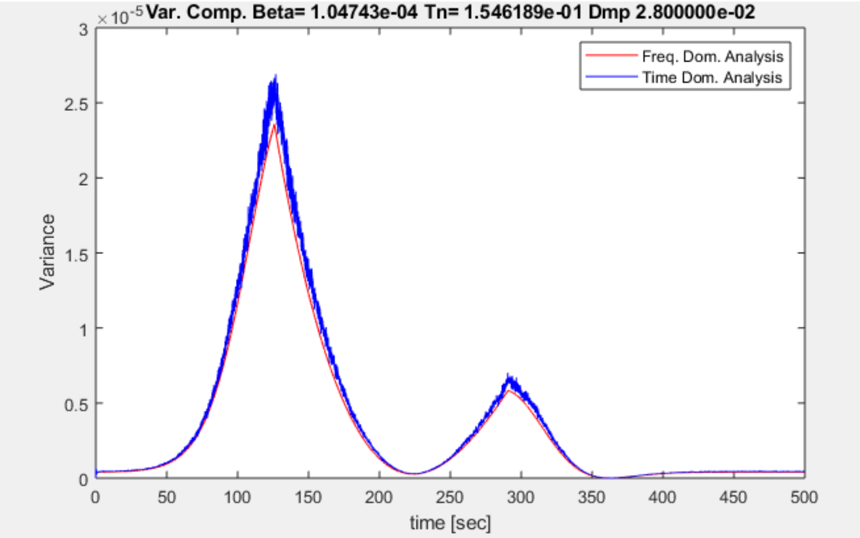
Var. Comp. Beta= 1.04743e-04 Tn= 1.546189e-01 Dmp 2.800000e-02
×10^-5
Freq. Dom. Analysis
Time Dom. Analysis
Variance
time [sec]
0
0.5
1
1.5
2
2.5
3
0
50
100
150
200
250
300
350
400
450
500

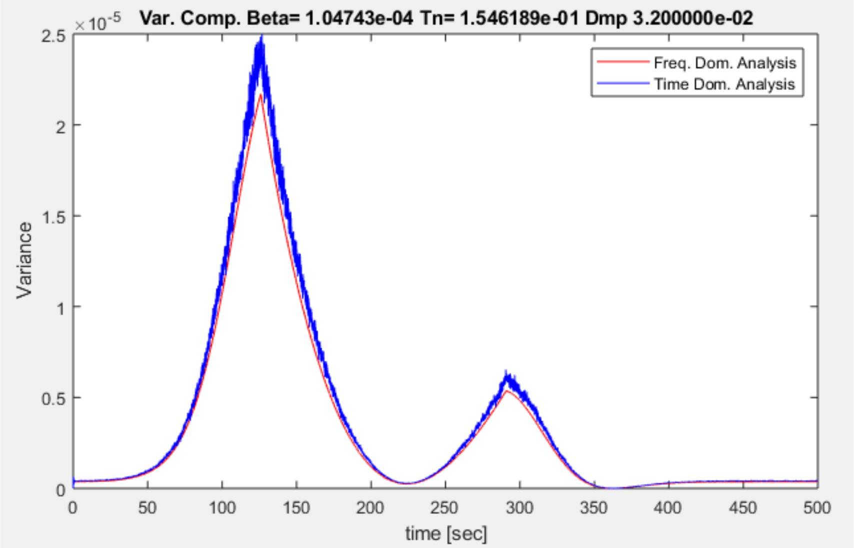
Var. Comp. Beta= 1.04743e-04 Tn= 1.546189e-01 Dmp 3.200000e-02
×10^-5
Freq. Dom. Analysis
Time Dom. Analysis
Variance
time [sec]
0
0.5
1
1.5
2
2.5
0
50
100
150
200
250
300
350
400
450
500

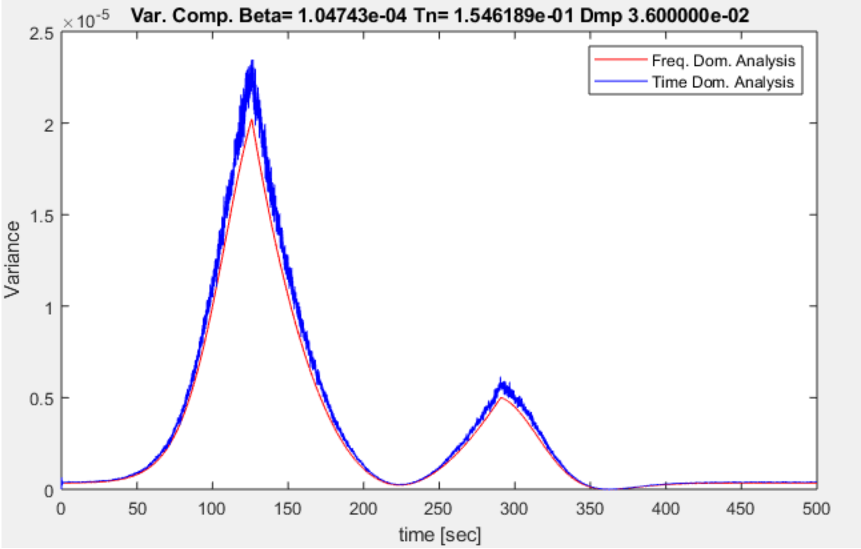
Var. Comp. Beta= 1.04743e-04 Tn= 1.546189e-01 Dmp 3.600000e-02
×10^-5
Freq. Dom. Analysis
Time Dom. Analysis
Variance
time [sec]
0
0.5
1
1.5
2
2.5
0
50
100
150
200
250
300
350
400
450
500

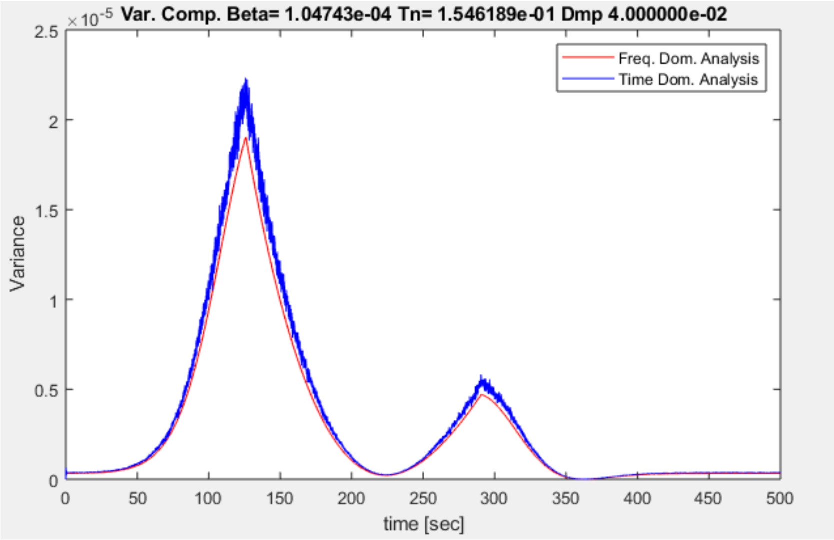
Var. Comp. Beta= 1.04743e-04 Tn= 1.546189e-01 Dmp 4.000000e-02
× 10^-5
Variance
2.5
2
1.5
1
0.5
0
0
50
100
150
200
250
300
350
400
450
500
time [sec]
Freq. Dom. Analysis
Time Dom. Analysis

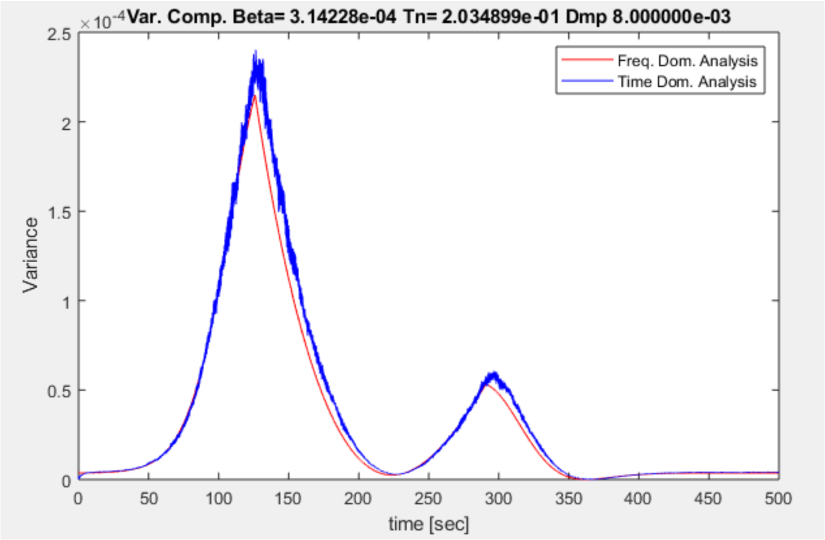
Var. Comp. Beta= 3.14228e-04 Tn= 2.034899e-01 Dmp 8.000000e-03
× 10^-4
Variance
2.5
2
1.5
1
0.5
0
0
50
100
150
200
250
300
350
400
450
500
time [sec]
Freq. Dom. Analysis
Time Dom. Analysis

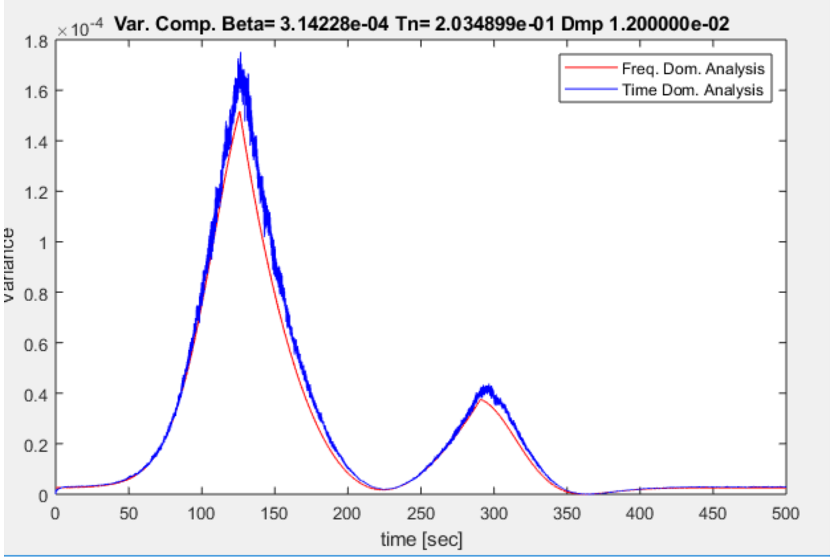
Var. Comp. Beta= 3.14228e-04 Tn= 2.034899e-01 Dmp 1.200000e-02
× 10^-4
Variance
1.8
1.6
1.4
1.2
1
0.8
0.6
0.4
0.2
0
0
50
100
150
200
250
300
350
400
450
500
time [sec]
Freq. Dom. Analysis
Time Dom. Analysis

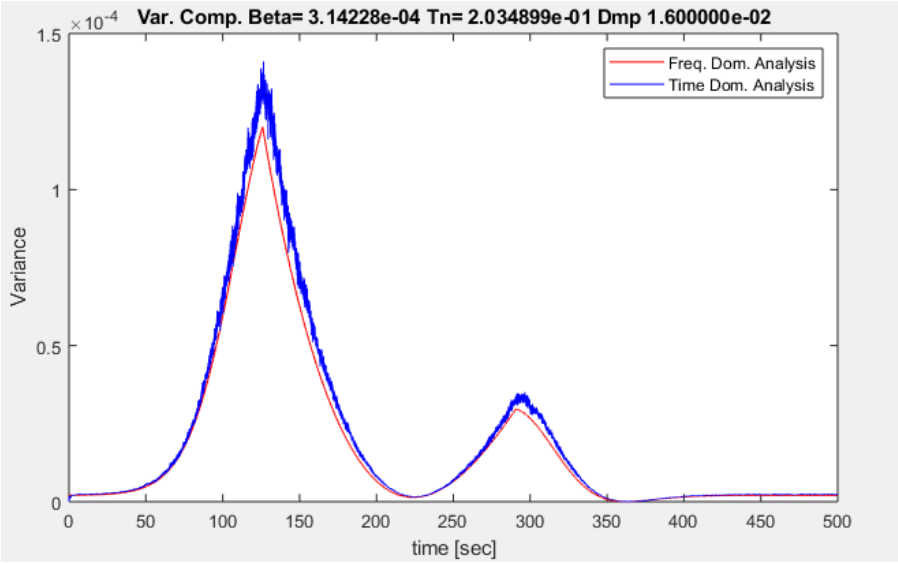
Var. Comp. Beta= 3.14228e-04 Tn= 2.034899e-01 Dmp 1.600000e-02
× 10^-4
Variance
1.5
1
0.5
0
0
50
100
150
200
250
300
350
400
450
500
time [sec]
Freq. Dom. Analysis
Time Dom. Analysis

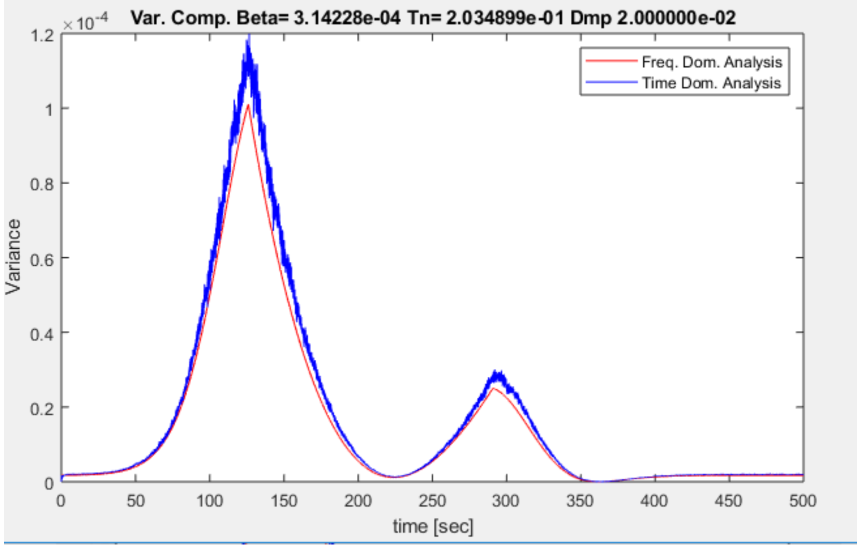
Var. Comp. Beta= 3.14228e-04 Tn= 2.034899e-01 Dmp 2.000000e-02

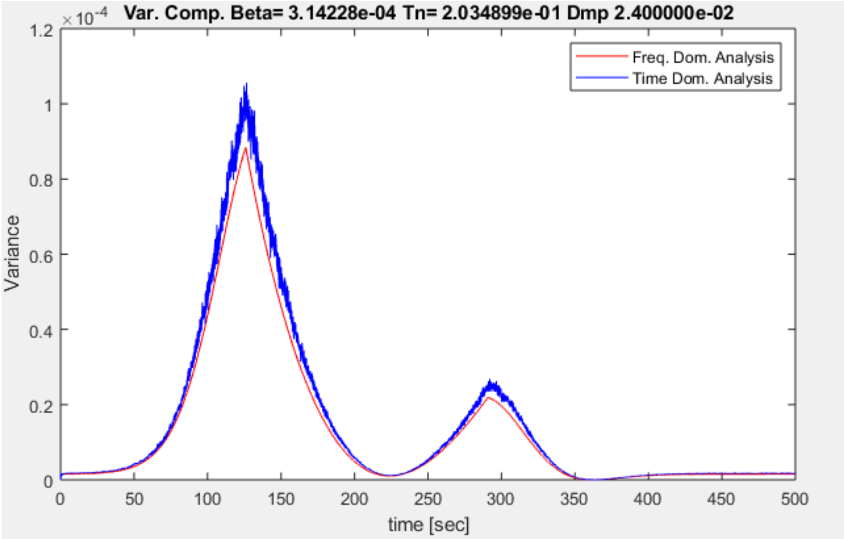
Var. Comp. Beta= 3.14228e-04 Tn= 2.034899e-01 Dmp 2.400000e-02

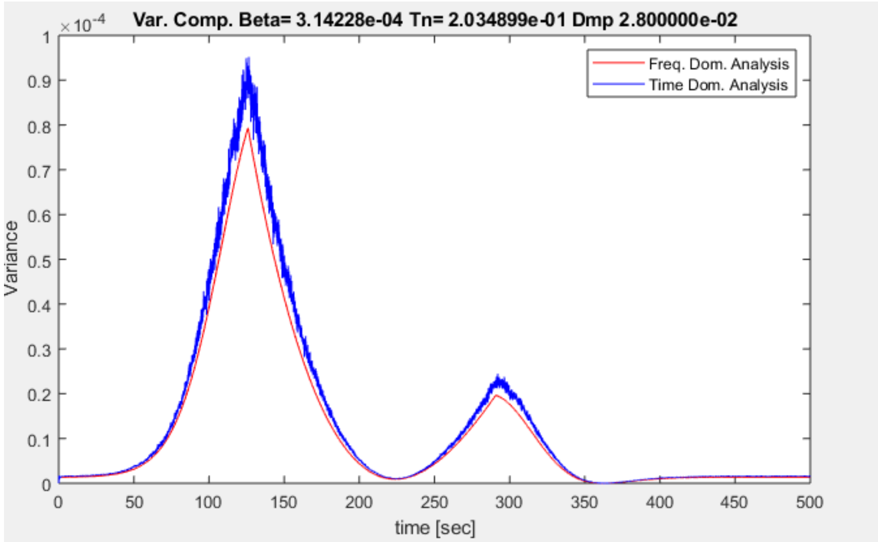
Var. Comp. Beta= 3.14228e-04 Tn= 2.034899e-01 Dmp 2.800000e-02

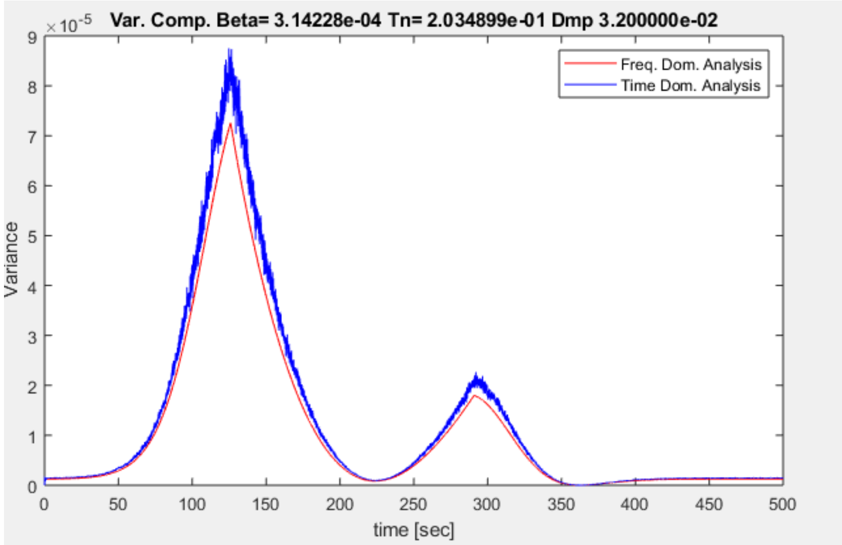
Var. Comp. Beta= 3.14228e-04 Tn= 2.034899e-01 Dmp 3.200000e-02

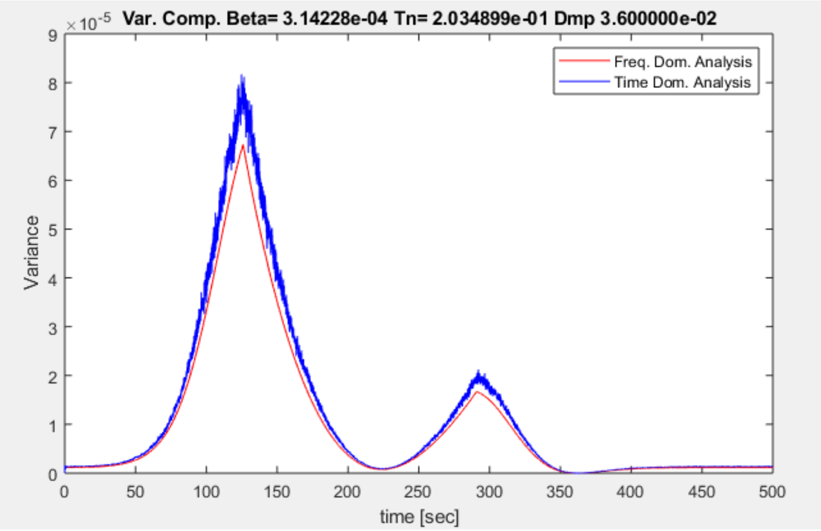

Var. Comp. Beta= 3.14228e-04 Tn= 2.034899e-01 Dmp 3.600000e-02

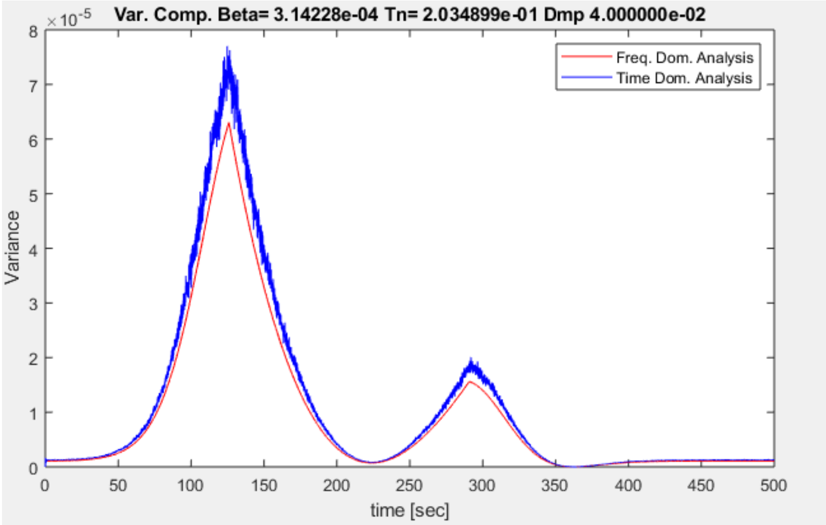

Var. Comp. Beta= 3.14228e-04 Tn= 2.034899e-01 Dmp 4.000000e-02

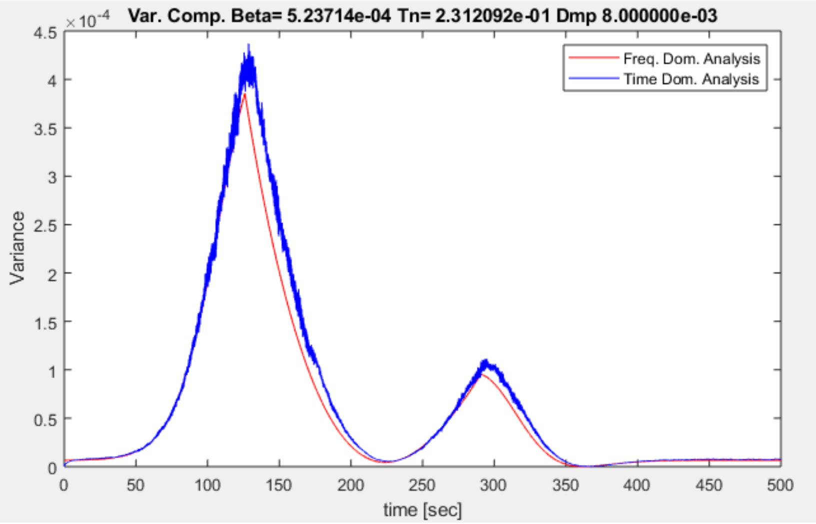

Var. Comp. Beta= 5.23714e-04 Tn= 2.312092e-01 Dmp 8.000000e-03

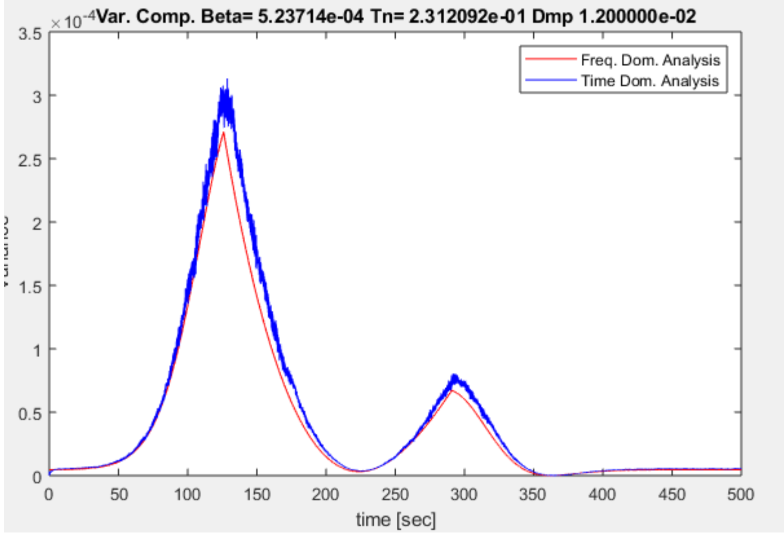

Var. Comp. Beta= 5.23714e-04 Tn= 2.312092e-01 Dmp 1.200000e-02

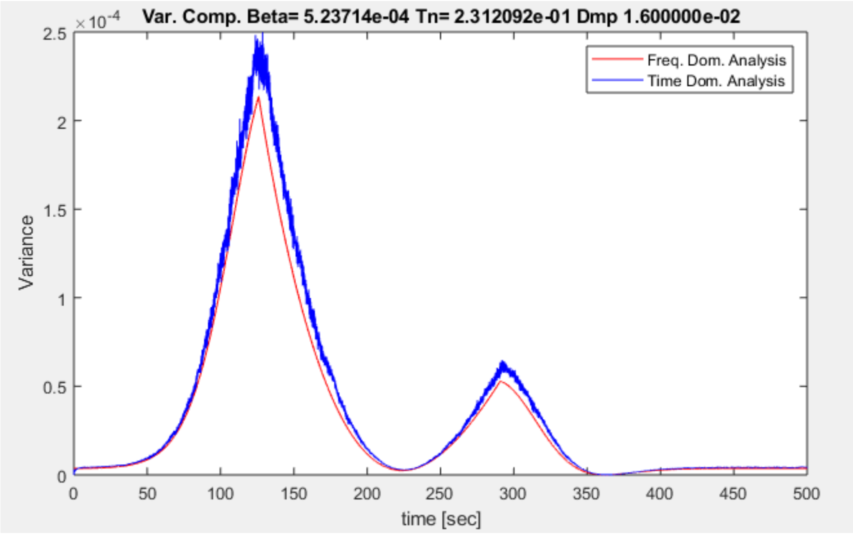
Var. Comp. Beta= 5.23714e-04 Tn= 2.312092e-01 Dmp 1.600000e-02
×10^-4
Variance
0
0.5
1
1.5
2
2.5
time [sec]
0
50
100
150
200
250
300
350
400
450
500
Freq. Dom. Analysis
Time Dom. Analysis

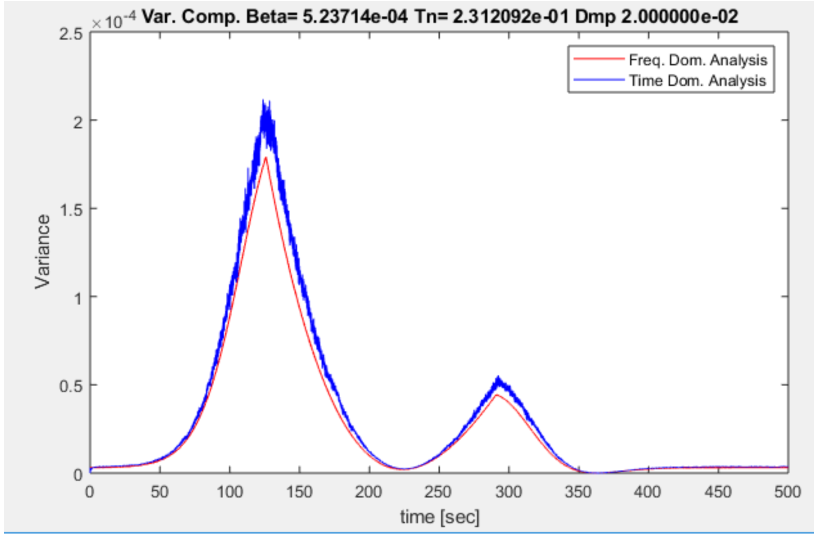
Var. Comp. Beta= 5.23714e-04 Tn= 2.312092e-01 Dmp 2.000000e-02
×10^-4
Variance
0
0.5
1
1.5
2
2.5
time [sec]
0
50
100
150
200
250
300
350
400
450
500
Freq. Dom. Analysis
Time Dom. Analysis

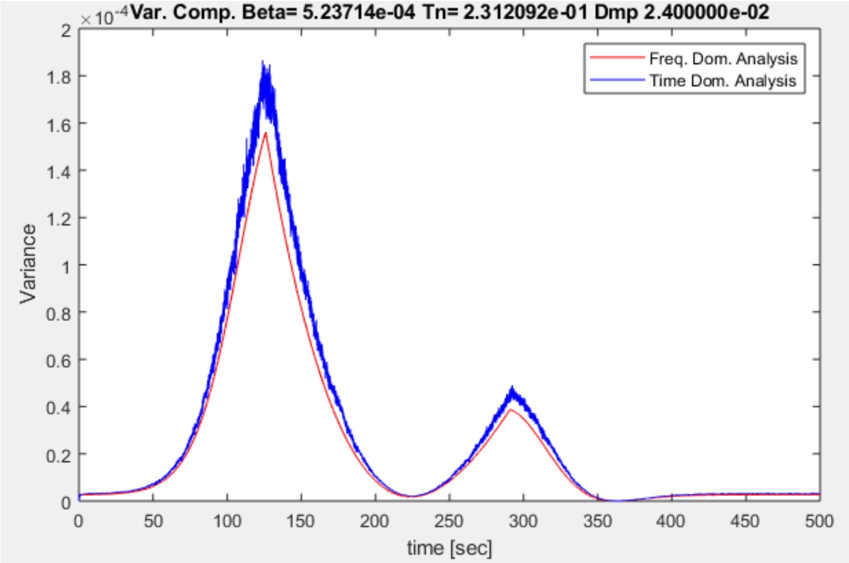
Var. Comp. Beta= 5.23714e-04 Tn= 2.312092e-01 Dmp 2.400000e-02
×10^-4
Variance
0
0.2
0.4
0.6
0.8
1
1.2
1.4
1.6
1.8
2
time [sec]
0
50
100
150
200
250
300
350
400
450
500
Freq. Dom. Analysis
Time Dom. Analysis

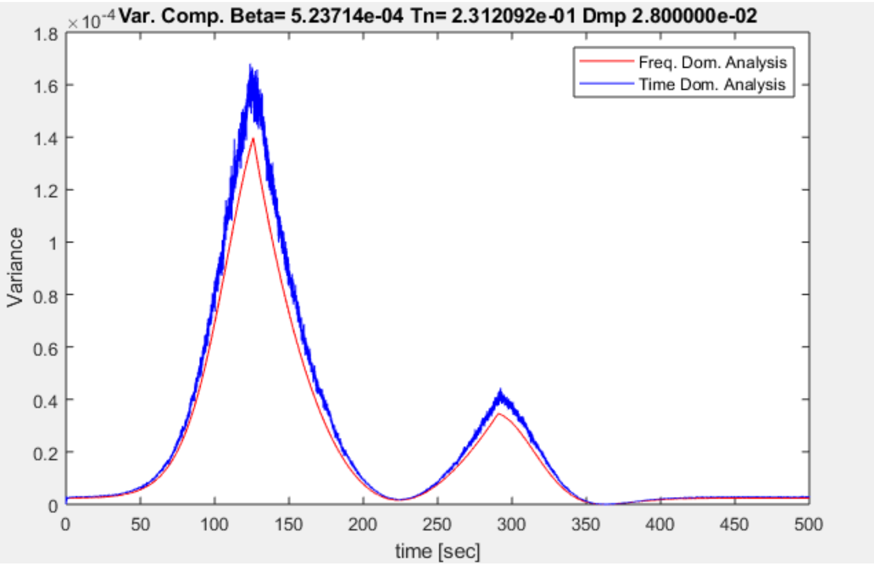
Var. Comp. Beta= 5.23714e-04 Tn= 2.312092e-01 Dmp 2.800000e-02
×10^-4
Variance
0
0.2
0.4
0.6
0.8
1
1.2
1.4
1.6
1.8
time [sec]
0
50
100
150
200
250
300
350
400
450
500
Freq. Dom. Analysis
Time Dom. Analysis

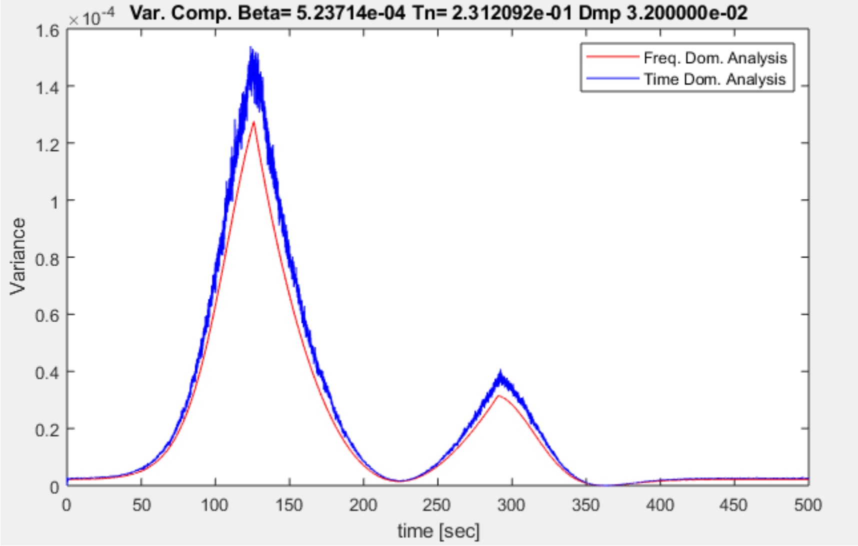
Var. Comp. Beta= 5.23714e-04 Tn= 2.312092e-01 Dmp 3.200000e-02
×10^-4
1.6
1.4
1.2
1
0.8
0.6
0.4
0.2
0
Variance
0
50
100
150
200
250
300
350
400
450
500
time [sec]
Freq. Dom. Analysis
Time Dom. Analysis

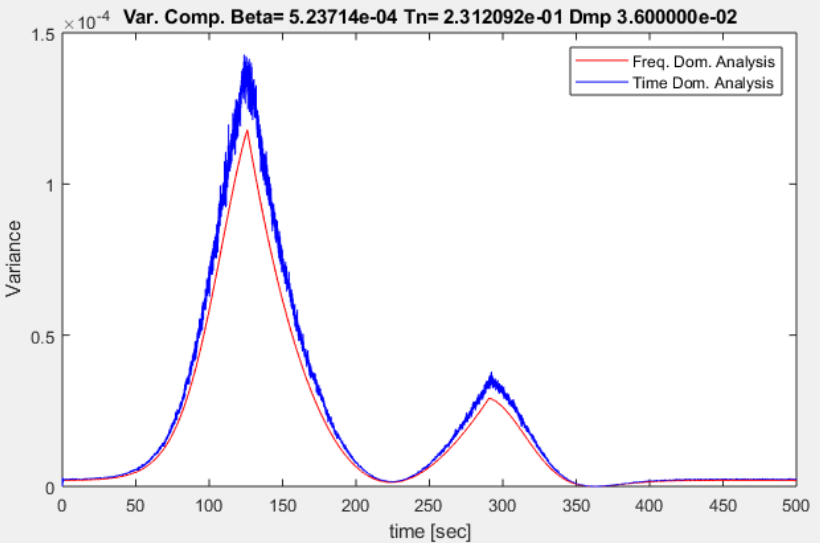
Var. Comp. Beta= 5.23714e-04 Tn= 2.312092e-01 Dmp 3.600000e-02
×10^-4
1.5
1
0.5
0
Variance
0
50
100
150
200
250
300
350
400
450
500
time [sec]
Freq. Dom. Analysis
Time Dom. Analysis

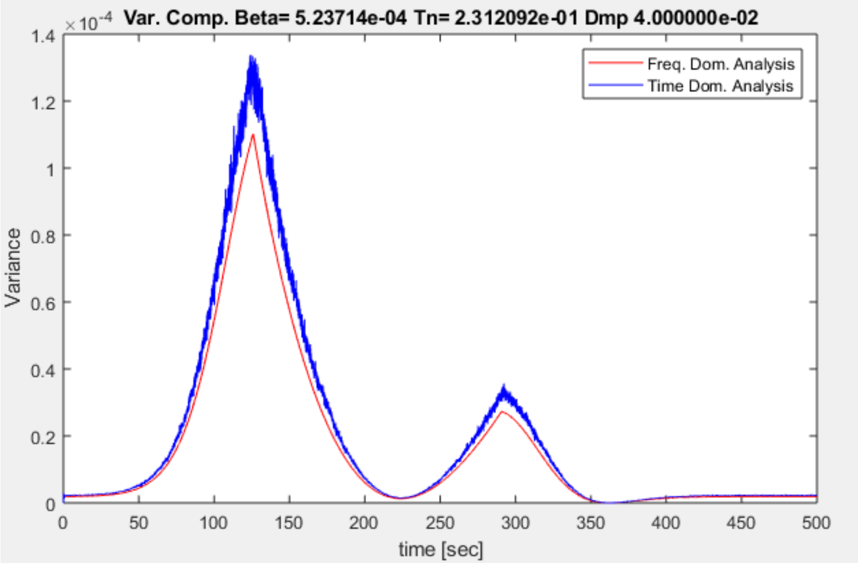
Var. Comp. Beta= 5.23714e-04 Tn= 2.312092e-01 Dmp 4.000000e-02
×10^-4
1.4
1.2
1
0.8
0.6
0.4
0.2
0
Variance
0
50
100
150
200
250
300
350
400
450
500
time [sec]
Freq. Dom. Analysis
Time Dom. Analysis

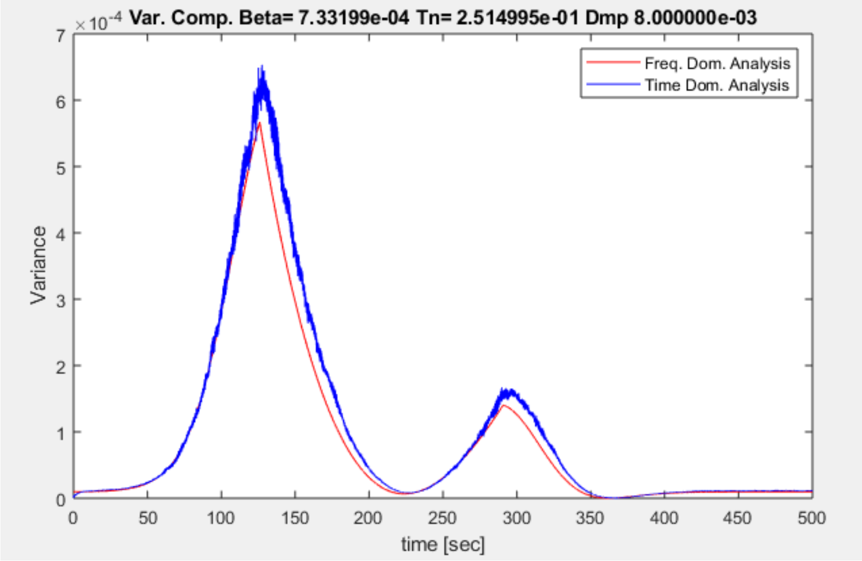
Var. Comp. Beta= 7.33199e-04 Tn= 2.514995e-01 Dmp 8.000000e-03
×10^-4
7
6
5
4
3
2
1
0
Variance
0
50
100
150
200
250
300
350
400
450
500
time [sec]
Freq. Dom. Analysis
Time Dom. Analysis

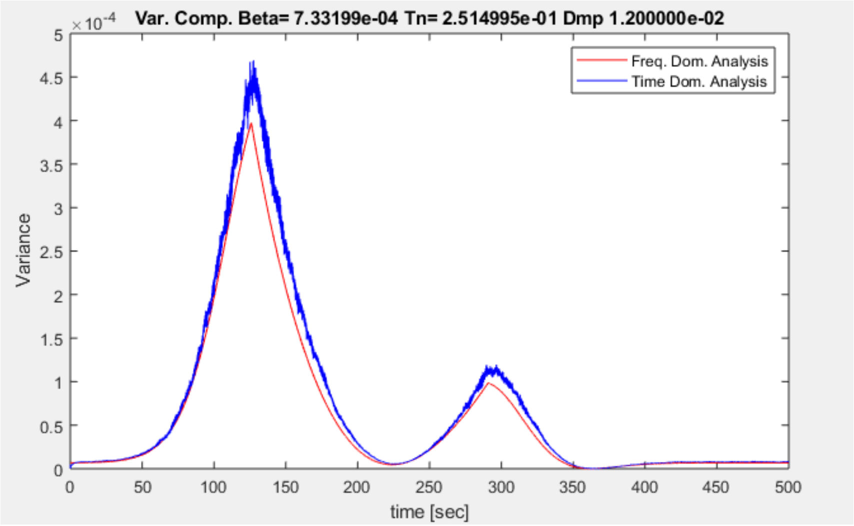
Var. Comp. Beta= 7.33199e-04 Tn= 2.514995e-01 Dmp 1.200000e-02
×10^-4
Variance
0
0.5
1
1.5
2
2.5
3
3.5
4
4.5
5
time [sec]
0
50
100
150
200
250
300
350
400
450
500
Freq. Dom. Analysis
Time Dom. Analysis

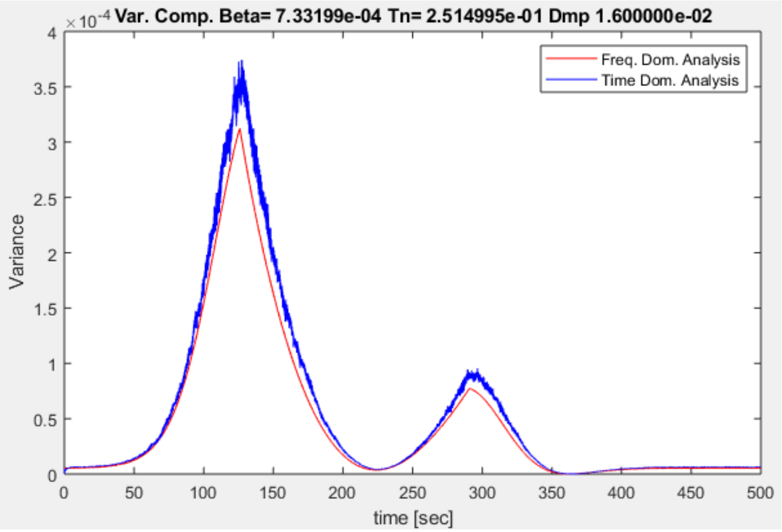
Var. Comp. Beta= 7.33199e-04 Tn= 2.514995e-01 Dmp 1.600000e-02
×10^-4
Variance
0
0.5
1
1.5
2
2.5
3
3.5
4
time [sec]
0
50
100
150
200
250
300
350
400
450
500
Freq. Dom. Analysis
Time Dom. Analysis

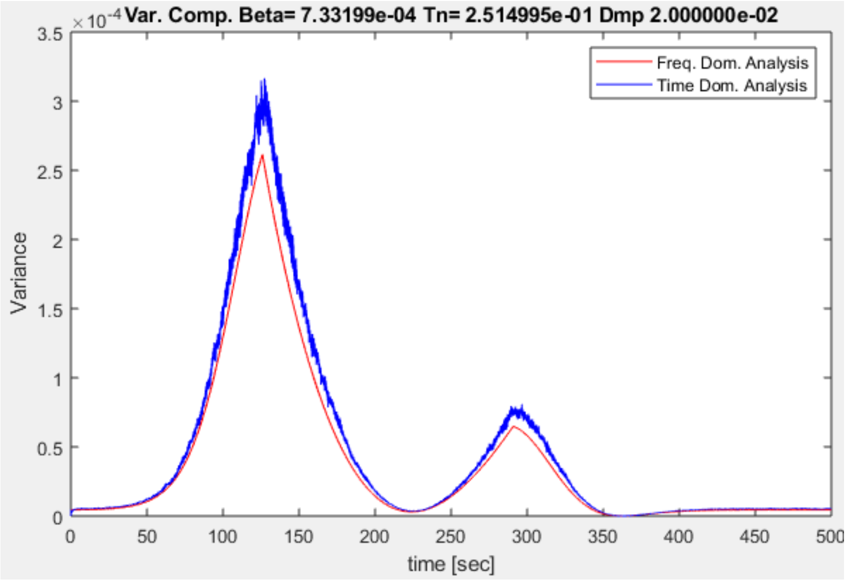
Var. Comp. Beta= 7.33199e-04 Tn= 2.514995e-01 Dmp 2.000000e-02
×10^-4
Variance
0
0.5
1
1.5
2
2.5
3
3.5
time [sec]
0
50
100
150
200
250
300
350
400
450
500
Freq. Dom. Analysis
Time Dom. Analysis

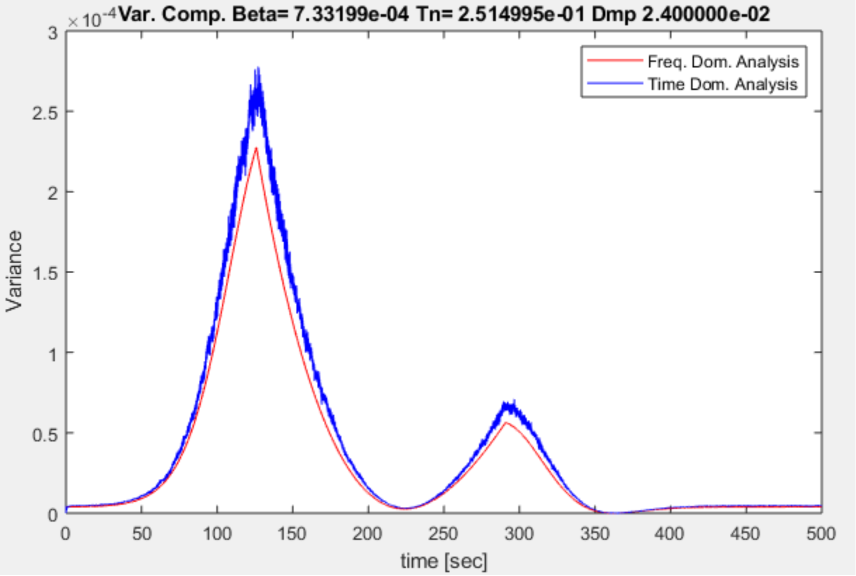
Var. Comp. Beta= 7.33199e-04 Tn= 2.514995e-01 Dmp 2.400000e-02
×10^-4
Variance
0
0.5
1
1.5
2
2.5
3
time [sec]
0
50
100
150
200
250
300
350
400
450
500
Freq. Dom. Analysis
Time Dom. Analysis

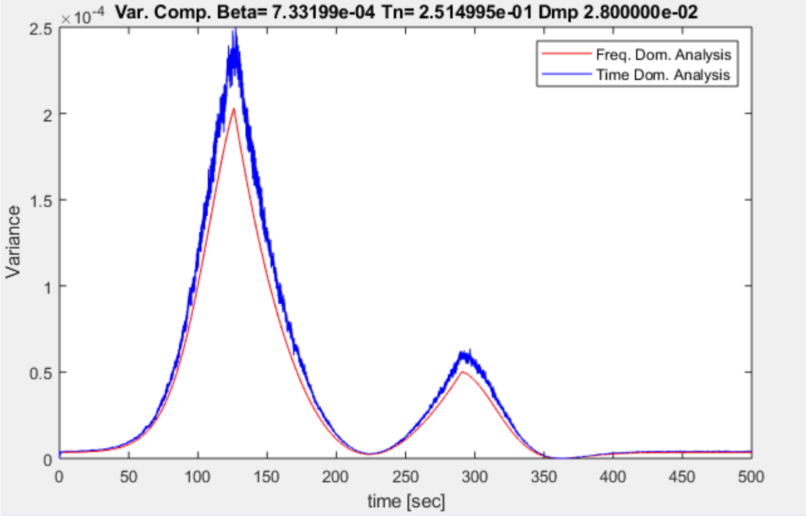
×10^-4
Var. Comp. Beta= 7.33199e-04 Tn= 2.514995e-01 Dmp 2.800000e-02
Freq. Dom. Analysis
Time Dom. Analysis
Variance
2.5
2
1.5
1
0.5
0
0
50
100
150
200
250
300
350
400
450
500
time [sec]

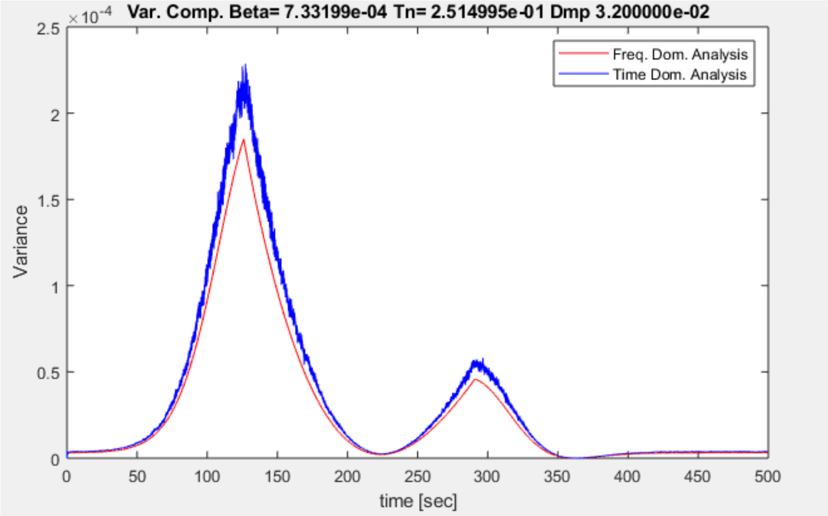
×10^-4
Var. Comp. Beta= 7.33199e-04 Tn= 2.514995e-01 Dmp 3.200000e-02
Freq. Dom. Analysis
Time Dom. Analysis
Variance
2.5
2
1.5
1
0.5
0
0
50
100
150
200
250
300
350
400
450
500
time [sec]

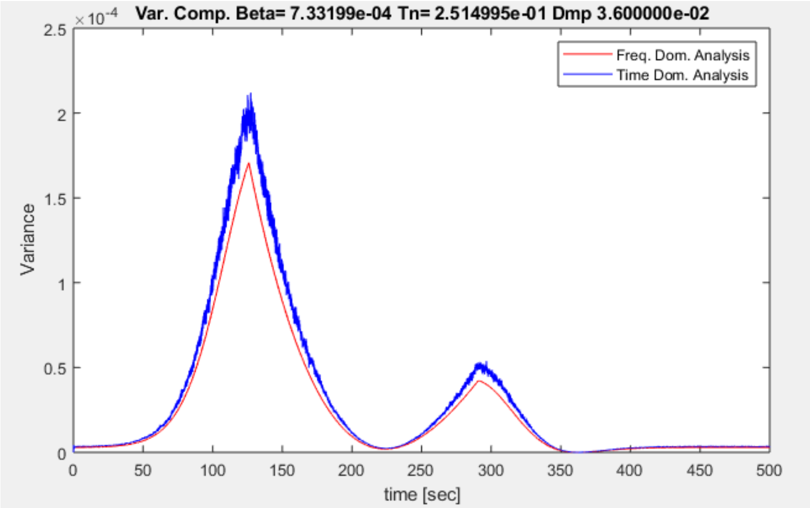
×10^-4
Var. Comp. Beta= 7.33199e-04 Tn= 2.514995e-01 Dmp 3.600000e-02
Freq. Dom. Analysis
Time Dom. Analysis
Variance
2.5
2
1.5
1
0.5
0
0
50
100
150
200
250
300
350
400
450
500
time [sec]

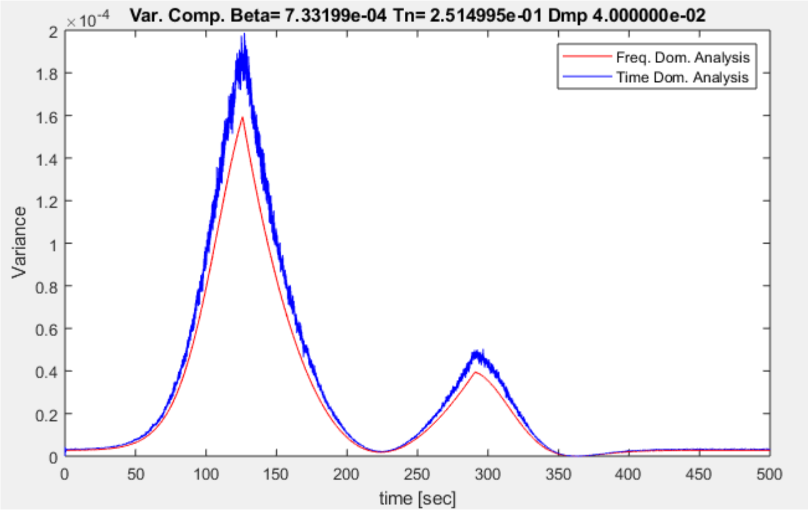
×10^-4
Var. Comp. Beta= 7.33199e-04 Tn= 2.514995e-01 Dmp 4.000000e-02
Freq. Dom. Analysis
Time Dom. Analysis
Variance
2
1.8
1.6
1.4
1.2
1
0.8
0.6
0.4
0.2
0
0
50
100
150
200
250
300
350
400
450
500
time [sec]

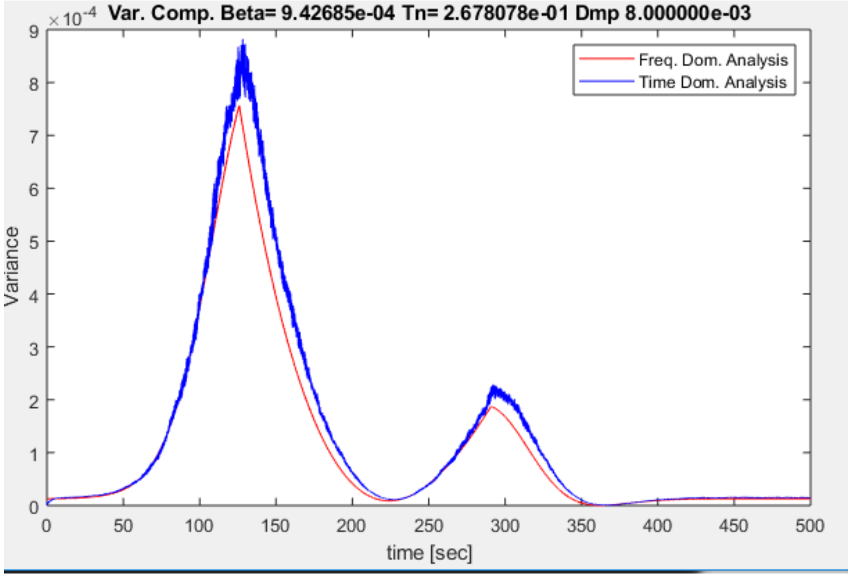
Var. Comp. Beta= 9.42685e-04 Tn= 2.678078e-01 Dmp 8.000000e-03
×10^-4
Variance
0
1
2
3
4
5
6
7
8
9
time [sec]
0
50
100
150
200
250
300
350
400
450
500
Freq. Dom. Analysis
Time Dom. Analysis

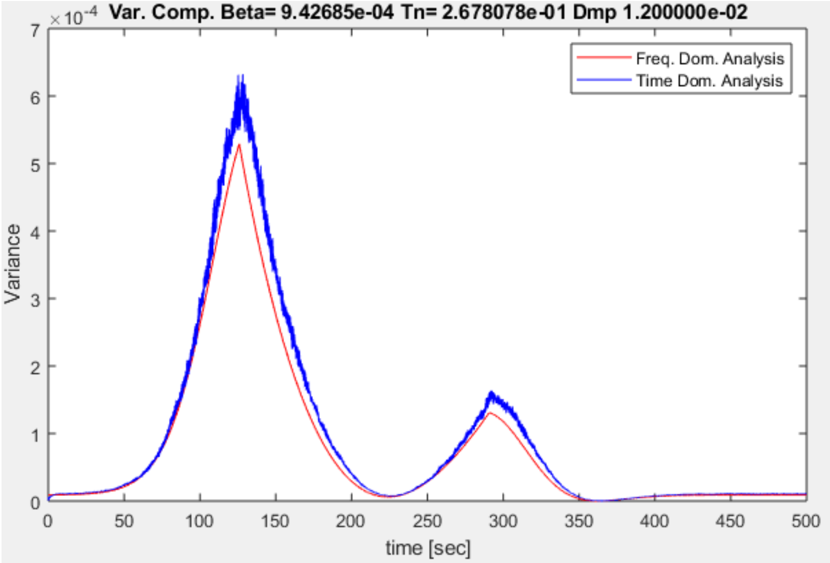
Var. Comp. Beta= 9.42685e-04 Tn= 2.678078e-01 Dmp 1.200000e-02
×10^-4
Variance
0
1
2
3
4
5
6
7
time [sec]
0
50
100
150
200
250
300
350
400
450
500
Freq. Dom. Analysis
Time Dom. Analysis

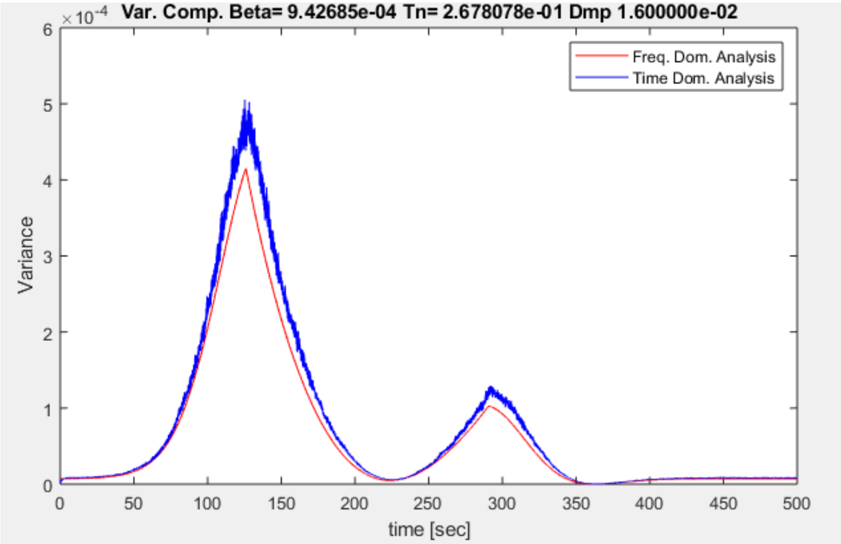
Var. Comp. Beta= 9.42685e-04 Tn= 2.678078e-01 Dmp 1.600000e-02
×10^-4
Variance
0
1
2
3
4
5
6
time [sec]
0
50
100
150
200
250
300
350
400
450
500
Freq. Dom. Analysis
Time Dom. Analysis

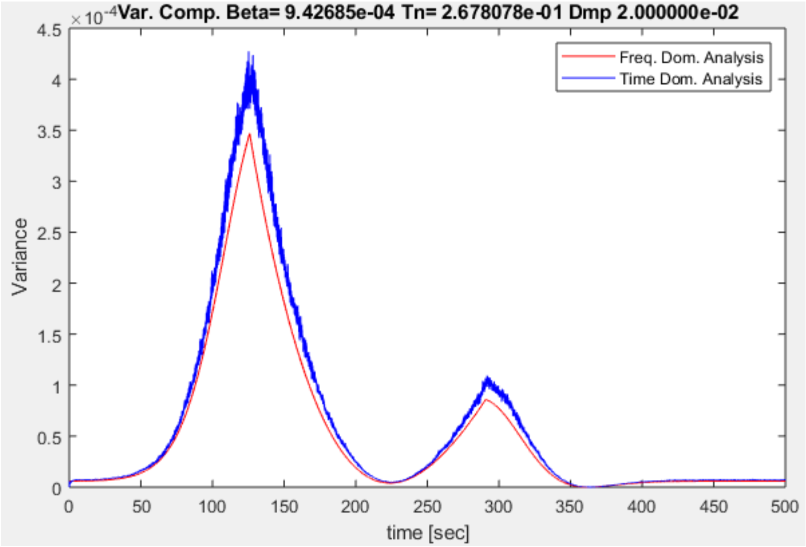
Var. Comp. Beta= 9.42685e-04 Tn= 2.678078e-01 Dmp 2.000000e-02
×10^-4
Variance
0
0.5
1
1.5
2
2.5
3
3.5
4
4.5
time [sec]
0
50
100
150
200
250
300
350
400
450
500
Freq. Dom. Analysis
Time Dom. Analysis

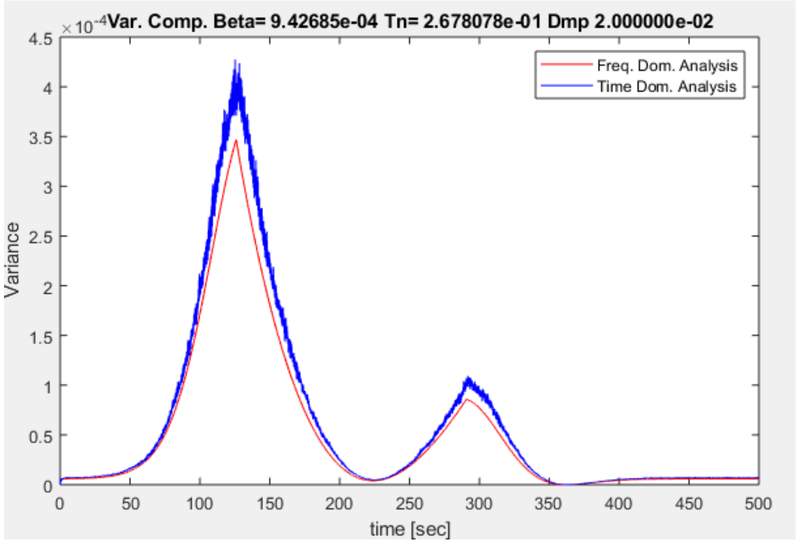
Var. Comp. Beta= 9.42685e-04 Tn= 2.678078e-01 Dmp 2.000000e-02

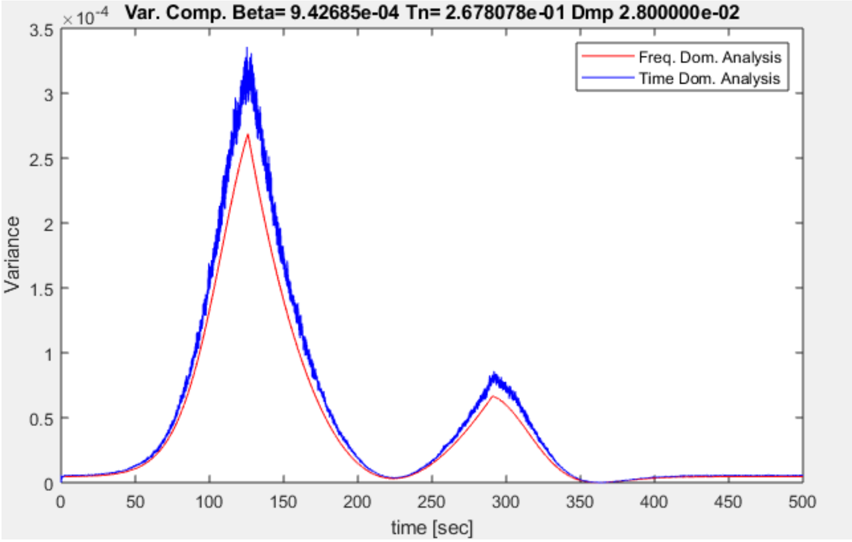
Var. Comp. Beta= 9.42685e-04 Tn= 2.678078e-01 Dmp 2.800000e-02

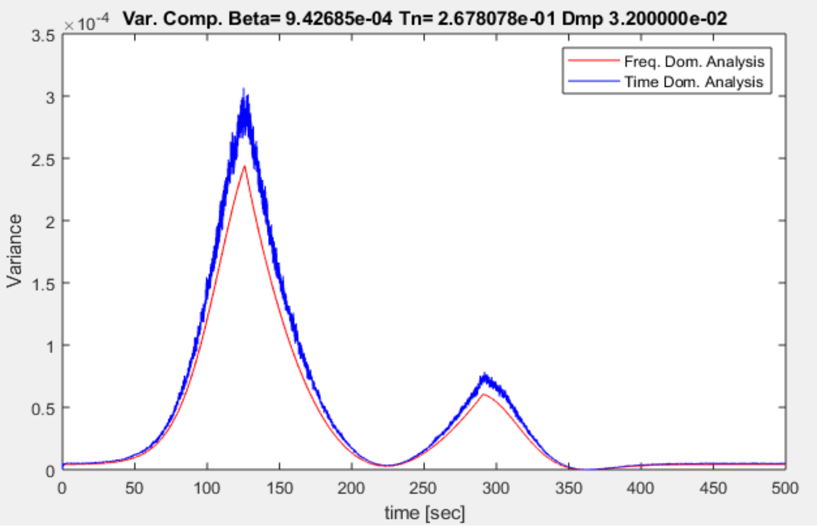
Var. Comp. Beta= 9.42685e-04 Tn= 2.678078e-01 Dmp 3.200000e-02

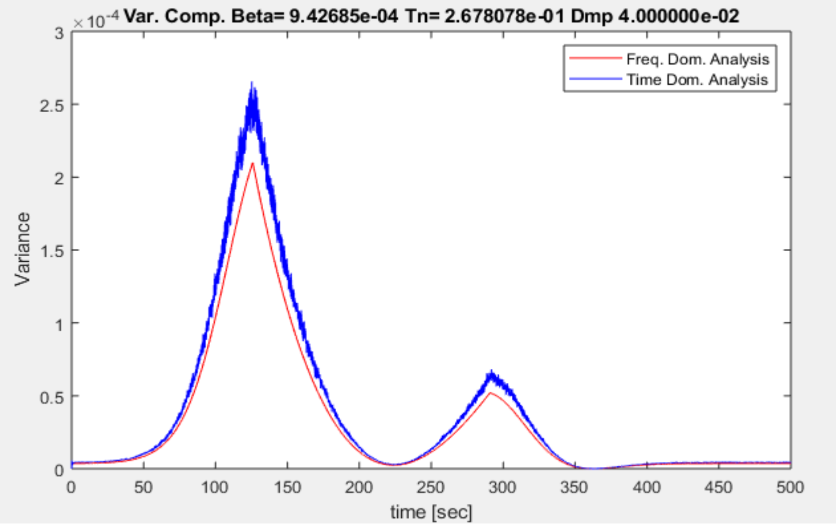
Var. Comp. Beta= 9.42685e-04 Tn= 2.678078e-01 Dmp 4.000000e-02